AD-A065 736 VARIAN ASSOCIATES BEVERLY MASS F/G 9/1
CFA DESIGN IMPROVEMENT PROGRAM. VOLUME II. COMPUTER MODELING ST--ETC(U)
JUN 78 H L MCDOWELL N00123-75-C-1294
UNCLASSIFIED NL

1 OF 4
AD
AD 65736

LEVEL II

AD A065735

CFA Design Improvement Program
Volume II--Computer Modeling Studies

-Final Report-

PREPARED FOR:

U.S. NAVY OCEAN SYSTEMS CENTER

271 CATALINA BOULEVARD

SAN DIEGO, CALIFORNIA 92152

CONTRACT NO. N00123-75-C-1294

2 JUNE 1978

VARIAN/BEVERLY

(1)

(6) CEA DESIGN IMPROVEMENT PROGRAM

VOLUME II - COMPUTER MODELING STUDIES

(9) FINAL REPORT

PREPARED FOR:

U.S. NAVY OCEAN SYSTEMS COMMAND

271 CATALINA BOULEVARD

SAN DIEGO, CALIFORNIA 92152

(15) CONTRACT NO. N00123-75-C-1294

(10) PREPARED BY:

HUNTER L. MCDOWELL

VARIAN ASSOCIATES, INC.

EIGHT SALEM ROAD

BEVERLY, MASSACHUSETTS 01915

Approved for public release; distribution is unlimited

(11) 2 JUNE 1978

(12) 324 P.

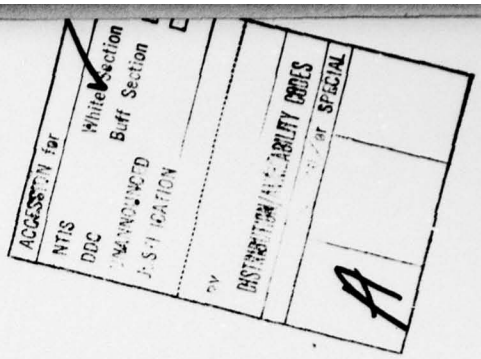

TABLE OF CONTENTS

TABLE OF CONTENTS
(continued)

TABLE OF CONTENTS

TABLE OF CONTENTS
(continued)

1.0 INTRODUCTION

This is the second volume of the final report on contract No. N00123-75-C-1294. The effort on this contract has encompassed combined experimental and computer modeling studies of forward wave, crossed-field amplifiers. An instrumented version of the SFD-261 CFA is being used as a vehicle in these studies. The overall objectives of the effort and the experimental studies were described in Volume I of this report. This second volume describes the computer modeling studies which were conducted in parallel with the experimental effort. The results of correlation studies between the computer model and an instrumented CFA are also described in this volume.

The computer model is of the two dimensional, single traveling wavelength variety. A program of this type was originally developed by Yu, Kooyers and Buneman.[1,2] An updated version of this program was obtained from G.P. Kooyers of Universal Computer Applications and modified by Varian--particularly in the area of data presentation procedures. Mr. Kooyers, operating under a subcontract from Varian to Universal Computer Applications (UCA), then assisted us in applying the program to the SFD-261 CFA and in installing the program on a Navy IBM 360/65 computer at the Naval Ocean Systems Center (NOSC), San Diego, California. After completion of the UCA subcontract, Varian further modified the program, most significantly in the areas of emission and taper procedures. The successive program modifications were installed on the Navy IBM 360/65 and

subsequently the Navy Univac 1110 computer at NOSC. Most of the results presented in this report were obtained using the Navy facility. Mr. H. Sorem of NOSC assisted us in submitting these runs and in transmitting results to Varian. Additional results were obtained by Varian using a commercial computer service in the Boston area.

The computer model is described in Section 2 of this report. The various assumptions involved in the use of this type of model are also discussed. The two dimensional, single wavelength model contains a number of simplifying assumptions, the use of which appears justified--at least for uniform interaction geometries operated in a space charge limited regime--by our ability to obtain a satisfactory correlation (within $\pm$10%) between computer model and instrumented CFA results. These correlation studies are discussed in Section 3 of this report.

When computations were conducted in an emission-limited regime or when the interaction geometry was not uniform around the circumference of the CFA, the correlations between computer model results and CFA results were not satisfactory. The problem with emission-limited calculations lies partly in a numerical instability in the program and partly in the validity of the secondary emission data supplied to the program. We believe the program problem has been corrected, but have not had the opportunity to verify the correction under this contract. The problem of what secondary emission data to use remains a significant one because the yield

obtained in an operating CFA environment frequently appears to differ from results obtained under ideal conditions in secondary emission testers. Recently, the Naval Research Laboratory (NRL) has obtained secondary emission data for beryllium which is used as the cathode secondary emitter in the SFD-261 CFA.[3] These data show an initial lower yield for a clean cathode than we used in our computations. In addition, the NRL data show the possibility of further yield reduction by poisoning. Fortunately, the calculations do not appear sensitive to the exact secondary emission yield in the space charge-limited regime. The problems with identifying the proper yield and making the simulation run correctly in the emission-limited regime must, however, be resolved before the computer program can be used to predict the maximum available currents from a postulated design.

The problem with tapered geometries may lie either in the computer model or in the secondary emission data. A study of our uniform geometry results suggests that the tapered geometries studied may be entering the emission-limited regime over part of the circumference. A further study of these problems is contemplated.

The ability to obtain a satisfactory correlation between the computer model and instrumented CFA in the space charge-limited regime is an important result. The existence of such a correlation has permitted us to use the model to further examine the mechanisms of amplification in a CFA. The results of such studies are presented in Section 4 of this report. These studies are leading us to

revise our understanding of forward wave CFA amplification in a number of respects. One of these revisions lies in the nature of the interaction between weak RF input signals and the space charge hub. The model suggests that weak signals cannot draw charge from the hub and that consequently there is no small signal regime of amplification under normal operating conditions. Instead, for gain levels above 10 to 13 dB, the input signal appears to interact first with recirculating charge above the hub level. The computer model suggests that much of the tapering of interaction space geometries that we do is for the purpose of optimizing the interaction with such recirculating charge. Another revision to our thinking lies in the view of steady state conditions. The computer model suggests that the reentrant CFA may not really have a steady state in the sense that the output power settles to a fixed value. Some preliminary correlations between noise output and fluctuations in the computed output have been obtained. It begins to appear as if the model includes some rough modeling of certain noise related phenomenon. This was not expected when we started on this effort.

The computer model, while not yet completely satisfactory for certain tapered geometries, has started to be a useful design tool. It can be used to study uniform interaction space designs which may be the basis for a design. The model also provides enough information for tapered geometries to suggest roughly a uniform design should be modified to improve its performance. Some preliminary results on modeling of improved CFA designs are presented in Section 5.

Results on both reentrant and non-reentrant designs are presented. The latter are found to have surprisingly high gain under the proper conditions and may merit reconsideration. The designs in Section 5 are not intended to represent suggestions for specific CFA developments. Rather they are intended as being illustrative of how the computer model may be usefully employed in the design process.

Some information in this report was acquired prior to the period of this contract. In particular, much of the computer program described in Section 2 existed prior to our effort. A description of the complete modified program is presented in Section 2 for the convenience of future users and as documentation of the approach in obtaining the results presented in subsequent sections. In addition, computer modeling results obtained on two Air Force-sponsored study programs [4,5] are quoted at several points to complete the descriptions of CFA performance in Section 4 and add to sample designs in Section 5. The computer model developed on this program was used in these studies. Information taken from these other contracts is so identified when it is presented.

There have been two former semi-annual reports issued on this contract.[7,8] The discussion of the computer model in the first of these reports is supplanted by the discussion in this final report. The second semi-annual report, however, contains information which is still applicable and will not be repeated in this report. Specifically, the second semi-annual report contains a detailed

discussion of the numerical instabilities encountered early in the effort and shows examples of these instabilities. It also contains a discussion of third dimensional effects and how they can be minimized by proper end space design.

2.0 DESCRIPTION OF THE COMPUTER MODEL

2.1 General Approach

The computer model of the CFA follows a single RF wavelength, as shown in Figure 1, through the CFA. The wavelength "interaction box" is advanced along the CFA circuit in small time steps (1/8 to 1/10 of a cyclotron period--about 1/10 to 1/40 of an RF wavelength depending on the frequency). The motion of the electrons, the growth of the RF wave, and the dissipation on the anode and the cathode are computed for each of the time steps. The model is two-dimensional. An interaction width (perpendicular to the paper in Figure 1) is assumed, but no motion of electrons or variation of the RF field in the third dimension is permitted.

The space charge in the interaction box of Figure 1 is represented by finite rods which are assigned variable amounts of charge. (They are rods because the model is two-dimensional.) Up to 4000 rods in a single wavelength may be employed, though closer to 2000 rods have been used in many of the simulations discussed in this report. The anode circuit is represented by a smooth surface supporting a single simusoidal RF wave which is allowed to grow as the wave progresses through the CFA. The potentials in the interaction space due to the d.c. field, the RF circuit field, and the space charge are simultaneously computed from Poisson's equation using a finite array with 48 vertical points and 96 horizontal points. The charge of the rods in the interaction space is

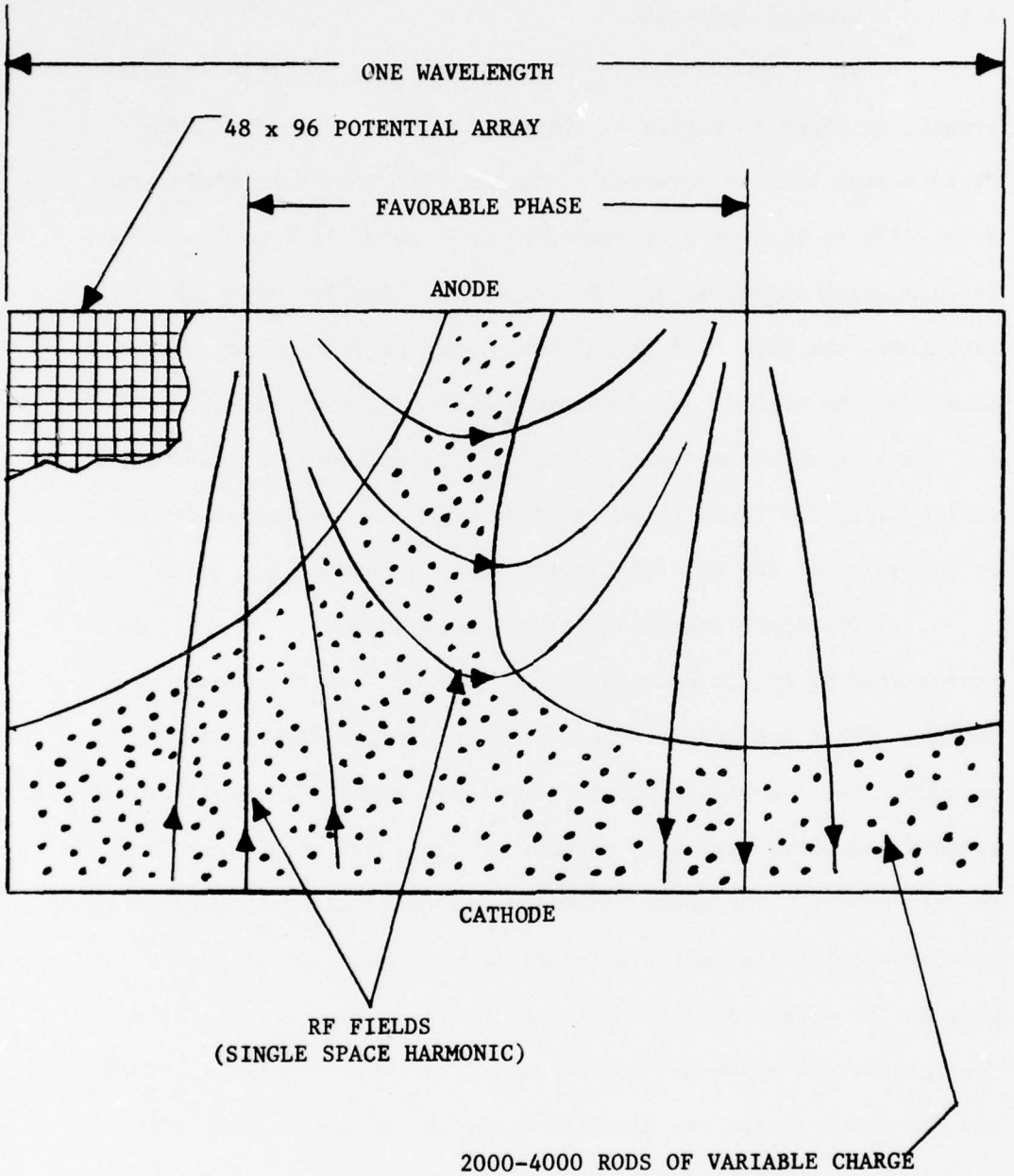

FIGURE 1

ONE WAVELENGTH OF THE RF WAVE AS FOLLOWED THROUGH THE CFA BY THE COMPUTER SIMULATION. The model represents a linear format CFA and is two dimensional.

assigned to the points in this array, and then Poisson's equation is solved numerically to determine the potential at all points in the interaction box. The RF and d.c. potentials at the anode surface enter into the solution as a boundary condition at the anode surface. From the potentials at the array points, the fields with which the charge rods interact may be determined. The cathode in Figure 1 is represented as a smooth surface having both thermionic and secondary emission capabilities which are determined from the input data.

Figure 2 shows a simplified block diagram of the computer program. First the input data is read and normalized for use in the computation and the program constants are calculated. The program then enters a loop in which the major program procedures are repeated for each time step. The first of these procedures is the Poission equation solution from which the potentials in the interaction box are determined. This is followed by the trajectory procedure which calculates the motion of each charge rod and the in-phase and quadrature-phase components of the RF current induced on the anode. If any rods are collected on the anode or cathode, the dissipated energies are computed, and in the case of cathode collection, the number of secondary electrons to be emitted on a subsequent time step is computed. The next procedure in Figure 2 increments the circuit wave by adding the induced currents to the wave current algebraically. The phase shift of the circuit wave as a result of the induced current is also calculated at this time and the position of all the rods corrected in

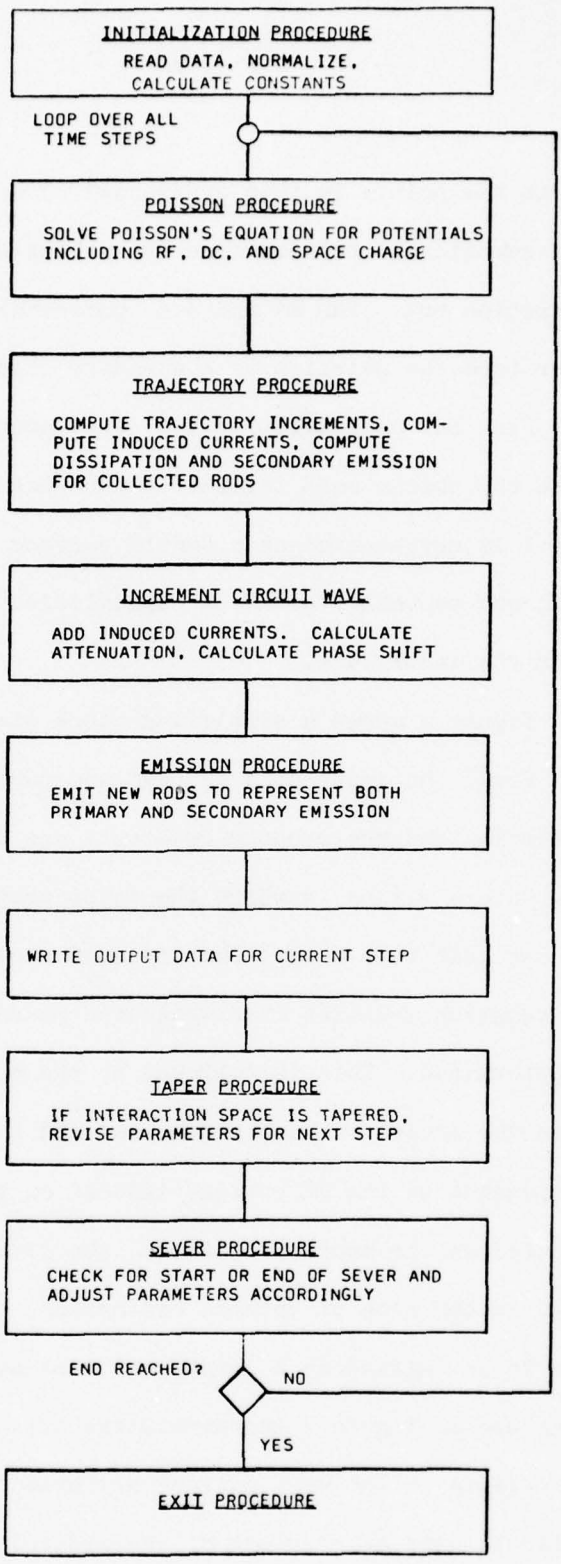

FIGURE 2

BLOCK DIAGRAM OF THE COMPUTER PROGRAM

accordance with the phase shift of the interaction box. The emission procedure now emits new rods from the cathode in accordance with the assumed thermionic emission and secondary emission properties of the cathode. The output data for the current time step is then written. Finally, the sever and taper procedures revise the interaction space geometry if the start or end of a circuit sever or attenuator is encountered on the current time step or if the interaction space is tapered.

In the case of a reentrant, emitting sole CFA, the computation described above must be repeated for a number of passes of the RF wave through the CFA. If the CFA uses secondary emission only, a small thermionic current is assumed for a few time steps in the first pass calculation to get the charge build up started. The thermionic emission is then "turned off" and the charge allowed to build up using secondary emission alone. The charge distribution at the end of the first pass calculation is then stored on a disk file. This charge distribution is used as part of the input to a second pass calculation. This procedure is usually repeated for four to six passes. This chaining of passes is shown schematically in Figure 3.

The computer model contains a number of assumptions which depart from physical reality, but which are necessary if a CFA is to be modeled with a reasonable amount of computer resources. Validation of the model by comparing results with those obtained on actual CFA's is, therefore, essential. Such comparisons are presented later in this report. The principle assumptions used in the

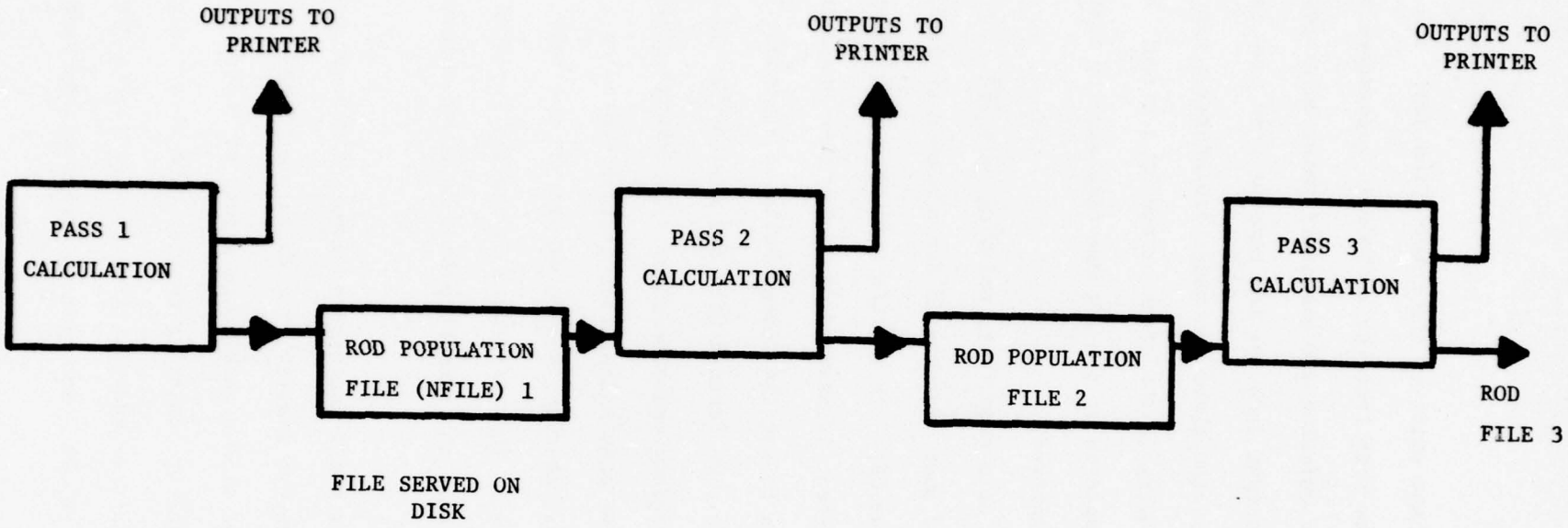

FIGURE 3--LINKING OF A MULTIPASS CALCULATION THROUGH THE ROD POPULATION FILES. (NFILES)

computer modeling are:

1. Granularity Assumption--The assumption that the granularity used in the computation is adequate to represent the physical situation. The three components of the granularity assumptions are:

   a. use of finite time steps of about 1/10 cyclotron period.

   b. use of 2000-4000 rods of charge in place of the essentially continuous charge distribution.

   c. use of a 48 x 96 finite point array to represent the potential distribution in the interaction space.

2. Single RF Wavelength Assumption--When computing the potentials in the wavelength interaction box, the computer model assumes that the wavelengths adjacent to the one being computed are the same; i.e., the model assumes that on any given time step the potentials are periodic with a one wavelength periodicity. This is obviously not the case for a growing wave. This assumption is believed not to cause serious error if the gain per wavelength is relatively small. The potential computation procedure also results in what might be called discontinuity errors at the ends of the circuit or at points where a sever occurs or there is a change in geometry. The model assumes that the change takes place suddenly on one time step and occurs simultaneously over a full wavelength. Thus, for example, at

the input the RF is applied suddenly over a full wavelength rather than gradually as the RF wavelength passes the input port. The point of application of the RF wave corresponds to the time when the center of the interaction box passes the input. The same type of discontinuity problem occurs at the output. As the interaction box passes the input or output, half of the rods are subjected to an RF field for half a cycle too long and half of the rods for half a cycle too little. Again, this is not believed to be a serious source of error.

3. Single RF Wave and Smooth Anode Assumption--The model considers only the fundamental component of the RF wave. Space harmonics, time harmonics, and backward waves are all neglected. The neglect of space harmonics means that we are not considering the finite geometry of the vane tips. The use of a smooth anode surface (which corresponds to the neglect of space harmonics) also means that penetration of the electron trajectories between the vane tips is being neglected.

4. Two-Dimensional Assumption--The model represents the CFA in only two dimensions. Variations in RF field, d.c. electric field, and magnetic field in the direction parallel to the magnetic field are not included and electron motion parallel to the magnetic field is not permitted.

The degree of variation in the axial direction in the SFD-261 was discussed in the second semi-annual report on this contract.[8] The discussion on these suggests that the effects

of axial variations will be second order. A method of designing the end space regions to further minimize the effects of axial variations (usually believed to be deletions) was also discussed in the second semi-annual report and will not be repeated in this report.

5. Linear Geometry Assumption--The model represents a CFA in a linear format only and does not include the effects of curvature. For many circular format, forward wave CFA's, the dimensions of the interaction space are such that curvature effects are minimal and the use of a linear format model does not greatly effect the results. To use the linear format model for CFA's with small curvature, a first order correction is made to the magnetic flux density before it is supplied to the model. This correction is commonly about 5%.

6. Slow Wave Assumption--The model assumes that the RF circuit wave has a velocity which is slow compared to the velocity of light. This means that the RF magnetic field can be neglected throughout the calculations and the electric fields expressed as the gradient of a potential.

It is believed that the essential features of CFA interaction are reasonably well modeled by the computer in spite of the above assumptions. The discussion in Section 3 will show that the results of the computer modeling are correlating well with experimental CFA results for a CFA with a uniform interaction space.

In the following subsections each of the major program procedures will be described in further detail. The procedures will be taken up in the order they appear in the block diagram in Figure 2.

2.2 Initialization Procedure--Input Data

The initialization procedure reads the input data (normally from punched cards) and the input rod population data (if required) saved on a disk file by a previous pass calculation. The input data is then normalized and all the necessary program constants are calculated. The input data, normalized input data, and key program constants are printed in the output. The normalizations used will be presented as part of the discussion in the subsequent subsections.

The required input data describing the CFA is listed in Table I. The table shows that provision is made for up to two severs or circuit attenuators. Tables describing the secondary emission ratio as a function of incident energy of the electrons are part of the input. Provision is made for up to four such tables--each of which applies over a different portion of the length of the calculation. Tables describing any tapering of the interaction space as a function of distance are also supplied. Provisions are made for simultaneously tapering anode-cathode spacing, circuit phase velocity, circuit interaction impedance and magnetic flux density.

In addition to the data describing the CFA, additional parameters describing the computation must be provided as part of the input data. These program parameters are listed in Table II. They include the time step size, number of rods to be emitted per time step, and certain smoothing parameters used in the emission process. (The use of these parameters will be described in Section 2.6.)

The detailed procedure for setting up the input data is not included in this report, but is described in a separate User's Manual.[6]

TABLE I

INPUT DATA REQUIRED BY THE COMPUTER MODEL

SLOW WAVE CIRCUIT DESCRIPTION

1. Circuit pitch.
2. Circuit width-parallel to magnetic field.
3. Frequency of RF input signal for this run.
4. Phase shift per section at above frequency.
5. RF interaction impedance at above frequency.
6. Attenuation in dB per inch at above frequency.
7. Length of circuit.
8. Location of up to two severs or attenuators plus attenuation values for the attenuators.

INTERACTION SPACE DESCRIPTION

1. Anode-cathode spacing.
2. Magnetic flux density.
3. Cathode voltage.
4. RF input power.

CATHODE DESCRIPTION

1. Primary emission current density (if any).
2. Length of cathode for which primary emission occurs.
3. Location along cathode of up to four different types of secondary emitters.
4. Secondary emission tables consisting of pairs of bombardment energy and secondary yield for each of the above secondary emission regions.

(continued)

TABLE I--INPUT DATA REQUIRED
BY THE COMPUTER MODEL

INTERACTION SPACE TAPER DESCRIPTION

Value of tapered parameters relative to their value at the input. Data supplied as a table of distances and values of following four parameters relative to their value at input:

1. Anode-cathode spacing.
2. Circuit phase velocity (represents either pitch or phase shift per section taper).
3. Interaction impedance.
4. Magnetic flux density.

TABLE II

PROGRAM PARAMETERS REQUIRED BY COMPUTER MODEL

MAJOR PARAMETERS

1. Time step size--fraction of a cyclotron period.

2. Rods emitted per time step--alternately decision to let model establish this value.

MINOR PARAMETERS WITH BUILT IN DEFAULT VALUES

1. Charge adjustment factor to correct for granularity of Poisson solution in determination of cathode field. (See Section 2.3) Default is 1.0.

2. Adjustment to Child's law constant. (See Section 2.6) Default is 1.0.

3. Smoothing parameter for charge applied before Poisson solution. (See Section 2.3) Default is no smoothing.

4. Factors to determine number of rods emitted per time step when program decides this value. See Section 2.6 for defaults.

5. Minimum normalized charge which may be assigned to a rod. See Section 2.6 for default.

6. Spacing smoothing parameter for secondary emission. See Section 2.6. Default is no smoothing.

7. Time smoothing parameter for secondary emission. See Section 2.6. Default is no smoothing.

8. Size of normalized charge unit. Default is 10,000 units to fill interaction box to Brillouin density.

9. Frequency of Poisson equation solution. Default is every time step.

OTHER CONTROL VARIABLES

1. Frequency of outputs to each of the files described in Section 2.10.

2. Presence or absence of input rod population data.

3. Presence or absence of data to restart an interrupted calculation.

2.3 Poisson Equation Procedure

The first step in the main loop of the program is the solution of Poisson's equation to yield the potentials at all points in the potential array. Poisson's equation is:

$$\frac{\partial^2 V}{\partial x^2} + \frac{\partial^2 V}{\partial y^2} = \frac{-\rho}{\epsilon_o} \qquad 2.3\text{-}1$$

which must be solved subject to the boundary conditions:

$$V\ (o,y) = 0 \qquad \text{at cathode}$$

$$V\ (a,y) = V_a \qquad \text{at anode}$$

$$\left.\begin{aligned} V\ (x,o) &= V\ (x,\lambda) \\ \frac{\partial V}{\partial y}(x,o) &= \frac{\partial V}{\partial y}\ (x,\lambda) \end{aligned}\right\} \text{at left and right boundaries}$$

Here x is the vertical coordinate and y the horizontal coordinate. Normalized values of these coordinates (x' and y') are used in the computation as shown in Figure 4.

Here also, a is the anode-cathode spacing

λ is the slow wave wavelength

v_a is the potential at the anode

The potential V includes the rf potential which varies along the anode surface in the interaction box and which is computed from the rf power and the interaction impedance by:

$$V_{rf} = \sqrt{2PK}\ \sin \frac{2\pi x}{\lambda} \qquad 2.3\text{-}2$$

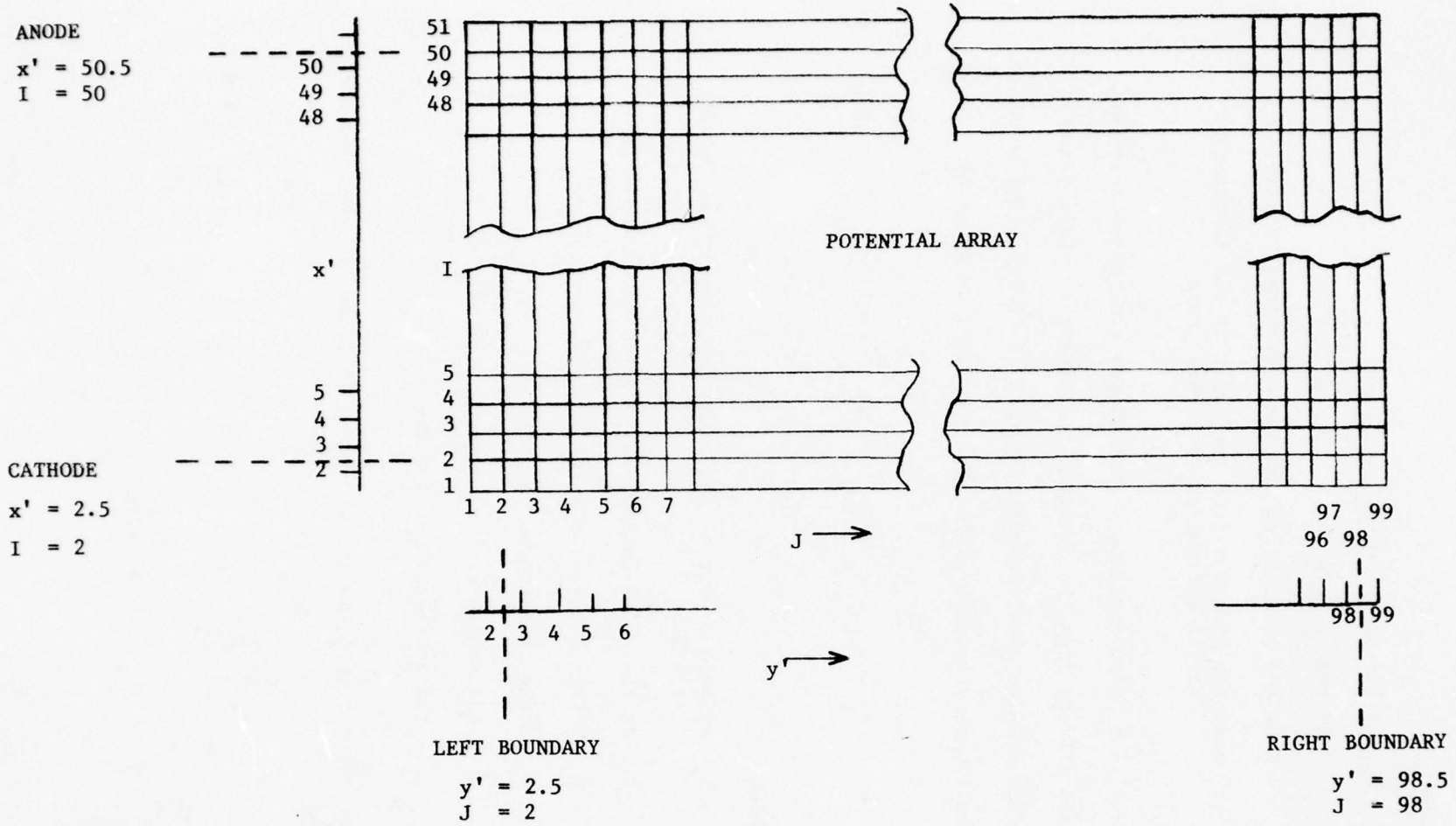

FIGURE 4--NORMALIZED x and y COORDINATES AND THE I, J COORDINATES OF THE POTENTIAL ARRAY.
Coordinate systems are displaced by one-half limit.

where

V_{rf} is the rf voltage

P is the rf power

K is the interaction impedance (an input variable)

x is the distance from the start of the interaction box in the moving reference frame

The potential V_a also includes a part of the d.c. potential--that part which differs from the potential necessary to yield space charge-free average electron velocity (E/B drift velocity) equal to the circuit wave velocity. This d.c. potential is given by:

$$V_m = V_{ak} - V_s = V_{ak} - v_s Ba \qquad 2.3\text{-}3$$

where

V_m is the d.c part of the potential used in the Poisson solution

V_{ak} is the anode-cathode voltage (an input variable)

V_s is the anode-cathode voltage for snychronism

v_s is the synchronous velocity

B is the magnetic flux density

a is the anode-cathode spacing

The phase velocity, v_s, is in turn given in terms of input variables by:

$$v_s = \frac{\omega d}{\theta} \qquad 2.3\text{-}4$$

where

ω is the radian frequency

d is the slow wave circuit pitch

θ is the slow wave circuit phase shift per circuit section

The reason for including only a portion of the d.c. potential in the anode potential will become clear in the next section. It will be seen there that the portion of the d.c. potential corresponding to the synchronous potential ($V_s = v_s Ba$) drops out of the equations of motion when they are converted to a frame of reference moving in synchronism with the circuit wave. The remaining portion, V_m, is the d.c. field in the moving reference frame.

The potential at the anode in the Poisson solution is the sum of the rf potential and the moving frame d.c. potential.

$$V_a = V_m + V_{rf} \qquad 2.3\text{-}5$$

The boundary conditions listed above also express the fact that the potential is zero at the cathode and the assumption that the potential is periodic with a one wavelength periodicity.

Expressing Poisson's equation in finite difference form gives:

$$V(I+1,J) - 2V(I,J) + V(I-1,J) + r^2 \left[V(I, J+1) - 2V(I,J) + V(I, J-1) \right] = \frac{-\rho(I,J)\ (\Delta x^2)}{\varepsilon_o} \qquad 2.3\text{-}6$$

where I is the index corresponding to the x direction and J is the index corresponding to the y direction, and V(I,J) is the potential at the Ith row and Jth column. (See Figure 4.) The factor is is the ratio of the cell size in the x direction to the size in the y direction.

The computer program utilizes normalized variables in the computation. All potentials are normalized by dividing by the Hull cut-off voltage. Thus, the normalized anode-cathode d.c. voltage is:

$$\phi_{ak} = \frac{2\eta V_{ak}^{\ 2}}{(a\omega_c)^2} \qquad 2.3\text{-}7$$

where

η is the charge to mass ratio for electrons

V_{ak} is the unnormalized cathode-to-anode voltage

a is the anode-cathode spacing

ω_c is the cyclotron radian frequency which is given by:

$$\omega_c = \eta B \qquad 2.3\text{-}8$$

where

B is the magnetic flux density

The normalized rf voltage is:

$$\phi_{rf} = \frac{2\eta V_{rf}}{(a\omega_c)^2} \qquad 2.3\text{-}9$$

where V_{rf} is the voltage gien by:

$$V_{rf} = \sqrt{2PK} \qquad 2.3\text{-}10$$

where P is the circuit power and K is the interaction impedance. The normalized synchronous potential is:

$$\phi_s = \frac{2\eta}{(a\omega_c)^2} \quad (v_s Ba) \qquad 2.3\text{-}11$$

using

$$v_s = \frac{\omega}{\beta} = \frac{\omega}{2\pi} \lambda \qquad 2.3\text{-}12$$

where λ is the slow wave wavelength, the normalized synchronous potential becomes:

$$\phi_s = \frac{2}{\pi} \left(\frac{\omega}{\omega_c}\right) \left(\frac{\lambda}{2a}\right) \qquad 2.3\text{-}13$$

The quantity ω/ω_c is used throughout the program for normalized frequency. The quantity $2a/\lambda$ which we will designate by r is the ratio of the vertical to horizontal dimension of a cell of the potential array. The quantity occurs repeatedly in the computer program.

The normalized moving refernce frame d.c. potential is $\phi_{ak} - \phi_s$ and the total normalized potential applied to the

interaction box is $\phi_{ak} - \phi_s + \phi_{rf}$.

A further set of normalized potentials is defined in the computer program. These potentials (ϕ') are obtained by multiplying the above normalized potentials by 576r. This normalization is used in supplying the rf potential and the d.c. potential above the synchronous potential to the Poisson procedure. This is done so that the normalized fields used in the trajectory procedures may be obtained directly from differences in the normalized potentials.

Multiplying both sides of the finite Poisson's equation by the two normalizing factors--i.e. by:

$$F = \frac{2\pi}{(a\omega_c)^2} 576r \qquad 2.3\text{-}14$$

yields the normalized potentials (ϕ') in place of the unnormalized potentials (V) on the left side. The right side may be further manipulated using for Δx in 2.3-6:

$$\Delta x = a/48 \qquad 2.3\text{-}15$$

and further by defining N_b as the number of negatively charged rods of unit normalized charge required to fill the interaction box to the Brillouin density. The charge per unit normalized charge then becomes:

$$q' = \frac{-(a\lambda h)\ (\eta\epsilon_o B^2)}{N_b} \qquad 2.3\text{-}16$$

where h is the interaction width and the remaining variables have been previously defined.

The charge density corresponding to one normalized charge unit assigned to one point in the 48 x 96 charge array then becomes:

$$\rho(I,J) \approx \frac{q'}{(\frac{a}{48})(\frac{\lambda}{96})h} = \frac{q'}{a\lambda h}(48)(96) \qquad 2.3\text{-}17$$

or using the expression for q' from 2.3-16:

$$\rho(I,J) \approx \frac{-(\eta\varepsilon_o B^2)}{N_b}(48)(96) \qquad 2.3\text{-}18$$

For N normalized charge units assigned to a point in the charge array the charge density is N times this value.

Inserting this value for ρ and using 2.3-14 and 2.3-15 above, the expression for the right hand side of the normalized Poisson equation becomes:

$$RHS = N(I,J)\ (\frac{48^2 r}{N_b}) \qquad 2.3\text{-}19$$

where N(I,J) is the number of normalized charge units assigned to the point (I,J). (The complete right hand side is referre- to as L(I,J) in prior descriptions of this procedure.[1.2]) Here

$r = 2a/\lambda$ as defined previously.

The Poisson procedure first evaluates the N(I,J) values at each point in the array. This is done by summing the contributions of all the rods with the charge of each rod assigned to the four surrounding matrix points as shown in Figure 5. The charge contributions to each of the surrounding points is weighted by the distance to the corresponding point as shown in the figure.

Once the N(I,J)'s have been evaluated, we are left with 47 (vertical) by 96 (horizontal) points with known charge, but unknown potential. This yields 47 x 96 = 4512 equations in as many unknowns which must be solved simultaneously. These equations could be directly inverted using standard numerical techniques. Instead, however, a much more rapid technique due to Hockney which takes advantage of the periodic nature of the potentials is employed.[1,2] This procedure is described in the references cited and will not be repeated here.

Once the $\emptyset'(I,J)$'s have been determined by the Hockney technique, they are stored by the program in the same array as was used by the N(I,J)'s. These values of $\emptyset'$ may subsequently be used by the trajectory procedure to determine the force on a charge rod.

Because of the limited number of cells in the potential array across the width of the space charge hub, there is a numerical error in the computation of the fields from the potential array. The magnitude of this error has been found by setting up a charge distribution equivalent to an ideal Brillouin hub and then solving

for the field at the cathode using the program's Poisson procedure. Ideally, this field should be zero. In most cases, we have found that it departs from zero. It can be reduced to near zero by reducing the right hand side in equation 19 by about 5%. The exact value to use appears to depend on the case being studied--we have found values of 4 to 6% over the cases investigated. The program includes the capability for making this correction to the constant in equation 19 with the value of the correction factor being an input variable. While we have used this correction in our calculations, omitting it appears to have only a minor effect on the computed results.

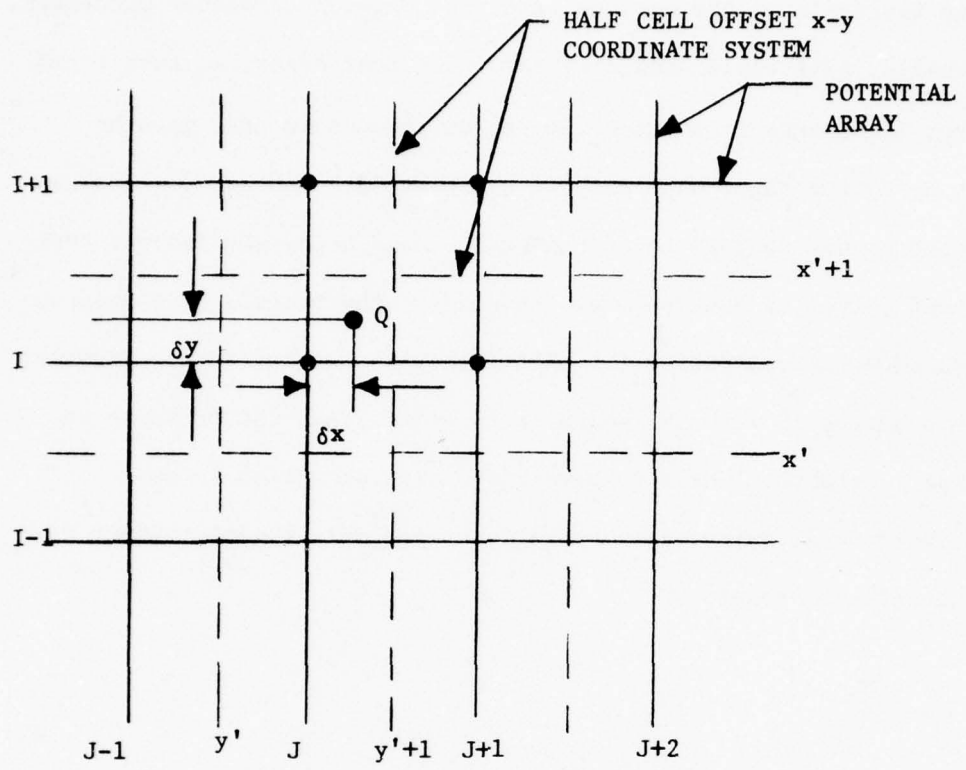

$\delta x = (x' - 0.5) - I$

$\delta y = (y' - 0.5) - J$

$Q(I,J) = Q(1 - \delta x)(1 - \delta y)$

$Q(I+1, J) = Q(\delta x)(1 - \delta y)$

$Q(I, J+1) = Q(1 - \delta x)\ (\delta y)$

$Q(I+1, J+1) = Q(\delta x)(\delta y)$

FIGURE 5

METHOD OF ASSIGNING CHARGE OF A ROD TO THE POINTS IN THE POTENIAL ARRAY.

2.4 Trajectory Procedure

The trajectory procedure consists of a program loop over all of the rods as shown in Figure 6. The procedure advances the rod trajectories, collects rods which have intercepted on the electrodes and calculates their dissipation and calcualtes the induced RF currents.

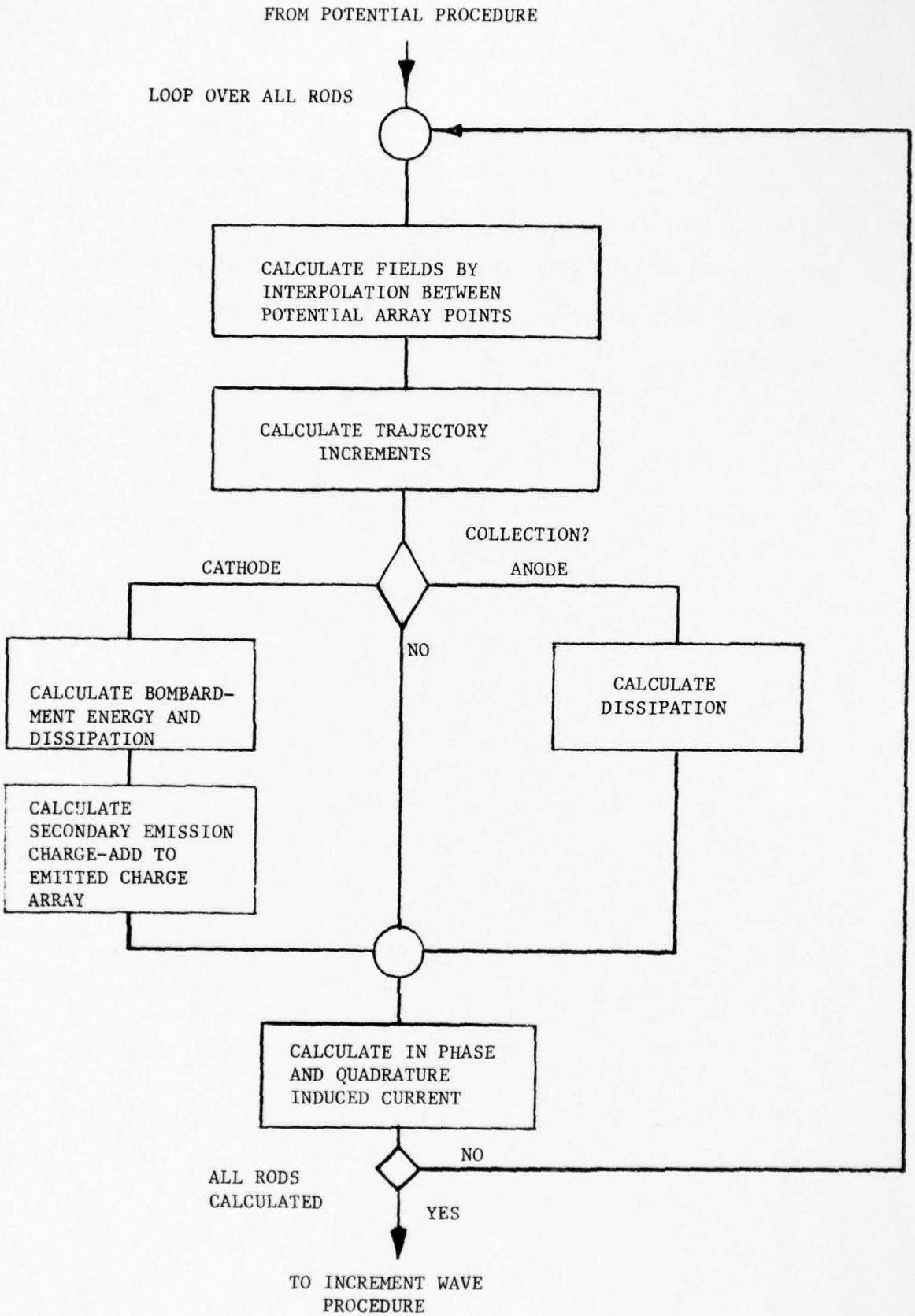

FIGURE 6--BLOCK DIAGRAM OF TRAJECTORY PROCEDURE

2.4.1 Trajectory Equations

The equations of motion for the negatively charged rods in a fixed frame reference are:

$$\ddot{x} = - \eta E_x - \eta B \dot{y} \qquad 2.4\text{-}1$$

$$\ddot{y} = - \eta E_y + \eta B \dot{x} \qquad 2.4\text{-}2$$

where the x and y coordinates are as defined in Figure 4 and the dots indicate differentiation with respect to time. Also,

E_x, E_y are the x and y components of electric field (dc + rf) and

η is the charge to mass ratio for and electron.

In the computer model it is desired to follow the motion of the charged rods in the interaction box which is traveling at a velocity synchronous with the rf circuit wave velocity. Therefore, the equations of motion are transformed into a moving reference frame at the synchronous velocity. This means that we define a new y coordinate in the moving frame of reference defined by:

$$y = y - \int_0^t v_s dt \qquad 2.4\text{-}3$$

where y_m is the y coordinate in the moving frame and v_s is the reference frame (circuit wave) velocity in the presence of the interaction.

The integral is used in place of $v_s t$ because the synchronous velocity in the presence of the interaction may differ from the cold circuit velocity and may change slightly as a function of distance. Substituting the above transformation into the equations of motion and using

$$v_s = \frac{\omega}{\beta} \qquad 2.4\text{-}4$$

we obtain the following transformed equations of motion:

$$\ddot{x} = -\eta(E_x - v_s B) - \eta B\dot{y}_m \qquad 2.4\text{-}5$$

$$\ddot{y}_m = -\eta(E_y + \frac{1}{\eta}\frac{\partial v_s}{\partial t}) + \eta B\dot{x} \qquad 2.4\text{-}6$$

Now define a quantity E_{xm} by

$$E_{xm} = E_x - v_x B \approx E_x - \frac{\omega}{\beta} B \qquad 2.4\text{-}7$$

This is just the x directed rf field plus the effective d.c. field as seen by an observer in the moving frame. This value E_{xm} is given by

$$E_{xm} = V_m/a + E_{rfx} \qquad 2.4\text{-}8$$

where V_m is the moving frame d.c. potential defined in the last section and

a is the anode-cathode spacing

E_{rfx} is the x directed rf field

The term $\frac{1}{\eta}\frac{\partial v_s}{\partial t}$ is a y directed d.c. field which arises out of the transformation when the reference frame velocity is not constant. This field may be visualized as trying to speed up (or retard) electrons to reposition them in a frame of reference which is changing its velocity. This term arises in practice because the phase pushing of the space charge causes a small shift in the circuit wave phase which is equivalent to a small velocity change. Normally this is a very small term. In the past it has been included in the transformed equations of motion. Experience with such equations has shown them somewhat unstable. The phase of the circuit wave tends to oscillate about an equilibrium. A numerical instability apparently occurs with the phase changes (and hence velocity changes) giving a significant oscillating $\frac{1}{\eta}\frac{\partial v_s}{\partial t}$ term which when applied to the space charge sets up oscillations in the trajectories which reinforce the cyclic phase variations. This numerical instability has seemed to cause hunting of the solution about the proper value.

In reality the term $\frac{1}{\eta}\frac{\partial v_s}{\partial t}$ should be quite small. Thus in the present computer model, the term is neglected in the force equations and the shift of the wave relative to the space charge is taken into account separately by repositioning the rods relative to the wave on each time step after the wave phase shift is calculated. This procedure is discussed in the next section. This approach to the trajectory equations has also been previously used in computer programs for injected beam CFA's.

With the elimination of the term in $\partial v_s/\partial t$ and with the definition of E_{xm} given above, the moving frame equations of motion become:

$$\ddot{x} = - \eta E_{xm} - \eta B \dot{y}_m \qquad 2.4\text{-}9$$

$$\ddot{y}_m = - \eta E_y + \eta B \dot{x} \qquad 2.4\text{-}10$$

These equations look like the original equations of motion in the fixed frame (equations 2.4-1 and 2.4-2) but with the moving frame coordinate y_m replacing the fixed frame coordinate y and the modified d.c. field E_{xm} replacing the original field E_x. The value of E_{xm} and E_y may be determined from the potential array computed using V_{rf} and V_m as defined in the last section as boundary conditions at the anode.

The above equations may be combined into a single equation which then may be solved directly by introducing:

$$z = x + jy_m \qquad 2.4\text{-}11$$

$$E = E_x + jE_y \qquad 2.4\text{-}12$$

After substitution, the combined equation of motion becomes:

$$\ddot{z} - j\omega_c\dot{z} = -\eta E \qquad 2.4\text{-}13$$

where $\omega_o = \eta B$ has also been introduced. This equation will be repeatedly applied to each charge rod on each time step to calculate small trajectory increments. During the calculation for a particular time step it will be assumed that E is constant over the trajectory increment. This implies constancy of E in both space and time over the trajectory increment. This is one of the granularity assumptions inherent in the computer model.

For E constant 2.4-13 has a solution of the form:

$$z = A + \frac{\eta E}{j\omega_c}\, t + Be^{j\omega_c t} \qquad 2.4\text{-}14$$

where A and B are constants which may be determined from the initial conditions:

when $t = t_o$

$z = z_o$ and

$\dot{z} = \dot{z}_o$

Using these conditions to evaluate A and B we find:

$$z = z_o + \frac{\dot{z}_o}{j\omega_c} (e^{j\theta} - 1) - \frac{\eta E}{\omega_c^2} (1 - e^{j\theta} + j\theta) \qquad 2.4\text{-}15$$

where $\theta = \omega_c(t - t_o)$. 2.4-16

This gives the new position z in terms of an old position z_o and the angle θ which is a time increment. For θ negative the old position is given in terms of the new position by a similar equation with the positions of z and z_o interchanged and the sign of θ reversed. These two equations may then be decomposed by substituting $z = x + jy$ to obtain four equations--one pair relating x and y to x_o, y_o, $\dot{x}_o$ and $\dot{y}_o$ and another pair relating $\dot{x}$ and $\dot{y}$ to $(x - x_o)$ and $(y - y_o)$. (All y's in moving frame.)

In the computer program the equations are normalized as follows:

$$x' = \frac{48x}{a} \qquad \text{normalized position} \qquad 2.4\text{-}17$$

$$y' = \frac{96y_m}{\lambda} = \frac{48ry_m}{a}$$

$$T = \omega_c t \qquad \text{normalized time}$$

where x' and y' are the normalized coordinates corresponding to the real coordinates x and y_m and

a is the anode-cathode spacing

λ is the slow wave wavelength

$r = 2a/\lambda$

$\omega_c = \eta B$

The normalized velocities are given by:

$$\dot{x}' = \frac{dx'}{dT} + \frac{48\dot{x}}{\omega_c a} \qquad 2.4\text{-}18$$

$$\dot{y}' = \frac{dy'}{dT} = \frac{96\dot{y}_m}{\omega_c \lambda} = \frac{48r\dot{y}_m}{\omega_c a}$$

In place of these velocities, the program uses finite difference quantities.

$$v_x' = \dot{x}'\,\theta$$

$$v_y' = \dot{y}'\,\theta \qquad 2.4\text{-}19$$

where

$$\theta = \frac{\omega_c t}{g} = \frac{T}{g}$$

and g is the number of time steps per cyclotron period

The program also uses normalized field variables given by:

$$G_x = \frac{96}{a}\,\frac{r}{\omega_c B}\,E_{xm} \qquad 2.4\text{-}20$$

$$G_y = \frac{96}{a}\,\frac{1}{\omega_c B}\,E_y$$

These normalizations make the normalized x dimension of the interaction box equal to 48.0 and the normalized y dimension equal to 96.0. The interaction box used has the cathode position arbitrarily set at x = 2.5 and the anode at 50.5. The left side of the box is placed at y = 2.5, and the right side at 98.5. These definitions make available rows of the potential array outside of the interaction box for use in matching boundary conditions and determining fields at the electrodes (see Figure 4).

Substituting the above normalizations into the four equations obtained by decomposing the z equations above, we obtain the normalized trajectory equations:

$$\Delta x' = x_2' - x_1' = K_1 v_x' + K_2 v_y' + K_3 Gx_1 + K_4 Gy_1$$

$$\Delta y' = y_2' - y_1' = K_5 v_x' + K_6 v_y' + K_7 Gx_1 + K_8 Gy_1 \qquad 2.4\text{-}21$$

$$v_{x2}' = K_9(\Delta x') + K_{10}(\Delta y') + K_{11} Gz_2 + K_{12} Gy_2$$

$$v_{y2}' = K_{13}(\Delta x') + K_{14}(\Delta y') + K_{15} Gx_2 + K_{16} Gy_2$$

In these equations the subscript 1 refers to the start of a trajectory increment and the subscript 2 to the end of the increment.

The $\Delta x'$, $\Delta y'$, and v_x', v_y' normalized variables are now both expressed in terms of normalized position differences which occur in one time step--i.e., they are in matrix units in Figure 4 per time step. As shown in Figure 7, the $\Delta x'$, $\Delta y'$ variables are actual

position differences whereas the v_x', v_y' variables are slopes of the trajectories.

The normalized potentials have previously been defined so that the normalized fields (G's) may be obtained directly from the differences in normalized potential at points in the potential array. Thus for a rod located as shown in Figure 8, the values of the G's are given in terms of differences in the normalized potentials (Ø') by:

$$G_x = G_{xo} + \left(\frac{\Delta G_x}{\Delta x'}\right) a + \left(\frac{\Delta G_x}{\Delta y'}\right) b$$

where a and b are defined in Figure 7 and

$$G_{xo} = \text{Ø}'(I + 1,J) - \text{Ø}'(I - 1,J)$$

$$\left(\frac{\Delta G_x}{\Delta y'}\right) = 2\ \text{Ø}'(I = 1, J) - 2\ \text{Ø}'(I,J) + \text{Ø}(I - 1,J)$$

$$\left(\frac{\Delta G_x}{\Delta y}\right) = 1/2\Big[\text{Ø}'(I + 1, J + 1) - \text{Ø}'(I - 1, J + 1) + \text{Ø}'(I - 1, J - 1) - \text{Ø}'(I + 1, J - 1)\Big]$$

and

$$G_y = G_{yo} + \left(\frac{\Delta G_y}{\Delta x'}\right) \delta x' \left(\frac{\Delta G_y}{y'}\right) \delta y'$$

with

$$G_{yo} = \text{Ø}'(I, J + 1) - \text{Ø}'(I, J - 1)$$

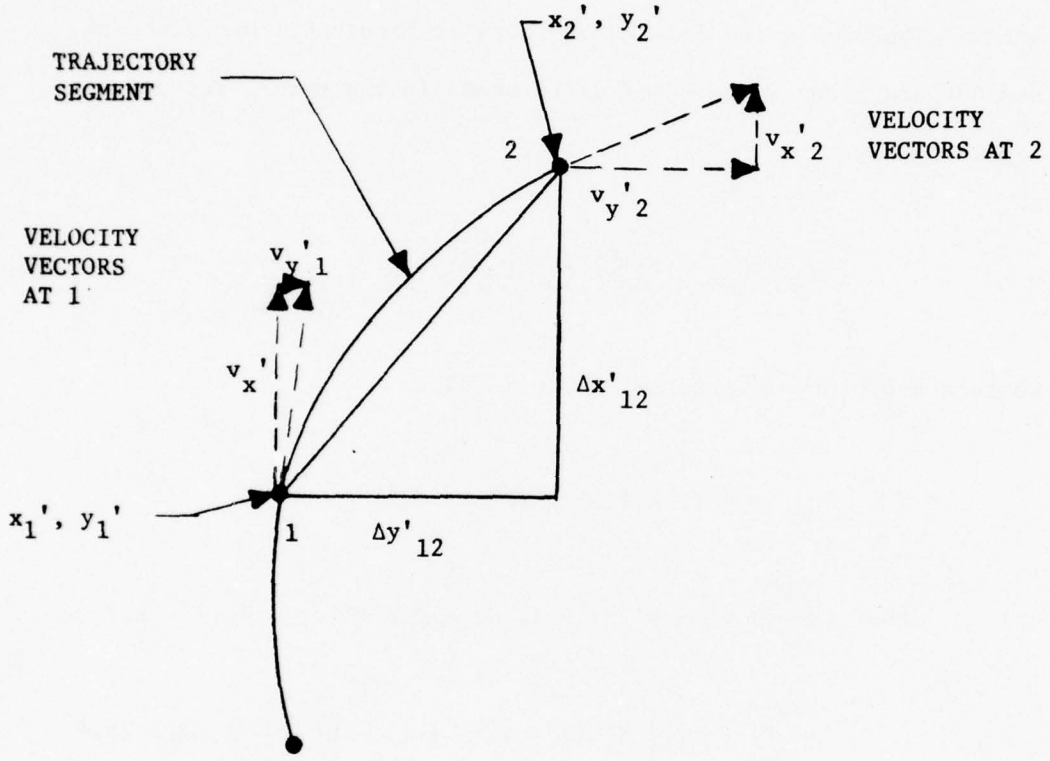

FIGURE 7

POSITION AND VELOCITY VARIABLES FOR A TRAJECTORY SEGMENT. When rod reaches Point 2, the values of x_2', v_2', and $\Delta x'_{12}$ and $\Delta y'_{12}$ are saved. The velocities are calculated as part of the trajectory procedure, but are not saved.

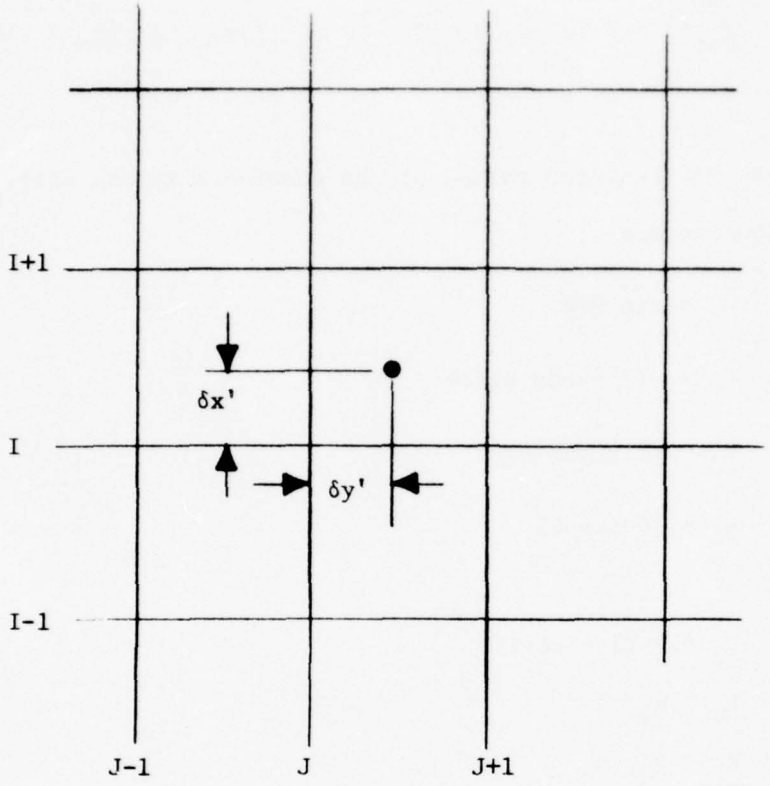

$$\delta x' = (x' - 0.5) - I$$

$$\delta y' = (y' - 0.5) - J$$

FIGURE 8

LOCATION OF ROD IN POTENTIAL ARRAY SHOWING QUANTITIES EMPLOYED IN FIELD DETERMINATION EQUATIONS.

$$\left(\frac{\Delta G_y}{\Delta x'}\right) = \left(\frac{\Delta G_x}{\Delta y'}\right) \qquad 2.4\text{-}22$$

$$\left(\frac{\Delta G_y}{\Delta y'}\right) = 2\,(\emptyset'(I, J = 1) - 2\,\emptyset'(I,J) + \emptyset'(I, J - 1)$$

With the G's so defined, the values of the constants in the trajectory equations become:

$$K_1 = \sin\theta/\theta$$

$$K_2 = -(1 - \cos\theta)/r\theta$$

$$K_3 = (1 - \cos\theta)/r$$

$$K_4 = (\theta \sin\theta)$$

$$K_5 = r\,(1 - \cos)/\theta$$

$$K_6 = K_1$$

$$K_7 = K_4$$

$$K_8 = r(1 - \cos\theta)$$

$$K_9 = \theta \sin\theta/2(1 - \cos\theta)$$

$$K_{10} = -\theta/2r$$

$$K_{11} = \theta^2/2r$$

$$K_{12} = -\theta\left(1 - \theta \sin\theta/2\,(1 - \cos\theta)\right)$$

$$K_{13} = r\theta/2$$

$$K_{14} = K9$$

$$K_{15} = -K_{12}$$

$$K_{16} = K_{11}$$

2.4-23

The manner in which these equations are applied is shown in Figure 9. Arrays in the program contain the last calculated values of x' and y' and $\Delta x'$ and $\Delta y'$. The values of v_x' and v_y' are not saved. On each time step the values of v_x' and v_y' are first calculated using the $\Delta x'$ and $\Delta y'$ values from the last time step and the field at the rod location which corresponds to position 2 of the last trajectory increment. Using the x', y', v_x' and v_y' values and the fields at this position which also corresponds to position 1 of the present trajectory increment, the new values of $\Delta x'$ and $\Delta y'$ are calculated and the trajectory is advanced.

A source of error in trajectory calculations is the fact that the field over a trajectory increment calculated on a given time step is not constant, but varies from one end of the increment to the other. This is in violation of the condition assumed when equation 2.4-14 was solved. Reference to Figure 9 shows that the velocities at the end of a given trajectory increment are calculated from the field at a point ahead of the midpoint of the increment while the position increments are calculated from the field at a point behind the midpoint of the increment. This apparently causes a first order correction to the errors which occur because of a spacial variation in electric field over a trajectory increment.

The trajectory equations have been checked by determining that they cause rods to properly trace theoretical cycloids in space charge-free fields. They have also been checked by releasing rods into a linearly varying field with a charge density somewhat less

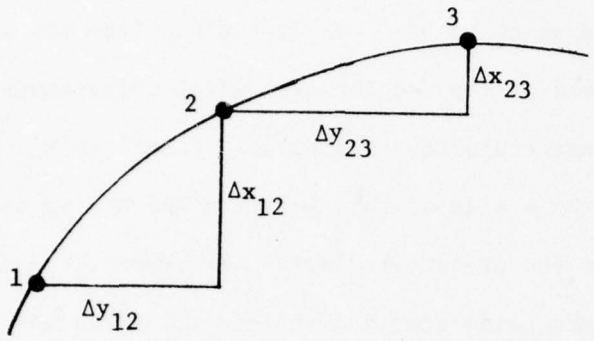

Step N--Rod goes from Point 1 to Point 2

$$\Delta x_{12} = F_1 (E_1, v_x'_1, v_y'_1)$$

$$\Delta y_{12} = F_2 (E_1, v_x'_1, v_y'_1)$$

Step N+1--Rod goes from Point 2 to Point 3

$$v_x'_2 = F_3(E_2, \Delta x_{12}, \Delta y_{12})$$

$$v_y'_2 = F_4(E_2, \Delta x_{12}, \Delta y_{12})$$

$$\Delta x_{23} = F_1(E_2, v_x'_2, v_y'_2)$$

$$\Delta y_{23} = F_2(E_2, v_x'_2, v_y'_2)$$

FIGURE 9

FUNCTIONAL FORM OF TRAJECTORY EQUATIONS. Position increment from Point 1 to Point 2 is calculated from field and velocities at Point 1. However, velocities at Point 2 are calculated from field at Point 2 rather than at Point 1.

than that in a Brillouin hub--see Figure 10. We have not solved for the theoretical trajectory shape in this field configuration. but we do know that the rods sould return to their starting point. This they do within good accuracy. Using a time step of 1/10 cycloid, rods released with an initial energy of four volts returned and struck the cathode with an energy of about two volts after having reached an energy of over 3000 volts at the top of the trajectory.

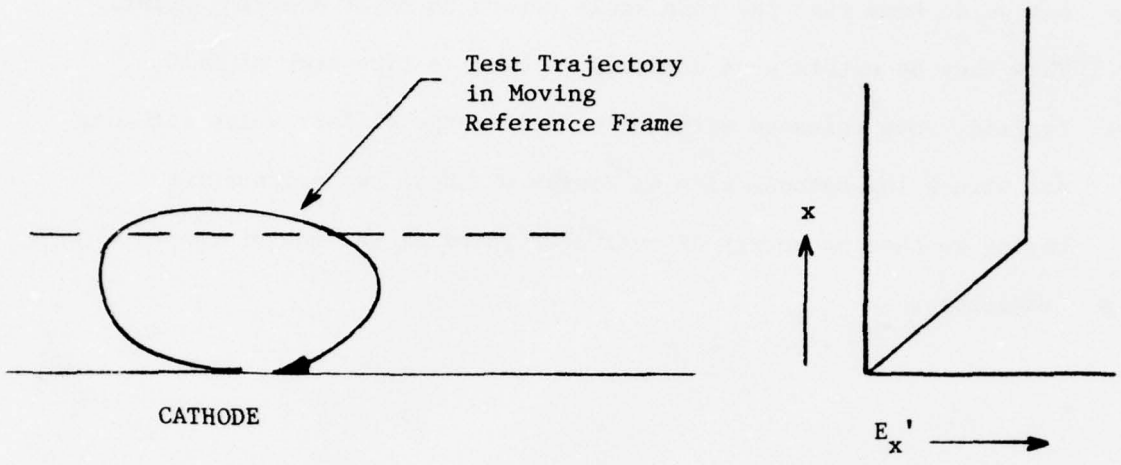

FIGURE 10

TRAJECTORY EQUATION TEST. Trajectory is traced through electric field having a gradient about two-thirds that in a Brillouin hub as shown at right. Trajectory should return to its starting point.

2.4.2 Collection of Rods on Cathode or Anode

If a trajectory intercepts the anode or the cathode it becomes necessary to calculate the energy dissipated. This can be done from a knowledge of the charge of the rod and the velocity at the point of interception. There is, however, a problem in knowing the correct velocity. This problem is particularly important for rods returning to the cathode because they are rapidly loosing kinetic energy as they move against the d.c. field while approaching the cathode. As shown by Figure 11, taking the velocity at the end of the last trajectory increment before striking gives much too high an energy when we use a typical time step value of one-tenth of a cyclotron period. Similarly taking the velocity at the end of the increment which is actually below the cathode surface gives to low a value of bombardment energy. To obtain an accurate value for the cathode bombardment energy it is necessary to take very small trajectory increments as the trajectory approaches the cathode. To use such small increments over the full trajectory would be uneconomical of computer time. Thus, a procedure for subdividing the last trajectory increment before interception of the trajectory before interception of the trajectory has been devised.

When the program senses that a rod has been collected by its trajectory going through the cathode or anode surface, it is first backed up to the end of the last segment before interception. The time step for the trajectory calculation is then halved and a

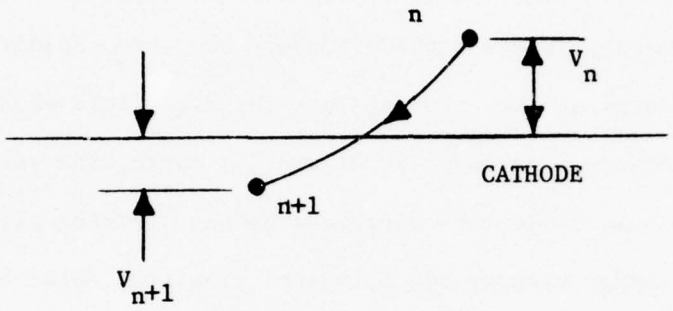

FIGURE 11

TRAJECTORY APPROACHING CATHODE. For normal trajectory steps of one-tenth cyclotron period, the potential V_n at the point prior to collection or the potential V_{n+1} at the next point below the cathode surface can be significant relative to the kinetic energy. Thus, neither the kinetic energy at n nor n+1 gives an adequate measure of the dissipated energy. To obtain the dissipation accurately, the trajectory segment must be subdivided into smaller increments. At the last point above the cathode, the potential energy must be much less than the kinetic energy. The kinetic energy at this point may then be taken as the energy dissipated.

half trajectory segment is calculated. If this half segment does not reach the electrode, it is accepted and the trajectory correspondingly advanced. If the half segment intercepts on the electrode it is rejected and the rod is not advanced. The time size for the trajectory calculation is then halved again and a quarter segment calculated and accepted or rejected depending on whether it intercepts the cathode. This process is repeated a total of eight times so that the last trajectory segment before collection is 1/256 of a normal trajectory segment. For a time step of 1/10 cyclotron period. The last trajectory segment is 1/2560th of a cyclotron period. The last trajectory segment accepted by the procedure will always take the rod to a position slightly above the cathode or below the anode. The rod will, however, be so close to the electrode that the d.c. potential will be very close to the electrode potential and negligible error will result from taking the bombardment energy equal to the kinetic energy at this point. In the simulations to be discussed in this report, the error in cathode bombardment energy arising from stopping the trajectory above the cathode surface is a maximum of about 4 volts in the space charge-free case or about 2 volts in the presence of space charge. The average error is less than this. The average bombardment energy for these cases is about 100 volts. The trajectory procedure calculates a normalized energy (W') dissipated per rod intercepted as:

$$W' = 1/2\, N_q \left[(v_x')^2 + \frac{(v_y' + v_s')}{r^2} \right] \qquad 2.4\text{-}24$$

where

v_s' and v_y' are the normalized velocities in matrix units per time step.

v_s' is the normalized frame velocity--to be further defined in the next subsection

N_q is the normalized charge per rod

$r = 2a/\lambda$

This energy is used in the generation of secondary emission. It is also accumulated over all ords collected to give the dissipation per time step. The collected charge, N_q, is also accumulated over all the rods and later used to calculate collected current.

The normalized incident energy per unit charge (V') is given by:

$$V' = \frac{\eta\varepsilon'}{N_q} \qquad 2.4\text{-}25$$

where η is the charge to mass ratio of an electron and the remaining quantities are as defined.

The initialization procedure normalizes the incidnet energies in the secondary emission table in the manner of V' defined above so that the normalized incident energies may be used directly to determine the secondary emission ratio. The normalization constant may be determined from:

$$V = \frac{1}{2\eta}(\dot{x}^2 + \dot{y}^2) \qquad 2.4\text{-}26$$

where $\dot{x}$ and $\dot{y}$ are the real velocities upon collection and V is the incident energy per unit charge.

Using 2.4-18, 2.4-19, 2.4-24 and 2.4-25 we find:

$$V' = 2\eta \left[\left(\frac{2\pi}{g}\right) \left(\frac{48}{a\omega_c}\right) \right]^2 V \qquad 2.4\text{-}27$$

where

g is the number of time steps per cyclotron period

a is the anode-cathode spacing

ω_c is the radian cyclotron frequency = ηB

V' is the normalized incident energy per unit charge

V is the actual incident energy per unit charge

Once a rod has been intercepted on the cathode and its incident energy calculated, the secondary emission table appropriate for the current distance of the wavelength interaction box from the input is used to calculate the secondary emission ratio. Linear interpolation between points in the table is employed. The charge of the incident rod is multiplied by the secondary ratio to determine the new charge to be emitted. This charge value is stored in a 96 element array (emitted charge array)--one position for each cell of the potential array along the cathode. The charge may all be stored in the array element corresponding to the nearest column of arrival of the trajectory or alternately it may be spread over the array elements corresponding to several cells of the potential array.

Spreading the charge is known as space smoothing of the emitted charge. This is done to help compensate for the granularity of the collection process in which on the average less than one rod per time step is collected per column of the potential array.

If the space smoothing procedure is employed, the charge to be emitted is spread over three cells on either side of the array cell at which collection occurs--a total of seven cells. The charge (q) to be emitted is spread over these cells in accordance with the following procedure.

$$\text{Center Cell Charge} = Sq/D \qquad 2.4\text{-}28$$

$$\text{Cell } \pm 1 \text{ Charge} = S^2 a/D$$

$$\text{Cell } \pm 2 \text{ Charge} = S^3 q/D$$

$$\text{Cell } \pm 3 \text{ Charge} = S^4 q/D$$

$$D = S + 2S^2 + 2S^3 + 2S^4$$

The parameter S has been made an input variable. For S = 0 no smoothing occurs. For $0 < s < 1.0$ smoothing takes place in accordance with the above procedure. In all of the calculations discussed in this report an S value of 0.5 has been employed.

2.4.3 Induced Current Calculation

In addition to incrementing the trajectories and collecting rods, the trajectory procedure calculates the RF current induced in the anode by the motion of the rods. The expression for induced current may be deduced from conservation of energy. Thus, the energy lost by a rod averaged over an RF cycle is:

$$W = \frac{-q}{T} \int_0^T \vec{\Delta z} \cdot \vec{E}_{rf} \, dt \qquad 2.4\text{-}29$$

where

W is the energy lost

q is the rod charge

Δz is the vector position change of the rod = $z - z_o$ where z_o is the position at t = 0.

E_{rf} is the vector electric field

T is the RF period

Dividing by time t we obtain:

$$\frac{dW}{dt} = \Delta P = \frac{-q}{T} \int_0^T \left(\frac{dz}{dt}\right) \cdot E_{rf} \, dt \qquad 2.4\text{-}30$$

where

$\frac{dz}{dt}$ is the vector velocity

ΔP is the time averaged power per cycle

For finite time steps the integral may be replaced by a sum over the finite time steps. The power lost per rod per time step becomes:

$$\Delta P = \frac{-q}{T} \frac{\vec{dz}}{dt} \cdot \vec{E}_{rf} \qquad 2.4\text{-}31$$

Now if we consider all the rods in the interaction box, the power lost by the rods and delivered to the wave in one time step over a length ΔL is:

$$\frac{\Delta P}{\Delta L} = \frac{1}{T} \sum_{N} -q_n \left(\frac{\vec{dz}}{dt_n}\right) \cdot \vec{E}_{rfn} \qquad 2.4\text{-}32$$

where

the sume is taken over the N rods within the interaction box and:

q_n is the charge of the nth rod

$\frac{dz}{dt}$ is the vector velocity of the nth rod

E_{rfn} is the RF field at the position of the nth rod

ΔL is the distance the interaction box moves forward in one time step

The power is related to rf voltage V_{rf} by:

$$P = \frac{V_{rf}^2}{2Z_o} \qquad 2.4\text{-}33$$

where

Z_o is the interaction impedance

Differentiating:

$$\frac{dP}{d\ell} = \frac{V_{rf}}{Z_o} \frac{dV_{rf}}{d\ell} \qquad 2.4\text{-}34$$

For finite time steps we use:

$$\frac{\Delta P}{\Delta L} = \frac{V_{rf}}{Zo} \frac{\Delta V_{rf}}{\Delta L} \qquad 2.4\text{-}35$$

or

$$\Delta V_{rf} = \frac{Z_o \Delta P}{V_{rf}} \qquad 2.4\text{-}36$$

Substituting the expression for ΔP:

$$\Delta V_{rf} = \frac{Z_o}{T} \sum_{N} -q_n \left(\frac{\vec{dz}}{dt}\right)_n \cdot \frac{\vec{E}_{rfn}}{V_{rf}} \qquad 2.4\text{-}37$$

Defining a wave current by:

$$I_{rf} = v_{rf}/Z_o \qquad 2.4\text{-}38$$

We obtain:

$$\Delta I_{rf} = I_{induced} = \frac{1}{T} \sum_{n} -q_n \left(\frac{\vec{dz}}{dt}\right)_n \cdot \frac{\vec{E}_{rfn}}{V_{rf}} \qquad 2.4\text{-}39$$

As is usual with induced current calculations, the factor $\vec{E}_{rfn}/V_{rf}$ is a geometrical factor which depends on the location of the rod but not on the amplitude of the rf field.

The induced current given by the above relation is not usually in phase with the current of the rf wave. The induced current is thus split into in-phase and quadrature components of induced current.

The ratios E_{rf}/V_{rf} may be evaluated by simple field theory for the x and y components of E_{rf}. The components of induced current per rod are then given by:

In phase component:

$$i = \frac{\beta q v_x}{T} \frac{\cosh(\beta x)}{\sinh(\beta a)} \sin(2\pi y/\lambda) + \frac{\beta q v_y}{T} \frac{\sinh(\beta x)}{\sinh(\beta a)} \cos(2\pi y/\lambda) \qquad 2.4\text{-}40$$

quadrature component:

$$i = \frac{\beta q v_x}{T} \frac{\cosh(\beta x)}{\sinh(\beta a)} \cos(2\pi y/\lambda) - \frac{\beta q v_y}{T} \frac{\sinh(\beta y)}{\sinh(\beta a)} \sin(2\pi y/\lambda) \qquad 2.4\text{-}41$$

where y is the distance of a rod from the left side of the interaction box and the velocities v_x and v_y are in a fixed reference frame. The x velocities are the same in the fixed and moving frame, and we can thus replace v_x by $\dot{x}$ as obtained from the trajectory equations.

For v_y we write:

$$v_y = \vec{y} + v_s = \vec{y} + \omega/\beta$$

where

$\vec{y}$ is the velocity in the moving frame of reference

v_s is the frame velocity

ω is the radian frequency

β is the phase constant of the rf wave

The quadrature component of induced current as defined above lags the in-phase component in space as shown in Figure 12. In the computer program the sine, cosine, and hyperbolic functions are precomputed at locations corresponding to each point in the potential array. The functions for the point closest to the trajectory point and prior to the incrementing of the trajectory are used in calculating the induced current resulting from the subsequent rod motion. (See Figure 13a.) The contributions of the motion of each rod to the induced currents are calculated as soon as the trajectories are incremented and are added to the cumulative sums of the induced current.

The induced current calculation takes place in normalized coordinates. The charge is normalized so that N_b rods of unit normalized charge are required to fill the interction box to the Brillouin density. A value of N_b = 10,000 has been used in all

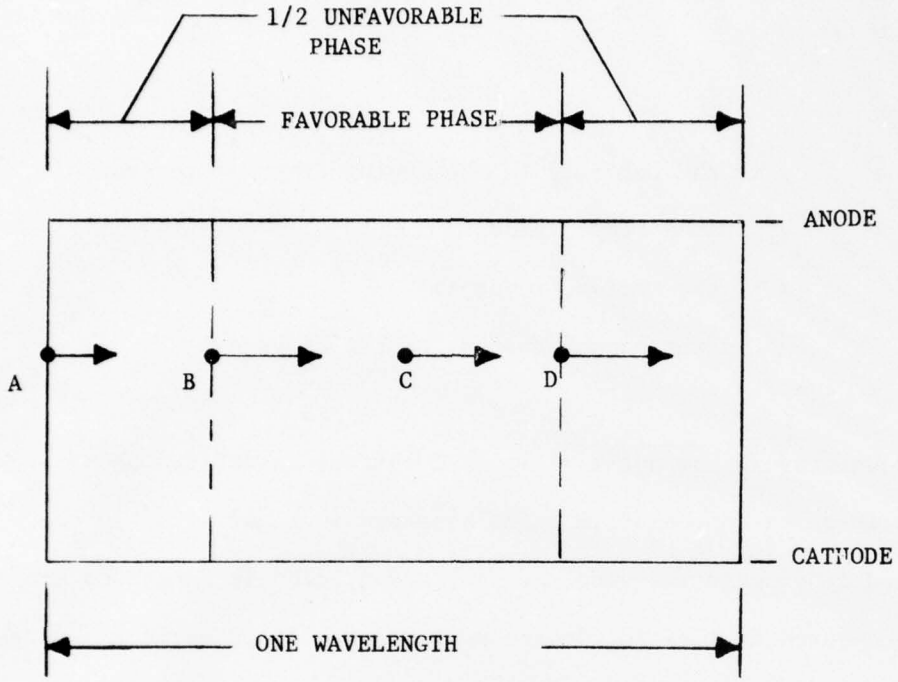

FIGURE 12

LOCATION OF RODS FOR DIFFERENT PHASES OF INDUCED CURRENTS. Rods moving forward at "A" produce induced currents 180 degrees out of phase with circuit wave. Rods moving forward at "C" produce induced currents in phase with circuit wave. Rods moving forward at "B" or "D" produce induced currents in quadrature with circuit wave. Rods A & C produce positive quadrature components which slow down the circuit wave and increase phase relative to the cold circuit phase. Rods at "D" produce negative quadrature components which speed up the circuit wave and reduce phase relative to the cold circuit phase.

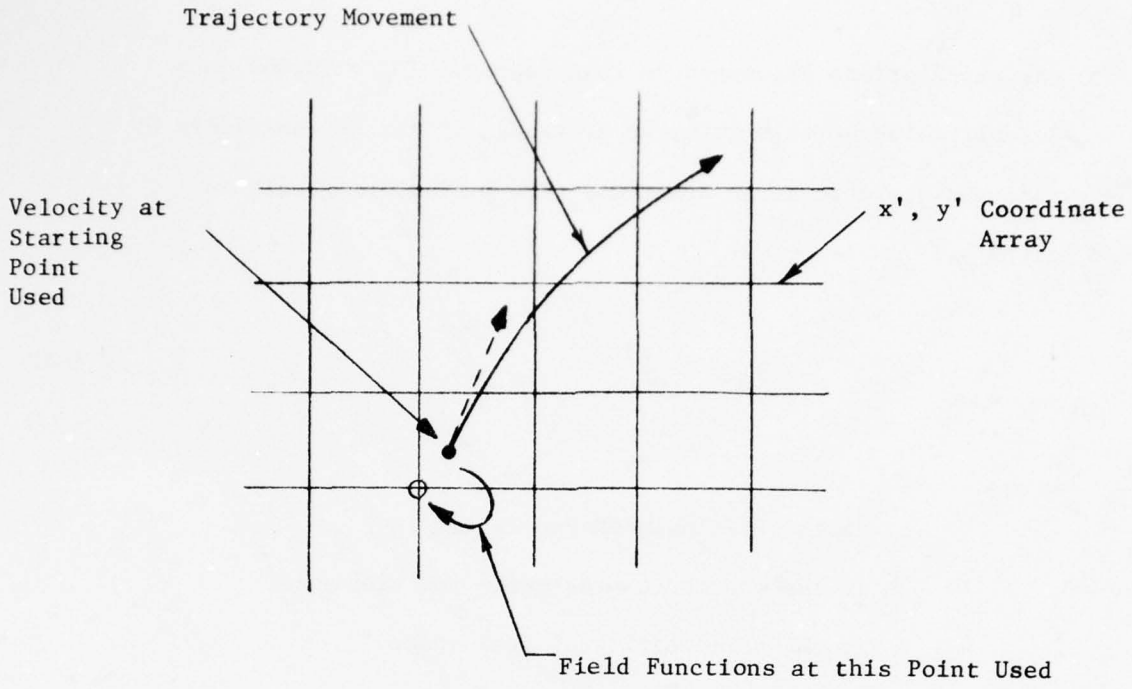

FIGURE 13a--VELOCITY AND FIELD FUNCTIONS USED IN INDUCED CURRENT COMPUTATION.

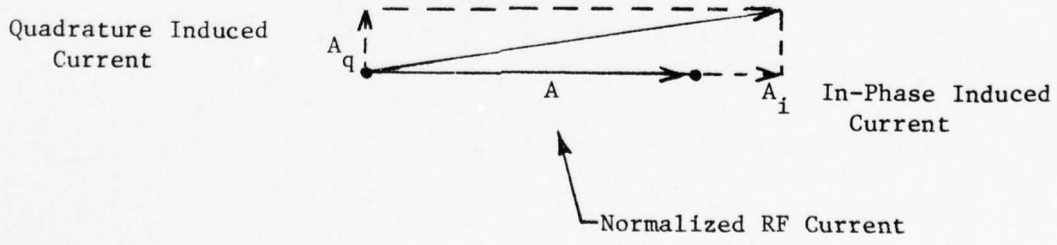

FIGURE 13b--ADDITION OF IN PHASE AND QUADRATURE COMPONENTS OF INDUCED CURRENT.

the calculations discussed in this report. (N_b = 10,000 is a default value written into the program. It may be overridden by an input variable if so desired.) The Brillouin density is given by:

$$\rho_B = \eta \varepsilon_o B^2 \qquad 2.4\text{-}42$$

where

ρ_B is the Brillouin charge density

η is the charge to mass ratio for electrons

ε_o is the permittivity of free space

B is the magnetic flux density

The normalized velocities are defined in equation 2.4-19 replace the velocities $\dot{x}$ and $\dot{y}$. The normalized frame velocity becomes the normalized y distance the frame moves in one time step.

$$v_s' = \frac{96}{\lambda} \left(\frac{\omega}{\beta}\right) \frac{1}{\Delta T} \qquad 2.4\text{-}43$$

where ΔT is the time step length.

Using:

$$\Delta T = \frac{2\pi}{g\omega_c}$$

where g is the number of time steps per cyclotron period and

$$\beta = \frac{2\pi}{\lambda}$$

we obtain:

$$v_s' = \frac{48}{\pi} \left(\frac{\omega}{\omega_c}\right) \left(\frac{2\pi}{g}\right) \qquad 2.4\text{-}44$$

The normalized induced current contributions for each rod are then given in terms of the normalized finite difference variables by:

In-phase component

$$A_i = -N_q\, v_x' \, \frac{\cosh\,(\pi x'/48)\, \sin(\pi y'/48)}{\sinh\,(\pi r)}$$

$$+ N_q\, r \, \frac{(v_y' + v_s')\, \sinh\,(\pi x'/48)\, \cos(\pi y'/48)}{\sinh\,(\pi r)} \qquad 2.4\text{-}45$$

Quadrature component

$$A_q = N_q \, \frac{v_x'\, \cosh\,(\pi x'/48)\, \cos(\pi y'/48)}{\sinh\,(\pi r)} \qquad 2.4\text{-}46$$

$$+ N_q r \, \frac{(v_y' + v_s')\, \sinh\,(\pi x'/48)\, \sin\,(\pi y'/48)}{\sinh\,(\pi r)}$$

where A_i and A_q are the normalized in-phase and quadrature components of induced current.

N_q is the number of normalized charge units per rod.

N_q is assumed to represent a negative charge and the signs of 2.4-41 and 42 have thus been reversed as compared with 2.4-36 and 37 which were for the general case of a positive charge.

The above expressions can be taken as defining the amplitudes of the normlaized currents. The necessary factor required to relate these normlaized currents to the normalized rf voltage will be presented in the next section.

2.5 Increment Circuit Wave Procedures

Once the contributions of all the rods to the induced currents have been calculated, the circuit current wave may be incremented by algebraically adding the induced current. (See Fibure 13b.) The magnitude of the new current wave is thus:

$$A' = \sqrt{(A + A_i)^2 + A_q^2} \qquad 2.5\text{-}1$$

where

A' is the new normalized current amplitude

A is the old normalized current amplitude

A_i is the in-phase component of induced current

A_q is the quadrature component of induced current

The wave is also shifted in place by:

$$\Delta\theta = \arctan \frac{A_Q}{A + A_i} \qquad 2.5\text{-}2$$

where

$\Delta\theta$ is the phase shift during the current time step

The angle of the induced current relative to the circuit wave is also calculated:

$$\Psi = \arctan \frac{A_q}{A_i} \qquad 2.5\text{-}3$$

The program assumes the favorable phase to remain in the center of the interaction box. Hence, when the wave phase shifts we must introduce a corresponding shift in the phase of the rods--i.e., if the wave phase shifts forward we must shift the rods backwards by a corresponding amount. The amount the rods are shifted is given by:

$$\Delta y' = \frac{48}{\pi} \Delta\theta \qquad 2.5\text{-}4$$

where $\Delta y'$ is the shift in the normalized y coordinate.

The $\Delta y'$ shift is positive for positive $\Delta\theta$. A positive θ means the phase of the circuit wave is increased. This corresponds to a slowing down of the wave or a relative motion of the interaction box to the left. The compensating motion of the rods is thus to the right.

These shifts in rod positions are now introduced. Both this procedure and the trajectory procedure move some of the rods outside of the interaction box across the right or left hand boundaries. The computer model assumes the space charge in the wavelengths to the right or left of the one being calculated to be the same as in the interaction box. Thus, when a rod moves out of the box across the right hand boundary a similar rod is assumed to move into the box across the left hand boundary. Similarly, if a rod moves out across the left boundary a similar rod is assumed to move in across

the right boundary. All the rods which have moved outside the interaction box are, therefore, now brought back inside the box by adding or subtracting 96.0--the normalized y dimension corresponding to one wavelength.

At this point the effect of circuit attenuation is introduced by decreasing the normalized current by the attenuation factor per time step. The power lost is temporarily represented by an amplitude A_ℓ given by:

$$A_\ell = A\sqrt{1 - \alpha} \qquad 2.5\text{-}5$$

where α is the attenuation per time step.

The rf voltage may now be calculated from the rf current and the interaction impedance. In the case of the unnormalized quantities.

$$V_{rf} = ZI_{rf} \qquad 2.5\text{-}6$$

where

V_{rf} is the voltage and I_{rf} is the rf current

The normalized voltage is similarly related to the normalized current by:

$$\phi_{rf} = KA \qquad 2.5\text{-}7$$

where

ϕ_{rf} is the normalized voltage

A is the normalized current

K is a normalization constant

The value of the constant K may be determined from a comparison of the unnormalized equations 2.4-36 and the normalized equation 2.4-41. From these equations we find:

$$V_{rf} = \frac{(a\omega_c)^2}{2\eta} \quad \phi_{rf} = \frac{\omega\beta q'}{2\pi} Z\left(\frac{a}{48}\right) A \qquad 2.5\text{-}8$$

where q' is the real charge per unit normalized charge.

$$q' = \frac{(\eta\varepsilon_o B^2) a h \lambda}{N_b} \qquad 2.5\text{-}9$$

Substituting 2.5-9 in 2.5-8 yields for the constant K in 2.5-7.

$$K = (2\eta\varepsilon_o hBZ)\ \left(\frac{1}{48}\frac{\omega}{\omega_c}\frac{1}{N_b r}\right) \qquad 2.5\text{-}10$$

where all quantities have been previously defined. The quantity in the first parenthesis is treated by the program as a normalized impedance. The quantity in the second parenthesis is treated as a program constant, i.e.

$$Z_{norm} = 2\eta\varepsilon_o hBZ \qquad 2.5\text{-}11$$

where Z_{norm} is the normalized impedance.

2.6 Emission Procedure

In Section 2.4 we described the creation of the emitted charge array. This is a linear, 96 element array having one entry for each of the columns of the potential array. When a rod is collected on the cathode, the charge of the rod is multiplied by the secondary emission ratio. This ratio is in turn determined from the calculated incident energy and a supplied secondary emission table. The resulting charge array is added to the charge in the emitted charge array--either being added to the array element corresponding to the column where the rod is collected or optionally spread over several array elements as described in Section 2.4.

Figure 14 shows a schematic representation of the arrays used in the emission procedure. In the middle is the "interaction box" shown divided into the 48 x 96 cells of the potential array. Above the interaction box we show two linear arrays containing the field at the cathode for each of the 96 columns of the potential array. One of these arrays contains the field directly as computed from the Poisson solution. The second contains the field after smoothing using the following function:

$$\varepsilon_{Sj} = \frac{S^4}{D}(\varepsilon_{j-3} + \varepsilon_{j+3}) + \frac{S^3}{D}(\varepsilon_{j-2} + \varepsilon_{j+2}) + \frac{S^2}{D}(\varepsilon_{j-1} + \varepsilon_{j+1}) + \frac{S}{D}\varepsilon_j \qquad 2.6\text{-}1$$

where

ε_{Sj} is the smoothed field for "cell" j

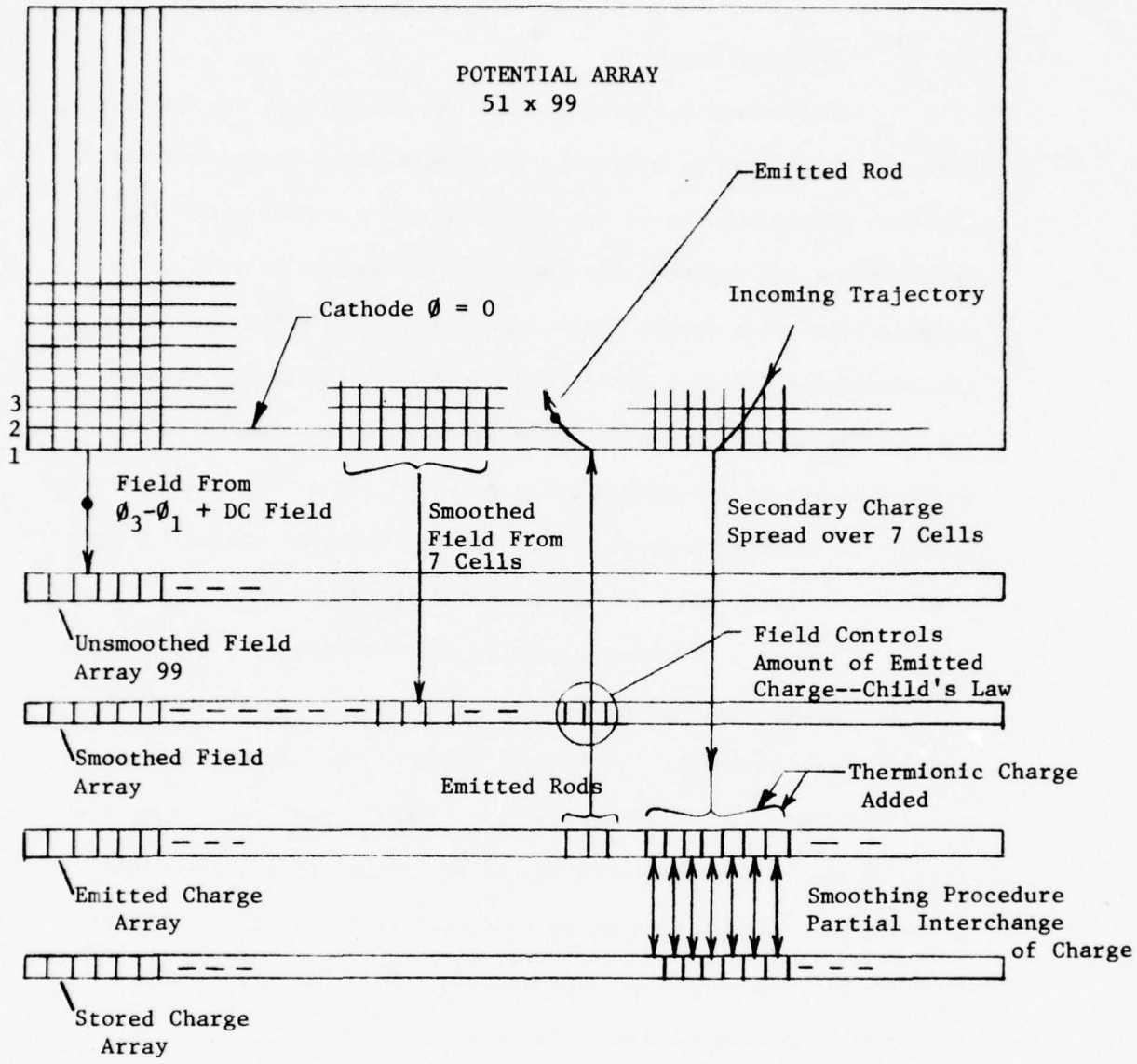

FIGURE 14

SCHEMATIC DRAWING OF ARRAYS USED IN THE EMISSION PROCEDURE.

ε_j, ε_{j+1}, etc. are the unsmoothed fields for cell j, j+1, etc.

S is the same smoothing parameter as discussed in connection with 2.4-28

D is as defined in 2.4-28.

Below the interaction box in Figure 14, we have shown the emitted charge array--a linear array of 96 elements or "cells". A rod striking the cathode is shown contributing charge to several cells of this array. Also shown is a stored emitted charge array used in connection with time smoothing of emitted charge as will be described below. Figure 15 shows a block diagram of the complete emission procedure--part of which is located in the trajectory calculation and part in the emission procedure. The first line of boxes occurs prior to the emission procedure discussed in this section. The field at the cathode is calculated subsequent to the solution of Poisson's equation. The loop following this represents the procedure for rods collected on the cathode as discussed in Section 2.4.

The first part of the emission procedure under discussion in this section is an optional time smoothing of the emitted charge. If this procedure is invoked, the secondary charge collected on a given time step will be emitted spread over several successive time steps. This procedure makes use of the second 96 cell array called the stored emitted charge array. This array contains charge from

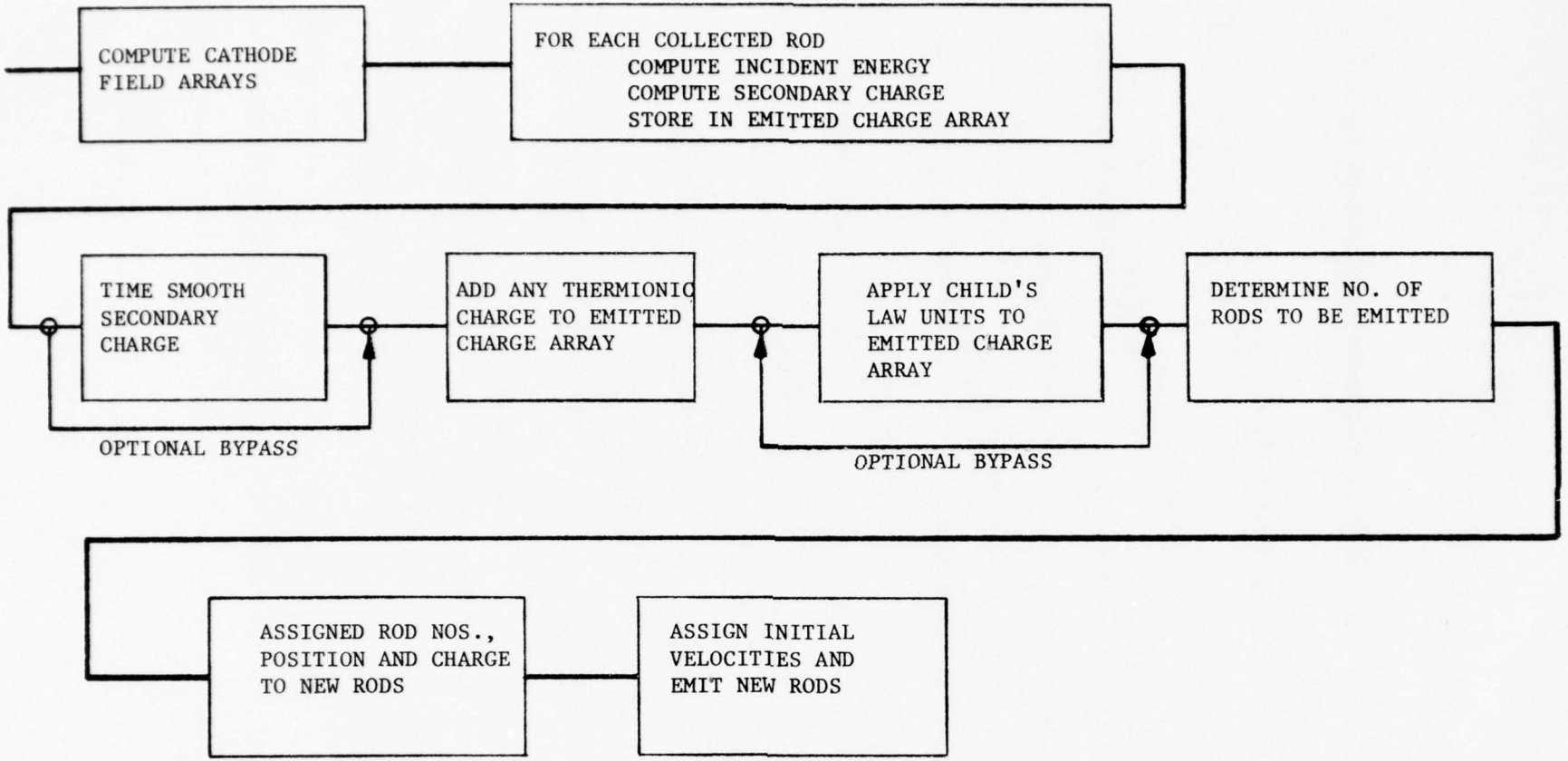

FIGURE 15--BLOCK DIAGRAM OF EMISSION PROCESS. First two blocks occur in trajectory procedure for Step N. Last block occurs in trajectory procedure for Step N+1. Remaining blocks are part of emission procedure.

prior steps which is to be emitted on the current step. For each cell of the array, the charge stored in the emitted charge becomes:

$$q = uq_c + (1 - u)\, q_s \qquad 2.6\text{-}2$$

where

q is the new charge placed in the emitted charge array

q_c is the charge previously accumulated in the emitted charge array as a result of rod interception during the current time step

q_s is the charge stored from prior time steps

u is an input variable (time smoothing factor) under control of the user

Once revised emitted charge values are determined, the stored charge array values are set equal to the emitted charge array values (q_s set equal to q).

We can see how this procedure works for a charge q_1 placed in the emitted charge array at time step M as follows:

Step M	uq_1 emitted
	uq_1 stored
Step M+1	$u\,(1-u)\,q_1$ emitted
	$u\,(1-u)\,q_1$ stored

Step M+2 $u\ (1-u)\ q_1$ emitted

$u\ (1-u)\ q_1$ stored

etc.

The total emitted charge is thus:

$$uq_1\ (1 + (1-u) + (1-u)^2 + ...) \qquad 2.6\text{-}3$$

The infinite series in parenthesis sums to 1/u so the total emitted charge sums to the original charge q_1 accumulated at step M.

The justification for using the time smoothing procedure is, again, the granularity in the number of intercepted rods per cell. One-half to one rod is intercepted per cell per step on the average. This number is a function of the granularity (time step size and number of rods) and not of the input parameters of the particular CFA under study. Because this number is relatively small, it is possible to go for several steps without intercepting a rod in a given cell and then to intercept several in one step. The time smoothing procedure smooths the secondary emission resulting from the fluctuating number of intercepted rods. Again, the smoothing procedure is a means of reducing fluctuations in the model which arise from program granularity and are a great deal larger than the random fluctuations which occur in nature.

This time smoothing procedure is the one we have found necessary to invoke to eliminate the instabilities arising in the secondary emission procedure. By successive trials we have found

that a value of the parameter u of 0.125 accomplishes the required smoothing. The procedure described above is an infinite series which emits the total charge in an infinite number of steps. The decay rate of the series with u of 0.125 is such that 75% of the charge generated on a given step is emitted over the successive 10 steps which constitute one cyclotron period of the calculation for the time step being used. Over a total of 25 steps, 96% of the charge is emitted. Use of this degree of smoothing is justified by the fact that space charge distributions in the moving frame of reference change slowly over a cyclotron period.

In the second semi-annual report[8] we discussed the effects of emission procedure instabilities in some detail. It was shown that if we did not invoke time smoothing, traveling voids developed in the space charge distribution and the V-I curve of the CFA was displaced from its proper location along the voltage axis.

The next procedure in Figure 15 is the addition of any thermionic charge to the emission array. Input variables set the amount of charge per cell to be emitted and the number of time steps over which emission occurs. The current represented by one rod emitted per time step can be computed from the program parameters and normalization constants. The number of time steps corresponds to a physical distance the interaction box has traveled. Thus, the initial thermionic charge can be associated with a value of total priming current and priming current density employed on the first pass. Most of our subsequent computations have used 48 thermionic

rods of 0.1 normalized charge per step for 10 steps to prime the first pass calculation. The corresponding priming current is 0.24 amps and the priming current denstiy is 0.75 amps/cm^2. This is, of course, much more priming current than really exists in the first pass of the build up process in a cold cathode CFA. (10^{-9} amps resulting from field emission appears more reasonable.) However, the use of priming sources having comparable emission capability has not appeared to affect the performance of some experimental CFA's as long as the RF drive power was adequate to insure cold cathode starting. From the nature of the model, it is expected that the choice of priming current for the first pass calculation will not affect the computed values to which subsequent passes settle down.

The next procedure in Figure 15 is an optional space charge-limiting procedure. This procedure limits the maximum charge emitted per cell to one equivalent to the space charge-limited current from Child's law:

$$I = 2.33 \times 10^{-6} V^{3/2}/d^{4/3}$$

In the computation of this current, the potential one matrix unit above the cathode surface is employed for V and matrix unit spacing is employed for d. The use of Child's law near the cathode surface is justified by the fact that electron trajectories (in the laboratory reference frame) travel through the first cell of the potential array

in a direction almost vertical to the cathode and without significant deflection caused by magnetic field forces. Thus, the trajectories in the first row of cells are similar to what they would be in a space charge-limited diode.

A departure from the conditions in the first row of cells from a diode occurs because current is flowing in two directions--away from the cathode and back towards the cathode. If these two currents provided equal contributions to the charge in the first cell, the one way current flow should be calculated by dividing the total Child's law current given above by two. In an operating CFA the returning electrons have significant kinetic energy gained from the RF interaction, Thus, the charge density associated with the returning current is low compared with that associated with the outgoing current. As a consequence, we have neglected the contribution of the returning current to the charge in the first row of cells and computed the space charge-limited current from the normal form of Child's law shown above. The program calculates the Child's law constant normalized as required by the emission procedure. An override procedure is provided so that this constant can be adjusted if conditions are such that the contributions of the returning current to the charge in the first row of cells is not negligible. This would be the case, for example, if computations were to be conducted with zero RF drive. The permissible range of adjustment of this constant is from the

value computed by the program to half this value.

The Child's law procedure examines the charge to be emitted in each element of the emitted charge array, and if it is larger than permitted by Child's law, it replaces the charge by the maximum charge permitted by Child's law. If the space smoothing of emitted charge described in Section 2.4 is employed, the smoothed cathode field array is used in the Child's law procedure. Otherwise, the unsmoothed array is used. If the electric field at the cathode is retarding at any columns of the potential array, the emission procedure sets the charge in the corresponding element of the emitted charge array to zero.

As an option, the Child's law emission procedure contains a means of neglecting elements in the emitted charge array which will not contribute significantly to the interaction. Electric fields which are accelerating, but of small value, are not permitted to cause emission. The minimum field for emission is set at a value which results in emission of 1/20th of a normalized charge unit. This value can be overridden by an input variable and the whole minimum charge procedure skipped if so desired.

There has been considerable discussion about whether or not a Child's law limit should be imposed on the emission. At the start of the program we did not impose such a limit. In the absence of an imposed limit, space charge limiting occurs when sufficient charge has accumulated to cause the field at the cathode to become retarding. At this point, the original program suppressed

emission from the corresponding cell along the cathode. The space charge then drained until the cathode field again became accelerating. At this point, emission was reinstituted. This procedure resulted in a cathode field which periodically fluctuated from accelerating to decelerating. The same result would have occurred if we had attempted to model a space charge-limited diode by emitting disks of fixed charge with zero initial velocity. In our CFA model, the fluctuations appeared almost at random from cell to cell so that the cathode field varied from positive to negative as a function of distance in the moving reference frame. We believed this type of self-limiting imposed by the model was more arbitrary than the imposition of the Child's law procedure. Since imposition of the Child's law procedure, we have found that the cathode field still fluctuates somewhat erratically, but rarely become retarding. These fluctations will be discussed further in Section 3.6

An alternative to the use of the Child's law procedure would have been an attempt to model the phenomenon in the vicinity of the potential minimum. Such a procedure would have involved giving initial rods random initial velocities in accordance with a half Maxwellian distribution. One objection to such a procedure is that with 48 to 96 rods emitted per time step, we don't have enough rods to effectively implement random statistics. Another objection lies in the distance of potential minimum from the cathode relative to the mesh size of the potential array.

For thermionic emission this distance is given by:

$$x_m = 0.0156\ (1000J)^{-1/2}\ (\frac{T}{1000})^{3/4} \qquad 2.6\text{-}5$$

where

x_m is the distance from the cathode surface to the potential minimum

J is the current density in milliamps/cm^2

T is the absolute temperature in °K

For a typical CFA assuming T = 1350°K and J = 10 amps/cm^2 peak, the value of s_m is less than 0.00025 inch. For secondary emission we can assume an equivalent temperature higher by about a factor of 40 because of the higher initial velocities which are known to exist for secondary electrons. (The temperature in the above formula is a measure of the initial energy.) This increases x_m to about 0.0016 inches. The mesh size of the potential array in the direction from anode to cathode is 0.0018 inches. Thus, for thermionic emission the potential minimum lies much less than one matrix unit away from the cathode while for a secondary emission it lies just under one matrix unit away. For a simulation of potential minimum phenomenon by the computer program we should have several matrix cells over the region from cathode to potential minimum. This would require constructing a fine grain matrix just over the cathode surface. This would be possible, but would have involved a very substantial increase in the program complexity. As an

alternative, the use of the Child's law procedure rather than a detailed simulation of phenomenon at the potential minimum appeared adequate.

The next step in the emission procedure is the determination of the number of rods to be emitted. This number controls the total number of rods which become active in the simulation. The emission procedure contains two options for the determination of the number of rods to be emitted. The first option specifies a number to be emitted per step as an input variable which remains constant throughout the run. The second option allows the program to determine the number to be emitted based on the number already active in the simulation. This option results in a variable number emitted per step during the course of the run. Most of the results reported were obtained using the first of these options.

With either emission option an interpolation procedure associates charge from one or more elements of the emitted charge array with a rod to be emitted. This procedure permits splitting the charge in any element and associating different fractions of it with two adjacent rods. Thus, there does not have to be an integral relationship between number of rods to be emitted and number of elements in the emitted charge array. The emitted rods are spaced at uniform increments along the cathode surface.

In the case of a fixed number of rods to be emitted per time step, the number of rods (up to 96.0) is taken from the

value specified in the input data. If, however, the charge of any rod is zero, emission of that rod is skipped. In the case of a variable number of rods per time step, the number of rods is determined from:

$$N_e = R_1 - R_2 N$$

where

N_e is the number of rods to be emitted

R_1 and R_2 are constants

N is the number of rods currently active in the simulation

Default values of R_1 and R_2 are provided by the program as follows:

$$R_1 = 132.0$$

$$R_2 = 0.042$$

These values may be overridden by the user using input variables to establish other values for R_1 and R_2. The variable number of rods procedure is intended for use when the cathode is emission limited. As discussed in Section 3, use of a fixed number of rods per time step under these conditions leads to a drift of the total number of rods in the simulation to an unacceptably low number.

Once the number of rods has been determined, the charge per rod is determined from the emitted charge array using the interpolation procedure and the location of the emitted rods along

the cathode is calculated and stored. Associated with each rod there is also a control variable of six-digit length known as the age.

This variable contains the column of origin in the first two digits and the age in time steps in the last four digits. To signify emission the column of origin is entered, the last four digits are set to zero and the whole variable is set negative. The rod charge, normalized coordinates, and "age" have thus been set. The initial velocities are subsequently set in the trajectory procedure when the first segment of the rod's trajectory is calculated.

The last block in Figure 15 is located in the trajectory procedure and occurs on the subsequent time step. When the negative age is encountered by the trajectory procedure, the rod is treated as newly emitted and the v_x' and v_y' calculations are skipped. Instead, v_y' is given a value equal to the negative of the frame velocity and v_x' is given an initial value which is 1/20th of the frame velocity as might be typical for secondary electrons for the designs studied. Use of zero initial v_x' has been used in earlier calculations reported in the second semi-annual report. Little difference in results of the simulation appears evident for v_x' varied from 0 to 1/20th the frame velocity. The age is then set positive to indicate that the rod is active in the interaction space.

A rod is not recognized as contributing to the space charge until it has been emitted and the age has been set positive. If after emission the rod has moved less than one matrix unit--i.e., if it lies between x = 2.5 (the cathode) and x = 3.5, its charge is distributed between two adjacent points in row 3 of the potential array. Once the rod has moved beyond x = 3.5, its charge is distributed to the four surrounding points of the potential array as described in Section 2.3.

2.7 Main Output List Procedure

The program is now ready to write the output data for the time step under consideration. The main output data as read to the printer is listed in Table III. All of this data is in unnormalized form. An auxiliary list of data is also (optionally) read to a disk file and may later be printed. This list contains some of the normalized variables and several variables relating to the taper procedures described in Section 2.8. The variables in this auxiliary list are summarized in Table IV.

The main output procedure must recover the real values of power, current, and dissipations from the normalized values and the real distance from the input from the time step number.

The rf power is calculated from the rf voltage by:

$$P = \frac{V_{rf}^2}{2Z_o} \qquad 2.7\text{-}1$$

with

$$V_{rf} = \left(\frac{a\omega_c}{2\eta}\right)^2 \phi_{rf} \qquad 2.7\text{-}2$$

where

V_{rf} is the actual rf voltage

ϕ_{rf} is the normalized rf voltage

A similar unnormalization gives the power lost in circuit attenuation from the value of A_ℓ defined in equation 2.5-5 in Section 2.5.

TABLE III

MAIN OUTPUT LISTING

Following output data is provided for each time step of the calculation:

1. time step number
2. distance of center of interaction box from RF input
3. RF power on slow wave circuit
4. cumulative power dissipated on cathode to present point in calculation
5. cumulative power dissipated by electron interception to present point in calculation
6. cumulative power dissipated in circuit attenuation to present point in calculation
7. power dissipated on cathode during current time step
8. power dissipated by electron interception on anode during current time step
9. cumulative anode current collected to present point in calculation
10. phase of RF circuit wave relative to the cold circuit wave
11. phase of induced current wave relative to the RF cold circuit
12. average energy of rods incident on cathode in the current time step
13. total number of rods participating in the calculation
14. number of rods emitted during the current time step
15. number of rods collected on the cathode during the current time step
16. number of rods collected on the anode during the current time step
17. number of charge units emitted during the current time step
18. number of charge units collected during the current time step

TABLE IV

AUXILIARY OUTPUT LISTING

Following output data is provided for each time step of the calculation.

1. time step number
2. distance in wavelengths
3. four taper parameters describing anode-cathode spacing, phase velocity, interaction impedance and magnetic flux density relative to values at input
4. normalized anode-cathode voltage
5. normalized d.c. potential in moving reference frame
6. normalized impedance
7. normalized charge unit size
8. current value of time steps per cyclotron period
9. normalized RF circuit current
10. normalized in-phase induced current
11. normalized quadrature phase induced current

To recover the power dissipated on the anode and cathode from the kinetic energies accumulated from 2.4-24, we proceed as follows:

$$\text{mass per rod} = \frac{\text{charge per rod}}{\eta} = \frac{N_q q'}{\eta} \qquad 2.7\text{-}3$$

where

η = e/m for electron

N_q = number of normalized charge units

q' = charge per unit normalized charge from equation 2.3-16

From the normalizations introduced in Section 2.4:

$$v_x = v_x' \frac{a}{48} \frac{1}{\Delta T}, \quad v_y = v_y' \frac{a}{48r} \frac{1}{\Delta T} \qquad 2.7\text{-}4$$

where

$$\Delta T = 2\pi/g\omega_c \qquad 2.7\text{-}5$$

and where g is the number of time steps per cyclotron period.

Using 2.4-24, 2.3-16, 2.6-3,4,5 we find the energy dissipated to be:

$$W = \frac{2\varepsilon_o (a\omega_c)^5}{(48)^2 \eta^2} \quad \frac{1}{(r)(2a/h)(\frac{2\pi}{g})^2 \omega_c N_b} \; W' \qquad 2.7\text{-}6$$

where W' is the normalized energy defined by 2.4-23.

AD-A065 736 VARIAN ASSOCIATES BEVERLY MASS F/G 9/1
CFA DESIGN IMPROVEMENT PROGRAM. VOLUME II. COMPUTER MODELING ST--ETC(U)
JUN 78 H L MCDOWELL N00123-75-C-1294
UNCLASSIFIED NL

2 OF 4
AD
AD 65736

To find the power dissipated we must divide the energy by the appropriate time. During a single transit of the interaction box through the CFA there will be n similar interaction boxes which pass through the CFA where n is the number of wavelengths in the CFA. The passage of the n wavelengths will result in n interceptions of rods similar to those which occur in the interaction box we are following. Thus the power dissipated becomes:

$$P_d = \frac{W}{T/n} \qquad 2.7\text{-}7$$

where

n is the number of wavelengths

T is the transit time of the interaction box through the CFA

However,

$$T/n = 2\pi/\omega \qquad 2.7\text{-}8$$

Thus:

$$P = \frac{4\pi\varepsilon(a\omega_c)^5(\omega/\omega_c)}{(48)^2 n^2 r(2a/h)(2\pi/q)^2 N_b} \quad W' \qquad 2.7\text{-}9$$

This relates the real dissipated power to the normalized kinetic energy from 2.4-24.

A similar argument may be used to relate the real anode current to the number of normalized charge units collected. Equation

2.3-16 gives the charge per unit normalized time. Using 2.6-8:

$$i_a = \left[\frac{2\varepsilon_o}{\pi} \frac{(a\omega_c)^3(\omega/\omega_c)}{\eta N_b\, r\, (2a/h)}\right] N_q \qquad 2.7\text{-}10$$

where N_q is the number of normalized charge units collected.

The distance the interaction box has traveled is found from:

$$D = vt = \left(\frac{\omega}{\beta}\right)\left(\frac{2\pi}{g\omega_c}\right) = \lambda\left(\frac{\omega}{\omega_c}\right)\left(\frac{1}{g}\right) \qquad 2.7\text{-}11$$

where

D is the distance traveled per time step

λ is the slow wave wavelength

g is the number of time steps per cyclotron period

The wavelength, λ, is found from the input quantities from:

$$\lambda = \frac{2\pi d}{(\beta d)} \qquad 2.7\text{-}12$$

where

d is the pitch

(βd) is the phase shift per section

2.8 Taper Procedure

If the interaction space is tapered, a final step in the computation for each time step is the revision of the normalized variables and program constants for the revised interaction space parameters. The program permits tapering of anode-cathode spacing, circuit phase velocity, circuit interaction impedance and magnetic field as a function of length. These quantities may be simultaneously tapered if desired. The taper shape is read in as input data giving the values of the above four variables relative to their values at the input as a function of distnace from the input.

Figure 16 shows a block diagram of the taper procedure. This procedure approximates the actual situation in which the geometry varies continuously by changing the interaction space parameters on every time step. With the exception of a first order correction to the d.c. electric field, the interaction space parameters are considered constant over the interaction box on a given time step. These parameters are gradually changed from step to step in accordance with the taper functions.

This procedure departs from the real situation in which the interaction space parameters vary over the length of the interaction box in the direction of propagation. Thus, the use of the taper procedure introduces additional assumptions into the model. If the slope of the taper functions are not great, it is believed that these assumptions will not greatly affect the results.

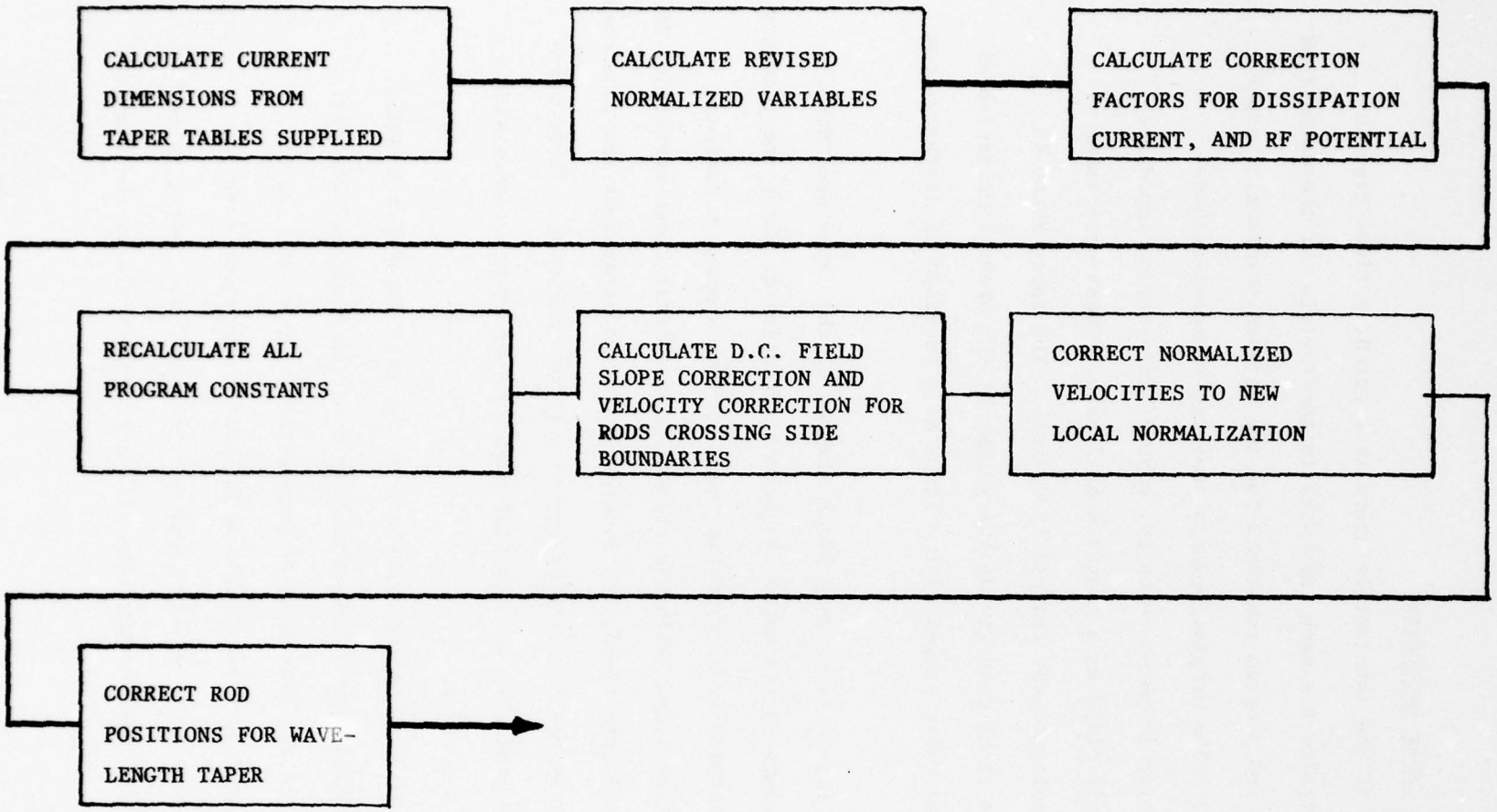

FIGURE 16--BLOCK DIAGRAM OF THE TAPER PROCEDURE

Implementation of the taper procedures involves a great deal of "housekeeping" to correct the normalized variables and program constants. It simplifies keeping these corrections simple if we think in terms of two sets of normalized parameters--one set in terms of the input parameters of the interaction space and one set in terms of the local parameters which vary in accordance with the taper function. The normalized RF voltage, normalized RF and d.c. current, the normalized dissipation are all expressed in terms of the input normalization. The constants relating these normalized variables to the real variables are thus not affected by the taper.

The results as calculated on each time step are in local normalization and they must be corrected to the input normalization before being added to the cumulative variables. Such corrections must be applied to the induced currents and the dissipated energies. The energy corrections are made immediately on collection of a rod. Thus, the normalized energy remains in the input normalization and the secondary emission routine is entirely in input normalization. The corrections to the induced currents are made as soon as they are calculated.

The first step in the normalization procedure is the calculation of four taper parameters as follows:

T_a = ratio of anode-cathode spacing to spacing at the input.

T_w = ratio of slow wave wavelength to wavelength at the input.

T_z = ratio of interaction space impedance to impedance at input

T_b = ratio of magnetic field to field at the input.

These ratios are obtained by linear interpolation between points in the supplied taper tables.

The revisions to the normalized parameters describing the interaction space are now made. These revisions may be derived directly from the definitions of the normalized variables.

$$\text{Normalized Frequency} = \omega/\omega_c \times \frac{1}{T_b} \qquad 2.8\text{-}1$$

$$\text{Normalized Anode Voltage} = \phi_a \times \frac{1}{(T_a T_b)^2} \qquad 2.8\text{-}2$$

$$\text{Normalized Impedance } Z' = \frac{4\varepsilon_o(a\omega_c)Z}{(2a/h)} \times T_b T_z \qquad 2.8\text{-}3$$

$$\text{Ratio } 2a/\lambda \times \frac{T_a}{T_w} \qquad 2.8\text{-}4$$

Parameter g (time steps per cyclotron period x $1/T_b$ 2.8-5

Parameter N_b = number of normalized charge units to fill interaction box to Brillouin density x $T_a T_w T_b^2$. 2.8-6

The correction to g is an arbitrary decision which is made to keep the distance in wavelengths the interaction box travels

forward in a time step constant as the magnetic field is tapered. When specifying g for a calculation in which the magnetic field is tapered, the variation of g must be kept in mind and a large enough g specified so that the smallest g occurring during the calculation is still adequately large for an accurate simulation.

The correction to the parameter N_b is made so that the charge of a given rod remains fixed.

The maximum charge per step in the Child's law procedure must also be corrected. By following through the normalization equations this correction may be found to be:

$$\text{charge per step} \times T_w/T_a^2 \qquad 2.8\text{-}7$$

The attenuation factors are corrected assuming the attenuation per wavelength is constant.

The correction factors for induced current and dissipation are next found by tracing the equations through the normalizations. These factors are:

$$T_i = \text{induced current correction} = T_z^{1/2} \qquad 2.8\text{-}8$$

$$T_x = \text{x directed energy correction} = T_a^2 \qquad 2.8\text{-}9$$

$$T_y = \text{y directed energy correction} = T_w^2 \qquad 2.8\text{-}10$$

A correction factor to the constant which relates the normalized potential $\emptyset'$ which must be in local normalization to the normalized potential $\emptyset$ in input normalization must also be calculated. This correction is calculated by the taper procedure and applied by

the procedure which calculates the program constants. This correction is again found by tracing through the normalizations and is equal to:

$$T_e = \frac{T_z^{1/2}}{T_a^2 T_b^2} \qquad 2.8\text{-}11$$

Once these factors have been calculated, the routine which calculates the program constants is recalled and the constants are calculated for the current interaction space dimensions.

Next, a first order correction for the variation of the d.c. field across the width of the interaction box and velocity corrections for rods crossing the left or right boundaries of the interaction box are calculated. The taper routine calculates the frame velocities at the left and right sides of the interaction box and from this finds the values of $\emptyset_m'$, the moving frame of d.c. potential at the left and right side of the box. From these potentials a correction factor for the normalized field G_x is obtained as follows:

$$S = \frac{\emptyset_m{}'_r - \emptyset_m{}'_\ell}{(2)(24)} \qquad 2.8\text{-}12$$

where $\emptyset_m{}'_r$ is the normalized moving frame d.c. potential at the right hand side of the box, $\emptyset_m{}'_\ell$ is the potential at the left side and S is the correction factor.

The factor of 2 in the denominator arises because the correction is applied as a $\pm$ value from the center of the interaction box. The factor of 24 in the denominator is required to convert a

normalized potential to a normalized field. The correction factor is applied to the normalized electric field G_x used in the trajectory procedure as follows:

$$G_{xc} = G_x + S\,\frac{(y'-2.5)}{48} - S \qquad 2.8\text{-}13$$

where

G_{xc} is the corrected x directed field on a rod

G_x is the uncorrected x directed field

y' is the normalized y coordinate

This correction is the first order correction for field variation across the interaction box referred to above.

Two velocity correction factors are also calcualted as follows:

$$C_1 = 1.0 - \frac{a_r}{a_\ell} - \frac{B_r}{B_\ell} \qquad 2.8\text{-}14$$

$$C_2 = 1.0 + \frac{a_r}{a_\ell} + \frac{B_r}{B_\ell} \qquad 2.8\text{-}15$$

where a_r and a_ℓ are the anode-cathode spacings at the right and left sides of the interaction box and B_r and B_ℓ are the magnetic filux densities at the right and left sides of the box.

When a trajectory leaves the interaction box along the right hand boundary, it is reintroduced at the same distance from

the cathode along the left boundary, but with the velocity corrected by the factor C_1 to account for the differing average velocities along the left and right boundaries. Similarly a rod crossing the left boundary reappears at the right boundary with the velocity changed by the factor C_2.

The next step in the taper procedure is to correct the normalized velocity of all the rods for the new local normalization. These corrections are:

$$v_{xc}' = v_x' \, T_{a2}/T_{a1} \qquad 2.8\text{-}16$$

$$v_{yc}' = v_y' \, T_{w2}/T_{w1} \qquad 2.8\text{-}17$$

where

v_{xc}' and v_{yc}' are the corrected normalized velocities

v_x' and v_y' are the normalized velocities before correction

T_{a2} and T_{w2} are the spacing and wavelength correction factors which have been calculated for the next time step

T_{a1} and T_{w1} are the correction factors used on the present step

In the case of a wavelength change, there is a further correction to be made. As shown in Figure 17 we visualize the rods as moving with a constant average velocity while the wavelength changes. This means that the relative position of the rods in the

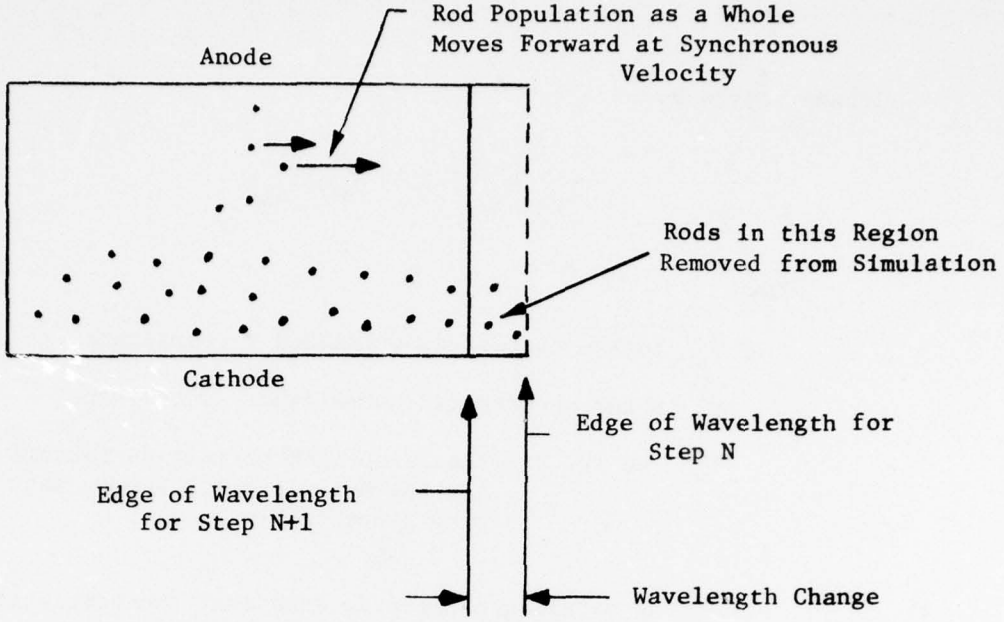

FIGURE 17a--WAVELENGTH CONTRACTION ON SUCCESSIVE TIME STEPS.
Amount of wavelength change in a single step greatly exaggerated.

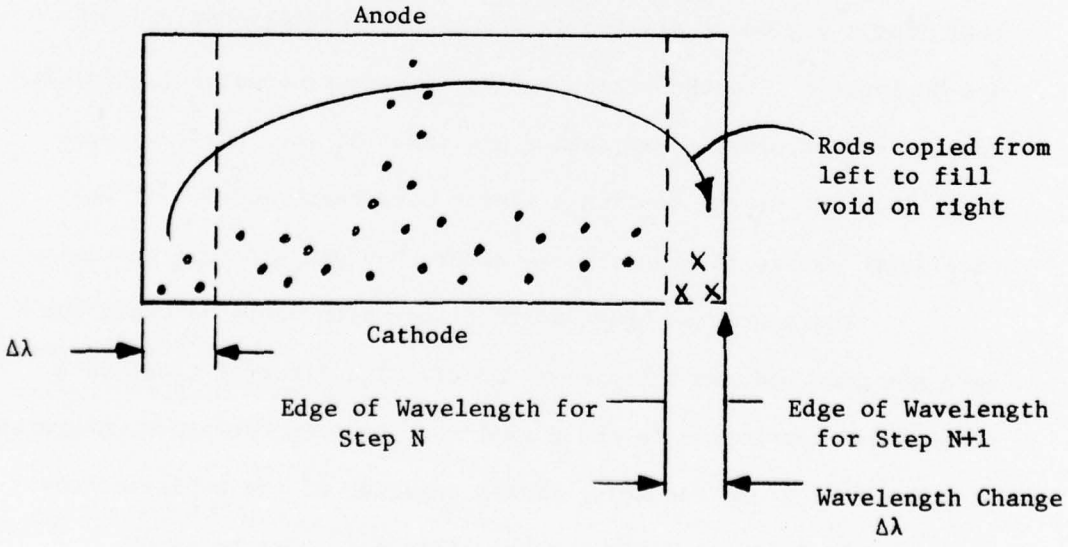

FIGURE 17b--WAVELENGTH EXPANSION ON SUCCESSIVE TIME STEPS. Amount of wavelength change in a single step greatly exaggerated.

frame shifts by:

$$y_c' = (y'-2.5)\ T_{w2}/T_{w1} \qquad 2.8\text{-}19$$

where

y_c' is the corrected normalized y coordinate

y' is the uncorrected normalized y coordinate

T_{w2} and T_{w1} are the wavelength correction factors for the next step and the present step respectively

If the wavelength taper is such that the wavelength decreases, there will be a region, as shown in Figure 17A, where rods originally inside the interaction box are now outside the box. These rods are simply removed from the simulation. If the wavelength increases there will be a region, as shown in Figure 17B, where the interaction box is devoid of rods. In this case, rods from a region of similar length on the left side of the box are duplicated into the vacant region. These procedures for adjusting the rod population may seem a bit unsatisfying, but they seem to be the best we can do with a single wavelength model. If the wavelength change is gradual, the error they cause should be minimal.

There are two other corrections which could be made, but have not been made in the present model. The first of these is a first order correction to the normalized field G_y for a d.c. component of y directed field resulting from a tapering of the anode-cathode spacing. Preliminary estimates show this d.c. term to be of

the same order as the RF electric field at the Brillouin hub surface. Thus consideration should be given to adding a correction for this y directed d.c. field. The second correction not currently employed is for the normalized position change when the anode-cathode spacing is changed. As shown in Figure 18, a change in the anode-cathode spacing changes the normalized x coordinate even though the actual position remains unchanged. The original reason for leaving out this correction was that the centers of electron trajectories are known to follow equipotentials for gradual changes in spacing. This corresponds to the normalized x coordinate remaining constant. In retrospect, we believe that this correction should also be added. The effect of the fields in the taper region will properly place the rod on the correct equipotential without its artificially being moved as is the effect of the present procedure.

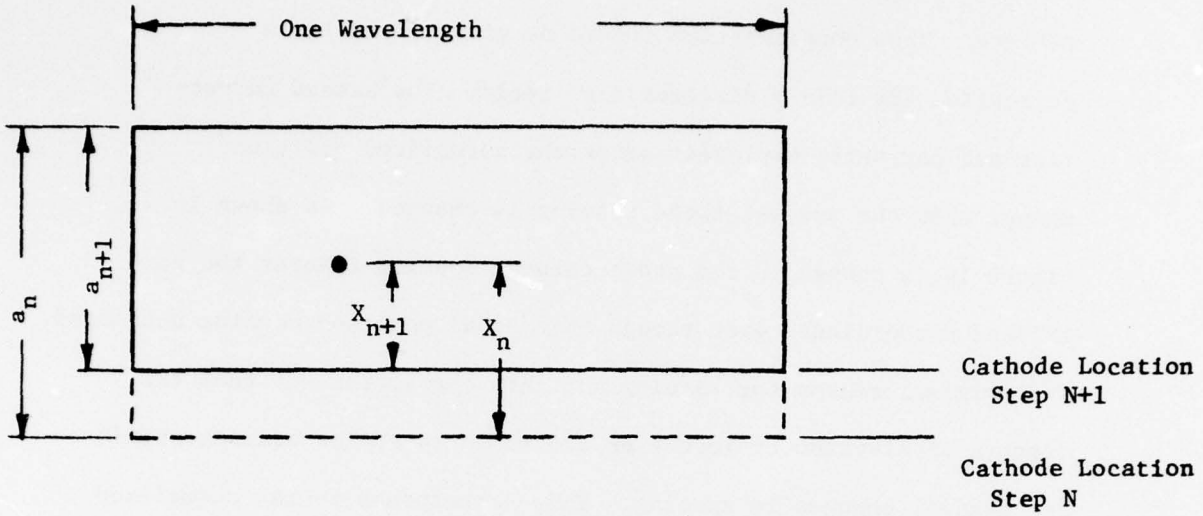

$$x'_{n+1} = 48 \frac{x_{n+1}}{a}$$

$$x'_n = 48 \frac{x_n}{a}$$

FIGURE 18

NORMALIZED POSITION ADJUSTMENT FOR FIXED REAL POSITION WHEN THE ANODE-CATHODE SPACING CHANGES. Size of position step in a single time step is greatly exaggerated.

2.9 Sever and Exit Procedure

The remaining blocks in Figure 2 are the sever and exit procedures. The sever procedure checks to see if the current time step is one at which a logical operation such as the beginning or end of a sever, the beginning or end of an attenuator, or the end of the tube occurs. A table of the time step numbers for these operations has been prepared by the input data from the initialization procedure. At the beginning of a sever, the amplitude of the circuit wave is set to zero and a control variable is set to indicate to the trajectory procedure that the incrementing of the circuit wave is to be skipped. Trajectory calculations are continued through the drift space under the influence of the d.c. and space charge fields. At the end of the sever, the control variable is reset to allow incrementing of the circuit wave. Build up of a circuit wave from any residual bunching in the space charge is then possible. An option for randomizing the space charge distribution in the y direction while maintaining the x coordinate may be invoked at the end of the sever. This has been used in some special studies to investigate the effect of complete debunching of the space charge in the drift space. It has not been used in the majority of studies discussed in this report.

When the end of the tube is reached, the sever procedure directs the computation to the exit procedure. This procedure makes a correction to the rod population data which is necessary if this data is to be used as the input to a subsequent pass calculation.

If the interaction box moves other than an integral number of wavelengths in a full transit around the CFA, it does not arrive opposite the input at the end of the pass at the instant the input fields have the same phase as they did at the start of the pass. Thus, the center of the favorable phase will not be at the center of the interaction box at the start of the subsequent pass. Since we assume the center of the favorable phase at the center of the box in the subsequent pass calculation, we must correct the rod locations. The amount of the correction is the fraction of a wavelength by which the interaction box travels around the CFA departs from an integral number of wavelengths. The correction to the normalized y coordinate is thus:

$$\Delta y' = -96 \left(\Delta\frac{L}{\lambda}\right) \qquad 2.9\text{-}1$$

where

$\Delta y'$ is the correction to the normalized y coordinate

$\Delta\frac{L}{\lambda}$ is the fractional number of wavelengths beyond an integral number which the interaction box has traveled in one transit around the CFA

If this correction shifts any rods outside the interaction box (i.e., to another wavelength) they are shifted back into the box by adding an additional $\Delta y'$ of ± 96 as required.

2.10 Additional Outputs

The program provides a number of optional outputs in additional to the main and auxiliary listings described in Section 2.7. The rod action data described below is written directly to the printer and intermixed with the main output. The remaining outputs are written to auxiliary disk files and later processed by a post processor program to produce additional output listings. The auxiliary file outputs occur at a number of points in the program. Figure 19 shows the block diagram of Figure 2 modified to show the outputs to the auxiliary files. A description of each of these auxiliary outputs follows.

Rod Action Data--This data is written on every rth step where r is a control variable provided in the input data. This data summarizes the average number of rods emitted and collected in each of the 96 cells of the interaction box along the cathode over the last r steps. It also summarizes the average charge densities and average velocities of rods in each of the 48 rows of the interaction box during the last r steps for this rod action listing.

Trajectory Data (KFILE)--Trajectory data including the position, velocities, charge and age of every kth rod is written to this file on every time step--where k is a control variable provided in the input data. These data are subsequently processed by a system sort utility to group all the data on each individual rod sequentially and they are then processed by the post processor to produce trajectory listings and a rough trajectory plot of the

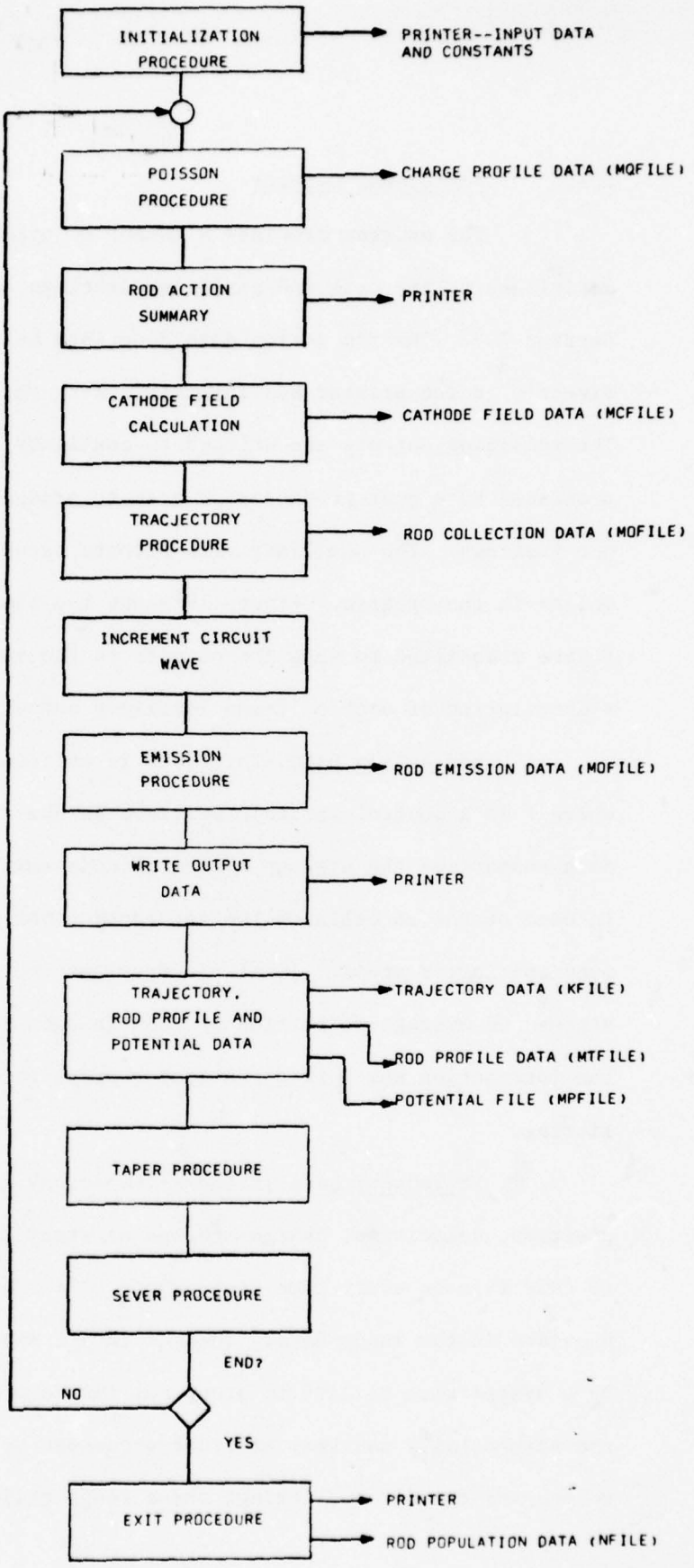

FIGURE 19

BLOCK DIAGRAM OF THE PROGRAM WITH OUTPUTS ADDED

kind shown in Figure 20. These data are written immediately following the main output procedure.

Field at the Cathode (MCFILE)--The field at the cathode in each of the 96 cells is written to an auxiliary file--usually on every time step. These data are subsequently processed by the sort utility and then by the post processor to provide a listing of the fields.

Trajectory End Points (MOFILE)--Data on the origin and termination of every ℓth trajectory is written to this file--where ℓ is an input control variable (usually equal to k used in KFILE write). These data are subsequently processed by the post processor to produce a listing telling where and how each trajectory begins and ends. The emission (starting point) data are written by the emission procedure and the collection data are written by the trajectory procedure.

Potential File (MPFILE)--The normalized potential at every point in the potential array is written to this file every m steps--where m is an input control variable. These data are processed by the post processor to produce listings of the potential array data. These data are written immediately following the main output procedure.

Charge Profile File (MQFILE)--The charge assigned to every point in the potential array is written by the Poission equation procedure every n steps where n is an input control variable. These data are processed by the post processor to produce charge profile plots such as shown in Figure 21. These plots are extremely useful in visualizing the space charge configurations and the nature of the

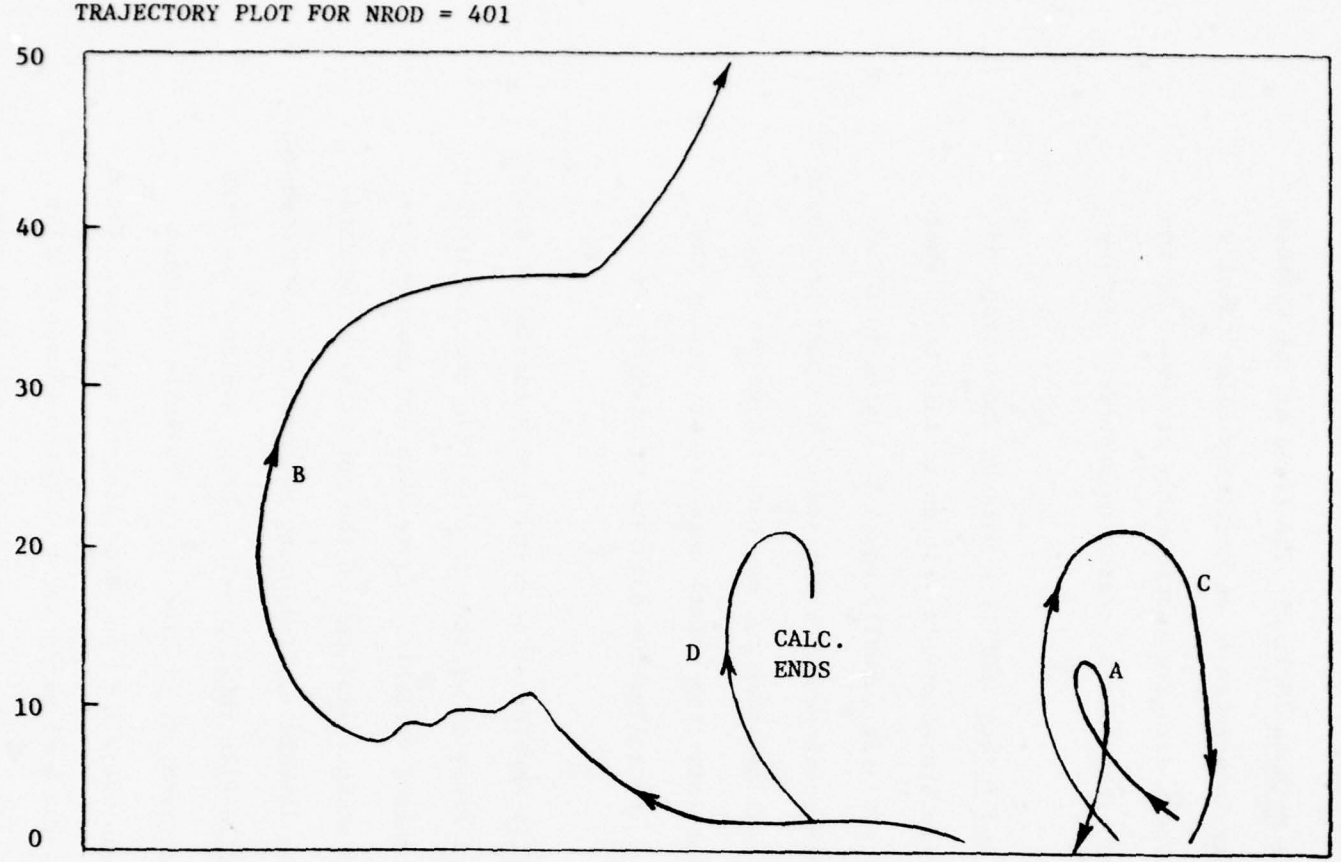

FIGURE 20

COMPUTER GENERATED TRAJECTORY PLOT. Computer prints successive symbols for rod position on successive time steps. Symbols may be joined manually using a listing of trajectory data which is printed simultaneously. Branches A, B, C, and D above represent successive emissions of rods which are assigned the same rod number.

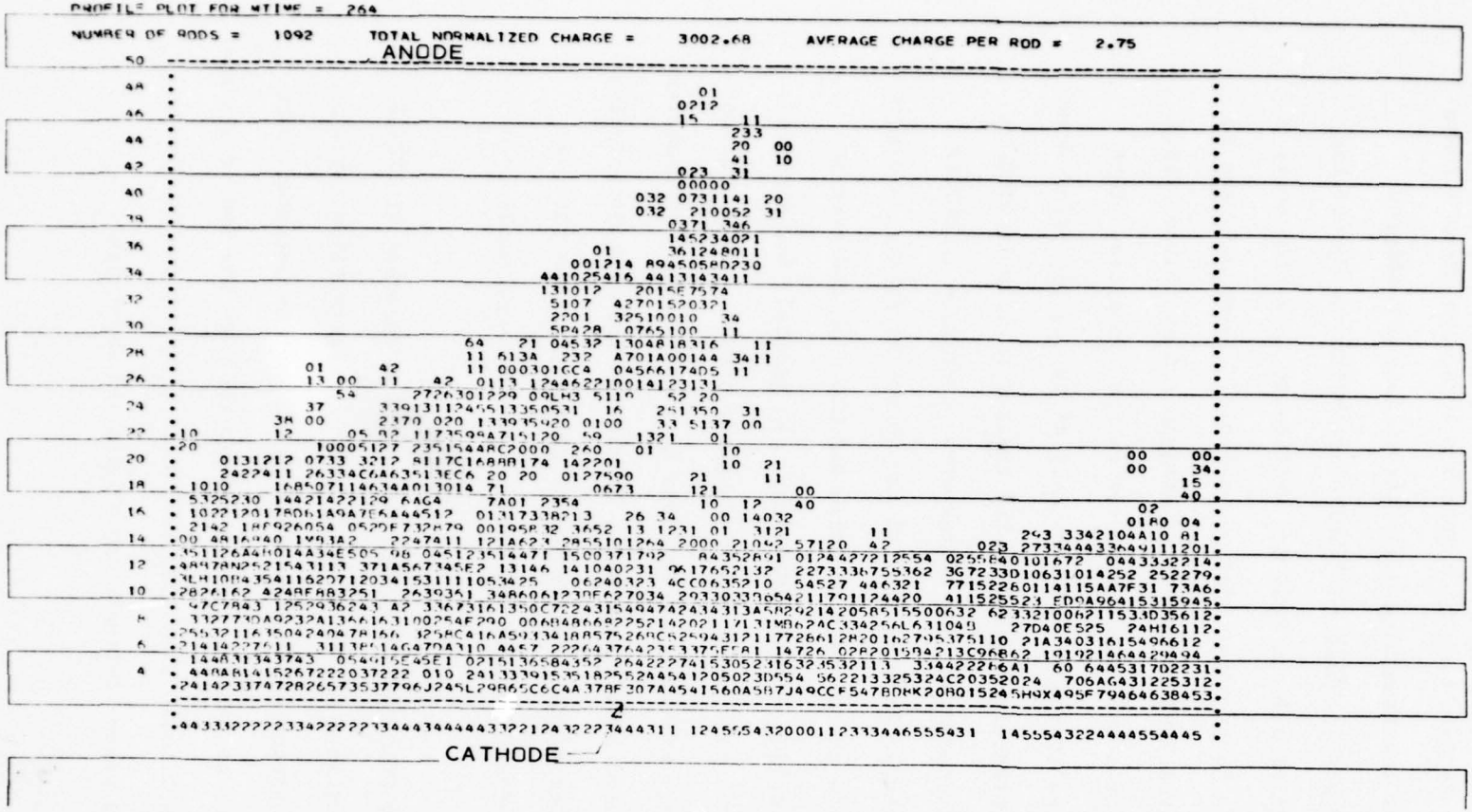

FIGURE 21--COMPUTER GENERATED PLOT OF THE SPACE CHARGE IN A ONE-WAVELENGTH INTERACTION BOX. The numbers are linearly proportional to the space charge in each cell of the potential array and are scaled so that 5 is equal to the Brillouin density. Numbers 10, 11, 12 etc. are represented by A, B, C etc. Numbers below the cathode surface represent the charge emitted from each cell of the emitted charge array on the preceding time step.

interaction. We have made it a practice to always prepare these plots, even if the remaining auxiliary outputs are skipped.

Rod Profile File (MTFILE)--The positions, velocities, charge and age of all the rods are written to this file every p steps--where p is an input control variable. These data may be processed by the post processor to produce rod population plots which appear much the same as the charge profile plots. Each rod contributes to a symbol in one cell of the 48 x96 print array. The symbol represents the sum of the charges or rods located in each cell. By contrast, the charge array continued in MQFILE reports the charge in each cell of the potential array. A single rod contributes charge to four cells and thus the rod profiles and charge profiles are not identical. In general, for a given number of rods, the charge profiles appear denser. Both rod profile and charge profiles are included in this report. In practice, they can be used interchangeably. We changed from the preparation of rod profiles to the preparation of charge profiles part way through the effort because the latter are more economical to process.

The post processor may also use the contents of MTFILE to produce listings of the data if desired. These files may also be used as "checkpoints" where the program may be restarted. The post processor contains a feature which will pick the rod population data for a particular time step from this file and rewrite it as an NFILE (see below) suitable for reading as input data.

Final Rod Profile File (NFILE)--This file is written by the exit procedure as described in the last section. It contains the positions, velocities, charge and age of all the rods in a form suitable for use as input data by a subsequent calculation. The post processor is capable of providing a listing of these data if so desired.

2.11 Energy Balance Procedure

On time steps for which the rod action outputs are written, the program does a computation of the kinetic and potential energy of all the rods in the interaction space. The results are reported following the rod action output and together with the circuit power, cumulative dissipations and the cumulative anode current may be used to do a conservation of energy balance as a check on the model's accuracy. The energies of the rods in the interaction space are reported as equivalent powers so that they may be used with the other reported powers in the energy balance calculation. For the kinetic energy this conversion is done by calculating the power which would be dissipated if the rods were collected with their current velocities. For the potential energies, we convert to an equivalent kinetic energy using $eV = 1/2\ mv^2$ and then convert to an equivalent dissipated power as we do for the kinetic energy.

The computation of the kinetic energy amounts simply to a summation of $1/2\ mv^2$ over all the rods and the conversion to a dissipated power as done for an intercepted rod using the normalization factor described for dissipation in Section 2.7. The computation of the potential energy is less straight forward since the system contains time varying fields. Thus, if a rod has reached a potential V_1, it does not mean that it has been accelerated along a trajectory for which:

$$\int eE \cdot ds = V_1 \qquad \text{(not required)}$$

The possible departure from this condition is greatest when a hub is forming and charge is building up in the interaction box. Since the potential at points in the interaction box varies with time during the charge build up, the above equality is not required.

We have been able to derive what appears to be a correct expression for the potential energy in the following way.

First, we subtract the RF circuit wave component of the potential at each rod location and find the remaining portion due to the d.c. voltage and the space charge. The potential energy of the rod distribution represents the energy required to set up the distribution including the effects of the space charge depression of potential. Now we consider each rod to be made up of many smaller rods of lesser charge. Assume we move one of these smaller charges for each rod to the final rod position. Since space charge is small for these charges we will be moving them essentially through the space charge-free d.c. field. We continue this process for the small increments of charge for each rod, and as we do so the potential in the space changes as space charge accumulates. The final increment of charge for each rod is moved through the potential in the presence of space charge. This process is shown schematically in Figure 22. Looking at the process in this manner we find that the correct potential to use in the energy balance procedure is a value midway between the space charge-free potential and the potential in the presence of space charge. (This arrangement is analogous to the one which leads to the factor of 1/2 in the energy storage in a dielectric = $1/2\,\varepsilon E^2$).

When the energies are calculated in this manner we find that energy balance is obtained to within a few percent. This is true even for initial passes in which the space charge hub builds up very rapidly.

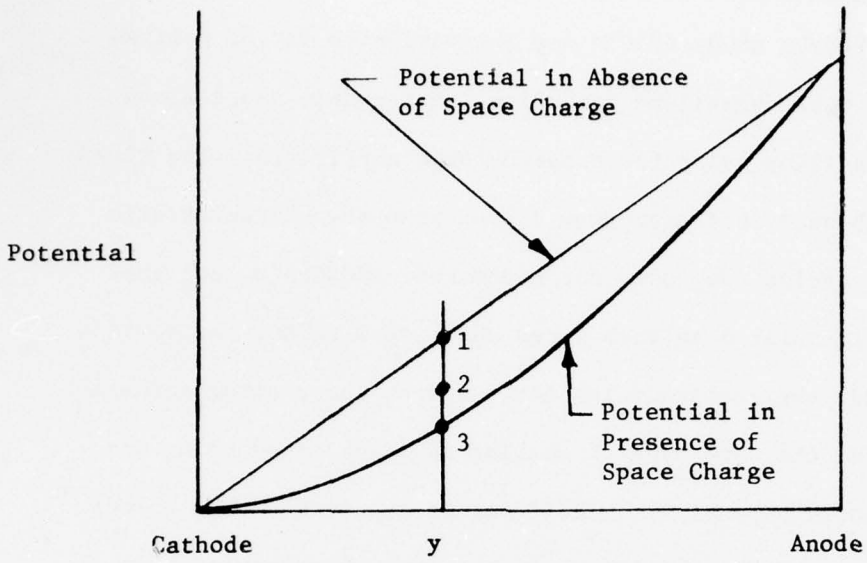

FIGURE 22

COMPUTATION OF THE POTENTIAL ENERGY OF A CHARGE DISTRIBUTION. Assume distribution to be made up of N rods. Subdivide each rod into G smaller rods at the same location. Set up the charge distribution by first moving one of the G increments of charge for each of the N rods from the cathode to its proper position in space. Repeat for each of G increments of charge. The first N increments will be moved through the space charge-free potential (An increment moved to y will be moved through a potential V_1.) The last N increments will be moved through the potential in the presence of space charge (V_3 at y). The average potential will lie midway between the space charge free and the full space charge potentials (V_2 at y).

2.12 Normalizations and Scaling Rules

From a study of the way the variables in the program combine to make normalized variables, we can draw conclusions about the scaling rules for crossed-field amplifiers. The normalizations used in the program differ from the characteristic scaling variables long used for magnetrons and CFA's, but they are directly related to them as we shall show below. As would be expected, the scaling rules derived from the program normalizations give the same type of scaling as is obtained using the characteristic variables. Additional information on the effect of impedance and circuit height is, however, forthcoming from a consideration of the normalized variables.

The interaction space design is described to the computer model by a set of unnormalized variables as follows:

a	cathode-anode spacing
h	circuit width parallel to magnetic field
d	circuit pitch
θ/π	phase shift per section divided by pi
K	interaction impedance
f	frequency
V_K	cathode-to-anode voltage
B	magnetic flux density

The nature of the equations for the CFA is such that the above eight variables may be reduced to six normalized variables which are adequate to both run the computation and recover the unnormalized values of the output variables. In shrinking the original eight-variable input set to the six normalized variables some information is lost--the original eight variable input set cannot be recovered from the six normalized variables. The normalized variables are defined as follows:

1. Normalized Voltage $(V_n) = \dfrac{2\eta V_K}{(a\omega_c)^2}$ 2.12-1

   where $\omega_c = \eta B$ is the cyclotron frequency and the other variables are defined above. The normalized voltage is equal to the ratio of the actual voltage to the Hull cut-off voltage.

2. Ratio $(r) = 2a/\lambda$ 2.12-2

   where λ is the slow wave wavelength given by $\lambda = d(\frac{\pi}{\theta})$

3. Ratio $2a/h$ 2.12-3

4. Ratio $(f_n) = \omega/\omega_c$

   where ω = radian frequency $2\pi f$ 2.12-4

5. Product $a\omega_c$ 2.12-5

6. Normalized Interaction Impedance

$$Z_n = 4\varepsilon_o (a\omega_c) K/(2a/h) \qquad 2.12\text{-}6$$

where ε_o is the primittivity of free space

A further reduction in parameters occurs when the equations for the CFA are written in normalized form. These equations involve only four of the above variables. The reduced set of normalized variables consists of:

$$V_n,\ r,\ f_n,\ Z_n$$

Without the additional two normalized variables (2a/h and $a\omega_c$) it is, however, not possible to recover the unnormalized values of the output variables. It is seen that cases involving the same set of the above four variables are closely related. If, in addition, the normalized input conditions and the normalized secondary emission curves were the same, the calculations would be identical even though the unnormalized variables may be quite different. The normalization procedure thus provides a means of scaling designs--i.e., interpreting the results of a calculation in terms of a whole series of designs having different values of $a\omega_c$ and 2a/h.

To completely specify a design, we require the input power and the length, in addition to the interaction space description discussed above. Within the program the input power is normalized in terms of the RF votlage which is, in turn, normalized by dividing the Hull cut-off voltage (as was the case for the d.c. voltage).

The RF voltage is given by:

$$V_{rf} = \sqrt{2P_i K} \qquad 2.12\text{-}7$$

where

V_{rf} is the input voltage

P_i is the input power

K is the interaction impedance

The normalized voltage is given by:

$$\text{Normalized rf Voltage } (V_{rfn}) = \frac{2\eta V_{rf}}{(a\omega_c)^2} \qquad 2.12\text{-}8$$

The program calculates a normalized secondary emission table in which the actual values of bombardment energy are replaced by normalized values defined by:

$$\text{Normalized energy} = \left(\frac{96\pi}{g}\right)^2 \left(\frac{2\eta}{(a\omega_c)^2}\right) V_b \qquad 2.12\text{-}9$$

where

V_b is the actual bombardment energy

g is the number of time steps per cyclotron period

and the remainder of the variables are as defined above.

The length data supplied to the program is normalized in terms of wavelengths. A review of the procedures in the preceding sections for recovery of the unnormalized variables from the normalized variables shows no new combinations of variables. Thus, designs which

maintain the above normalized variables (i.e., the four which describe the interaction space, the normalized RF input, the normalized secondary emission table and the length in wavelengths) the same will look identical to the computer model. A single design may thus be scaled by changing the real variables so that the normalized variables remain the same. The commonest form of scaling is frequency scaling. A review of the above normalized variables shows that they are unchanged if all dimensions are scaled proportional to wavelength and the magnetic field is scaled inversely proportional to frequency.

Another type of scaling is power scaling. We will maintain the normalized variables constant if we scale the pitch, length and anode-cathode spacing by a factor k; all voltages (including the incident voltage for a given secondary emission ratio) by k^2; and all powers by k^4. The height k is not scaled in this case. This type of scaling is never exactly accomplished since scaling of the secondary emission ratio is not possible. However, as long as the secondary emission is adequate, this scaling rule is a useful design tool.

A third type of scaling maintains the hZ product constant. Multiplying h by a factor k and Z by a factor 1/k results in the input and output powers being multiplied by k. The bombardment energy for a given secondary emission ratio is unaffected in this case. Constancy of the hZ product is characteristic of a number of slow wave circuits so this type of scaling may sometimes be encountered.

The program could have alternately used variables normalized in terms of the synchronous rather than the Hull cut-off voltage. A common set of variables used to describe the interaction is:

V_h/V_0 - ratio of Hartree voltage to synchronous voltage

V/V_H - ratio of operating voltage to Hartree voltage

βa = anode-cathode transit angle = $\frac{2\pi a}{\lambda}$
where a is the anode-cathode spacing and
λ is the slow wave wavelength

The Hartree voltage is given by:

$$V_H/V_0 = \frac{2\eta Ba}{v_o} - 1 \qquad 2.12\text{-}10$$

wehre

B is the magnetic flux denstiy

v_o is the circuit synchronous velocity

The Hartree voltage is the anode-cathode voltage for which the surface of a Brillouin hub becomes synchronous with the circuit wave. It is the approximate voltage at which interaction begins in a CFA or magnetron.

The above three parameters can be related directly to three of the four normalized parameters which describe the interaction space.

Thus:

$$V_H/V_O = \frac{2\pi r}{(\omega_c/\omega)} - 1 \qquad 2.12\text{-}11$$

$$V/V_H = V_n \frac{V_n(V_H/V_O + 1)}{4(V_H/V_O)} \qquad 2.12\text{-}12$$

$$\beta a = \pi r \qquad 2.12\text{-}13$$

The above three parameters do not constitute a complete description--a normalized impedance involving a hZ product is needed to complete the description.

2.13 Versions of the Computer Program

The computer program has gone through seven versions during the course of the effort. The first three versions were described in the second interim report. The first version (DECFA) appeared to work satisfactorily when thermionic emission was employed, but not with secondary emission. This version used a fixed charge per rod. Version DECFA1 introduced a variable charge per rod in an attempt to better model the secondary emission process. This attempt was not successful in eliminating the instabilities in the secondary emission process. Version DECFA2 for the first time introduced the emission of a fixed number of rods per time step and the space and time smoothing of secondary emission. This version gave us good correlation of the computer model and CFA performance. These calculations were described in the second interim report. Version DECFA3 further refined the emission procedures including the uniform spacing of emitted rods, the charge correction described in Section 2.3 and the addition of a small initial velocity. Version DECFA4 had the taper procedure added and the output formats revised. Version DECFA5 contained a further revision to the taper procedures. This version was used for most of the studies described in this report. Versions DECFA6 and DECFA7 included corrections to a number of small problems in the outputs of earlier versions. The energy balance procedure was also put in its final form. These programs were made compatible with the Univac 1110 computer. DECFA7 was made with rod arrays dimensioned for 4,000

rods rather than 6000 as in DECFA6 to save storage space. For all the calculations discussed in this report, the 4000 array size has proved adequate.

3.0 CORRELATION OF COMPUTER MODEL AND INSTRUMENTED CFA

In the second semi-annual report we presented the results of computations on a CFA with a uniform interaction space geometry using program version DECFA2. These computations showed a good correlation between computed and measured results at mid band. These results will not be reproduced here. Subsequently, we have conducted further correlation studies on both the SFD-261 CFA both at mid band and at band edges. These studies employed program version DECFA5 and were conducted using the IBM 360/65 computer at the Naval Ocean Systems Center, San Diego. Table V lists the input conditions for the uniform interaction space cases studied using DECFA5. The magnetic flux density is not that actually used in the CFA. It has been corrected downward from the value of 2530 gauss used in the CFA to provide a correction for the fact that the CFA is in circular format while the computer model is linear. The correction is made in accordance with the following formula:

$$B_c = B_\ell R \qquad 3.0\text{-}1$$

$$R = \frac{2r_a}{2r_a - r} \qquad 3.0\text{-}2$$

where:

B_c is the magnetic flux density for a given voltage and current in circular format

B_ℓ is the flux density for the same voltage and current in linear format

r_a is the anode radius

a is the anode-cathode spacing.

TABLE V

COMPUTER SIMULATION INPUTS USED
IN THE UNIFORM INTERACTION SPACE CORRELATION STUDIES

1.	Circuit pitch			$72D_1$	
2.	Width parallel to field			400 D_1	
3.	Frequency	f_o+0.1	f_o+0.3	f_o+0.5	
4.	Phase shift/pi	0.4333	0.5055	0.5805	
5.	Interaction impedance	68.0	45.0	30.0	ohms
6.	Attenuation dB/inch	0.35	0.35	0.35	dB/inch
7.	Cathode voltage	1.325	1.365 1.300 1.200	1.28 1.20	V_1
8.	Length of circuit up to drift space			4.52 D_2	
9.	Length of drift space			0.66 D_2	
10.	Anode-cathode spacing			92 D_1	
11.	Magnetic flux density			2400 gauss	
12.	RF input power			0.08 Po	

13. Primary emission

    1st pass--0.45 amps over first 0.14 D_2
    remaining length none

    remaining passes--none

14. Secondary emission table

Incident Energy (volts)	Secondary Yield
0.0	0.0
100.0	2.2
200.0	4.2
300.0	5.0
500.0	5.0
2500.0	1.0

(continued)

TABLE V--COMPUTER SIMULATION INPUTS USED
IN THE UNIFORM INTERACTION SPACE CORRELATION STUDIES

Program Parameters

Time steps per cyclotron period	10
Rods emitted per time step	48
Charge adjustment parameter	1.06
Space smoothing of emission parameter	0.5
Time smoothing of emission parameter	0.125

Remaining parameters--default values

Note: Normalizing parameters P_o, f_o, D_1, D_2 and V_1 are employed to permit this report to be published in unclassified form. Values of these parameters are classified confidential. They may be obtained from NOSC upon presentation of proper clearance and need-to-know.

This correction arises directly from the expression for the characteristic magnetic flux density B_o of a circular format interaction space and the limiting value of this flux density as the radius of curvature goes to infinity.

Table VI summarizes the results of the calculations on the CFA with uniform interaction geometry. For each case studied we calculated six passes of the interaction box (one RF wavelength) through the CFA. Figures 23 through 24 show V-I curves for the instrumented CFA with the computed points added. These points are the average of the second through sixth passes -- the first pass during the build up of charge being atypical. The computed and measured powers for equal currents are provided adjacent to the points in the V-I plane. Again, the computed points are the average value for the second through sixth pass. The computed points in the V-I plane lie within 3 per cent of the measured V-I curve along the voltage axis. The departure along the current axis is greater (e.g. 20 per cent) because of the flatness of the V-I curves. In practice, however, one tends to increase the voltage to a CFA until the desired current is obtained and then measure the voltage. If the voltage so measured came within 3 per cent of the design value, we would be quite satisfied with the result. The 3 per cent value is within the accuracy of the combined measurements of magnetic flux density and phase shift per section which enter into the calculated points in the V-I plane.

TABLE VI

DESCRIPTION OF TABLE HEADINGS

P-OUT is the output power.

P-DISS ANODE is the power dissipated by electron interception on the anode.

P-DISS ATT is the power dissipated in the circuit attenuation.

P-DISS CATHODE is the power dissipated by electron bombardment of the cathode.

P-DC (1) is the D.C. power input determined from the voltage times the current plus the RF input power.

P-DC (2) is the D.C. power determined from the sum of the output power, the three dissipated powers, and the RF input power.

All power values are normalized to Po.

P-DC RATIO is the ratio of P-DC(2) to P-DC(1). Ideally this should be 1.0.

EFF is the efficiency determined from.....

$$\%E = \frac{\text{P-OUT} - \text{P-IN}}{\text{P-DC}} \times 100\%$$

and using average of P-DC(1) and P-DC(2) above.

PHASE is the phase of the RF output wave relative to what it would be for the cold circuit alone.

NT is the maximum number of rods which has ever been ued in the computation on both present and prior passes.

TABLE VI

COMPUTED PERFORMANCE OF UNIFORM GEOMETRY CFA

CONDITION	PASS	GAIN	P-OUT	P-DISS ANODE	P-DISS CATHODE	P-DISS ATT	CURRENT AMPS	PHASE	P-DC (1)	P-DC (2)	P-DC RATIO	EFF	NI
Fo + 0.1	1	13.5	1.65	0.98	0.41	0.37	23.3	65.5	---	---	---	---	2105
$V_K = 1.325\ V_1$	2-6 Avg.	13.1	1.64	0.84	0.15	0.39	22.1	102.6	3.01	3.10	1.03	54	2214
Fo + 0.3	1	9.4	0.64	0.35	0.23	0.12	10.5	41.6	---	---	---	---	2352
$V_K = 1.200\ V_1$	2-6 Avg.	6.9	0.40	0.14	0.04	0.08	5.2	41.0	0.70	0.79	1.12	54	4452
Fo + 0.3	1	12.8	1.42	0.71	0.34	0.32	19.2	-10.8	---	---	---	---	1911
$V_K = 1.300\ V_1$	2-6 Avg.	12.4	1.40	0.57	0.10	0.34	17.7	2.9	2.38	2.49	1.05	57	2662
Fo + 0.3	1	14.1	1.95	1.05	0.43	0.35	25.3	-55.9	---	---	---	---	1767
$V_K = 1.365\ V_1$	2-6 Avg.	15.3	2.70	1.39	0.20	0.58	35.4	1.12	4.81	4.96	1.03	55	2406
Fo + 0.5	1	9.9	0.72	0.34	0.21	0.19	10.13	-40.8	---	---	---	---	2595
$V_K = 1.200\ V_1$	2-6 Avg.	8.9	0.62	0.23	0.05	0.16	8.23	-36.8	1.07	1.12	1.05	57	3999

The powers actually computed lie about 7.5% higher than the computed values shown in Figures 23-25 and Table VI. The computations used a value of attenuation taken from the data on one of the best of the standard tubes. The value for the instrumented tube is somewhat higher (0.5 instead of 0.35 dB/inch). We can correct approximately for this increased attenuation by increasing the power lost in circuit attenuation by the ratio of 0.5 to 0.35 and by subtracting the increased dissipation from the circuit power. This correction is included in Figures 23 through 25 and Table VI. When this correction is made, the calculated power is generally within a few percent of the measured power.

Figure 24 for the CFA at band center shows a deviation of the measured and calculated results at high currents. The calculated curve continues with a flat slope to high currents, whereas the measured curve develops an upward curvature. This upward curvature is characteristic of the CFA when the cathode emission is not adequate to provide the current called for by the interaction. It is believed that the failure of the computer model to show the upward curvature is an indication that too high a secondary emission ratio was being provided to the computer model. Data on beryllium cathodes recently obtained by the Naval Research Laboratories indicates the values we used were too high. To see if a lower secondary emission yield would improve the correlation at high currents, we arbitrarily reduced the secondary emission by a factor of two. (This was done before the NRL data was available.) The

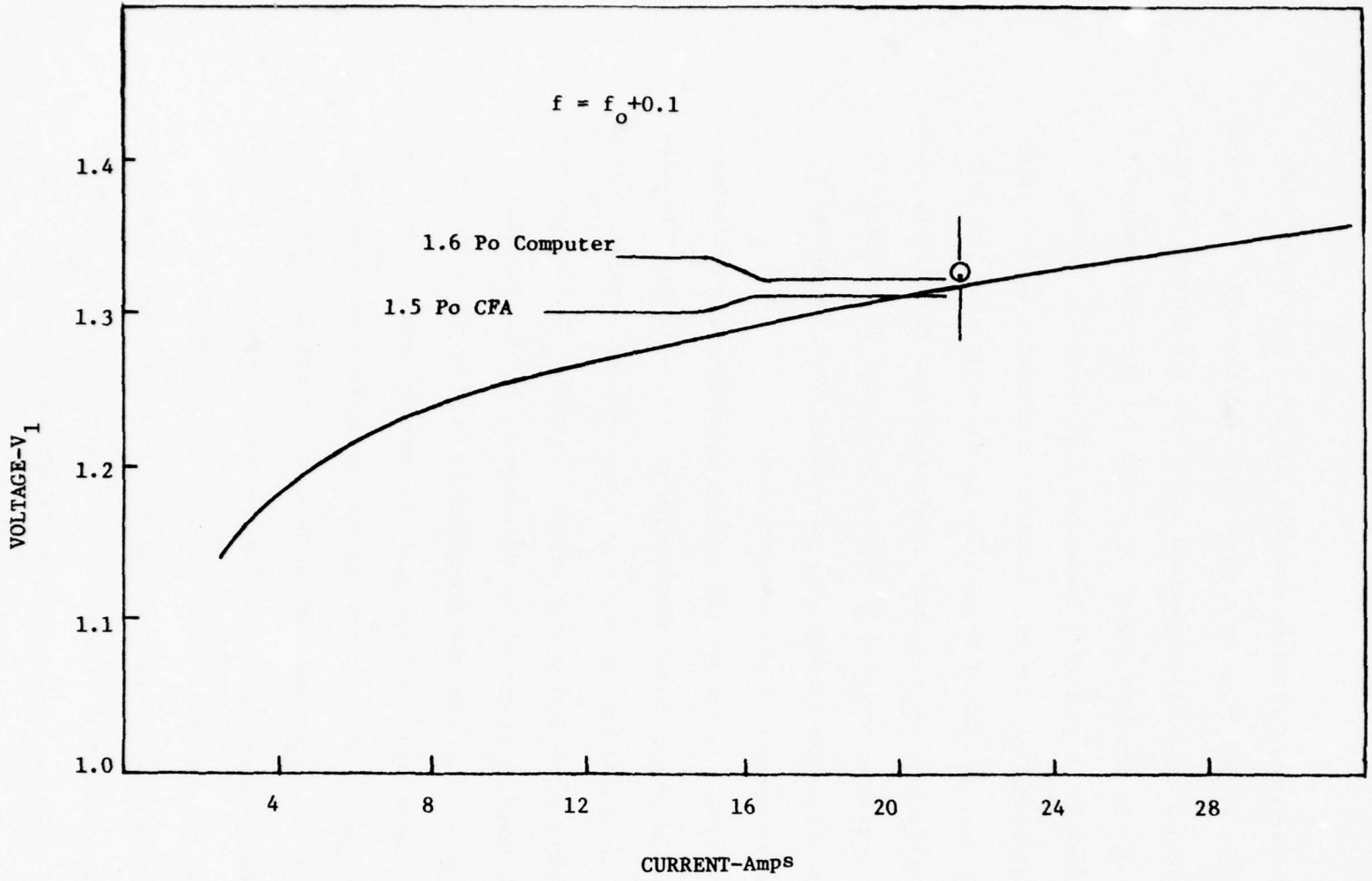

FIGURE 23--COMPARISON OF INSTRUMENTED CFA RESULTS (SOLID CURVE) WITH COMPUTER MODELING RESULTS (O) AT THE LOW FREQUENCY END OF THE BAND FOR THE CENTERED, ROUND CATHODE, INSTRUMENTED CFA.

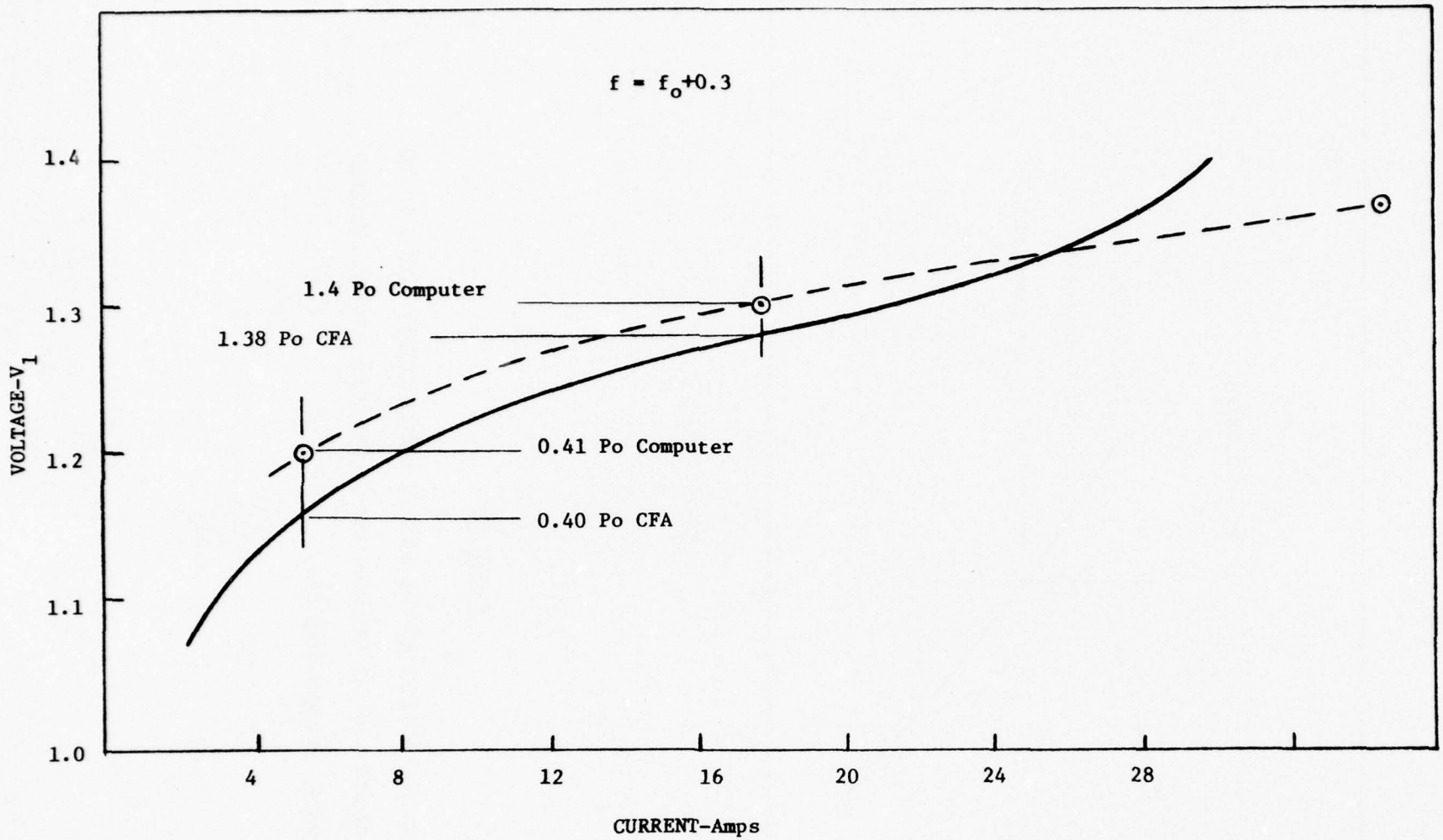

FIGURE 24--COMPARISON OF INSTRUMENTED CFA RESULTS (SOLID CURVE) WITH COMPUTER MODELING RESULTS (O) AT MIDBAND FOR CENTERED, ROUND CATHODE, INSTRUMENTED CFA.

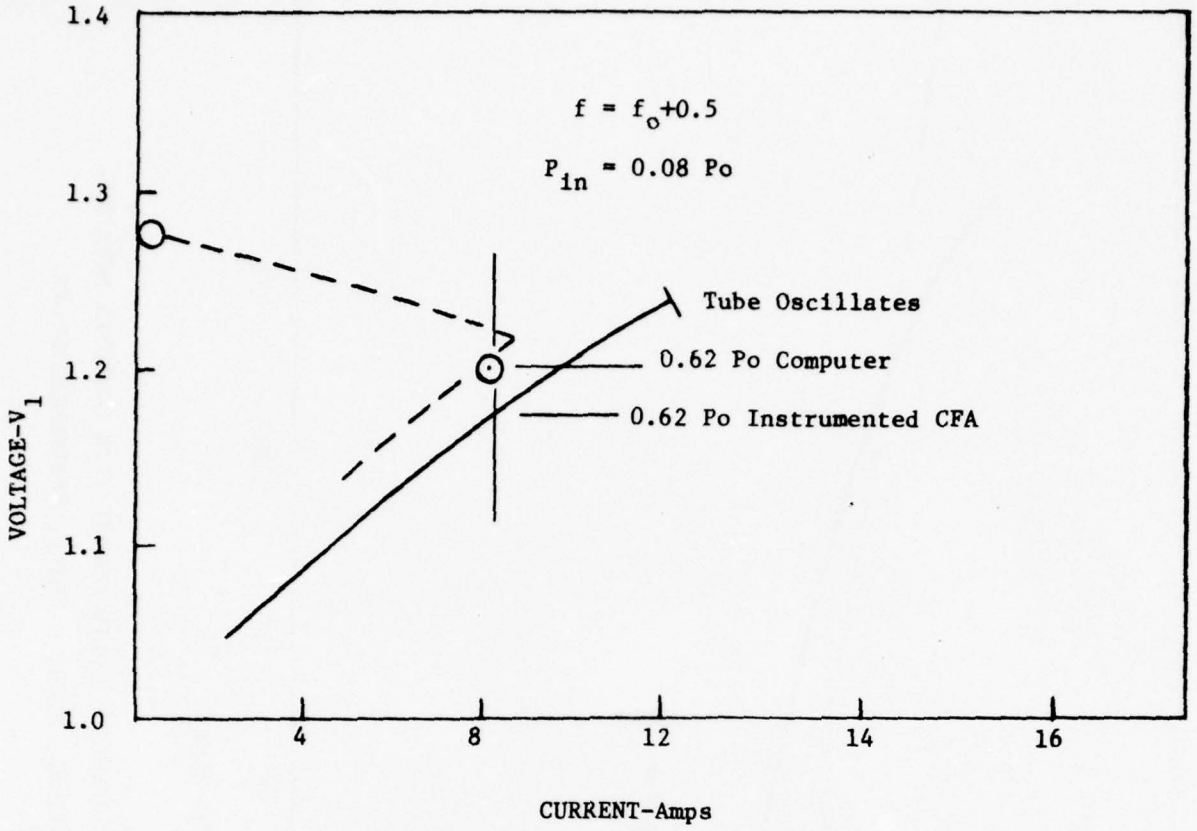

FIGURE 25

COMPARISON OF INSTRUMENTED CFA RESULTS (SOLID CURVE) WITH COMPUTER MODELING RESULTS (O) AT THE HIGH END OF THE BAND FOR THE CENTERED, ROUND CATHODE, INSTRUMENTED CFA.

resulting simulation using a fixed number of rods emitted per time step (48) drifted toward a small number of charge rods in the simulation with a large charge per rod. This yielded an altogether unacceptable degree of granularity. The results showed a slight increase rather than a decrease in current, but they were not creditable because of the granularity problem. Another series of calculations was made with the secondary emission ratio doubled from the value in Table V. These calculations produced almost the identical result to the first set of calculations. Apparently the calculated high current point in Figure 24 is in a space charge limited region in which an improvement in secondary emission does not affect the current drawn. The measured point for the CFA is apparently in an emission-limited region which occurs for a lower secondary emission ratio. With program version DECFA5 which emitted a fixed number of charge rods per step to represent the secondary emission, we were not able to carry the calculation into the emission-limited region because of the granularity problem described above. An improvement intended to avoid this limitation was incorporated in program version DECFA7 which is capable of emitting a variable number of rods per step with the number emitted depending on the number of rods currently active in the simulation. Preliminary tests suggest that this modification will avoid the granularity problem and permit us to conduct simulations in the emission-limited region. However, a complete set of calculations had not been completed by the end of this effort.

Figure 25 shows that at the high end of the band the CFA will not operate to as high a current as at midband. An attempt to operate the CFA at a peak current above about 12 amperes results in it oscillating at low frequencies. The computer model predicts correctly that the CFA will not operate at high currents--though it is, of course, unable to predict that it will oscillate at low frequency. The computed power output decreased from pass to pass until a low value was reached. (See Figure 36.) The computer model shows that the reason for the low gain lies in the space charge distribution recirculated from output to input. Figure 26 shows a computer prepared rod profile plot for this recirculated charge (see Figure 21 for explanation of a rod or charge profile plot). The charge becomes very diffuse with a continuous distribution of charge from hub to anode. This charge distribution produces a d.c. electric field distribution as shown in Figure 27 (combination of d.c. and space charge fields). Figure 27 is plotted from potential array data written by the computer model. The figure shows that much of the charge has an average E/B drift velocity significantly above the circuit wave velocity. At the high end of the band, the RF fields are not strong enough to capture this charge and form spokes.

From Figure 27 we would expect that tapering the interaction space so that the charge velocity is descreased at the input to synchronize it with the RF wave would improve the interaction. Thus the model would suggest, for example, an interaction space taper which yields a larger anode-cathode spacing at the input than

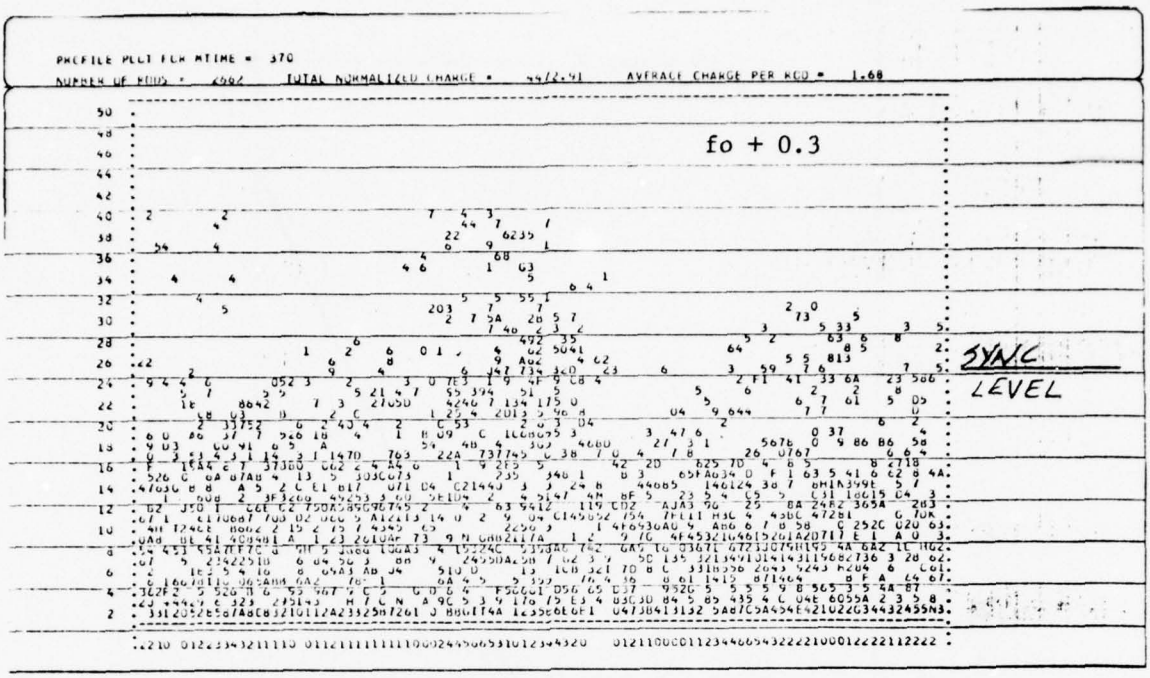

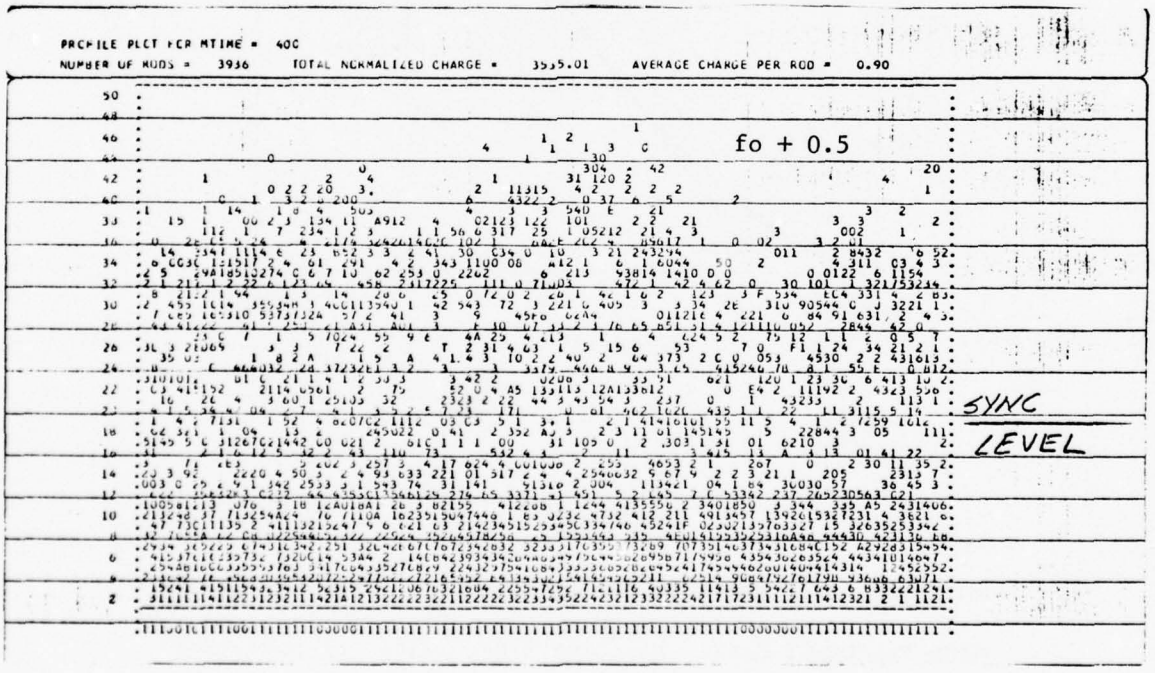

FIGURE 26

ROD PROFILE PLOTS GENERATED BY THE COMPUTER FOR THE START OF A MID BAND AND START OF A HIGH FREQUENCY COMPUTATION.

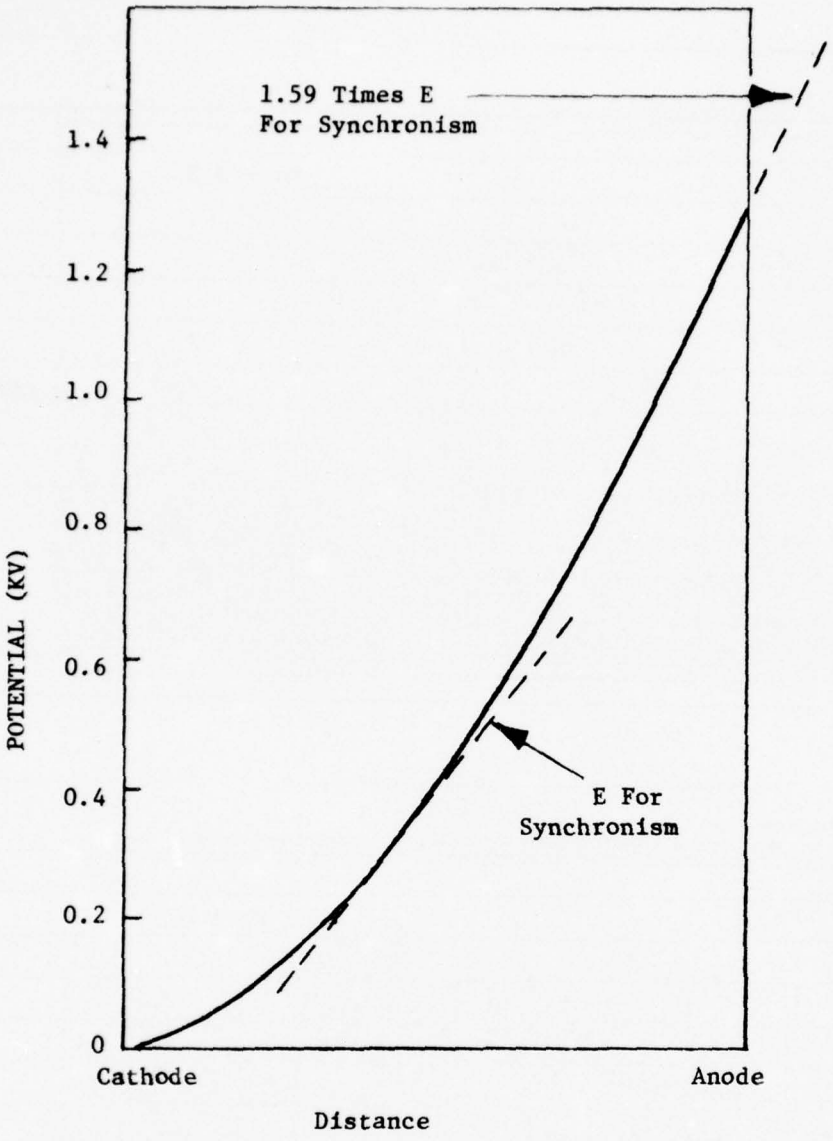

FIGURE 27

POTENTIAL AS A FUNCTION OF DISTANCE FROM CATHODE TO ANODE--HIGH FREQUENCY CASE. Electric field (slope of potential) is well above synchronous value for rods close to anode. At mid band ratio of E to synchronous value is reduced to 1.25 and amount of charge above synchronous level is reduced.

at the output. This is what has evolved in the actual SFD-261 by other means. Incorporation of the taper permits the CFA to operate to higher currents. The computer model appears to be telling us that the taper works because it provides more favorable conditions for interaction with the recirculating space charge than are obtained with the uniform geometry.

Figure 28 shows the computer power and the cumulative computed dissipations as a function of distance for a midband case at $1.3V_1$ anode-cathode voltage. These results are for a third case which has an output power about midway in the range produced by the second through sixth passes. The computed power as a function of distance is shown compared with the measured power as a function of distance from the instrumented CFA in Figure 29. The two curves compare very well. Figure 30 shows the envelope of all the curves of the second through sixth passes. The curves for different passes vary largely because of the state of the recirculating space charge from pass to pass. More will be said about these pass-to-pass variations in Section 4.

The anode dissipation density can be derived by taking the slope of the cumulative anode dissipation curves from Figure 28. The computer model prints the dissipation at every time step from which a dissipation density is directly obtainable. However, because there are a limited number of rods intercepted on the anode in each time step, this dissipation per step varies erratically from step to step. The technique of plotting the cumulative dissipation (also printed by the computer on each time step) and then graphically

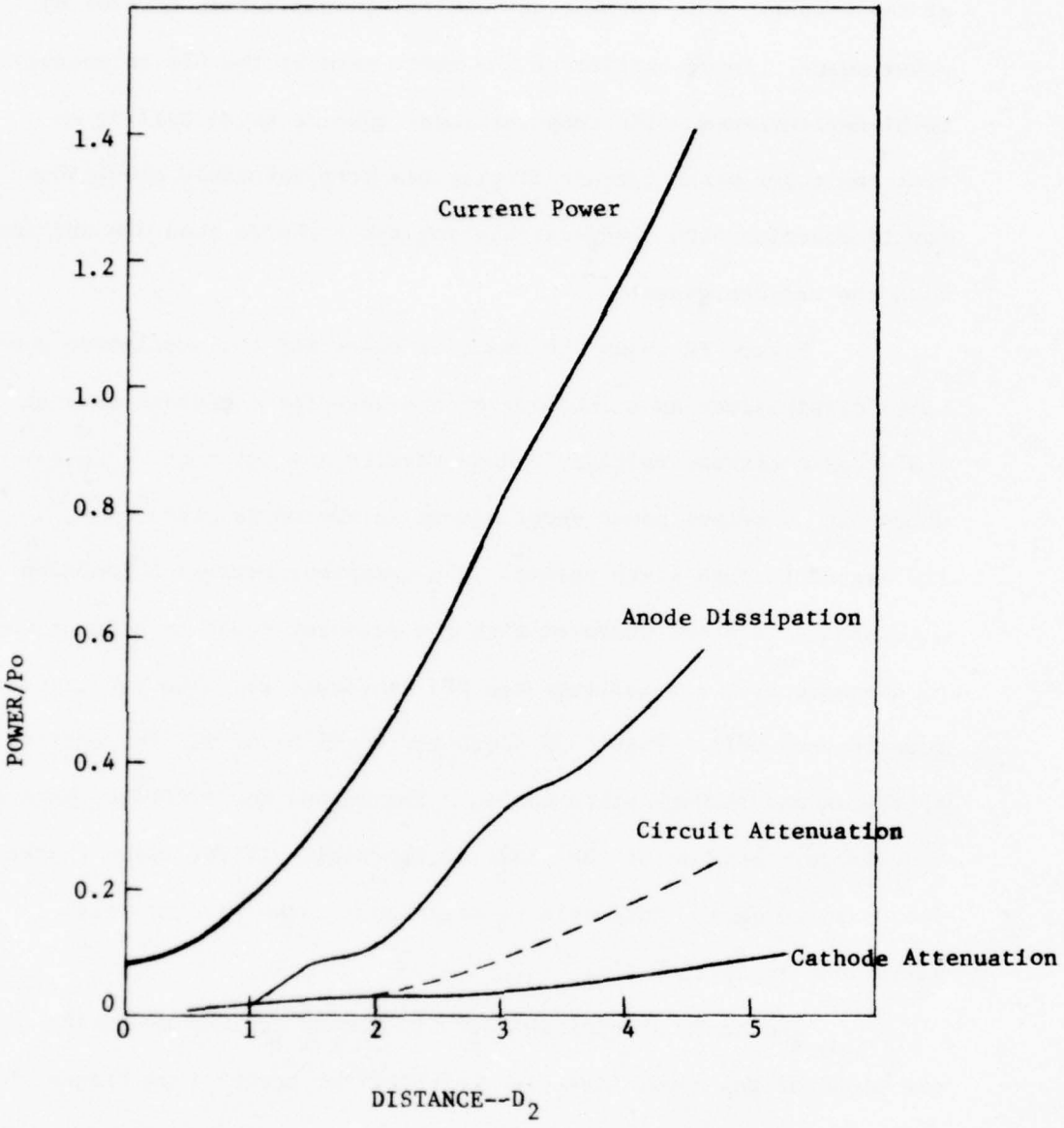

FIGURE 28

CIRCUIT POWER, CUMULATIVE DISSIPATION BY ELECTRON INTERCEPTION ON ANODE, CUMULATIVE DISSIPATION BY ELECTRON INTERCEPTION ON CATHODE AND CUMULATIVE DISSIPATION IN CIRCUIT ATTENUATION AS A FUNCTION OF LENGTH FROM COMPUTER SIMULATION. $f = f_o + 0.3$, $V_K = 1.3\ V_1$, $V_K/V_H = 1.13$, $I_K = 17.7$ amps, Pass 3.

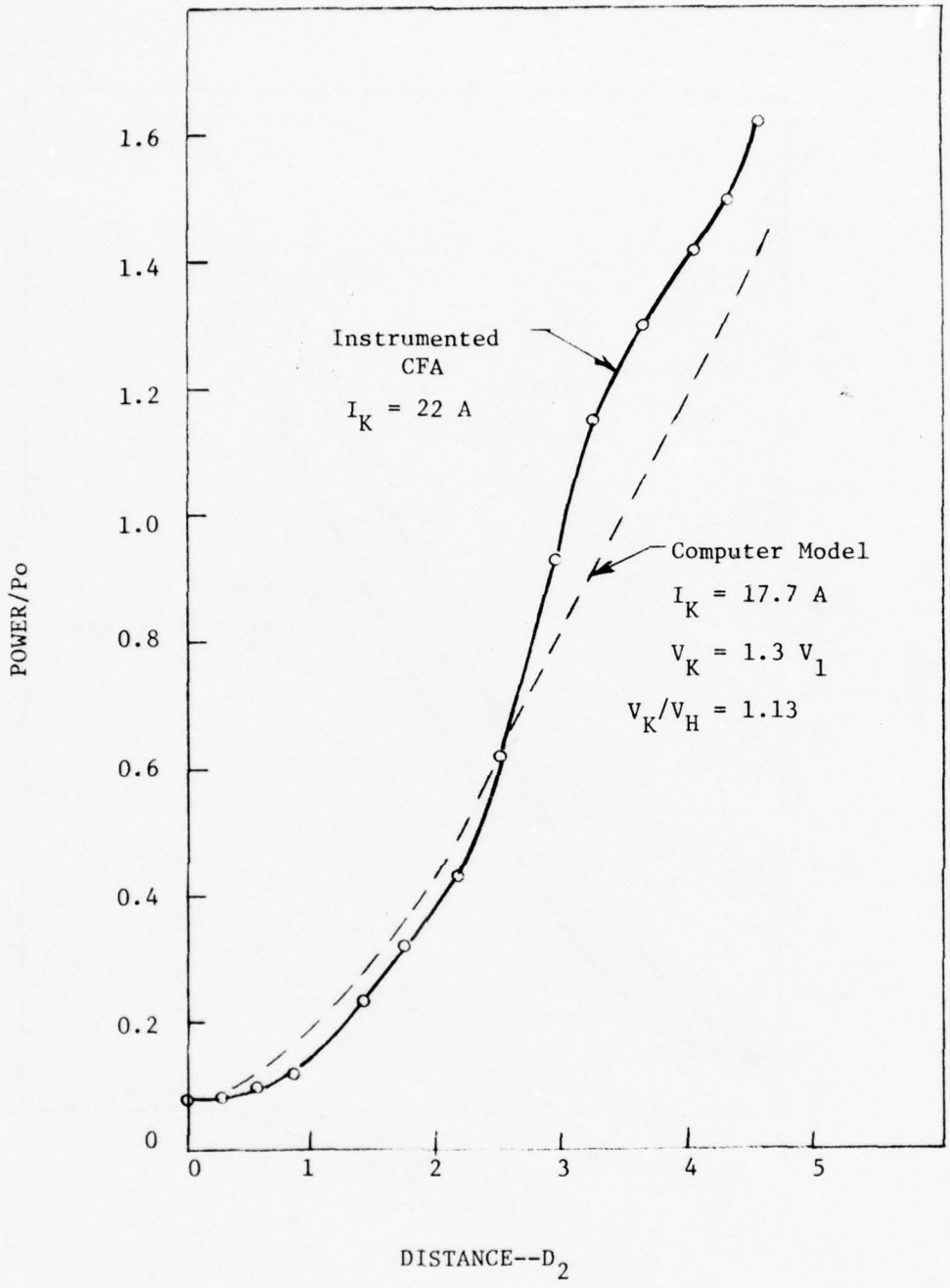

FIGURE 29

COMPARISON OF POWER AS A FUNCTION OF DISTANCE FOR INSTRUMENTED CFA AND COMPUTER MODEL. Conditions are slightly different for the two cases. Current was higher for CFA. Computer model results contain correction for excess attenuation of instrumented tube. $f = f_o + 0.3$.

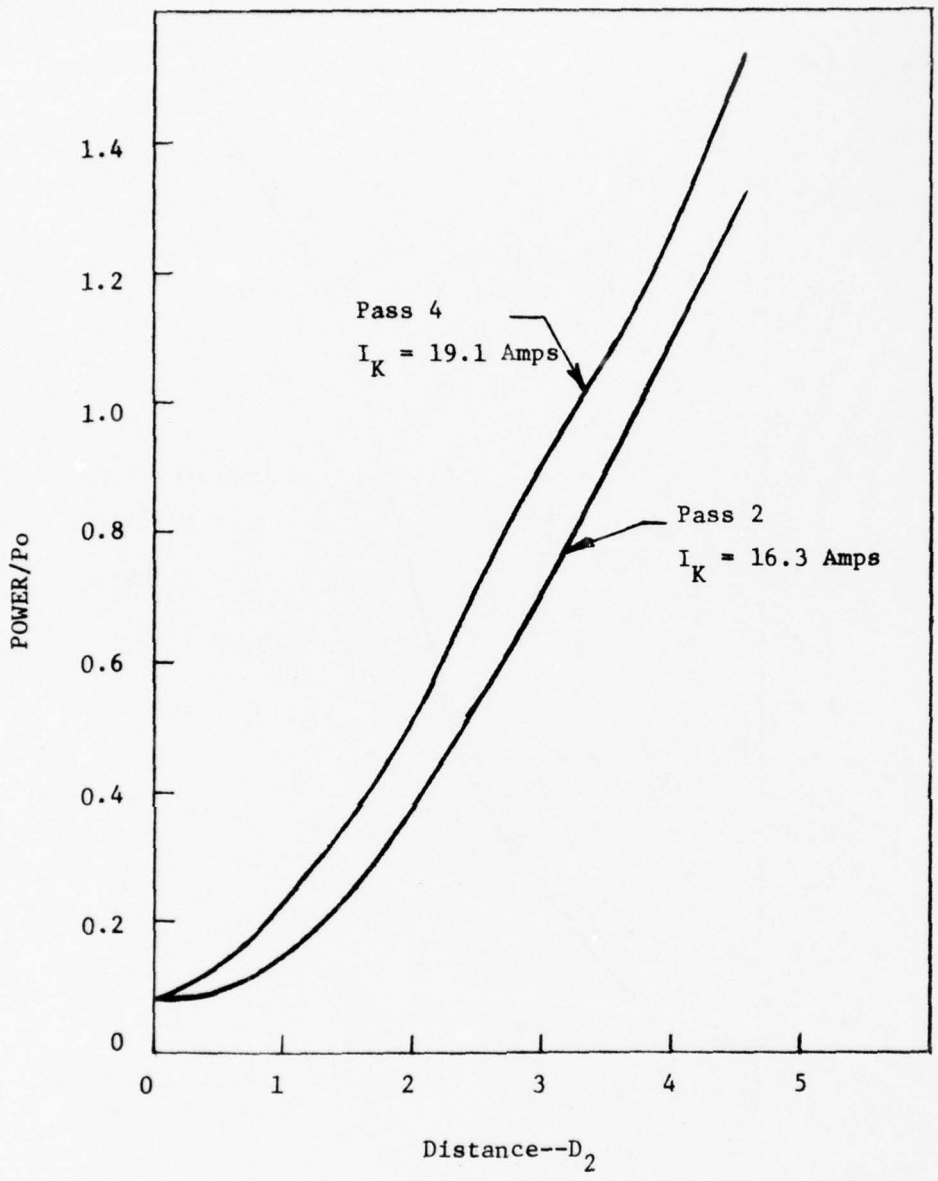

FIGURE 30

POWER AS A FUNCTION OF DISTANCE FOR THE PASSES THAT YIELDED MAXIMUM AND MINIMUM OUTPUT POWER. $f = f_o + 0.3$, $V_K = 1.3\ V_1$, $V_K/V_H = 1.3$.

differentiating it to obtain the density has been used as a smoothing technique. The resulting curves of cumulative dissipation are shown in Figure 31. From the slope of this curve which yields dissipation density and the thermal impedance of the vane which has been determinted separately by a different type of computer modeling, we then obtain the temperature as a function of distance. This result is shown together with the measured temperature from the instrumented CFA in Figure 32. This procedure should give a slightly higher temperature for the computed result since all of the power dissipated in the circuit attenuation is assumed to flow through the thermocouple instrumentation. Actually some of this power is dissipated near the vane base and does not flow through the thermocouple in the stub near the helix. This error is believed to be relatively small.

The calculated temperature distribution in Figure 32 lies slightly lower rather than higher than the measured distribution. The shape of the two distributions is, however, very similar. The correlation of the two distributions is reasonable in view of all the experimental erros which may be involved in the comparison. Certainly, the results are good enough to warrent use of the computer model in approximate dissipation density calculations.

Comparisons of computed and measured power growth and dissipation density at the lower and upper ends of the operating band are presented in Figures 33 through 35. These curves show that results of the computer model and the instrumented CFA correlate well for the low frequency case. We do not have an instrumented CFA

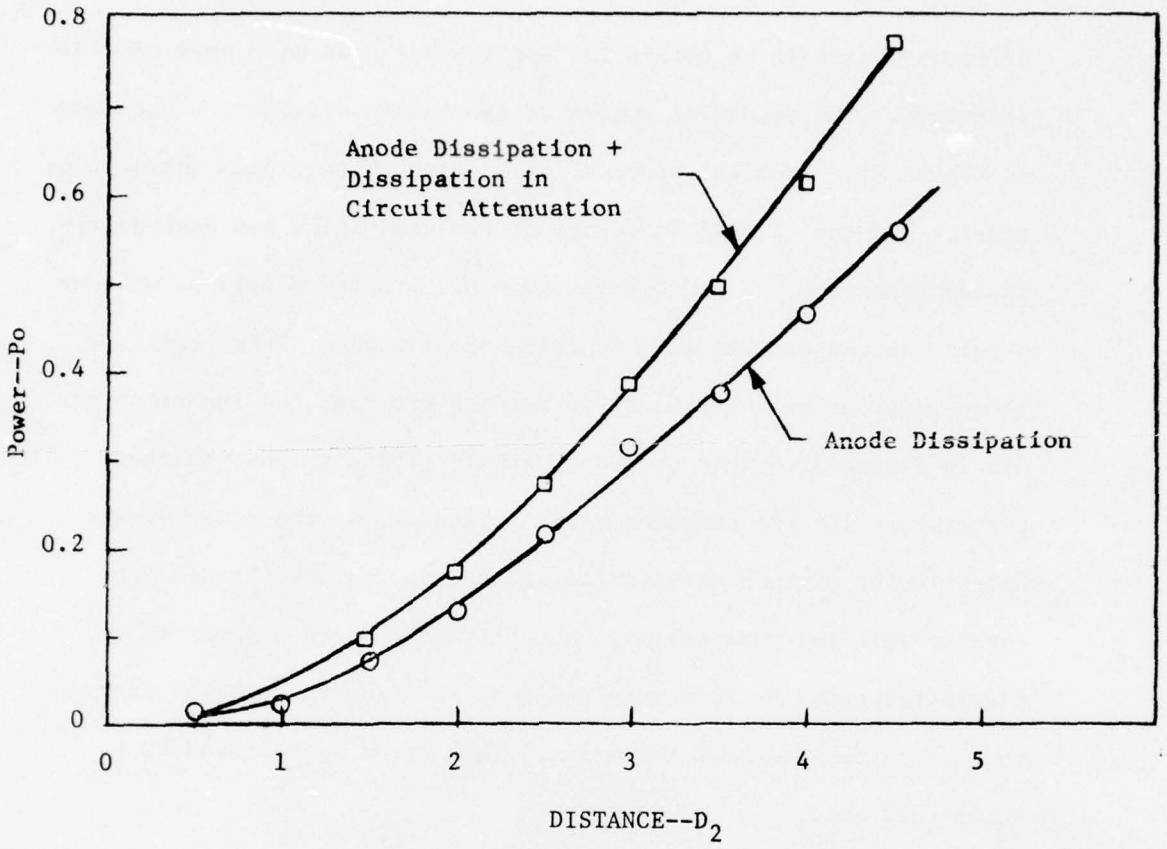

FIGURE 31

COMPUTED ANODE DISSIPATION BY ELECTRON INTERCEPTION AND ANODE DISSIPATION PLUS HALF THE DISSIPATION IN CIRCUIT ATTENUATION. These results are obtained by averaging the dissipation over passes 2-6. $f = f_o + 0.3$, $V_K = 1.3V_1$, $V_K/V_H = 1.3$.

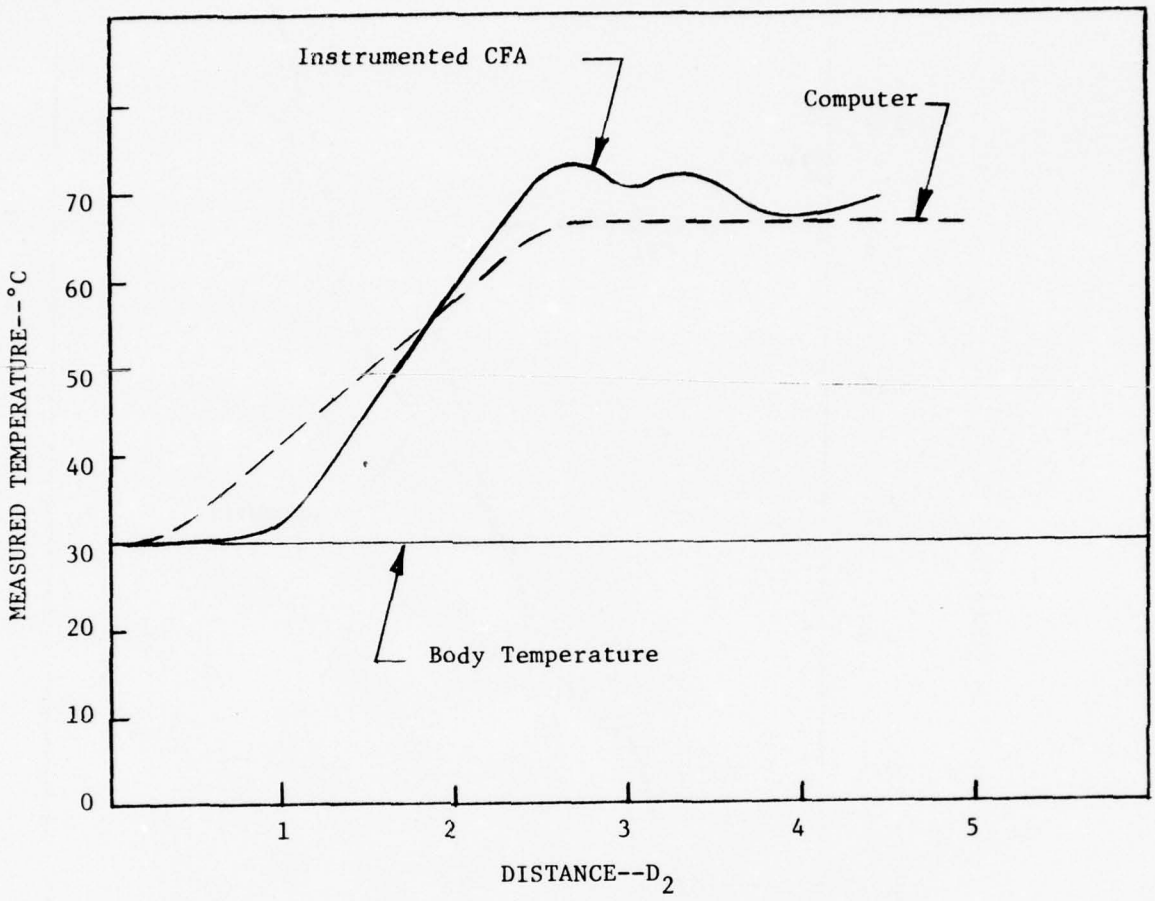

FIGURE 32

COMPUTED TEMPERATURE FROM DISSIPATION DATA OF FIGURE 31 AND ASSUMED ANODE THERMAL IMPEDANCE COMPARED WITH MEASURED TEMPERATURE OF INSTRUMENTED CFA.

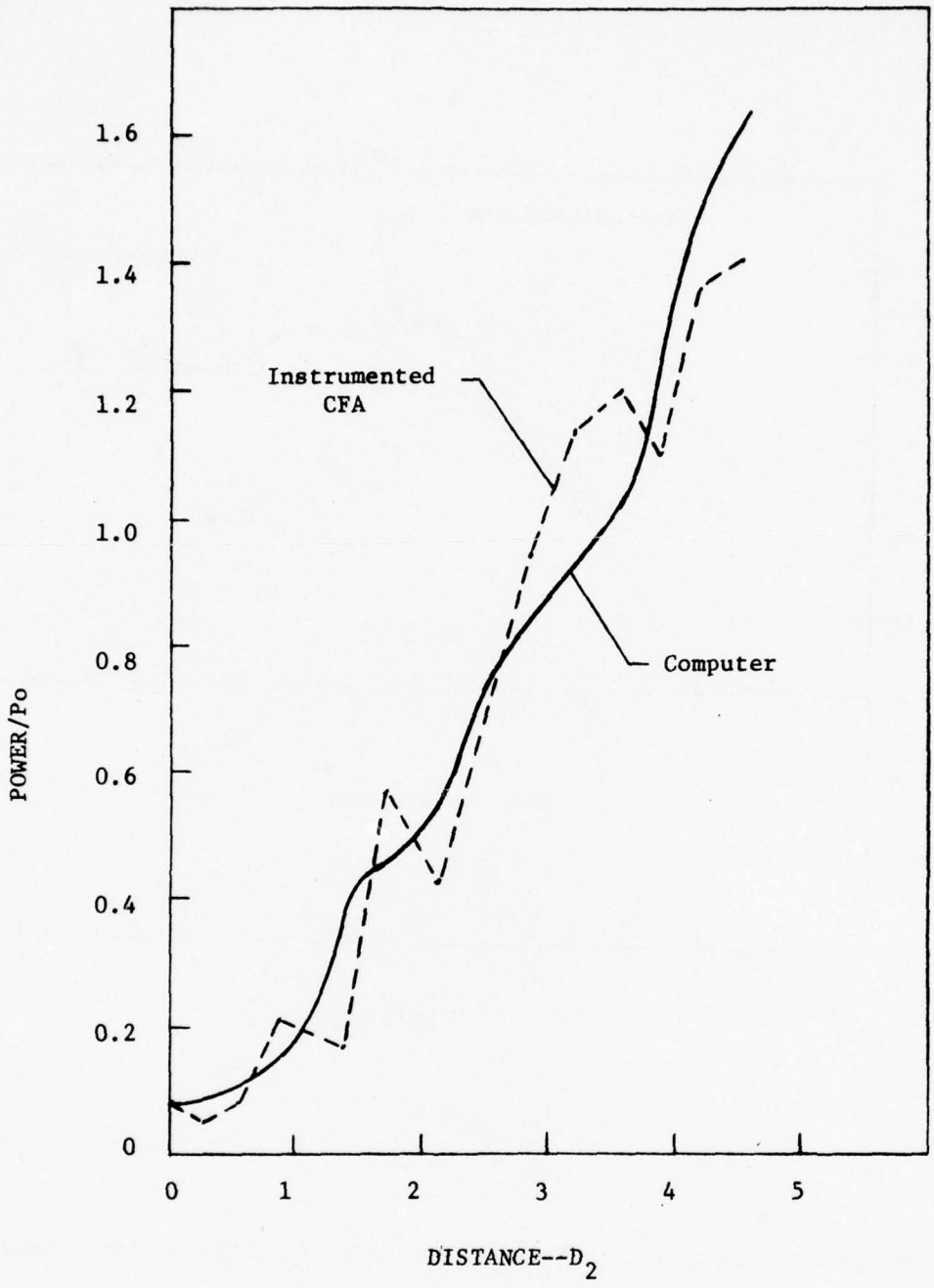

FIGURE 33

COMPARISON OF POWER AS A FUNCTION OF DISTANCE FROM COMPUTER MODEL AND FROM INSTRUMENTED CFA FOR UNIFORM GEOMETRY AT LOW END OF THE BAND. $f = f_o + 0.1$, $V_K = 1.325\ V_1$, $V_K/V_H = 1.07$.

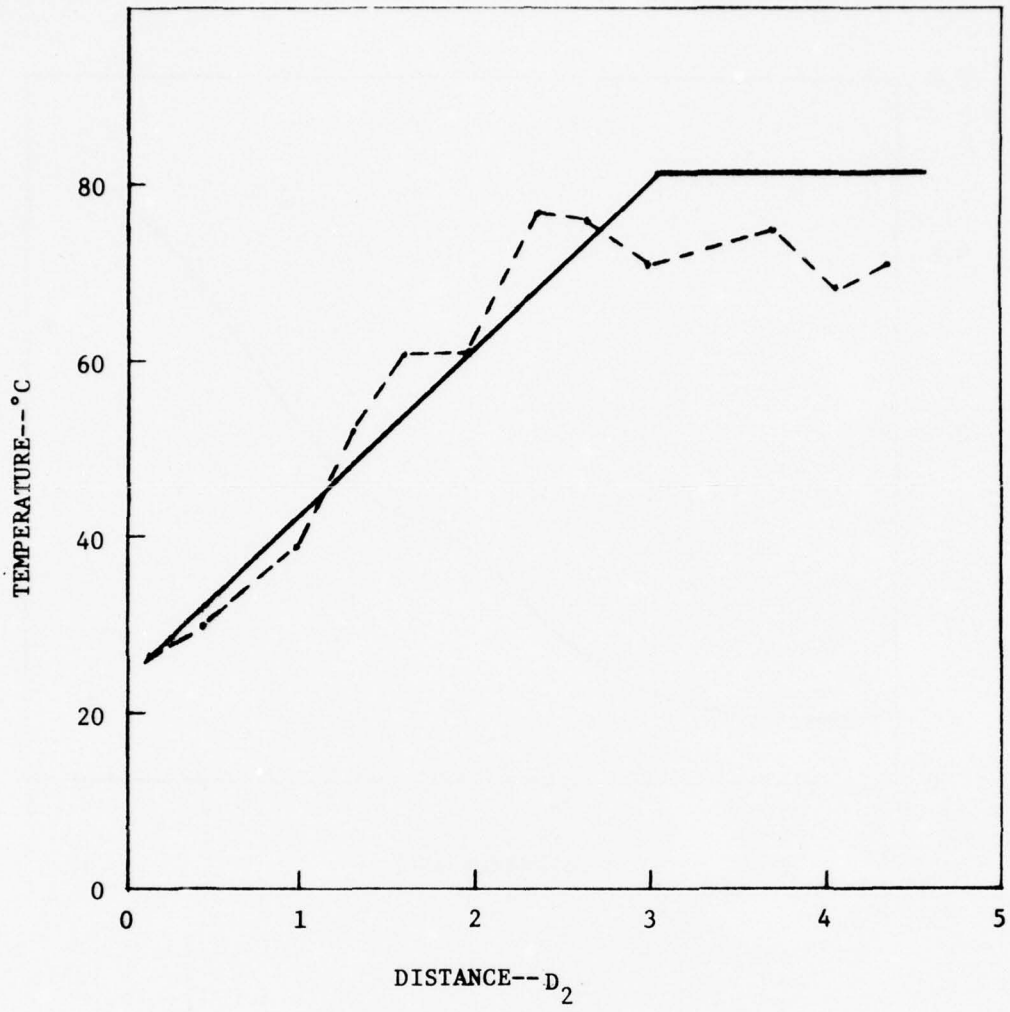

FIGURE 34

COMPARISON OF TEMPERATURE AS A FUNCTION OF DISTANCE FROM COMPUTER MODEL AND FROM INSTRUMENTED CFA FOR UNIFORM GEOMETRY AT LOW END OF BAND. $f = f_o+0.1$, $V_K = 1.325\ V_1$, $V_K/V_H = 1.07$.

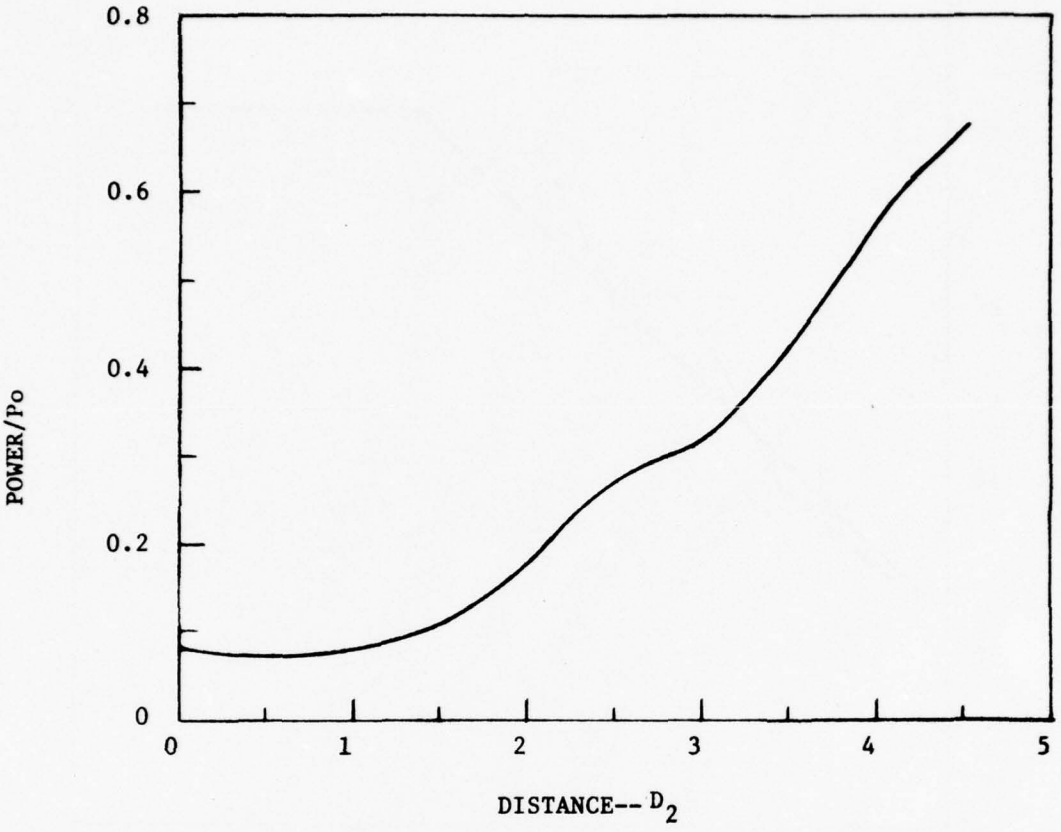

FIGURE 35

POWER AS A FUNCTION OF DISTANCE AT THE HIGH END OF THE BAND FROM THE COMPUTER MODEL. $f = f_o + 0.5$, $V_K = 1.2\ V_1$, $V/V_H = 1.12$

run for the conditions of the high frequency case. However, as discussed earlier in this section, the output power and the portion of the V-I curve over which the CFA will work are properly predicted by the computer model.

Figure 36 shows the peak power output variation from pass-to-pass for the cases we have been discussing. Included is a mid-band case with the RF input power decreased to $0.01P_o$ which we have not previously discussed. In this case, large pass-to-pass variations occur, and it does not appear that the calculation is going to settle down to a steady state. Under these conditions an actual CFA produces an extremely noisy output. The magnitude of the pass-to-pass variations also increases at $0.08P_o$ input when the voltage is raised. Again, this is a region where the CFA becomes noisy. There appears to be a rough correlation between regions of operation which yield high pass-to-pass variations and regions of operation where the CFA is noisy. This subject will be considered further in the next section.

Correlation studies have also been conducted using tapered interaction space geometries. Both tapered anode-cathode spacings and tapered pitch have been investigated. Table VI presents the input data for a tapered spacing calculation, and Table VIII summarizes the results for six-pass calculation. Figure 37 compares a typical calculated power growth curve with a measured curve obtained using an instrumented CFA having the same spacing

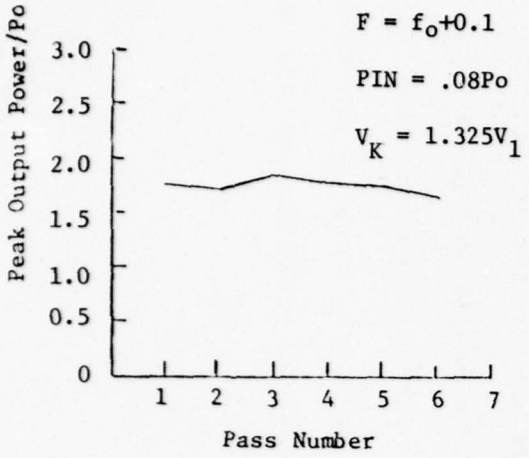

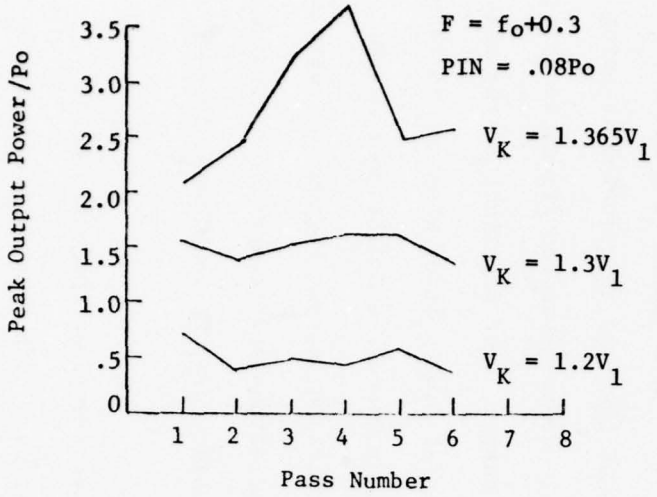

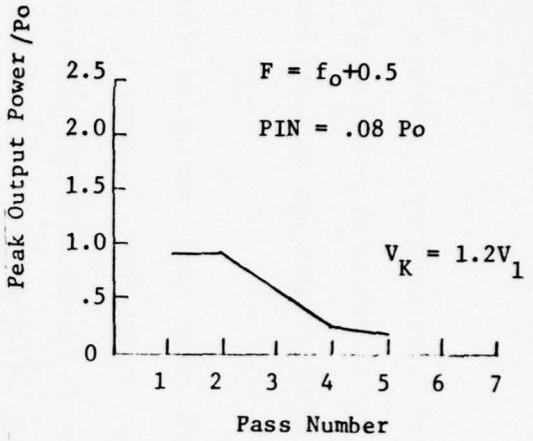

FIGURE 36--SUMMARY OF THE PASS-TO-PASS VARIATIONS FOR THE CENTERED, ROUND CATHODE INSTRUMENTED CFA.

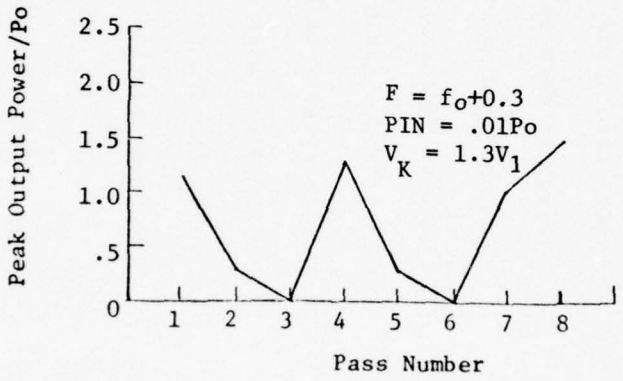

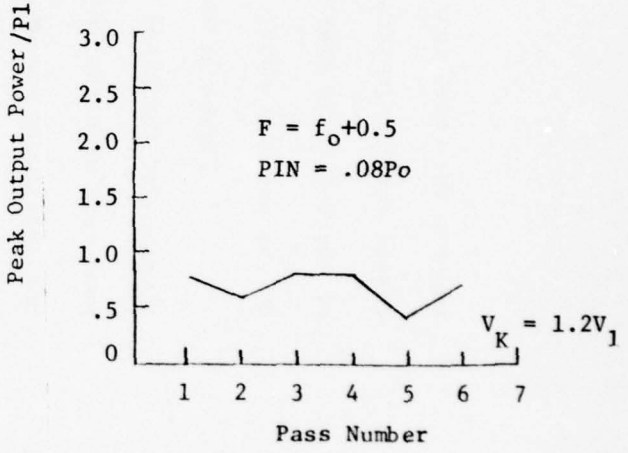

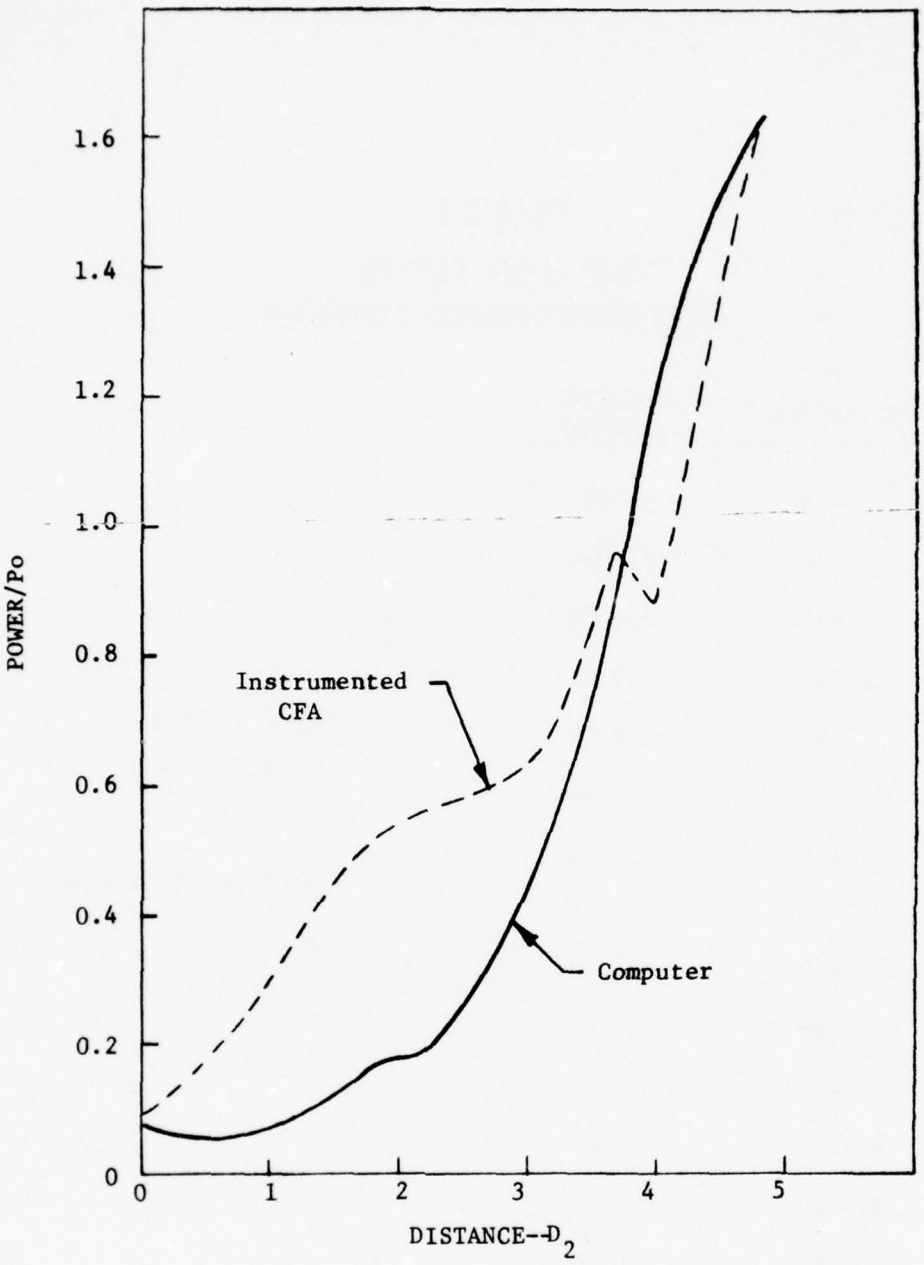

FIGURE 37

COMPARISON OF POWER AS A FUNCTION OF DISTANCE FROM COMPUTER MODEL AND INSTRUMENTED CFA FOR TAPERED ANODE-CATHODE SPACING. $f = f_o + 0.3$, $V_K = 1.3\ V_1$.

TABLE VII

TAPER TABLES USED FOR

ANODE-CATHODE SPACING SIMULATION

DISTANCE/D_2	RELATIVE SPACING
0.2878	1.0098
0.5756	1.0098
0.8633	1.0000
1.1511	0.9804
1.4389	0.9509
1.7266	0.9118
2.0144	0.8725
2.3022	0.8330
2.5900	0.8137
2.8788	0.7941
3.1656	0.7843
3.4533	0.7843
3.7411	0.7941
4.0289	0.8137
4.3167	0.8431
4.6044	0.9706
4.8922	0.9902
5.1800	1.000

Magnetic Flux Density = 2480 gauss

Remaining Inputs Per Table V

TABLE VIII

TAPERED ANODE-CATHODE SPACING CFA

CORRELATION OF COMPUTER MODEL AND INSTRUMENTED CFA

COMPUTER MODEL			
Frequency	f_o+0.1	f_o+0.3	f_o+0.5
V_K	1.325 V_1	1.300 V_1	1.270 V_1
Power	1.78 Po	1.54 Po	1.49 Po
Current	27 a	23 a	24 a

INSTRUMENTED CFA			
Frequency	f_o+0.1	f_o+0.3	f_o+0.5
V_K	1.33 V_1	1.304 V_1	1.270 V_1
Power	1.20 Po	1.51 Po	1.57 Po
Current	22 a	22 a	22 a

profile. Although the final output powers compare favorably in Figure 37, the overall correlation is poor with the power growing very much more rapidly in the instrumented CFA than it does in the computer model. This result illustrates the desirability of having an instrumented CFA with which to compare results. Had we compared only the final outputs, we would have been led to believe the correlation was satisfactory. Figure 37 shows the correlation to be far from satisfactory.

A similar problem arose when we attempted to compare computed and measured results for the tapered pitch CFA. This CFA had a pitch of $7.9D_1$ at the input which tapered linearly to $0.72D_1$ at the output. Figure 38 shows a comparison of a typical calculation with measured results obtained from an instrumented CFA with a pitch taper. Again, we see that the power growth in the CFA is much more rapid than predicted by the computer model.

The reason for the failure of the computer model to correctly predict the power growth for tapered geometries is as yet unknonw. The problem may be in the taper procedure or, alternately, it may lie in the data we are providing to the computer model. The lack of knowledge of the proper secondary emission ratio may be important in the tapered cases because the CFA may be operating into the emission-limited region near the output.

A brief study was conducted of the conditions of the recirculating space charge which would lead to a rapid power growth at the CFA input as is observed in the experimental tubes. A first

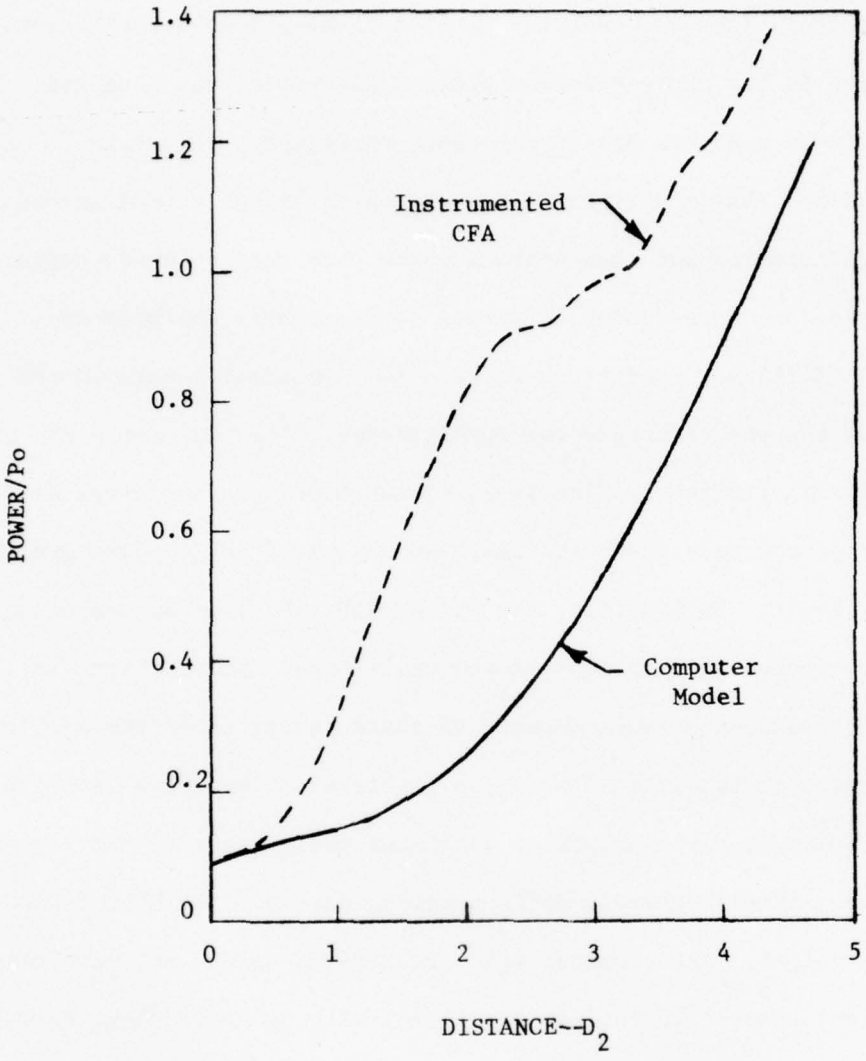

FIGURE 38

COMPARISON OF POWER AS A FUNCTION OF DISTANCE FROM COMPUTER MODEL AND FROM INSTRUMENTED CFA FOR TAPERED PITCH GEOMETRY AT BAND CENTER. $f = f_o + 0.3$, $V_K = 1.3\ V_1$

pass calculation was conducted until a broad-charge distribution, as shown in the charge profile plot of Figure 39, was obtained. This charge was then passed through a drift space to obtain a debunched charge distribution as shown in Figure 40. A second pass calculation was then started using this recirculated charge. This was done using three different anode-cathode voltages to provide different conditions of relative synchronism between the RF wave and the recirculating space charge. The computer power growth is shown in Figure 41. The results show that a broad-charge distribution of the kind shown in Figure 40 can yield rapid power growth at the input. By contrast, the charge distributions at the output of our tapered calculations showed well-formed spokes which, in turn, yielded only small amounts of space charge above the hub level at the end of the drift space--see Figure 42. The cases in which there is rapid power growth at the input thus appear to correspond to cases in which sharply defined spokes have not yet been formed at the output. The computer modeling studies appear to show that efficient power transfer can occur even without sharp spoke formation.

The results reported in this section show that the computer model correlates well with the instrumented CFA for a uniform interaction space geometry operated in a space-charge-limited region. The computed results correlate well with the measured results where the CFA operates well and they also correctly predict where the CFA will not operate at the high frequency end of the band. When the CFA enters an emission-limited region, the computer model did not

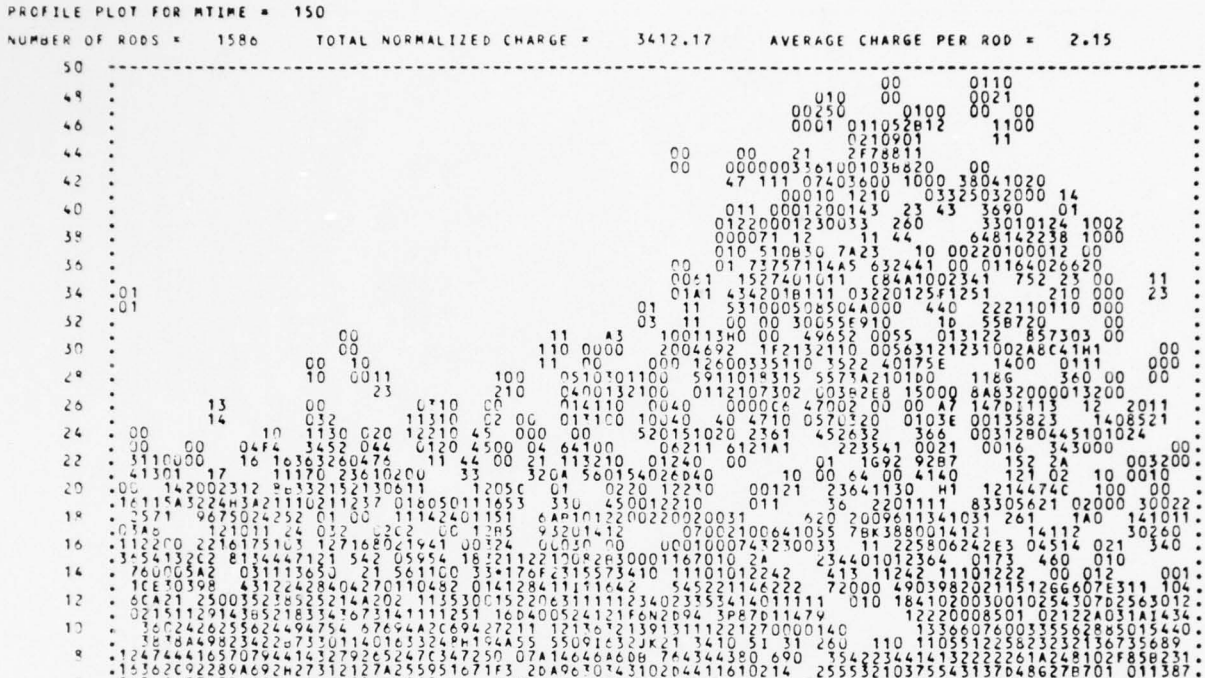

FIGURE 39

CHARGE PROFILE GENERATED FOR STUDY OF POWER GROWTH AT THE INPUT.

This profile was obtained by stopping a Pass 1 build up calculation after 150 time steps.

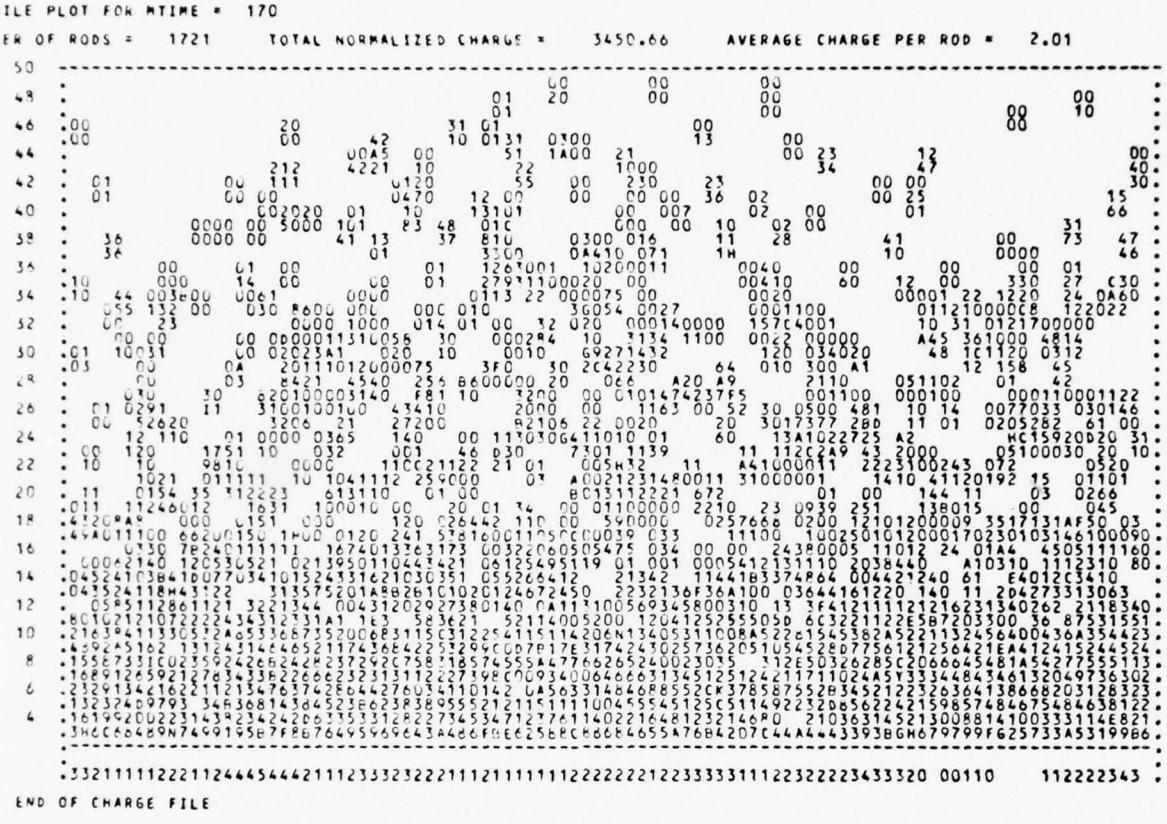

FIGURE 40

CHARGE PROFILE OF FIGURE 39 AFTER DEBUNCHING. Studies of debunching as shown in Figure 26 demonstrate that significant debunching occurs for a broad charge distribution. For this study the above charge distribution was arbitrarily generated by randomizing the horizontal position of the rods in the distribution of Figure 39.

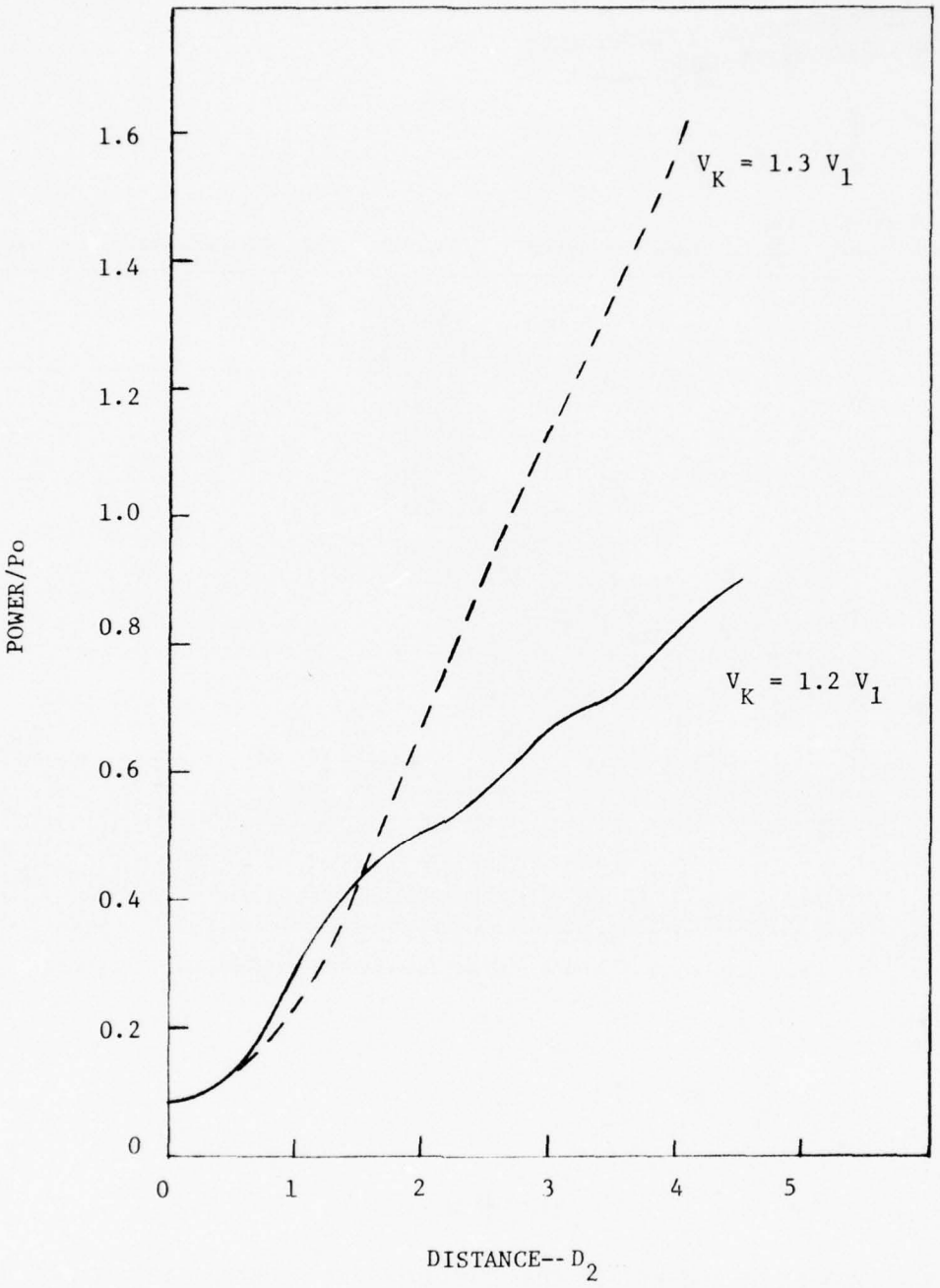

FIGURE 41

COMPUTED POWER GROWTH AT TWO VOLTAGES WHEN THE ROD POPULATION OF FIGURE 40 IS USED AS AN INPUT CONDITION.

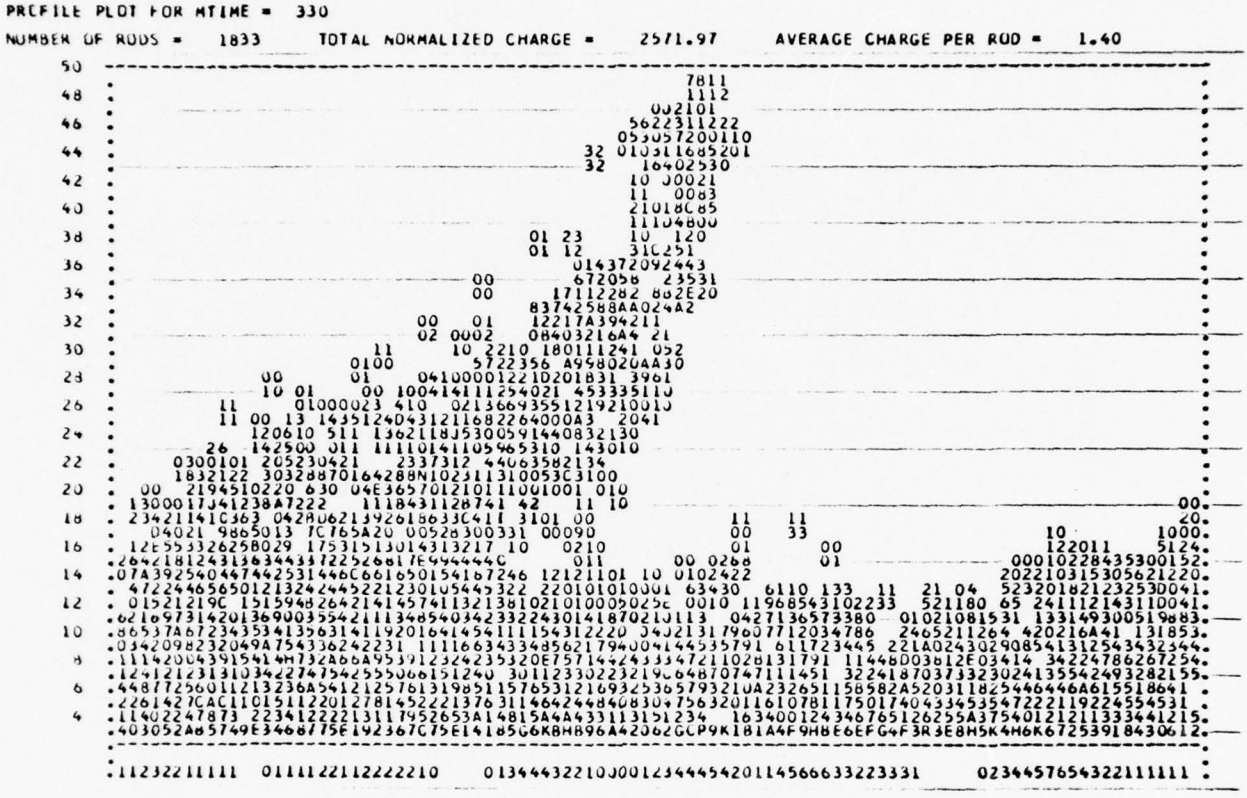

FIGURE 42

ROD PROFILE AT THE END OF THE CIRCUIT FOR A TAPERED CATHODE CALCULATION. This distribution does not provide enough charge above the hub when recirculated to the input to account for the rapid power growth observed in the instrumented CFA.

predict any satisfactory solution -- a problem which we believe has been corrected in the final version of the program. Further studies of performance in the emission-limited range must be conducted to confirm this. The computer model does not correlate well with the CFA for tapered geometries. The problem of program performance in the emission-limited range needs to be addressed and a more reasonable set of secondary emission ratios tried before returning to a study of why the correlation for tapered geometries is not satisfactory. In spite of the lack of correlation for tapered geometries, the computer model appears to be giving us useful physical insight into how these geometries improve CFA performance.

4.0 COMPUTER MODELING STUDIES OF CFA INTERACTION

The computer model has started to yield significant insights into the interactions in the CFA. These findings are beginning to change our view of CFA interaction in a number of respects. This section discusses these various findings.

4.1 Hub Buildup--Energy Exchange

The first pass calculations for all of the cases studied have shown significantly more cathode dissipation than subsequent passes. (See Table VI.) This observation led to the speculation that buildup of the space charge hub had associated with it an energy exchange mechanism which enhanced cathode bombardment. Studies were then conducted of the hub buildup when thermionic emission is present but RF power is absent. It was found that even in this case there is substantial energy exchange and cathode bombardment. Finally studies were conducted with just a few layers of charge to gain intuitive insight into the energy exchange process. We will present the results of these simplified cases first.

The simplest example of energy exchange occurs when we emit rods from the cathode for only two time steps and run the calculation for slightly longer than one cycloid (ten time steps) when the rows of rods have returned to the cathode. These calculations have been conducted with zero RF input power. The two rows of rods then proceed around a cycloid as shown in Figure 43. The electric field forces of the second row push the first row rods along their trajectories. On the upward portion of the trajectories of the

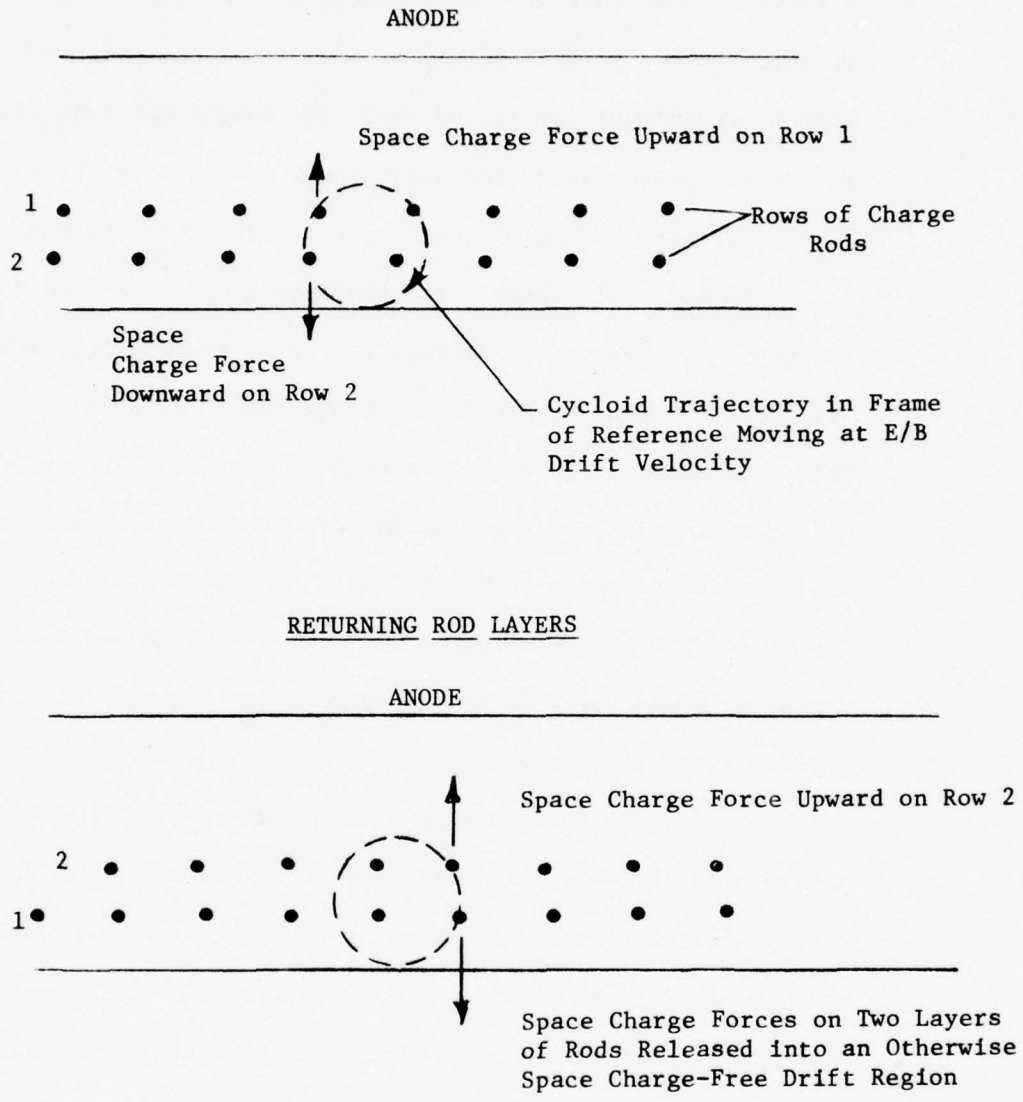

FIGURE 43

SPACE CHARGE FORCES ON TWO LAYERS OF RODS RELEASED INTO AN OTHERWISE SPACE CHARGE-FREE DRIFT REGION.

first row rods, they are pushed upward by the following second row. On the downward portion of the trajectories, the first row is pushed downward by the second row. The second row rods are correspondingly pushed backwards along their trajectories by the first row rods. As a result of these space charge interactions, the first row rods gain energy, and the second row rods lose energy. Because they have gained energy, the first row rods subsequently strike the cathode with a finite energy which is dissipated as heat on the cathode. Because they have lost energy, the second row rods cannot return to the cathode and continue to execute cycloidal trajectories as shown in Figure 44. The energy gained by the first row of rods is equal to the energy lost by the second row, and thus energy is conserved. No energy exchange occurs with the circuit because there is no longitudinal bunching.

When we run the computation with rows of rods of equal charge emitted for a series of steps over several cycloids, we find a very similar effect. The first row to return to the cathode does so with significant energy. The second row now also returns with significant energy as a consequence of the push it has received from following layers. However, because of the backward push of the first row, the second row strikes the cathode with less energy than the first row. This process continues with decreasing energy per layer until we reach a row of rods which no longer has enough energy to reach the cathode. These rods recirculate around a cycloidal trajectory a second time in the process contributing a space charge push

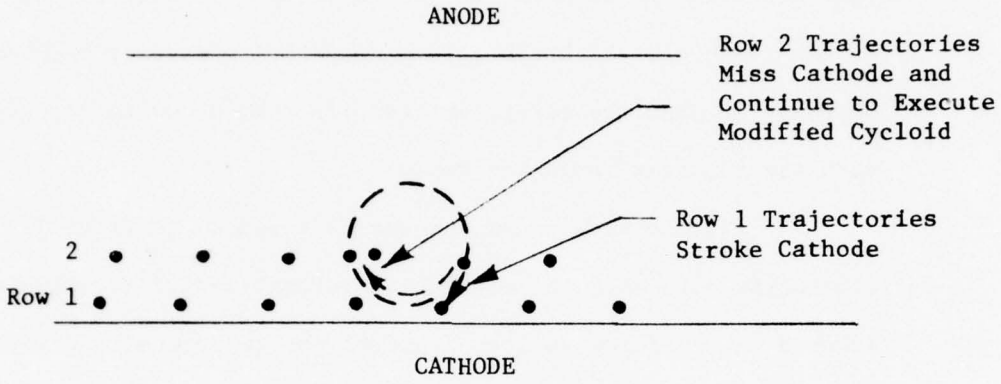

FIGURE 44

CONDITION WHEN ROW 1 RODS RETURN TO CATHODE. Row 1 rods strike cathode dissipating energy gained as a result of space charge force of row. Row 2 rods have lost energy as a result of space charge forces and cannot return to cathode. These rods continue to execute a modified cycloid above the cathode surface and are trapped in the interaction space.

to other rods ahead of them. Successive rows miss the cathode as we continue the computation until we reach rows which have received an extra push from the rows which have circulated around a trajectory for the second time. Figure 45 shows the bombardment energy of the rows striking the cathode for the first few cycloids for hub buildup in the absence of RF drive. This computation assumed secondary emission so that the charge emitted per step grows in accordance with the secondary emission ratio.

The above process has been allowed to continue for many time steps both with and without additional secondary emission. After a few cycloids we lose track of the individual rod layers, but we can still plot the average bombardment energy as a function of time. Either with or without secondary emission the charge trapped in the interaction space builds toward a value which represents a space charge limited condition. The buildup occurs more rapidly if secondary emission is present because then the charge per rod is multiplied by the secondary emission process. If the energy exchange in the space charge is sufficiently large to yield a cathode bombardment energy greater than the value for unity secondary emission ratio, the charge buildup will continue if we turn off the thermionic emission after a few time steps. This is the case even if we assume a drift space in place of the slow wave circuit. This is the condition which corresponds to the primed smooth bore magnetron in which charge buildup has experimentally been observed.

As the total charge per wavelength grows, the emission from the cathode begins to become space charge limited. This

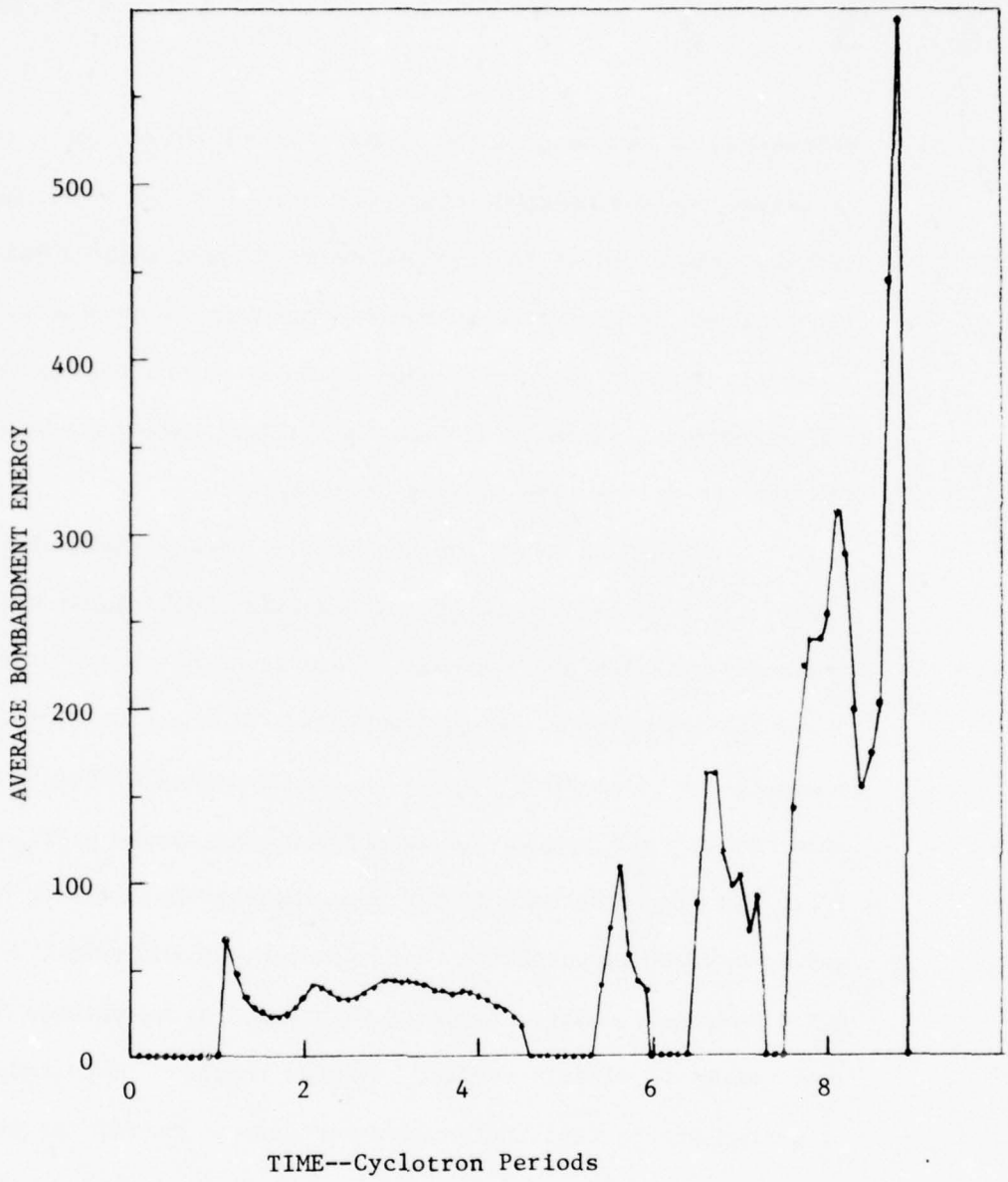

FIGURE 45

AVERAGE BOMBARDMENT ENERGY OF RODS STRIKING CATHODE IN ONE TIME STEP FOR THE FIRST FEW CYCLOTRON PERIODS OF THE HUB BUILD UP. These results show the cyclic nature of the bombardment during the initial build up.

phenomenon is included in the computer model which limits the amount of charge per rod emitted in accordance with a 3/2 power emission law when the field at the cathode drops below a value which can draw the full charge generated by the secondary emission process. When a certain maximum charge has been reached, the further growth of charge ceases. At the same time the rate of energy exchange and the cathode dissipation density decrease.

Figure 46 shows the hub buildup over a distance approximately equal to the length of the SFD-261. Both thermionic and secondary emission are assumed. There is no RF drive. The figure shows the bombardment energy, cumulative dissipation, total normalized charge in the interaction space and the location of the hub surface as a function of length. These computations assume a drift region; i.e., the slow wave circuit has been replaced by a smooth metal surface. The sudden charge buildup which can occur with a high yield secondary emitter together with the peak in cathode bombardment energy is clearly evident in these results. The sudden buildup of charge occurs when the cathode bombardment energy has increased to a value significantly greater than that required for unity secondary emission ratio. When this occurs, the charge per unit time released by the cathode is increased. As shown by Figure 46, this further increases the bombardment energy. Because the secondary emission yield initially increases with increased bombardment energy (up to about 500 volts energy), the rate of charge injection further increases. Thus, a type of avalanche process occurs which builds the charge up very rapidly.

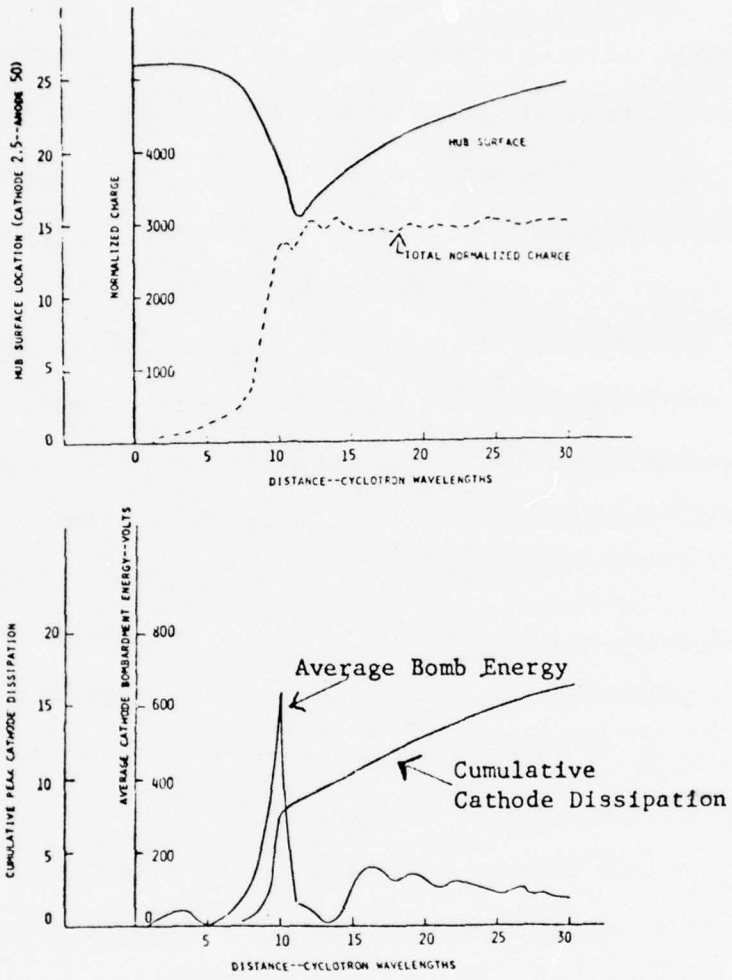

FIGURE 46

COMPUTED BUILD UP OF HUB IN A DRIFT REGION WITH SECONDARY EMISSION. Curves show hub surface location, normalized charge, average bombardment energy and cumulative peak dissipation on cathode as a function of distance in cyclotron wavelengths. Primary current density was 1.3 amps/cm^2. Secondary emission characteristics were those of beryllium (Table V).

Once a certain value of charge has been obtained, the rapid charge buildup process ceases. At this point we have space charge limitation of the emission process. A sheath of charge extending about 25% of the way from cathode to anode now exists. This sheath of charge superficially resembles a theoretical solution known as a Slater solution but departs from it in the detailed distribution of charge within the hub (it is lumpy in the computer model).

At this point it is worthwhile to digress to a short summary of the theoretical solutions for the space charge distribution. The lowest order solution is often called a Brillouin hub. This solution is sketched in Figure 47. In it the hub trajectories are parallel to the cathode surface. The electron velocity is a maximum at the hub surface and tapers linearly to zero at the cathode surface. The hub surface electron velocity and the thickness of the hub are functions of the anode-to-cathode voltage. The voltage which makes this velocity equal to the circuit synchronous velocity is known as the Hartree voltage. The charge density within the hub is constant at a value known as the Brillouin density. The expressions for the charge density, Hartree voltage, and hub thickness are given in Figure 47. Within the hub the d.c. electric field varies linearly from zero at the cathode surface to a maximum value at the surface. This value then remains constant in the charge-free region between the hub surface and the anode.

The next higher order, theoretical solution to the space charge distribution is called a first order Slater solution. The

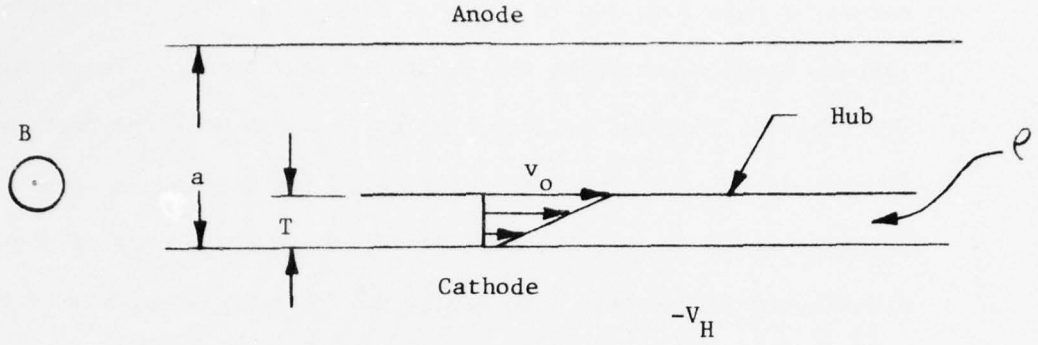

FIGURE 47

IDEAL BRILLOUIN HUB. Charge sheath of thickness, T, and uniform charge density, , exists above cathode. There is not charge above the hub. Hub trajectories are parallel to cathode as shown by arrows. Electron velocity is equal to circuit synchronous velocity, v_o, at hub surface and tapers linerly to zero at cathode surface. Following relations hold for the ideal hub:

$$\rho = \eta \varepsilon_o B^2$$

η is charge to mass ratio for an electron

ε_o is permittivity of free space

B is magnetic flux density

$$V_H/V_O = \frac{2\eta B a}{v_o} - 1 \qquad V_O = \frac{v_o^2}{2\eta} \text{ synchronous voltage}$$

$$t/a = \frac{2}{V_H/V_O + 1}$$

V_H is the "Hartree Voltage"; i.e., the cathode voltage required to make the hub surface velocity equal to v_o.

nature of this solution is shown in Figure 48. The trajectories execute loops which start and return to the cathode. These loops are twice as long and half as high as is a space charge-free cycloid. The hub surface thickness is the same as for the lowest order Brillouin solution as is the total charge in the hub. The charge is, however, distributed differently with maxima in the vicinity of the cathode and the hub surface. This solution has a higher total kinetic energy than the lowest order Brillouin solution. For this reason it has sometimes been argued that the initial charge distribution would look like the first order Slater solution which would permit charge to be drawn from the cathode and that the charge distribution would subsequently settle toward a Brillouin solution as energy is lost through collision processes.

In Figure 46 we see the gradual pull-in of the surface of the space charge from the thickness of the space charge-free cycloid to a value close to the theoretical hub thickness as the space charge density builds up. This occurs during the first eleven cyclotron wavelengths in Figure 46. At the point of minimum thickness the hub trajectories resemble first order Slater trajectories, but with an important difference. Since energy exchange has taken place, some of the rods will have given up energy and cannot therefore return to the cathode. There is consequently a distribution of trajectory shapes as sketched in Figure 49. Figure 50 shows a charge profile plot obtained at this time. The charge is seen to be uniform in the longitudinal (y) direction but to have variations in the transverse (x) direction.

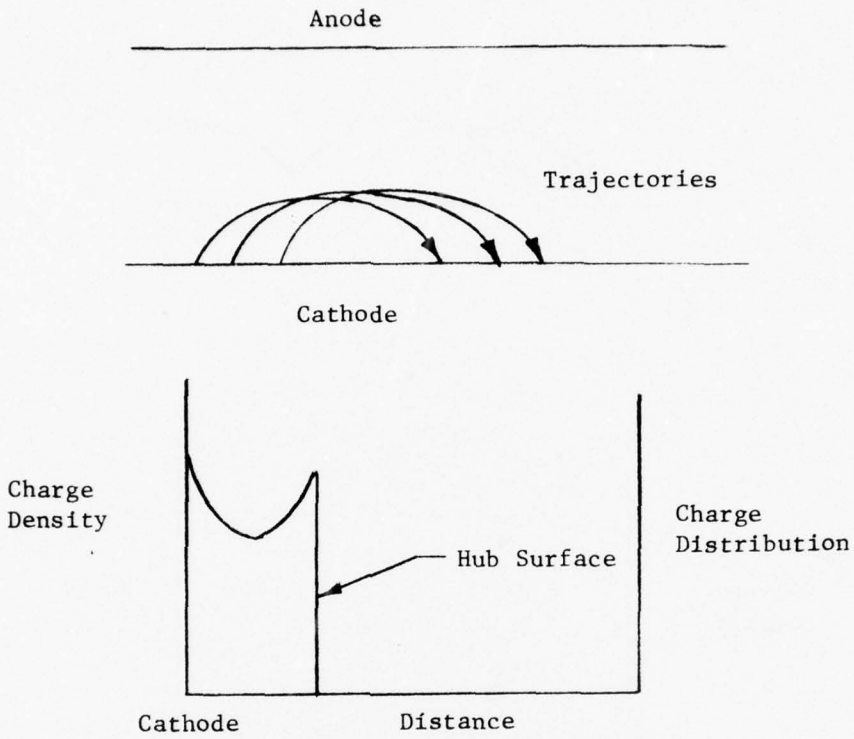

FIGURE 48

FIRST ORDER SLATER SOLUTION FOR THE HUB. Trajectories are twice as long and half as high as a space charge-free cycloid.

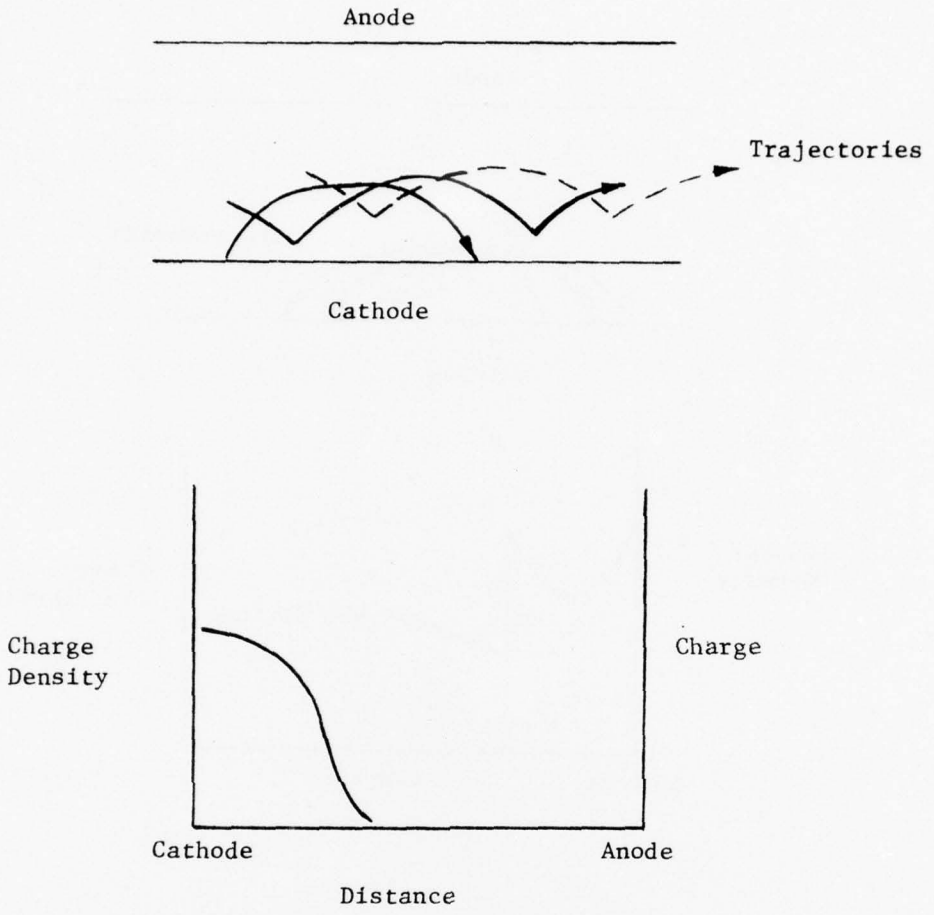

FIGURE 49

SKETCH OF HUB SOLUTION OBTAINED FROM THE COMPUTER MODEL. Because of energy interchange there are different kinds of trajectories--only some of which return to cathode. Edge of charge distribution is no longer sharp.

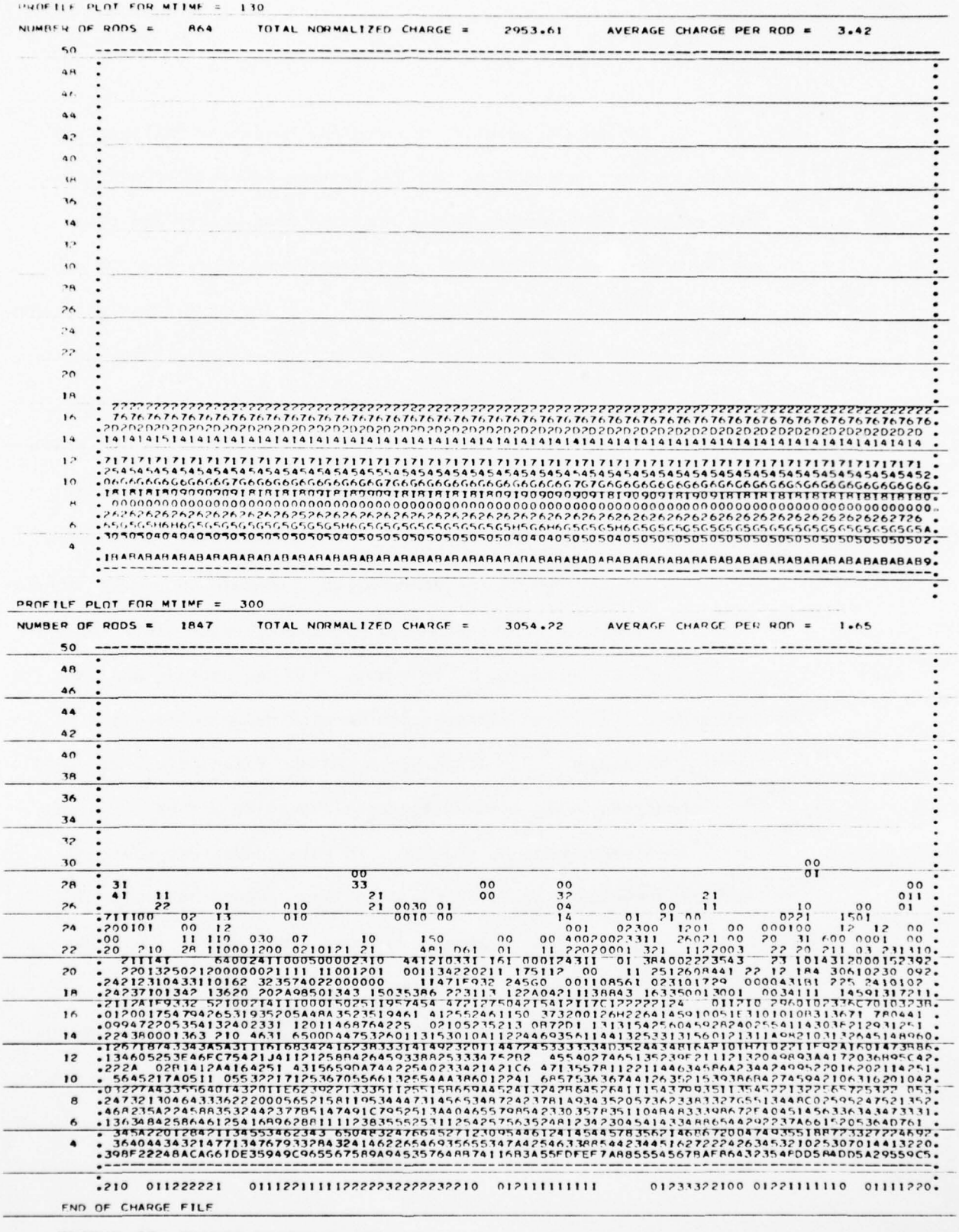

FIGURE 50--CHARGE PROFILES OBTAINED DURING BUILD UP OF HUB IN ABSENCE OF RF SIGNAL. Top profile occurs at Step 130 which is at approximate location of minimum hub thickness. Bottom profile occurs at Step 300.

Beyond the point of minimum hub thickness in Figure 46, the energy exchange process and the cathode bombardment continue. This results in some rods losing more and more energy and thus moving away from the cathode. As this process continues the hub surface, which was well defined up to the point of minimum thickness, becomes fuzzy. At the sametime, the uniform rows of charge which existed earlier (top of Figure 50) have broken up. The bottom profile in Figure 50 shows the charge distribution after 30 cyclotron periods. Figure 51 shows the charge distribution at this oint relative to the location of the ideal Brillouin hub surface.

At the end of the computation in Figure 46 energy exchange was still taking place though at a decreasing rate. This implies that rods are continuing to move away from the cathode and that the surface of the charge distribution is continuing to move toward the anode. We suspect that if we continued the calculation, we would find that rods would eventually reach the anode and that a steady state condition would be reached. In this condition, the d.c. current drawn would provide the d.c. input power to supply both anode and cathode dissipation. We would thus have a condition similar to that observed in smooth bore magnetron experiments.

The existence of substantial energy exchange in the hub is compatible with a number of observations. Experiments have been conducted in which smooth bore magnetron geometries are primed with small amounts of thermionic current and yet generate large amounts

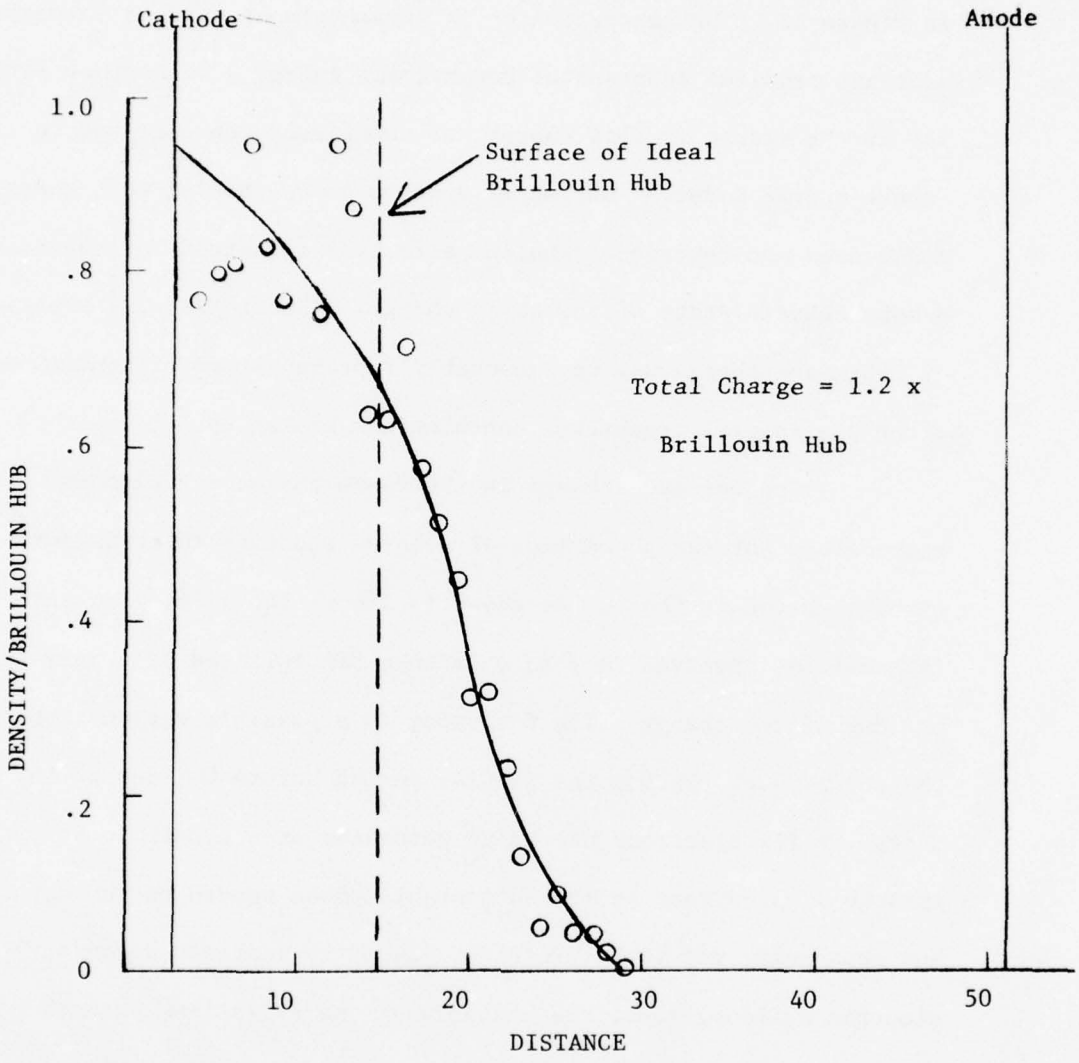

FIGURE 51

CHARGE DISTRIBUTION BETWEEN CATHODE AND ANODE FOR THE HUB GENERATED IN THE ABSENCE OF RF INPUT.

of current through secondary emission.[9,10,11] A typical experimental geometry is shown in Figure 52, and the currents generated are shown in Figure 53. The generation of large amounts of current by secondary emission requires substantial bombardment energy of electrons returning to the cathode. This energy has sometimes been ascribed to "space charge modes." Our model appears to be showing that these modes need not represent coherent effects but instead may represent a more chaotic state of the space charge. The statistical theories of hub space charge may be reasonably representative of conditions after the initial transverse bunching has broken up.[12]

The energy exchange in the space charge may also be responsible for the phenominon of delayed starting which is sometimes observed in CFA's. As shown in Figure 54, a delay in turn-on is sometimes observed in a cold cathode CFA followed by a very rapid buildup of the charge. The following is a possible explanation for the phenominon. During the initial period before buildup of the charge, a few electrons are being generated at the cathode by field emission. Electrons in the unfavorable phase return to the cathode but apparently not with sufficient energy to initiate secondary electron buildup, i.e., the bombardment energy is less than the energy for unity secondary emission ratio. At the same time, electrons in the favorable phase are losing energy to the RF wave and cannot return to the cathode. This charge is stored in the interaction space. When the stored charge becomes high enough, the energy exchange process is initiated and some charge returns to

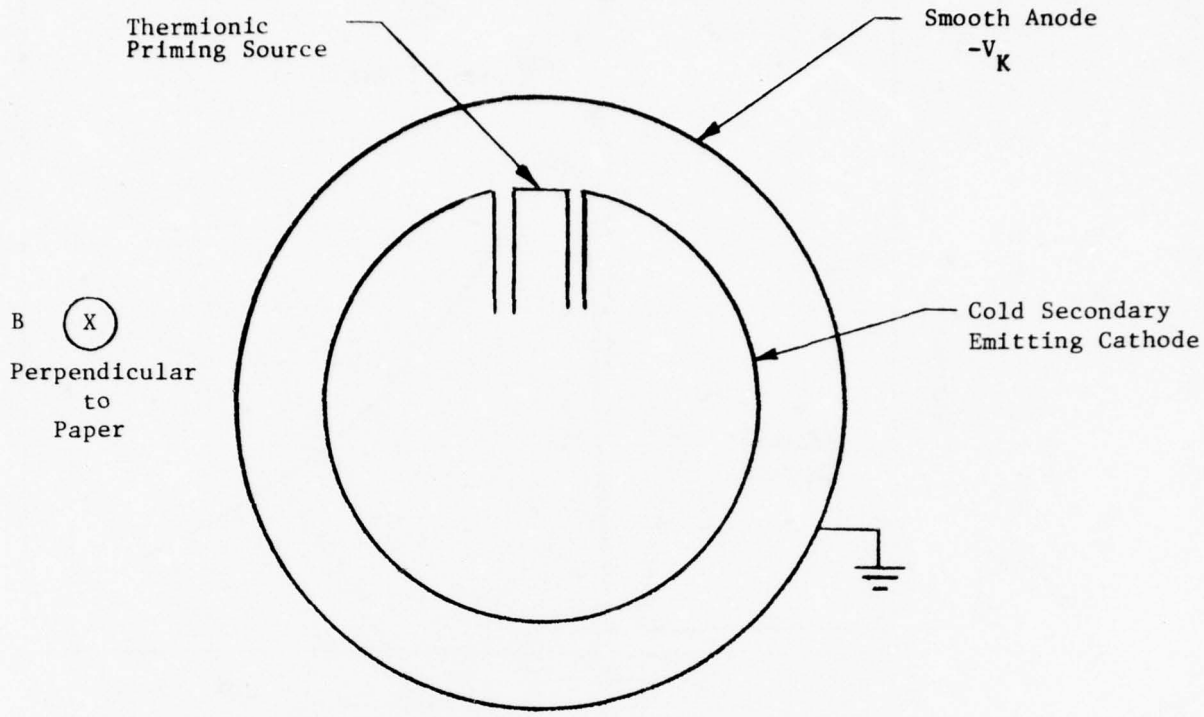

FIGURE 52

SKETCH OF A SMOOTH BORE MAGNETRON DIODE. Anode is as a smooth cylinder. Cathode consists of a main section with secondary emission only plus a small area thermionic priming cathode.

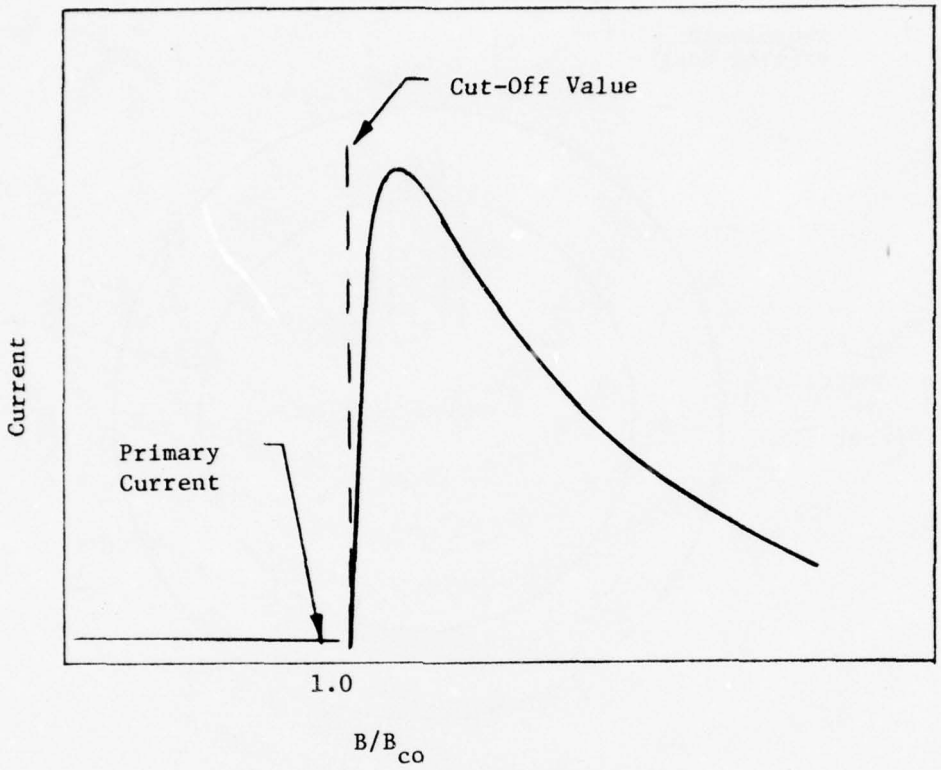

FIGURE 53

CURRENT DRAWN BY SMOOTH BORE MAGNETRON DIODE AS A FUNCTION OF MAGNETIC FIELD. A VERY HIGH CURRENT IS DRAWN AS SOON AS THE MAGNETIC FIELD IS INCREASED TO ABOVE THE CUT-OFF VALUE.

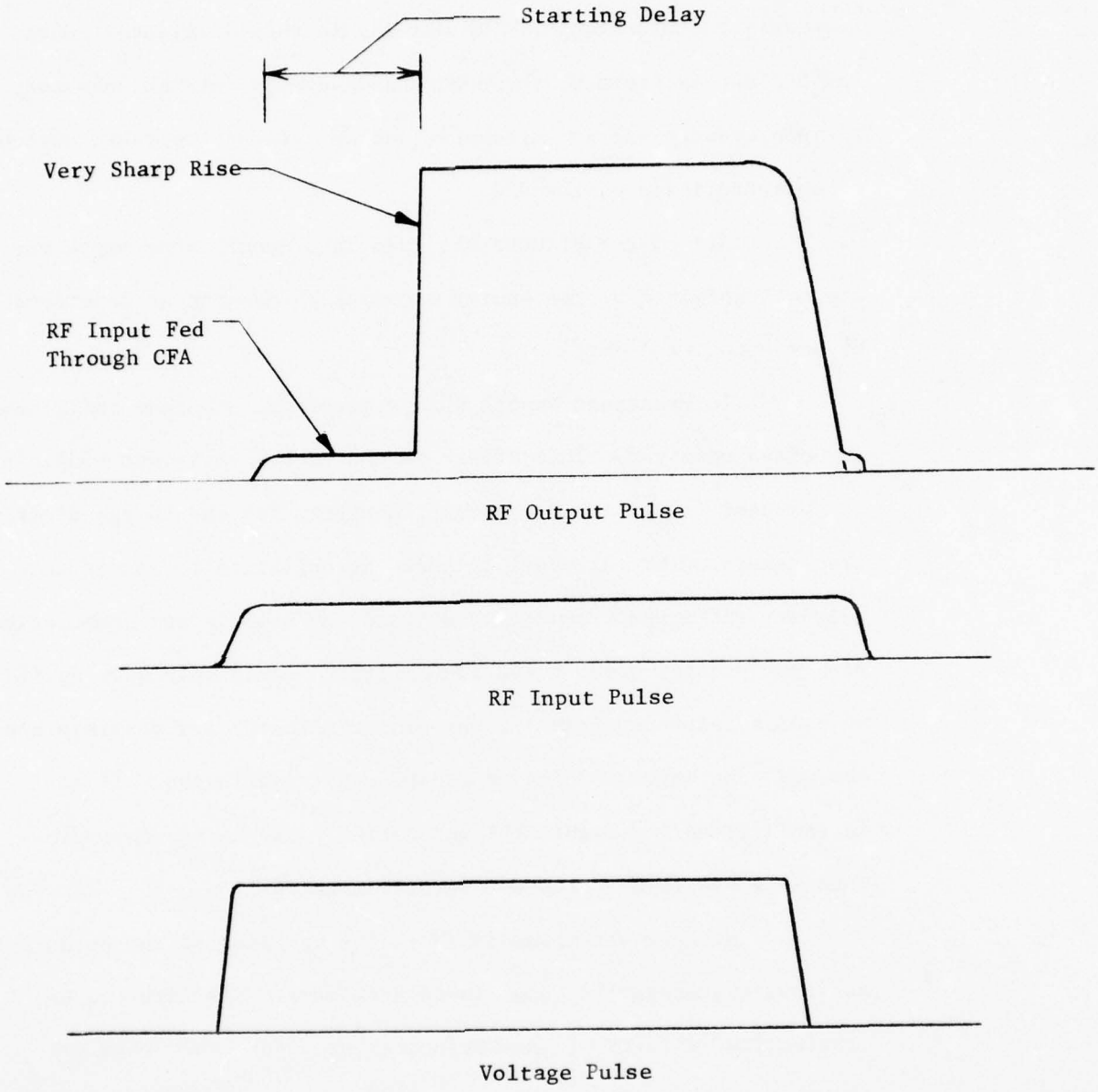

FIGURE 54

SKETCH OF THE PHENOMENON OF DELAYED STARTING WHICH IS SOMETIMES OBSERVED WITH CFA'S OPERATED FROM A D.C. POWER SUPPLY OR A HARD TUBE MODULATOR. Starting is delayed for a fixed period and then occurs very rapidly.

the cathode with an energy greater than that required for unity secondary emission ratio. The buildup is then initiated. Once the buildup is started, the energy exchange is further enhanced, the bombardment energy increases, and we observe the rapid switch on characteristic of the CFA.

All of the effects observed in a smooth bore magnetron are not explained by the energy exchange phenomenon as described by our computer model.

In reentrant smooth bore magnetrons, coherent oscillations are often observed. This effect is not picked up by our model in its present form. It is possible, however, for the charge distribution generated by our model to have instabilities for waves at a velocity different from the frame velocity used in our computation. With the present model these instabilities would only show up if we used a reference frame at the proper velocity and possibly also assumed some input modulation at the right wavelength. If an instability were present, the modulation would be found to grow. This is a possible course for future investigation.

We have attempted to check the validity of the computer model of the energy exchange in several ways. The first is to examine the validity of the trajectory procedure when rods are traced through a varying electric field. As discussed in Section 2.4.1, the procedure does not appear to cause any substantial error in the energy of rods returned to the cathode.

The second means of testing the energy exchange phenomenon was to compute several cycloids of charge buildup employing thermionic emission and no RF input. The bombardment energy of the charge layers returned to the cathode was then determined with the computation run with different degrees of granularity. In one set of computations we started with a time step size of 1/8 cyclotron period and then decreased the time step by factors of two and four. We also increased the number of rods emitted per step by a factor of two. We adjusted the initial charge per rod in these computations to yield the same value of emission current density in each case. The changes in granularity had little effect on the computed cathode bombardment energy. These results showed that the energy exchange observed was not simply a result of program granularity.

A third test we subjected the energy exchange process to is the conservation of energy. The energy balance procedure described in Section 2.11 was developed for this purpose. Applying this procedure to the run described in Figure 46, we obtain an energy balance to within better than 10%. (See Table IX.) While less than perfect, this result is believed to be good enough to provide confidence that the basic energy exchange mechanism described by the computer is correct.

TABLE IX

ENERGY SUMMARY FOR THE COMPUTER GENERATED HUB OF FIGURE 50

At Time Step 300

Cumulative Peak Cathode Dissipation	15.7 kW
Kinetic Energy of Rods In Interaction Space	14.1 kW
Total Energy Converted (Sum of Above)	29.8 kW
Potential Energy Input	27.2 kW
Ratio Energy Converted to Energy Input (should be 1.0)	1.09

AD-A065 736 VARIAN ASSOCIATES BEVERLY MASS F/G 9/1
CFA DESIGN IMPROVEMENT PROGRAM. VOLUME II. COMPUTER MODELING ST--ETC(U)
JUN 78 H L MCDOWELL N00123-75-C-1294
UNCLASSIFIED NL

3 OF 4
AD
AD 65736

4.2 Capture of Charge From the Hub-Spoke Formation

The space charge hub of Figure 50, which was generated in the absence of RF drive, was then used to investigate the mechanism of charge capture from the hub and spoke formation. The hub of Figure 50 was used as an input condition for a series of calculations using different power inputs and voltages. Since the hub generated in this manner had not been exposed to RF, there was no RF bunching present and no current well above the hub level. Thus we could study the mechanisms by which charge is bunched and drawn up from the hub separately from the interaction with recirculating charge.

Prior to conducting these calculations, it was believed that even very small RF input signals could draw current from the hub and form spokes. It was believed that to obtain spoke formation at low signal levels, the anode voltage had to be close to the Hartree value. This model was based on space charge free trajectory calculations starting from a Brillouin hub (Figure 47) which were conducted by Feinstein[13] many years ago before the computer modeling techniques we have employed were available.

The present computer model showed quite different behavior from the simple model described above. The major differences are apparently the result of starting from the real space charge condition in the hub rather than the ideal Brillouin model. The present model showed that it is very difficult for weak RF signals to draw charge from the hub. Figure 55 shows the power growth in 150 time steps (15 cyclotron periods) at four different input power

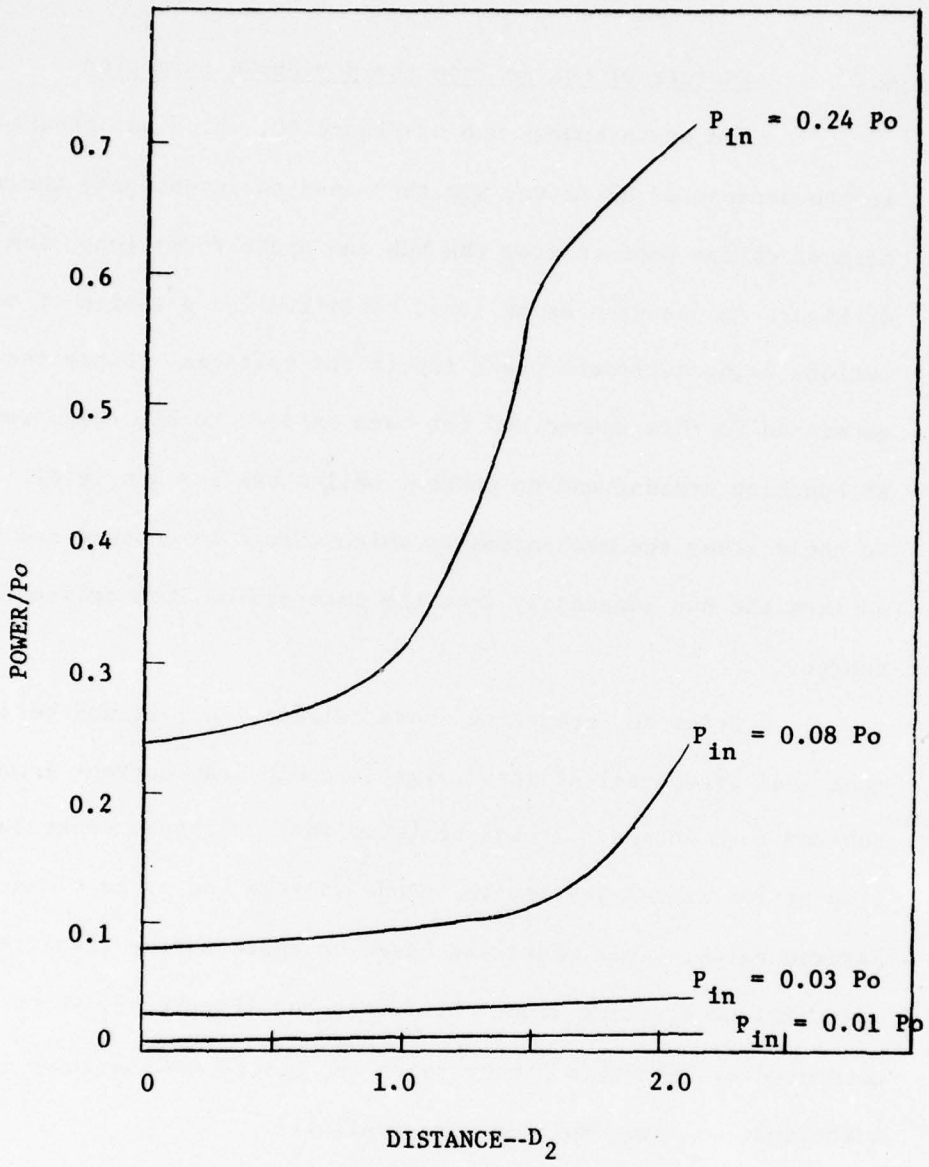

FIGURE 55

POWER GROWTH IN 150 TIME STEPS STARTING FROM AN UNNORMALIZED HUB. $f = f_o + 0.3$, $V_K = 1.3$ V, $V_K/V_H = 1.13$

levels. It is seen that the growth is very small at the lowest input level. Figure 56 shows the gain as a function of input power for the conditions of Figure 55. The gain is shown to increase with increasing input power until a "saturation level" is reached.

The variation in gain with voltage above Hartree is also different than had been expected. Figure 57 shows the power growth as a function of distance for different ratios of cathode-to-Hartree voltage for a peak input power of 0.03 P_o (a relatively low value). The power growth is seen to increase as the voltage is increased above the Hartree value rather than when it decreased toward the Hartree value.

There is a straightforward explanation for the results described above. The trajectories of electrons in the hub are subsynchronous relative to the circuit wave. In a frame of reference synchronous with the wave, as is followed by the computer simulation, these trajectories appear as shown in Figure 58. The lack of synchronism is a consequence of the reduction of the d.c. field within the hub caused by the hub space charge. (The variation of this field is shown in Figure 29.) Because of the reduced d.c. field in the hub, the average E/B drift velocity of hub electrons is substantially lower than the E/B drift velocity for any electrons above the hub. As a consequence of their lack of synchronism, a significant RF field strength is required to capture the charge and draw it out of the hub. One such charge capture has occurred and electrons have been drawn above the hub, they enter a region of

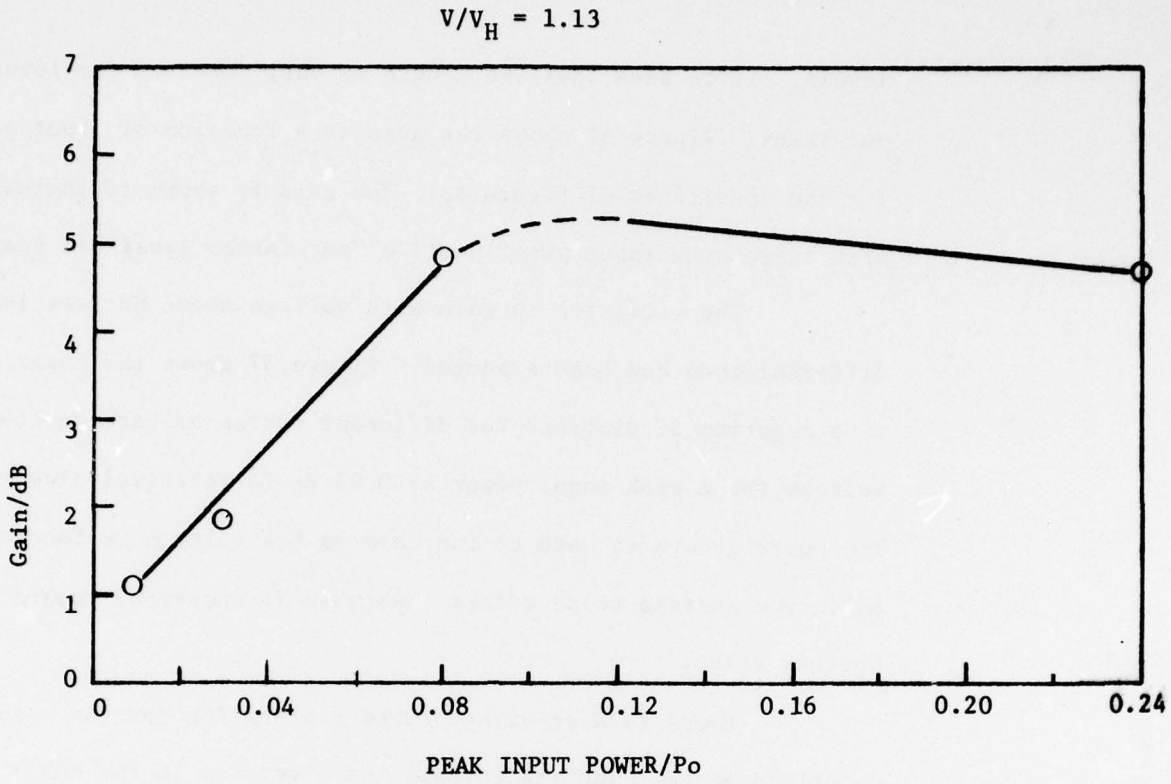

FIGURE 56

GAIN IN 150 TIME STEPS AS A FUNCTION OF PEAK INPUT POWER FOR THE COMPUTATIONS STARTING FROM AN UNMODULATED HUB. $f_o = f_o + 0.3$, $V_K = 1.3\ V_1$, $V_K/V_H = 1.13$

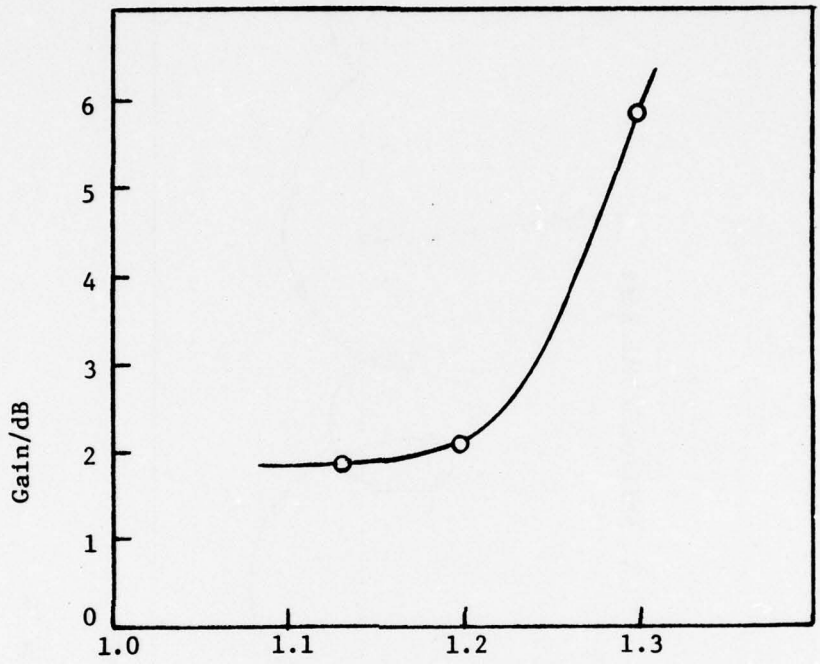

FIGURE 57

GAIN IN 150 TIME STEPS AS A FUNCTION OF THE CATHODE-TO-HARTREE VOLTAGE RATIO FOR THE COMPUTATIONS STARTING FROM AN UNMODULATED HUB. P_{in} = 0.03 Po, f = f_o+0.3

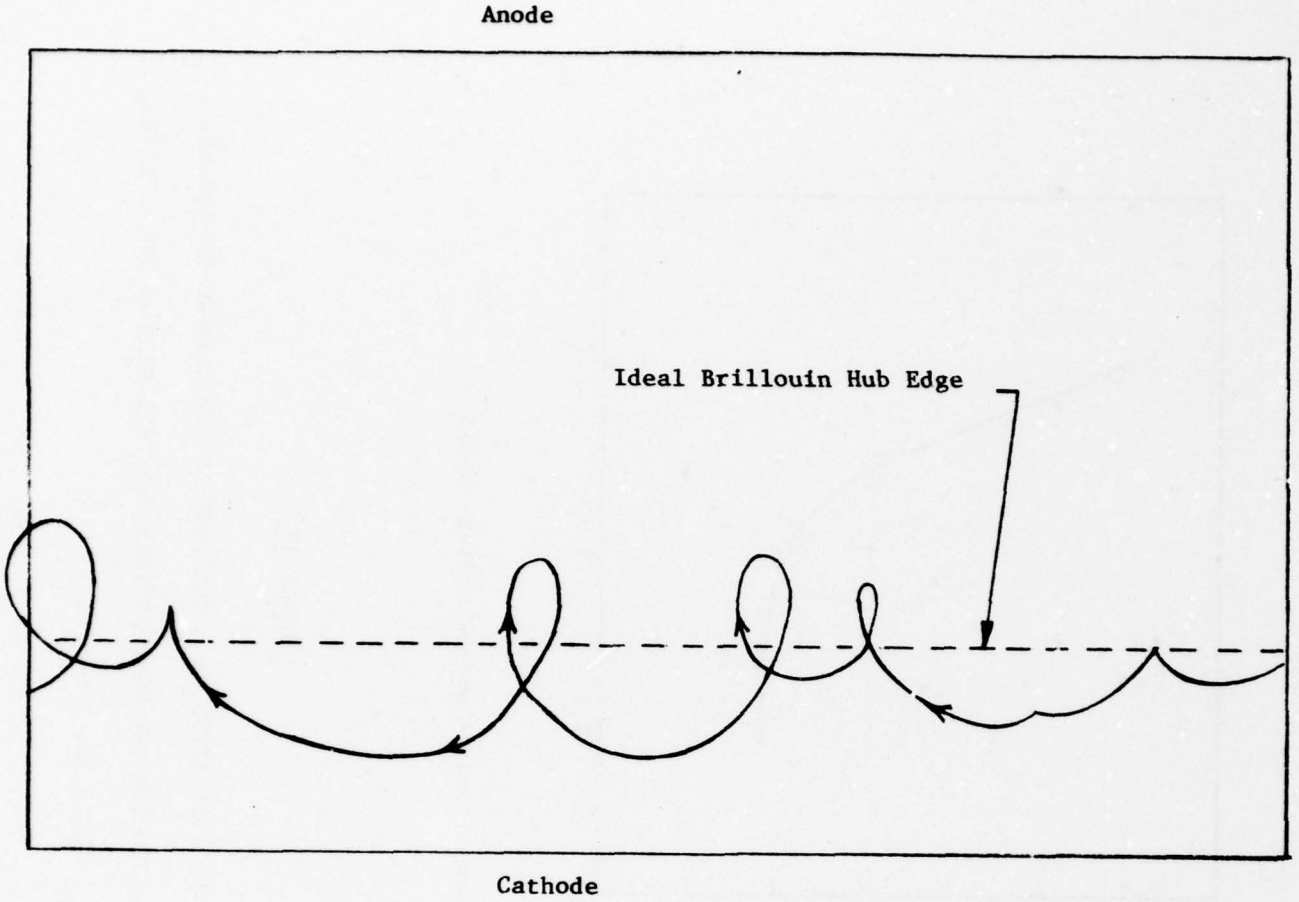

FIGURE 58

TYPICAL COMPUTER GENERATED HUB TRAJECTORY FOR THE HUB OF FIGURE 50. The trajectory moves backward through the interaction box thus indiciating that it has a velocity less than synchronous velocity. Average drift velocity of this trajectory is 78% of synchronous velocity.

higher d.c. field and subsequently drift at a velocity approximately synchronous with the circuit wave. Thus, an RF field strength of significant amplitude is required to draw charge from the hub and initiate interaction.

In the simplified model used by Feinstein a Brillouin hub was assumed. As a consequence the top layer of charge was synchronous with the circuit and the charge capture problem did not occur. The computer modeling studies show that the Brillouin hub model is far from the correct one. When the proper trajectories in the hub are taken into account, the charge capture problem described above becomes evident.

The studies conducted by Feinstein showed that a problem existed with the ability to form spokes when the RF field is low and the field above the hub is above that for E/B drift velocity synchronism with the circuit wave. This led to the concept of using a low V_K/V_H ratio near a CFA input and increasing this ratio by tapering either anode-cathode spacing or pitch as the power grew. The present computer model appears to show that the criteria for proper spoke formation once charge has been drawn above the hub are less stringent than had previously thought to be the case. This may be a result of electrons starting out with a backwards velocity in the moving frame of reference in the present model. Our subsequent discussion will show that tapering the V_K/V_H ratio as originally suggested by Feinstein is useful. This technique has long been used to improve CFA performance. The reasons for its

effectiveness appear, however, to be different from those originally suggested. Rather than improving interaction with charge newly drawn from the hub, the tapers appear to optimize interaction with recirculating space charge at the input. This concept will be further discussed in Section 4.4.

We do not have enough information on the charge capture phenomenon to generalize with a high degree of confidence on the location of the knee of the gain versus power curve as shown in Figure 56. As a working hypothesis it appears that this point should be primarily dependent on the ratio of the RF voltage at the hub surface to the synchronous voltage. The energy which must be added to the electrons to bring them up to the synchronous velocity is proportional to the synchronous voltage, V_0, and the ability of the RF wave to affect the trajectories in one RF cycle is proportional to the RF voltage. This RF-to-synchronous voltage ratio at the hub surface may be calculated from:

$$\frac{V_{RF}}{V_0} = \sqrt{\frac{2PK}{V_0}} \quad \frac{\sinh \beta y}{\sinh \beta a} \qquad 4.2\text{-}1$$

where:

V_{RF} is the RF voltage at the theoretical hub surface

V_0 is the synchronous voltage

P is the RF power on the anode

K is the anode circuit impedance

β is the phase constant

a is the anode-cathode spacing

y is the hub thickness (see Figure 47)

The hub thickness may be calculated from the expression in Figure 47.

For the cases studied, the knee of the gain versus RF power curve appears to be close to a V_{RF}/V_0 ratio of 0.05. We suspect that this is a good first order approximation for most practical designs.

The above arguments lead us to the conclusion that we cannot reduce the RF input power requirement for a given CFA interaction space design by simply making the circuit longer to increase the gain. This conclusion is in marked contrast to the situation in TWT's or injected beam CFA's where the theoretical gain can be indefinitely increased by increasing the circuit length and the practical gain levels achievable depend on how much small signal gain may be tolerated while maintaining stability against oscillations. The emitting sole CFA as described above has no small signal gain and requires a significant RF input power to initiate amplification.

The above expression for the V_{RF}/V_0 ratio shows how we can lower the usable input power. We can reduce the synchronous voltage, V_0, (K, the interaction impedance, is roughly proportional to $\sqrt{V_0}$ so $V_{RF}/V_0 = (1/V_0)^{3/4}$) or we can reduce the anode-cathode

spacing, a. If we want high gain in a CFA and as a consequence try to reduce V_0 so that the criterion described above is met for low input powers (eg. 20 dB below the output), we find that the circuit pitch often becomes very fine grained. In addition, the reduction of V_0 reduces peak output power so that a long circuit may be required to obtain the full peak output. Losses in circuit attenuation could then become very high.

There are alternatives to designing the CFA so that the V_0 criterion suggested above is met. One alternative is to use charge above the hub surface recirculated from output to input in a reentrant CFA to provide usable charge near the input. This charge should be enough to provide an initial gain of about 10 dB from the 1 kW peak input level. Beyond this point, the RF circuit wave will be strong enough to draw up fresh charge from the hub. We believe that this is the mechanism for gain at the input which currently exists in several of our CFA's. If this approach is to be followed, we must insure that enough charge above the hub is recirculated and that this charge is sufficiently debunched so that regeneration is minimized. We will discuss a CFA design of this type in the next section.

An alternative approach to the CFA design is to allow only the hub to recirculate in a reentrant design, but to change conditions at the input so that charge may be drawn from the hub. This means increasing the V_K/V_H ratio at the input to bring the average drift velocities within the hub closer to synchronism with

the circuit wave. The electric field above the hub is then far above that required for synchronism. Thus once charge has been drawn above the hub, the V_K/V_H ratio must be reduced so that this charge can interact with the circuit wave. A CFA design of this type is discussed in Section 5.

4.3 RF Interaction with the Space Charge Hub

Space charge hubs similar to the one described in Section 4.1 have been derived for several applied voltages and two frequencies and these hubs used as the input rod population for a series of calculations which cover the full length of a CFA. These conditions are artificial in that they eliminate recirculating charge above the hub level. However, they permit us to examine the interaction without the additional complexity of the effects of recirculated charge. We will first describe in detail a calculation of this type for band center and normal operating voltage. We will then describe how performance is altered when we change voltage or frequency.

4.3.1 Simulation at Band Center and Normal Operating Voltage

The input conditions for the run to be described in this section are the same as for the midband case in Table V except that the input rod population is the hub of Figure 50. Figure 59 shows the power growth and the cumulative dissipations for this run. Table X summarizes the results of the calculation. Figure 60 presents typical charge profile files for this computation. These plots are described in Figure 21. They differ from the rod profile plots presented in Section 3 in that they represent a picture of the charge array rather than the rod positions. Since each rod contributes charge to the four surrounding points, the charge profile plots appear more dense than the rod profile plots. Figure 60 shows the formation of a broad spoke at low power levels with the spoke center riding forward of the center of the favorable phase. As the RF power increases, the spoke becomes more sharply bunched by the RF wave and becomes more nearly centered in the favorable phase. This behavior is typical of all the computations we have run.

Figures 61A through 61C show trajectories of typical rods moving up through the spokes. Figures 61A is for a rod moving into the broad spoke at low power level. Figures 61B and 61C are the trajectories moving into the spoke at high power levels. Time step numbers are shown on the trajectory plots. These steps may be associated with the charge profiles in Figure 60.

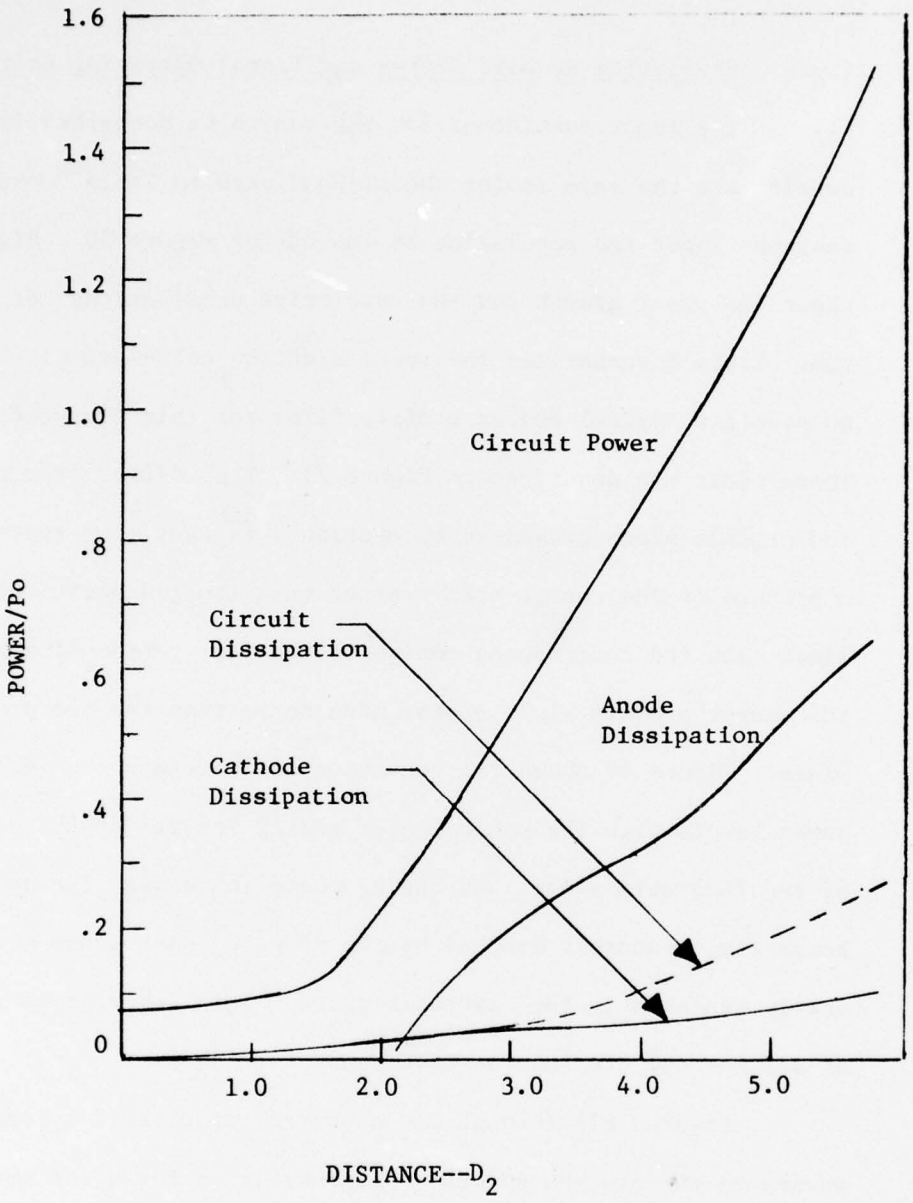

FIGURE 59

RESULTS OF COMPUTATION STARTING FROM UNMODULATED HUB. CIRCUIT POWER, CUMULATIVE DISSIPATION BY ELECTRON INTERCEPTION ON ANODE AND CATHODE AND CUMULATIVE DISSIPATION IN CIRCUIT LOSS ARE SHOWN AS A FUNCTION OF DISTANCE.

$f = f_o + 0.3$, $V_K = 1.3\ V_1$, $V_K/V_H = 1.13$

TABLE X

RESULTS OF COMPUTATION STARTING FROM
UNMODULATED HUB OF FIGURE 51

Input conditions of Table V excpet for length of $5.6D_2$.

$V = 1.3\ V_1$, $V/V_H = 1.13$.

Peak Output Power	1.47 Po
Peak Input Power	0.08 Po
Gain	12.6 dB
Dissipation by Electron Interception on Anode	0.62 Po
Dissipation in Circuit Attenuation	0.25 Po
Dissipation on Cathode	0.09 Po
Anode Current	18.51 Amps
Output Phase--Departure from Cold Circuit Phase	46.5 degrees
D.C. Input	
Voltage x Current	2.41 Po
Sum of Powers and Dissipation	2.51 Po
Ratio	1.04
Average Efficiency of Pass	60 %

FIGURE 60

CHARGE PROFILE PLOTS GENERATED BY THE COMPUTER FOR A COMPUTATION STARTING FROM AN UNMODULATED HUB AT MID BAND. $f = f_o + 0.3$, $V_K = 1.3\ V_1$, $V_K/V_H = 1.13$. Twenty one charge profiles taken every twenty time steps follow. Time step numbers are shown at the top of each plot. For each twenty time steps the interaction box moves forward $0.28\ D_2$. Circuit length for 400 time steps is $5.6\ D_2$.

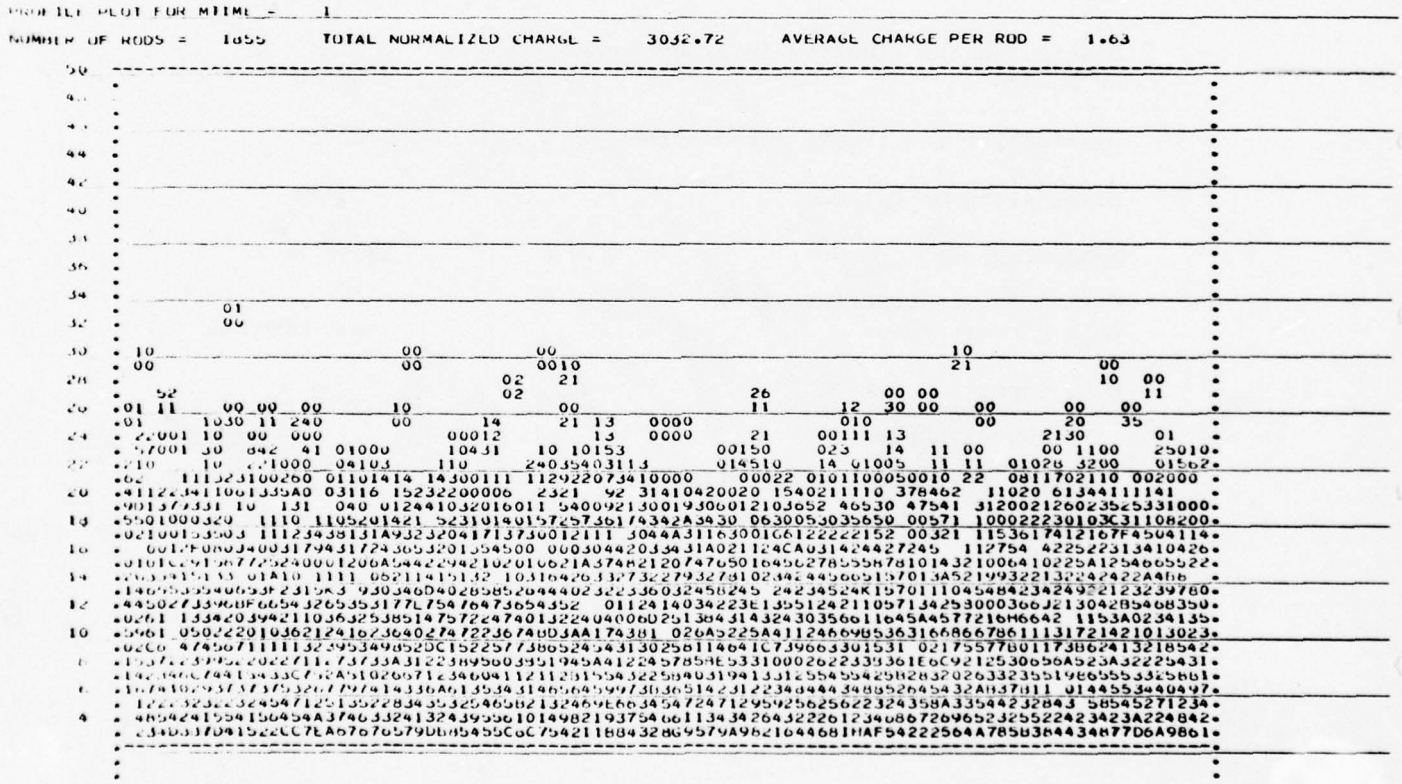

FIGURE 60 (continued)

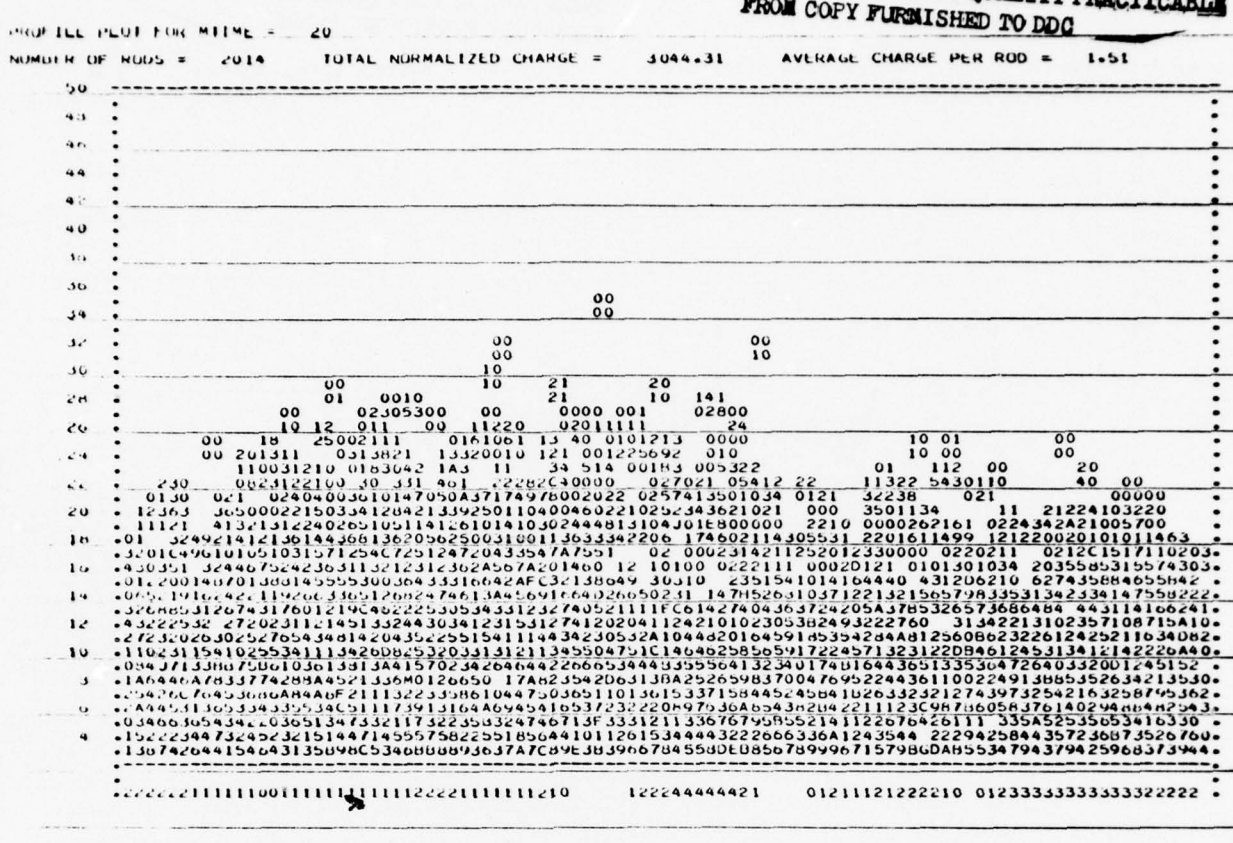

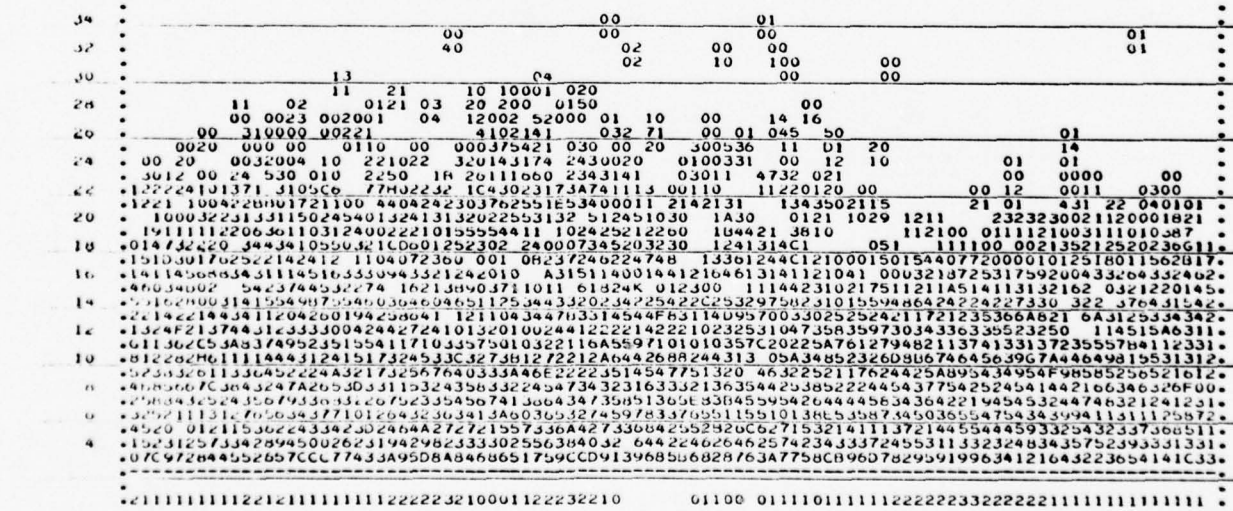

FIGURE C2 (continued)

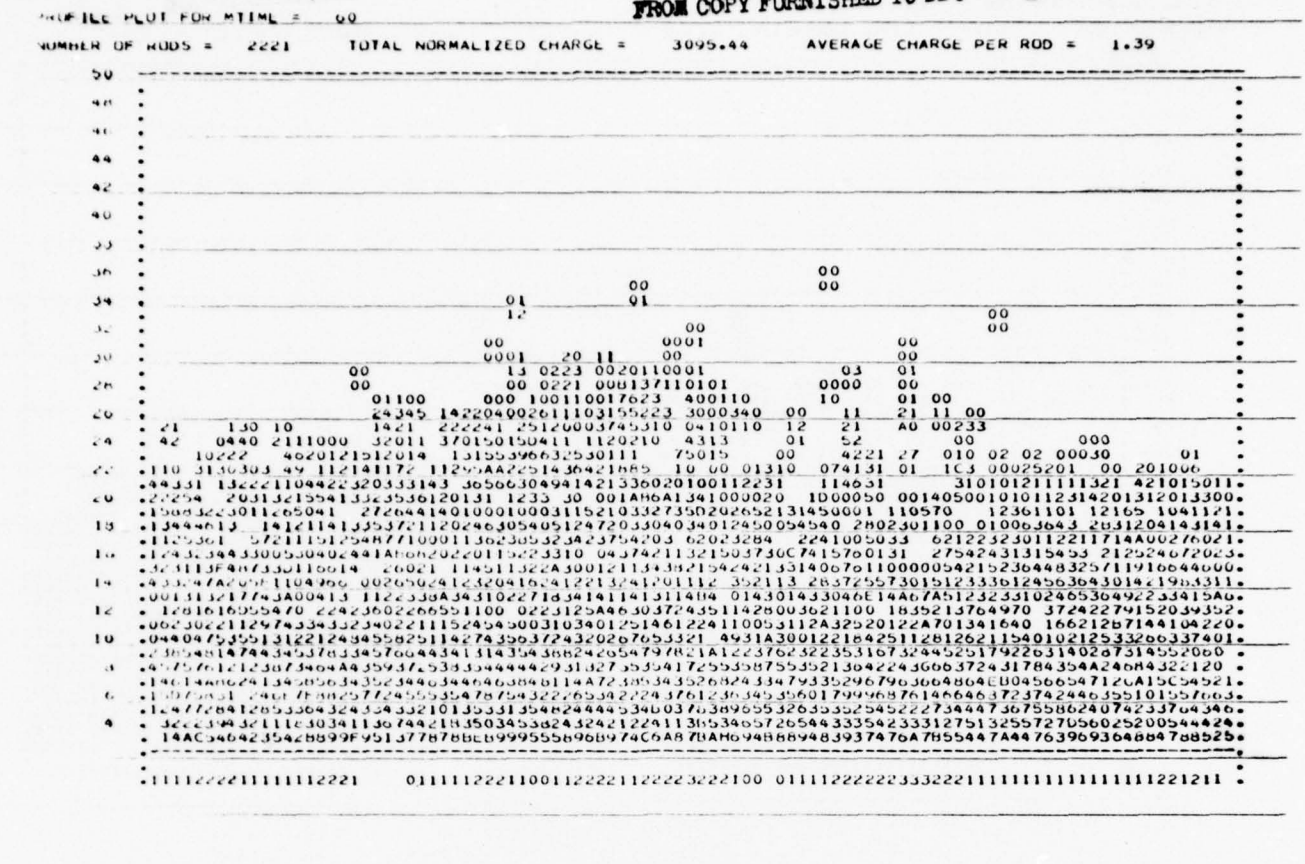

FIGURE 60 (continued)

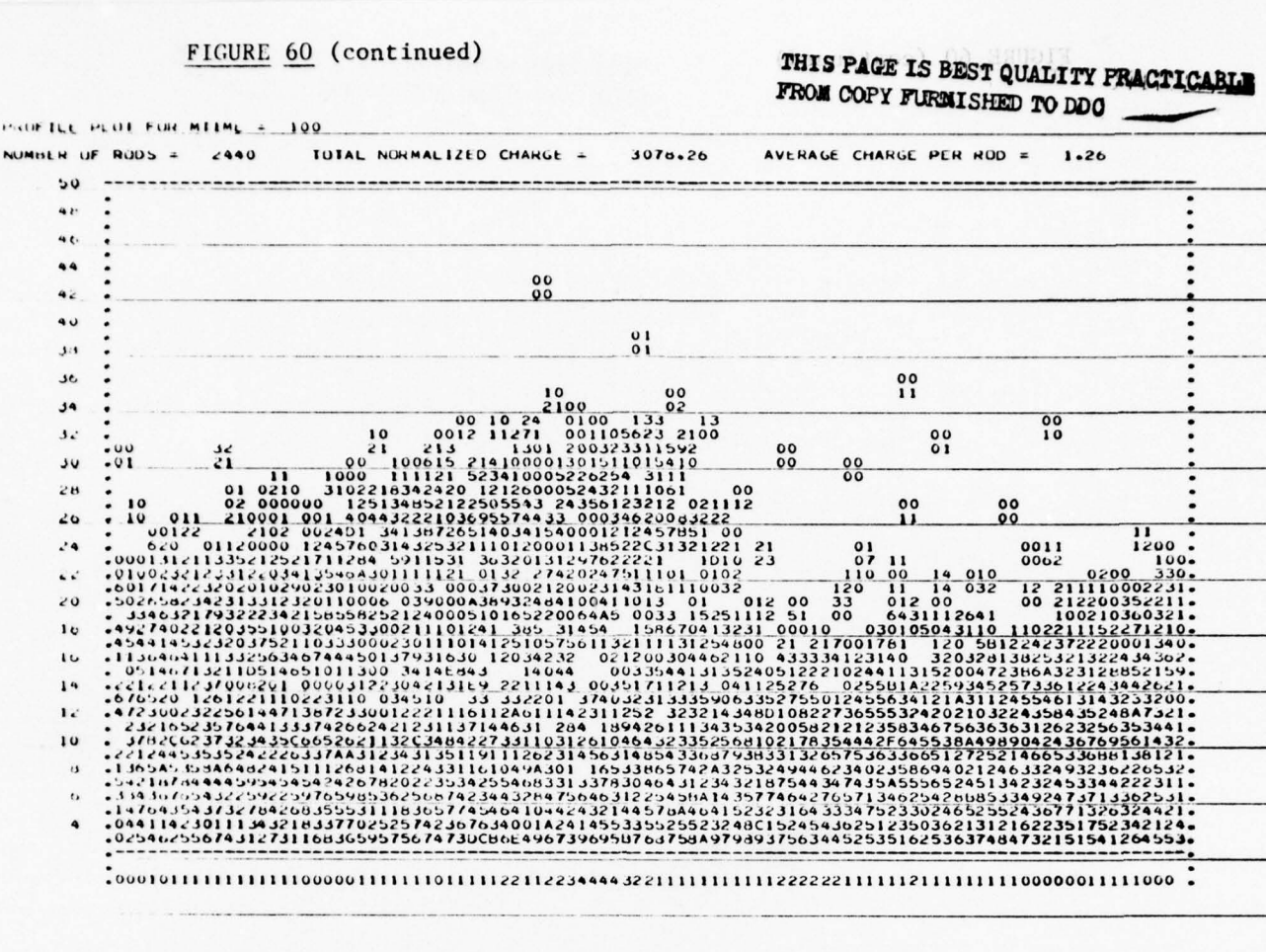

FIGURE 60 (continued)

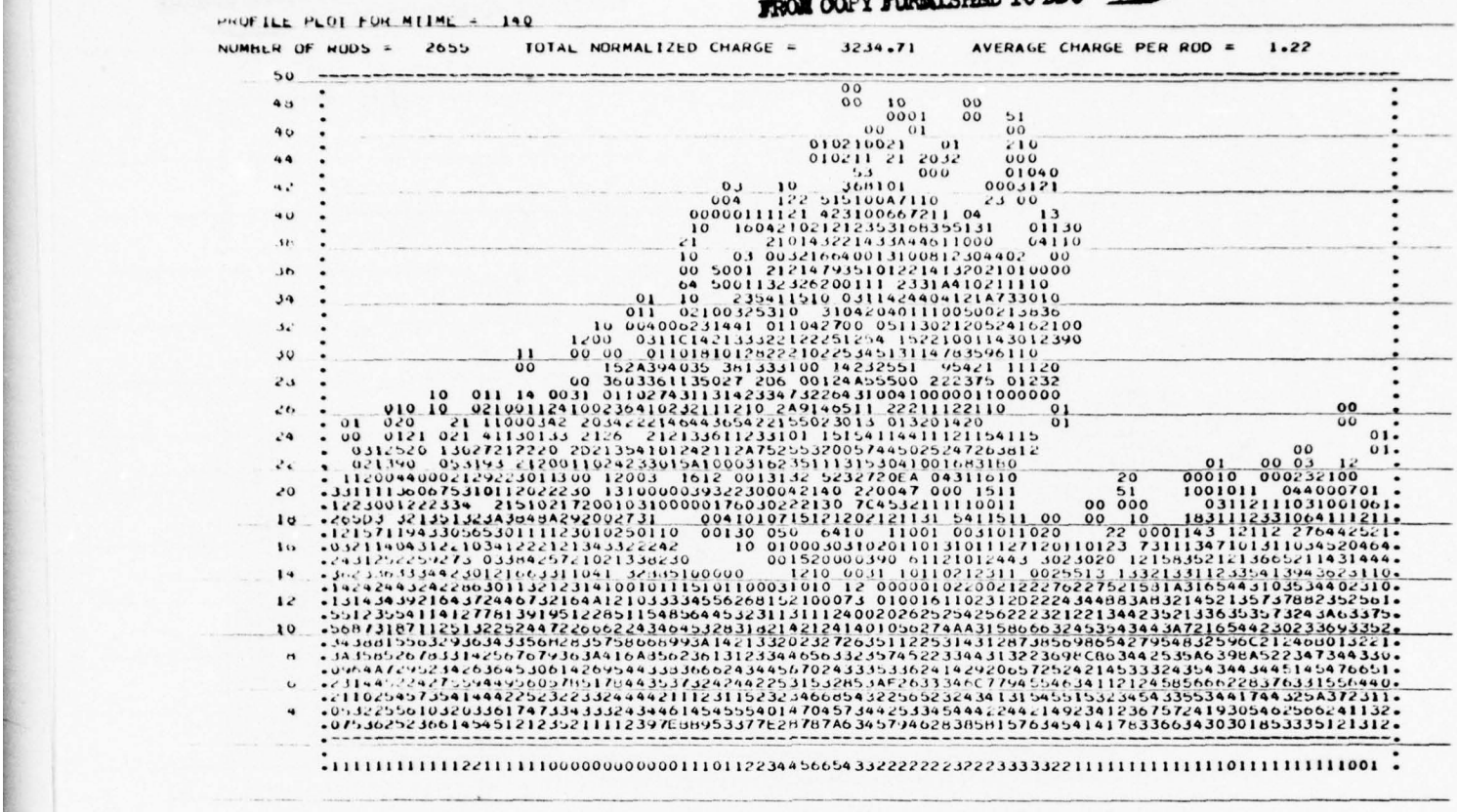

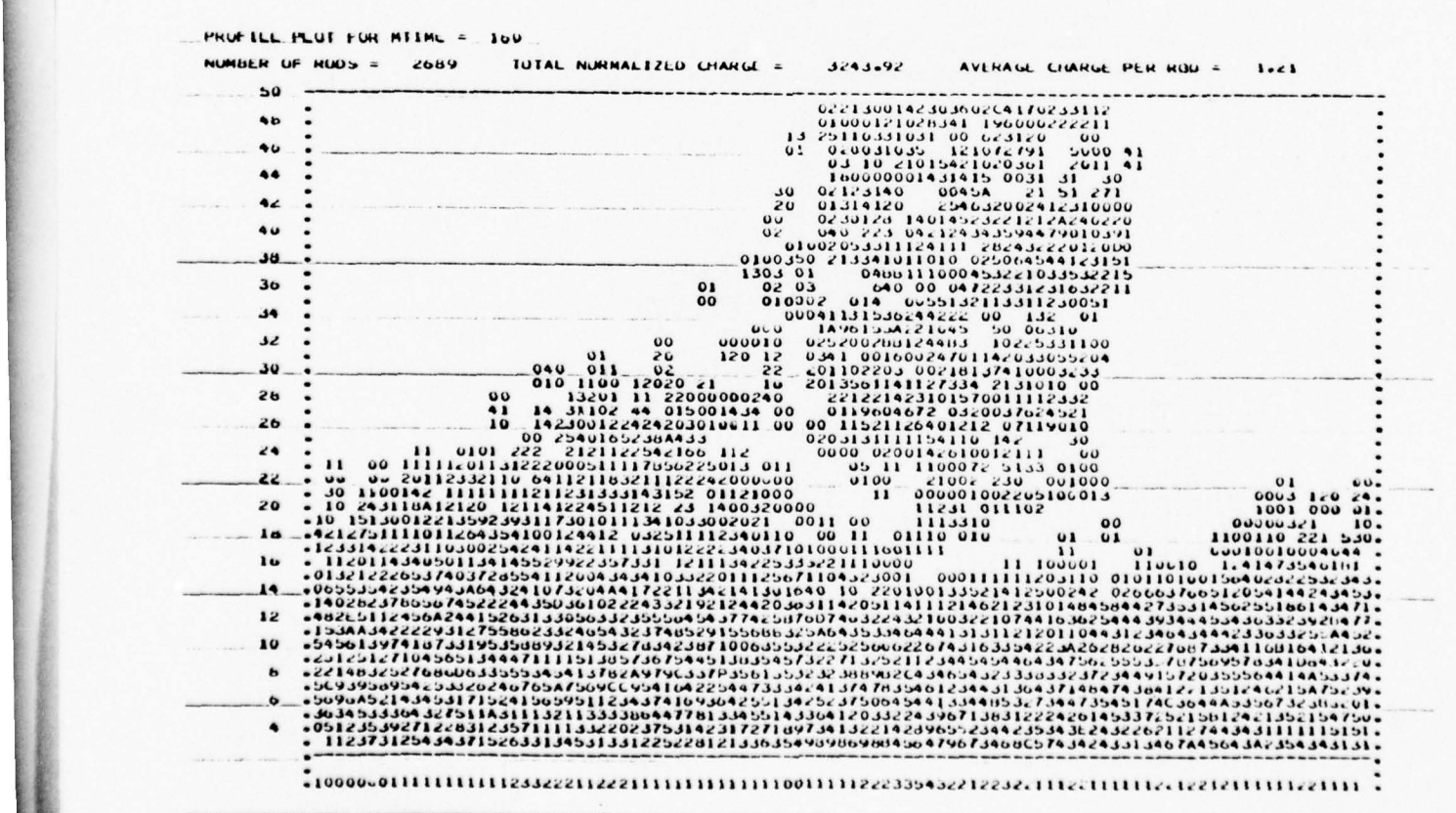

FIGURE 60 (continued)

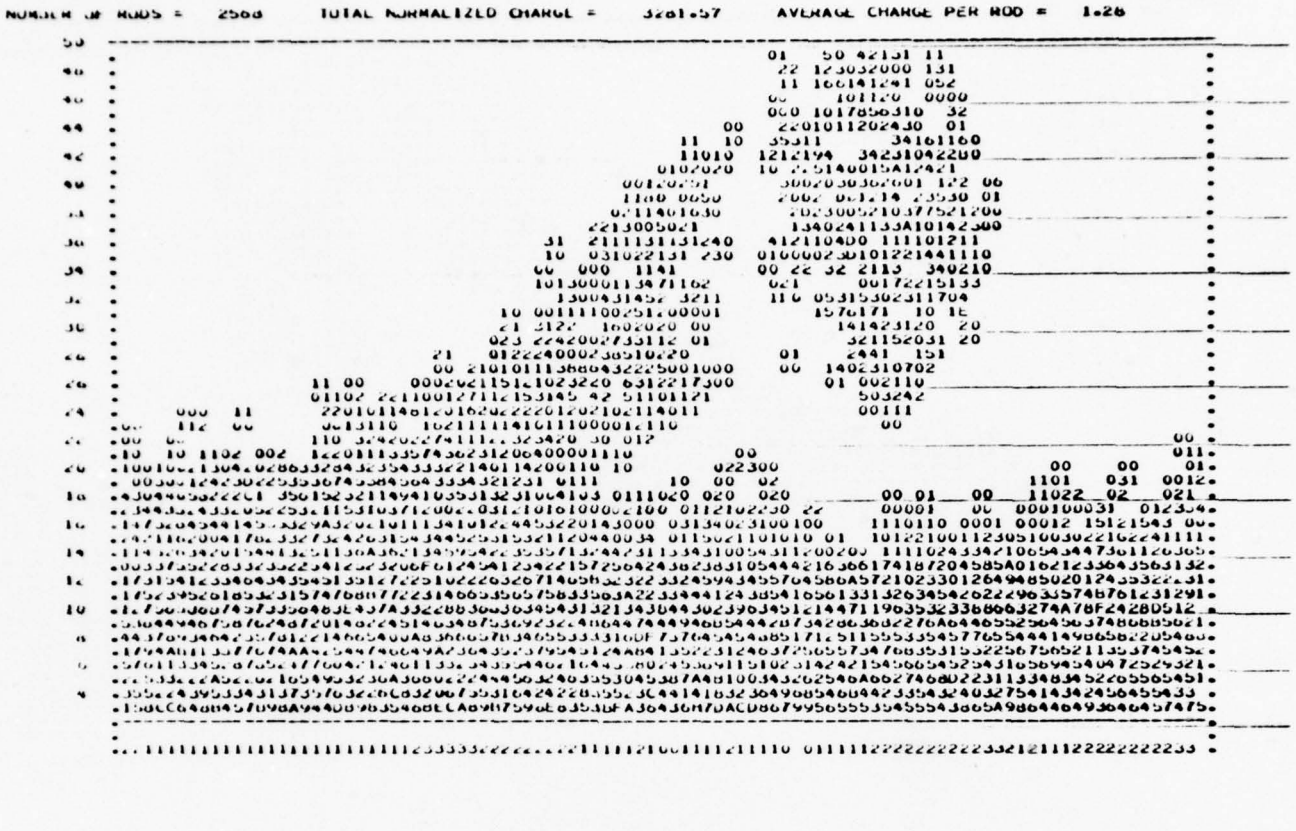

FIGURE 60 (continued)

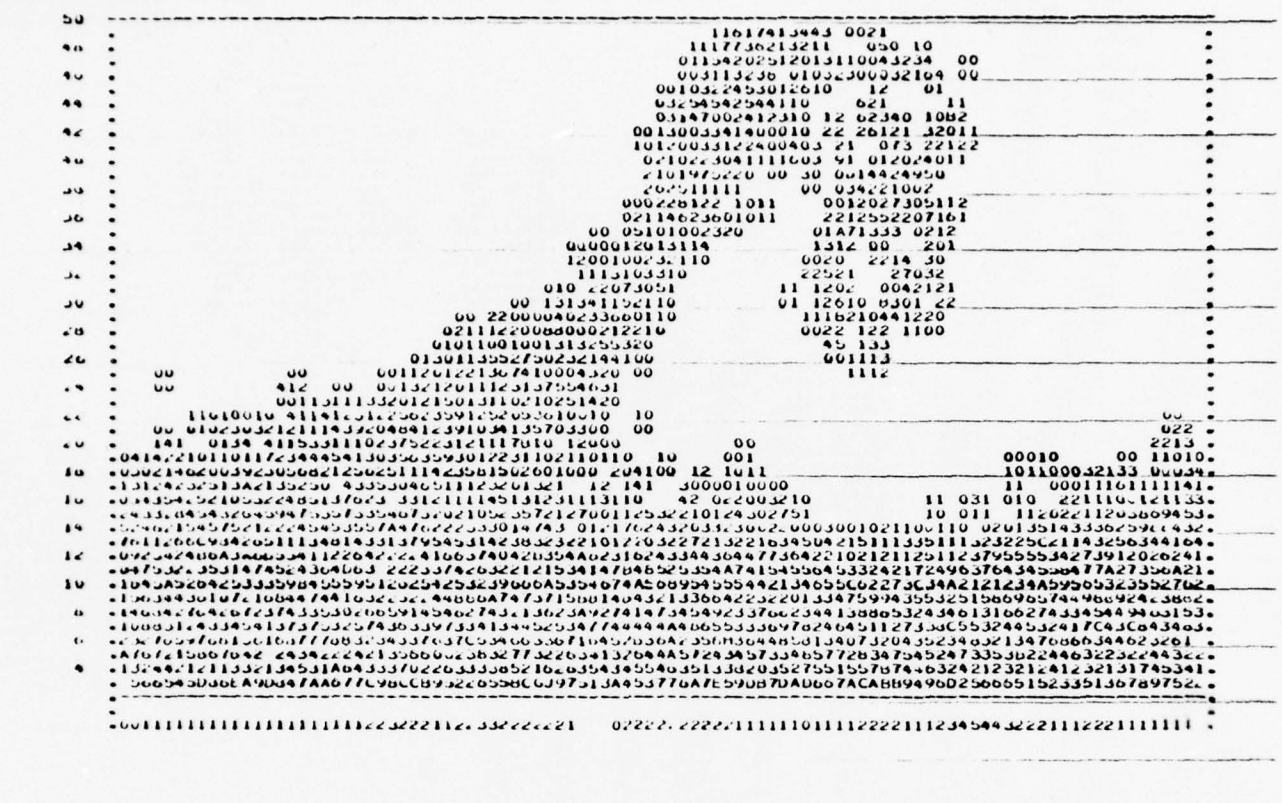

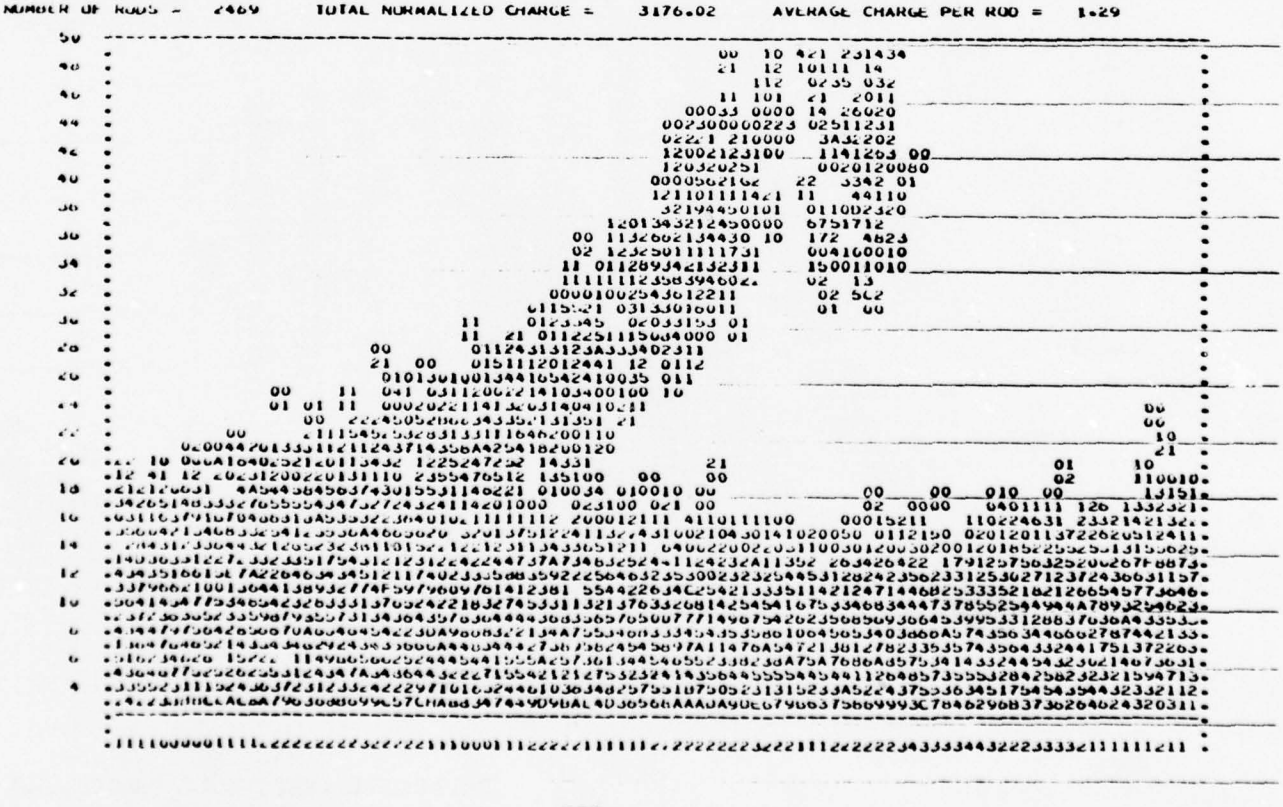

FIGURE 60 (continued)

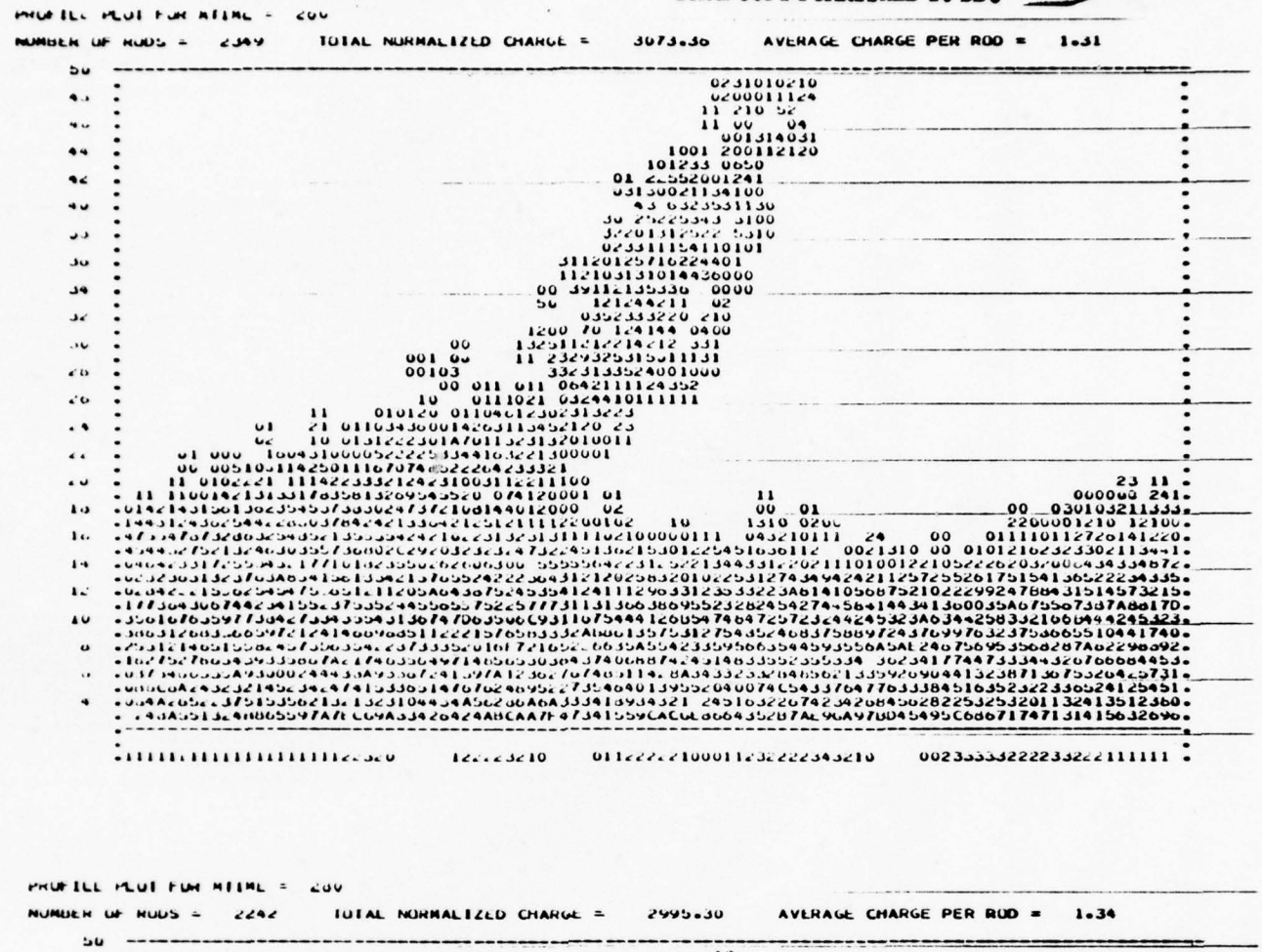

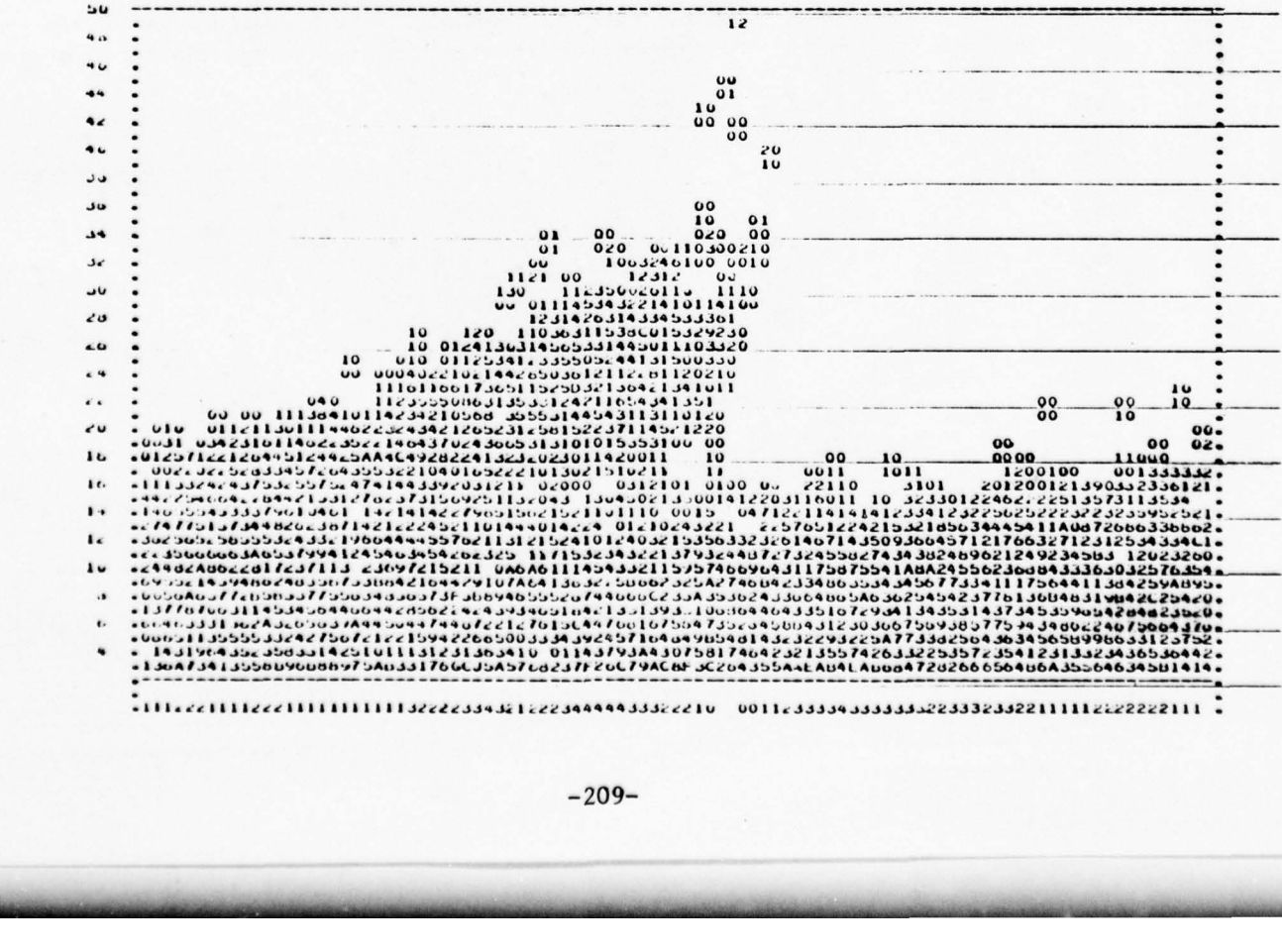

FIGURE 60 (continued)

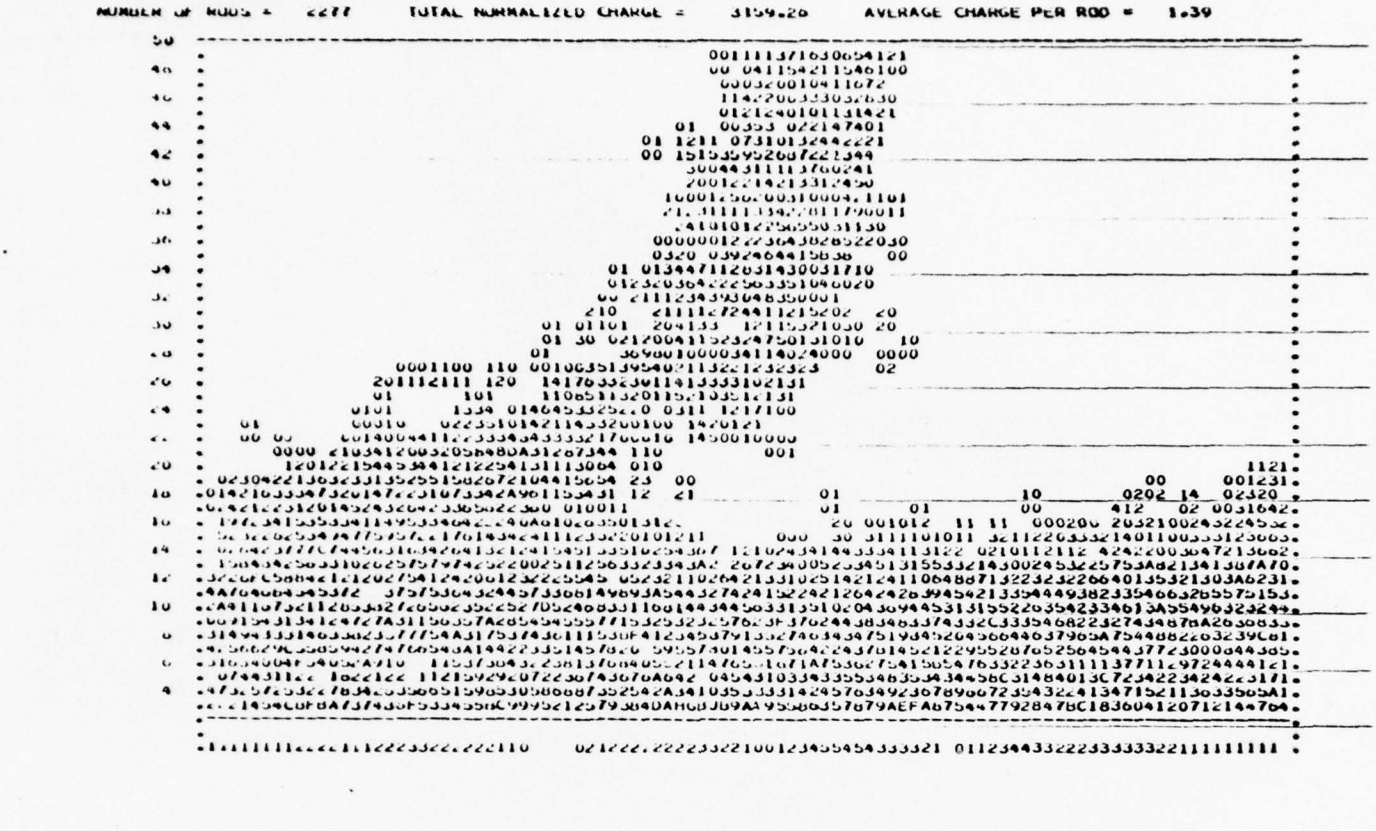

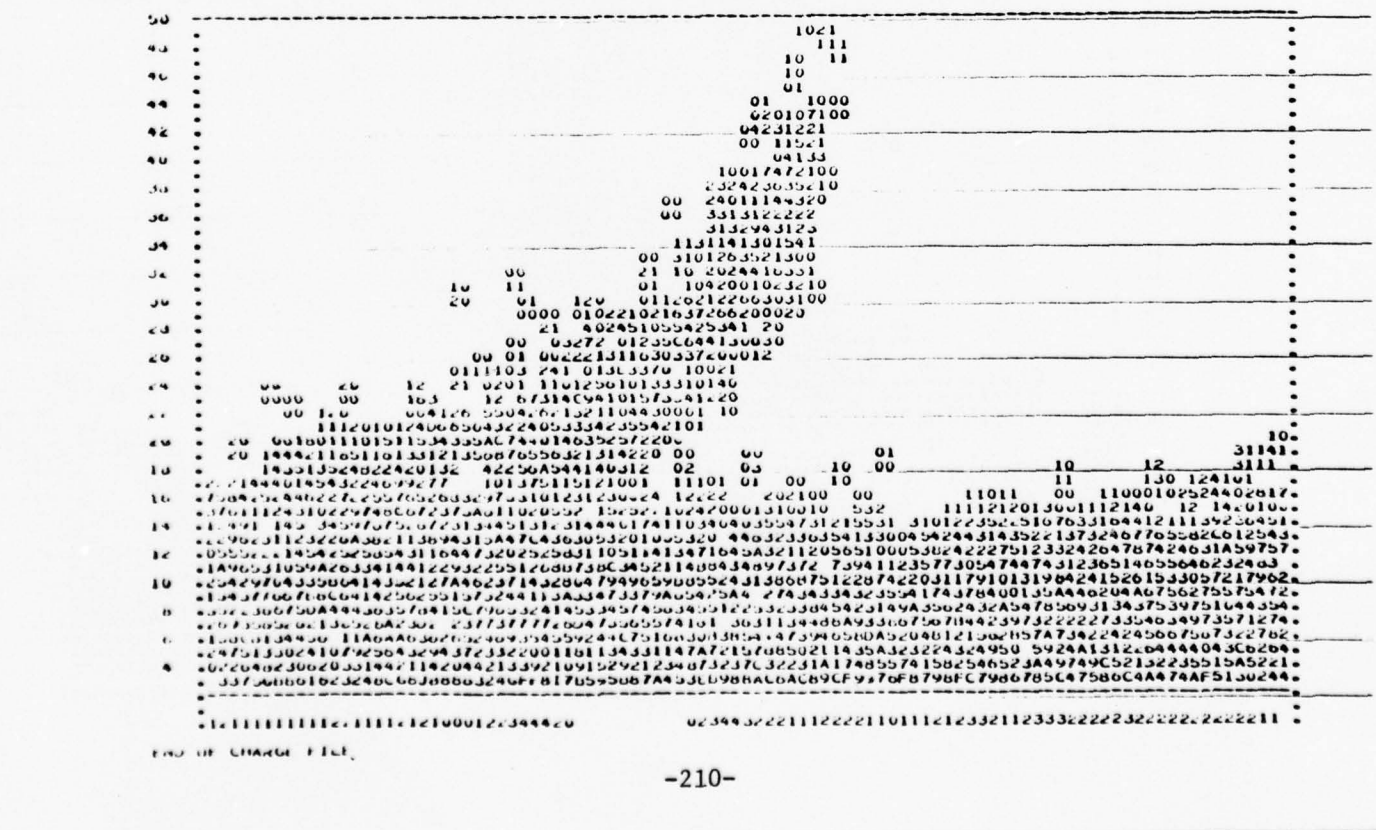

END OF CHARGE FILE

FIGURE 60 (continued)

PROFILE PLOT FOR MTIML = 340

NUMBER OF RODS = 2053 TOTAL NORMALIZED CHARGE = 3129.96 AVERAGE CHARGE PER ROD = 1.52

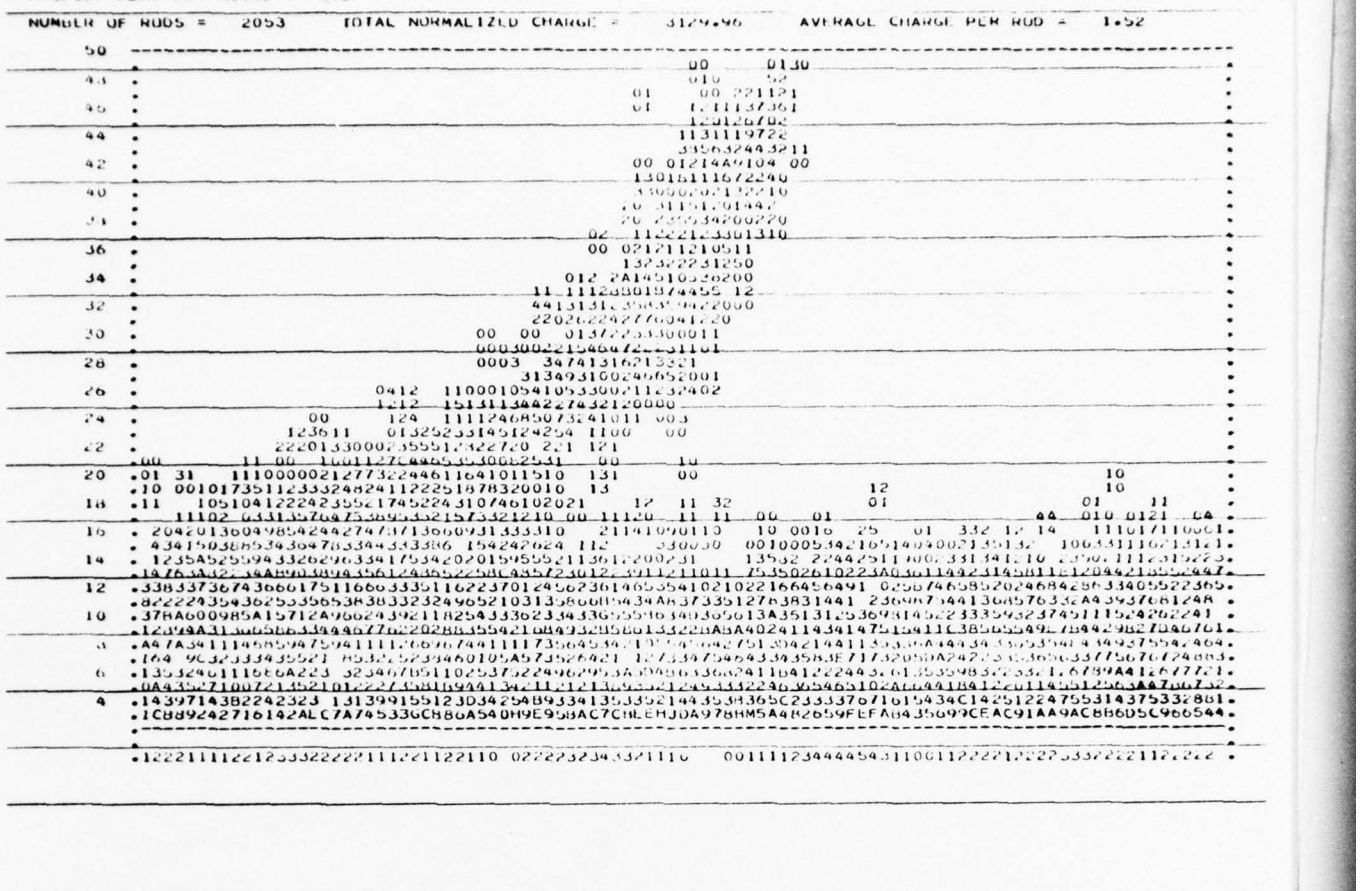

PROFILE PLOT FOR MTIML = 360

NUMBER OF RODS = 1885 TOTAL NORMALIZED CHARGE = 3039.26 AVERAGE CHARGE PER ROD = 1.61

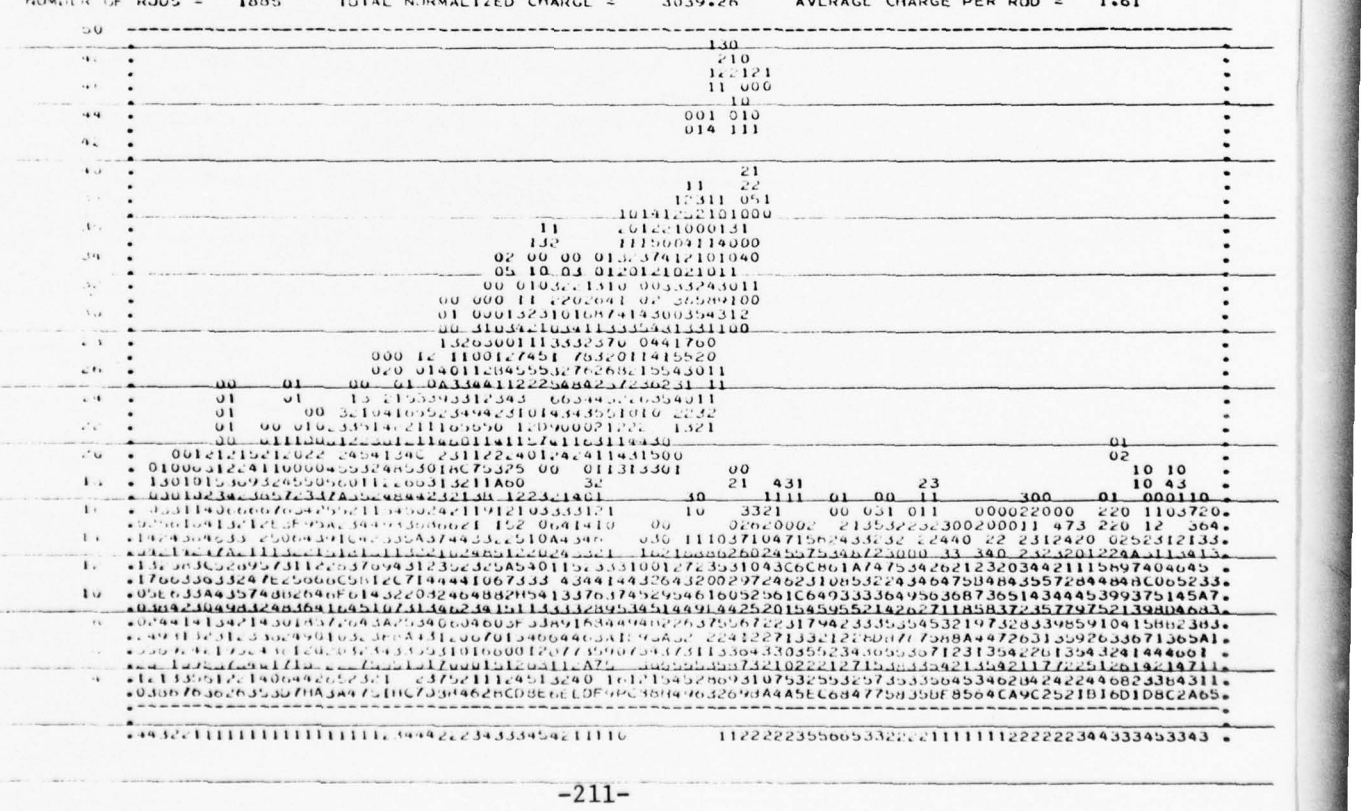

FIGURE 60 (concluded)

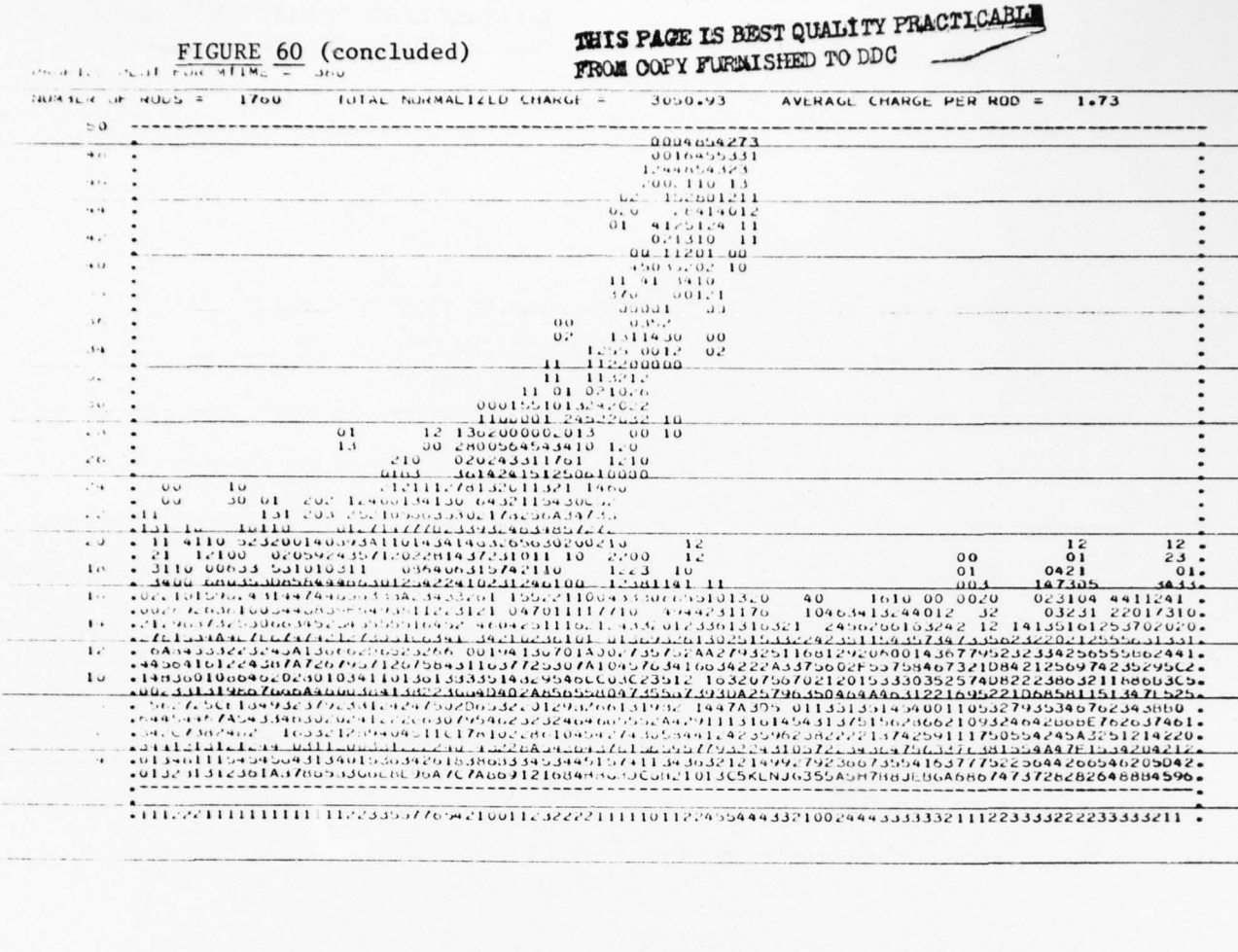

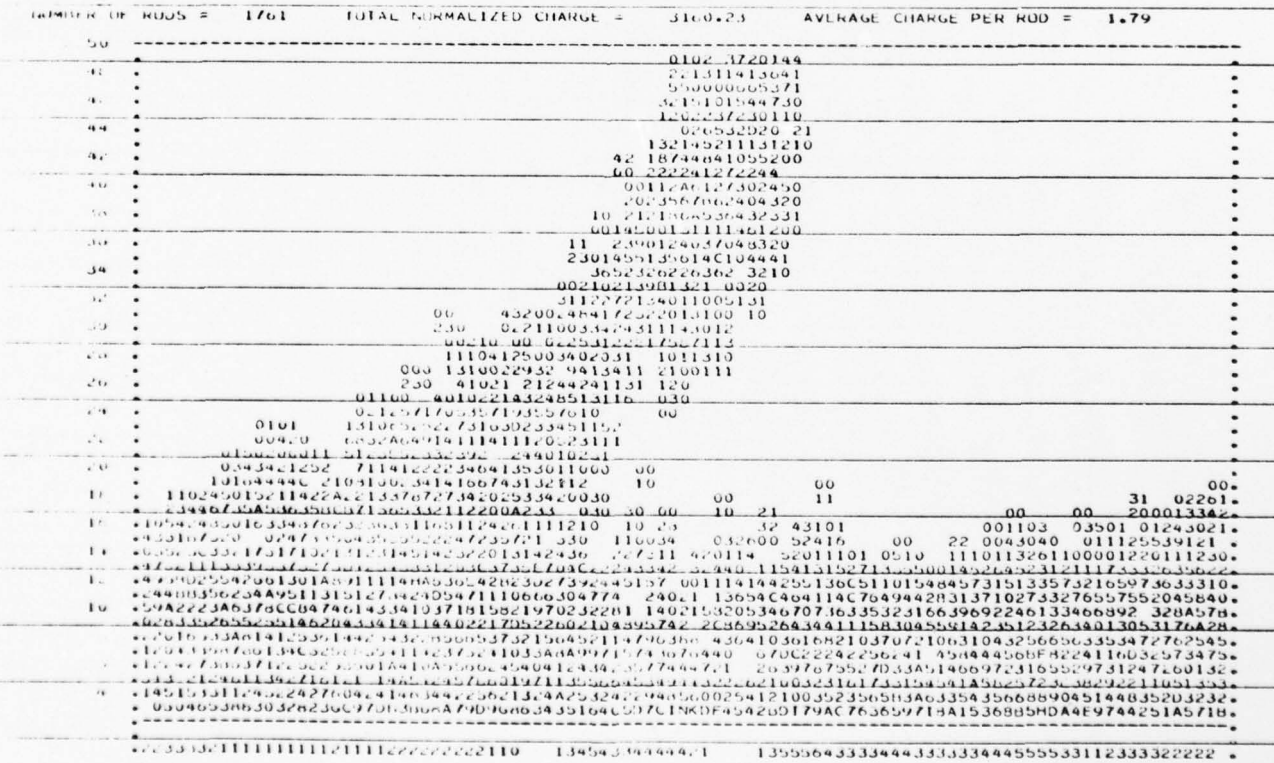

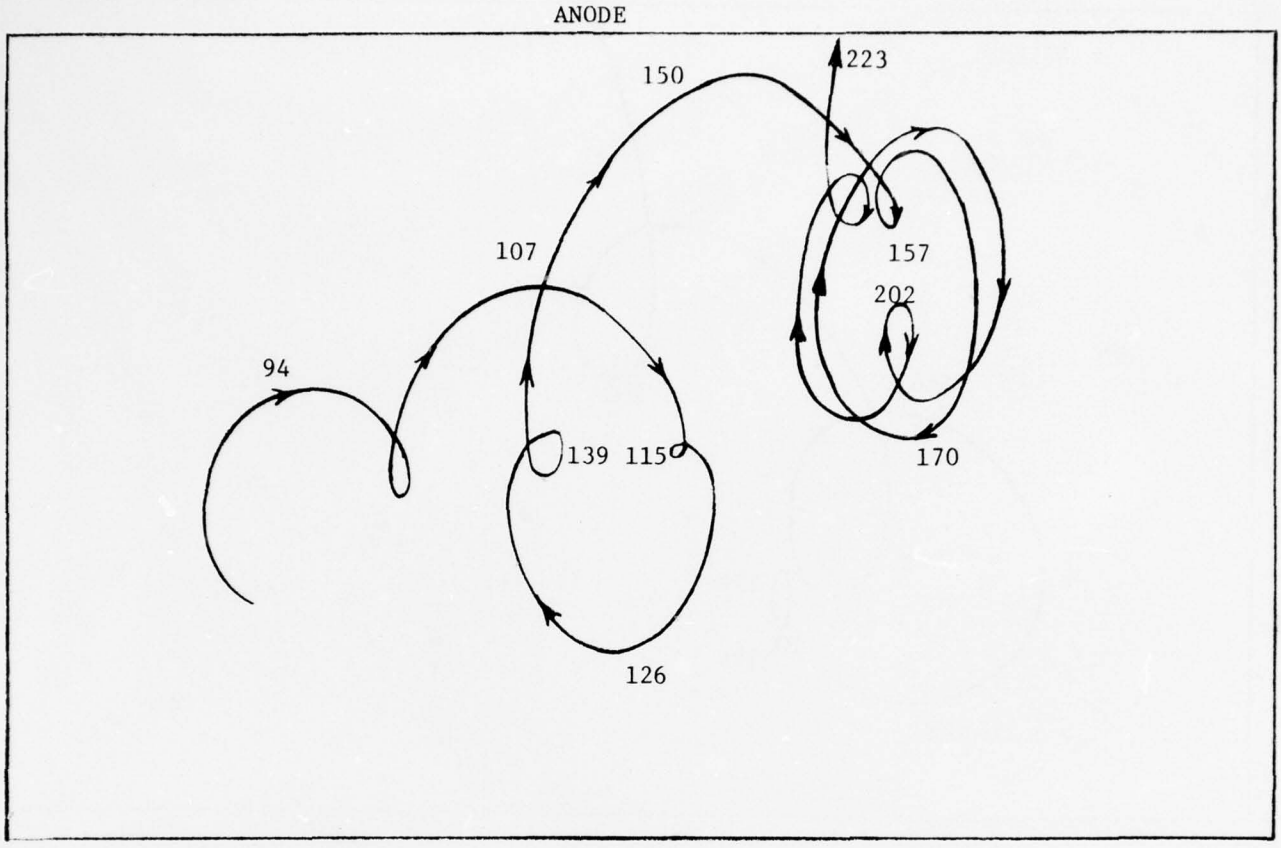

FIGURE 61A

TYPICAL TRAJECTORY IN LOW POWER REGION WHERE SPOKES ARE BROAD. Time step numbers along side trajectory correspond to time steps in Figure 60.

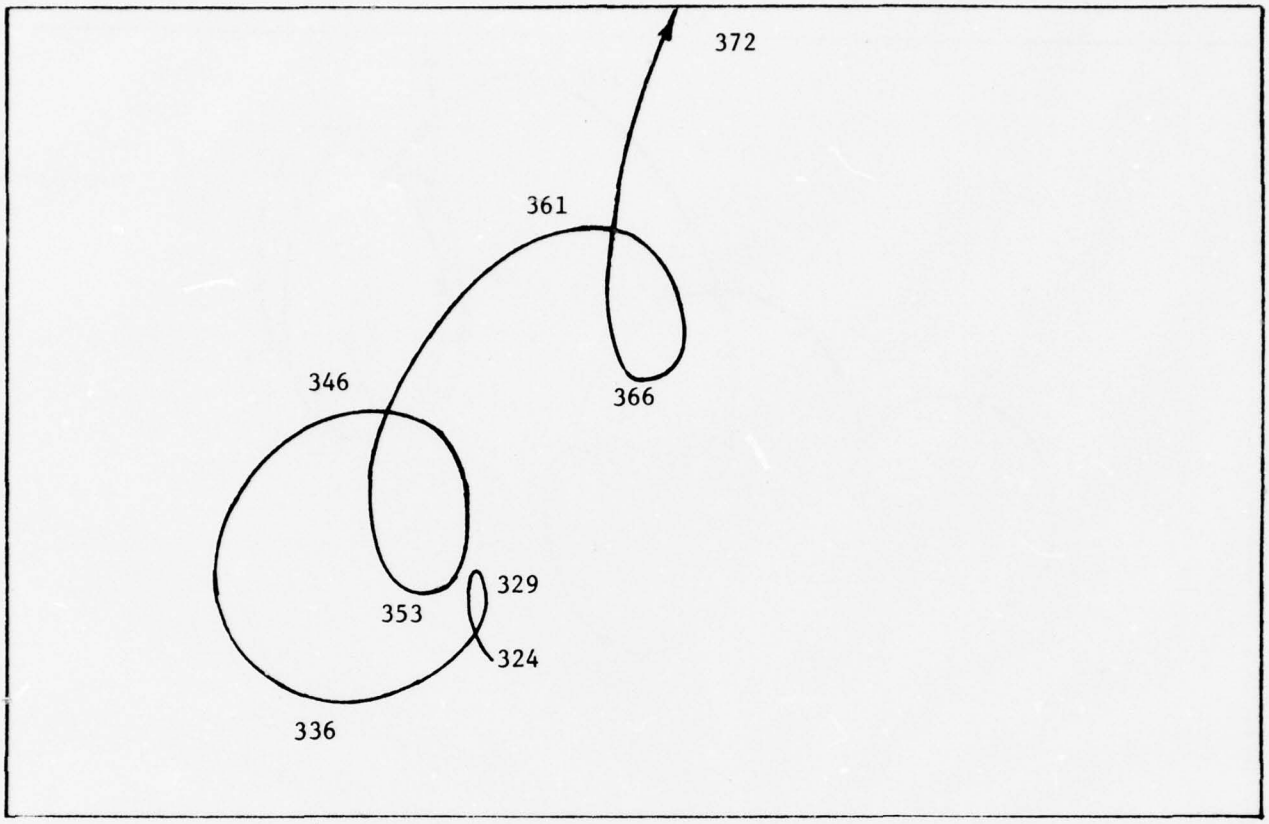

FIGURE 61B

TYPICAL TRAJECTORY IN HIGH POWER REGION WHERE SPOKES ARE WELL DEFINED. Time step numbers along side trajectory correspond to time steps in Figure 60.

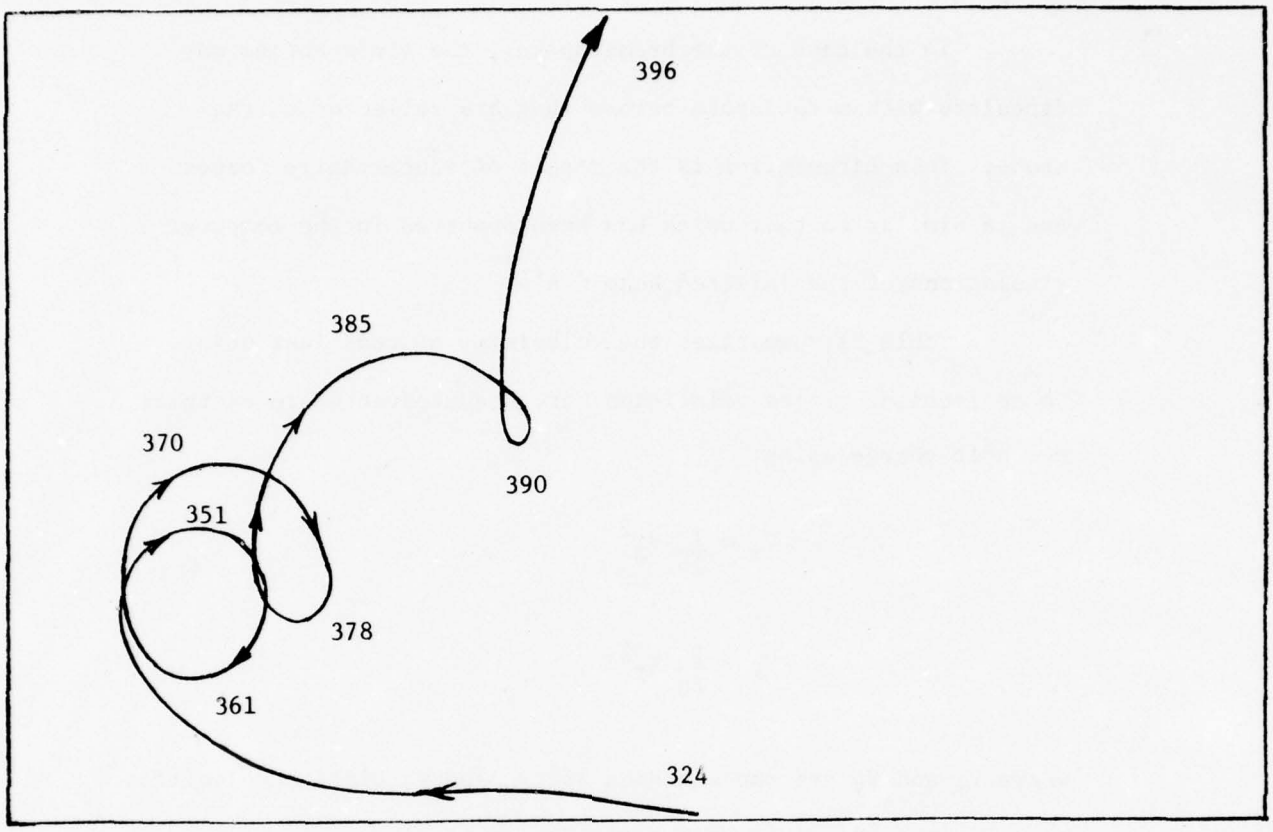

FIGURE 61C

TYPICAL TRAJECTORY IN HIGH POWER REGION WHERE SPOKES ARE WELL DEFINED. Time step numbers along side trajectory correspond to time steps in Figure 60.

In the case of the broad spokes, the trajectories may circulate within the spoke before they are collected on the anode. This circulation is the result of space charge forces and is similar to that which has been observed in the computer simulations of the injected beam CFA's.

Table XI summarizes the velocities of rods just prior to collection. These velocities have been converted to energies per unit charge using:

$$V_x = \frac{1}{2\eta} v_x^2 \qquad 4.3\text{-}1$$

$$V_y = \frac{1}{2\eta} v_y^2$$

where V_x and V_y are the energies and v_x and v_y are the velocities and η is the charge to mass ratio for an electron.

The energies have then been further expressed as a percentage of the synchronous voltage, V_o. Table XI includes summaries of the energy dissipated on the anode in the broad and narrow spoke regions. The relative ratios of the energy associated with the x and y velocities change in these regions (i.e., the angle of approach of the rods to the anode changes), but the total energy which will be dissipated is not greatly changed. Thus, the efficiency of the interaction in the region of the broad spoke is not markedly different than in the region of the well formed spoke. Thus, it does not appear to be essential to design a reentrant CFA so that the spokes are well defined at the output.

TABLE XI

AVERAGE ENERGIES OF COLLECTED RODS

COMPUTATIONS STARTING FROM UNMODULATED HUB

Case 1--V_K/V_H = 1.13	v/v_o	V/V_O
30 Steps Prior to D/D_2 = 2.52 (P/Po = 0.40)		
x directed (toward circuit)	0.36	0.13
y directed (propagation dirction)	1.59	2.52
Total Energy		2.65
30 Steps Prior to D/D_2 = 5.46 (P/Po = 1.38)		
x directed	0.73	0.54
y directed	1.26	1.58
Total Energy		2.12
Case 2--V_K/V_H = 1.3		
30 Steps Prior to D/D_2 = 4.2 (P/Po = 3.7)		
x directed	1.18	1.39
y directed	1.47	2.16
Total Energy		3.55

Figures 62 and 63 show typical distributions of the RF field along the cathode of the one wavelength interaction box. Figure 62 shows conditions near the input, and Figure 63 shows conditions near the output. Each figure shows the field distribution for a single time step and the field distribution averaged over a number of time steps. The fields for a single time step show considerable variation along the surface of the cathode. The fields at a particular location in the moving reference frame show a similar variation as shown in Figure 64. The fields in Figures 62 through 64 which have been averaged over a number of time steps are relatively smooth and vary as would be expected from the space charge distribution.

It is not known whether the field fluctuations at the cathode are representative of fluctuations which occur in the real CFA or whether they are greatly enhanced by the granularity of the simulation. The fluctuations are a property of the model and not the computer; if the same data is used and the calculation is repeated, exactly the same results are obtained for the fluctuation patterns.

The cathode field fluctuations and any consequent emitted current fluctuations do not contribute to output noise in the same manner they might in a beam tube. In the latter a sheet of charge emitted from the cathode at a given instant tends to maintain its identity in its travel through the tube. Thus, an instantaneous fluctuation in cathode current results in a fluctuation in the

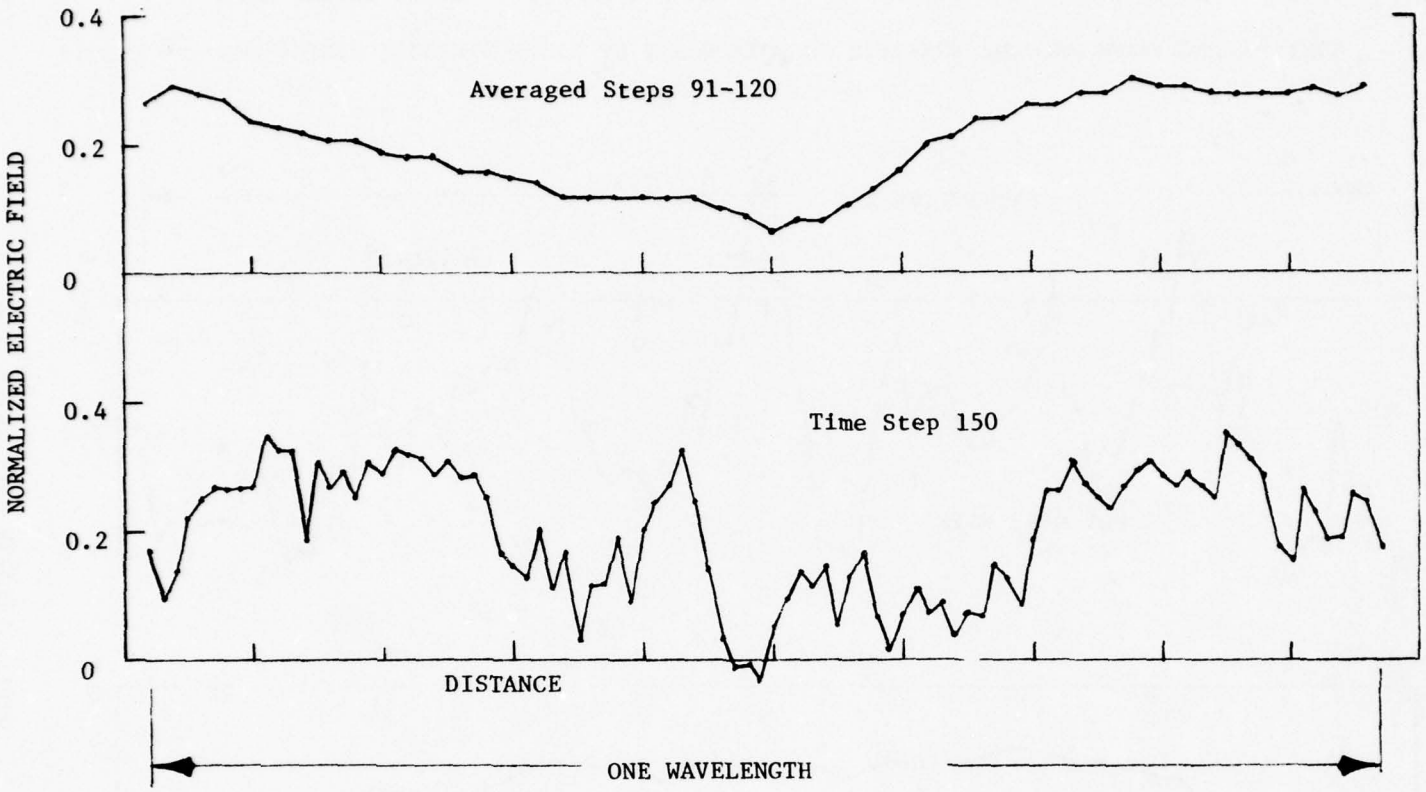

FIGURE 62--NORMALIZED ELECTRIC FIELD AS A FUNCTION OF DISTANCE FOR ONE WAVELENGTH--FIELD NEAR INPUT OF CFA. $f = f_o + 0.3$, $V_K = 1.3\ V_1$, $V_K/V_H = 1.13$. Conditions of Figure 60.

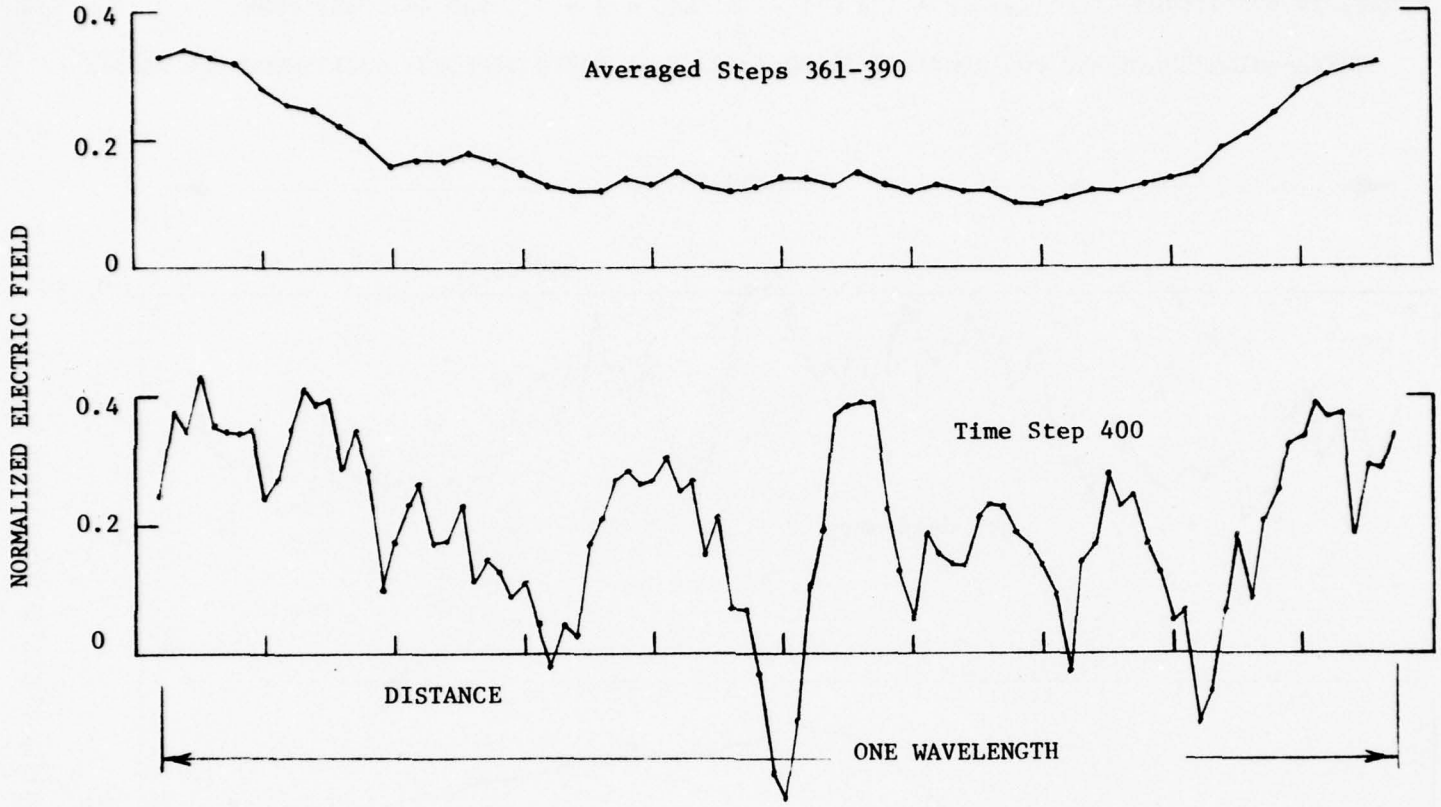

FIGURE 63--NORMALIZED ELECTRIC FIELD AS A FUNCTION OF DISTANCE FOR ONE WAVELENGTH--FIELD NEAR OUTPUT OF CFA. $f = f_o + 0.3$, $V_K = 1.3\ V_1$, $V_K/V_H = 1.13$. Conditions of Figure 60.

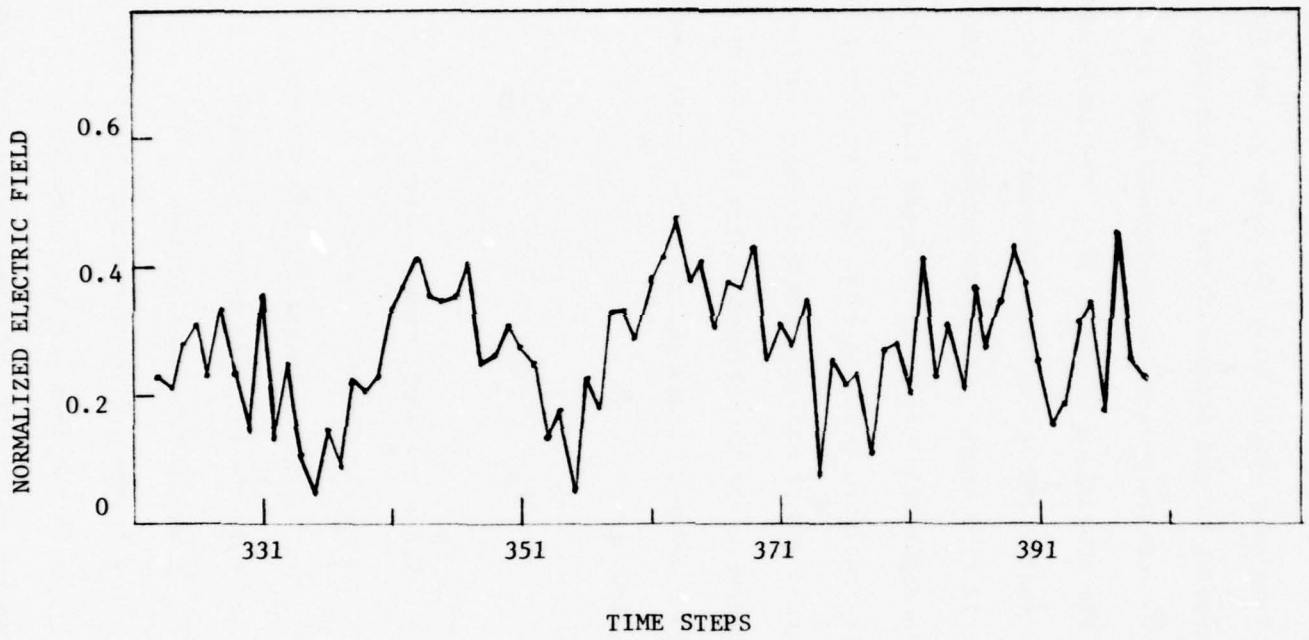

FIGURE 64--NORMALIZED ELECTRIC FIELD AT CELL 2 AS A FUNCTION OF TIME. Time steps 323-400, $f = f_o + 0.1$, $V_K = 1.3V_1$, $V_K/V_O = 1.13$. Conditions of Figure 60.

charge density reaching the output plane at a later time and a corresponding fluctuation in the RF output. In an emitting sole CFA the charge at any plane transverse to the wave velocity has originated from many points along the cathode, and there is thus some spacial averaging of the effects of the fluctuations.

The secondary emission conditions near the input and near the output are summarized in Table XII. The table gives the average bombardment energy and the average secondary emission yield over a period of 20 time steps. The distributions of bombardment energies are shown in Figure 65. It is to be noted that the bombardment energy varies relatively little from input to output (by a factor of 1.5) whereas the RF electric field strength varies by a factor of 4.5. Moreover, the bombardment energy is less than that at the input in the absence of space charge. The latter can be estimated from the following:

$$V_b = 2\pi \left(\frac{\omega}{\omega_c}\right) \sqrt{2\ PK}\ \frac{\sinh \beta y}{\sinh \beta a} \qquad 4.3\text{-}2$$

where V_b is the bombardment energy

ω is the radian frequency

ω_c is the cyclotron frequency = NB

P is the RF power on the circuit

K is the circuit impedance

y is the radius of a space charge free cycloid

a is the anode-cathode spacing.

This equation was originally obtained by the author by integrating

TABLE XII

INCIDENT ENERGY AND SECONDARY YIELD
SPACE-CHARGE LIMITED CONDITIONS

Average Incident Energy--Input	
20 steps near input (P = 0.08Po)	8.65 volts
Average Secondary Yield--Input	1.63
Average Incident Energy--Output	
20 steps near output (P = 1.4Po)	118 volts
Average Secondary Yield--Output	1.81

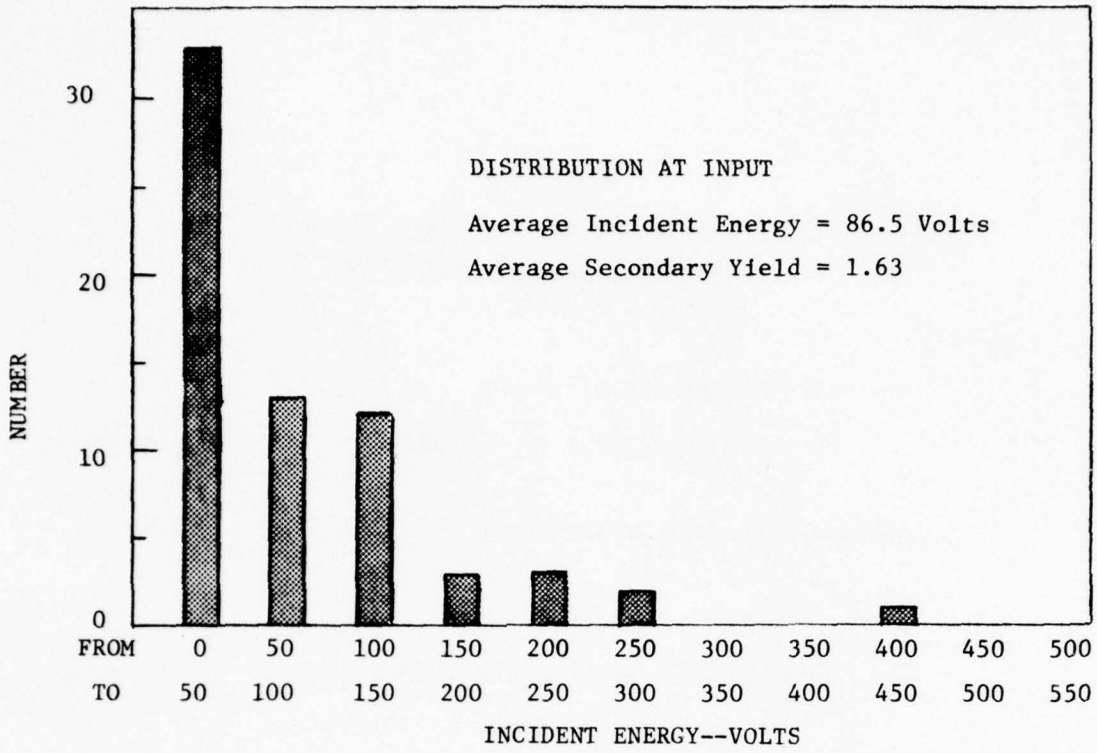

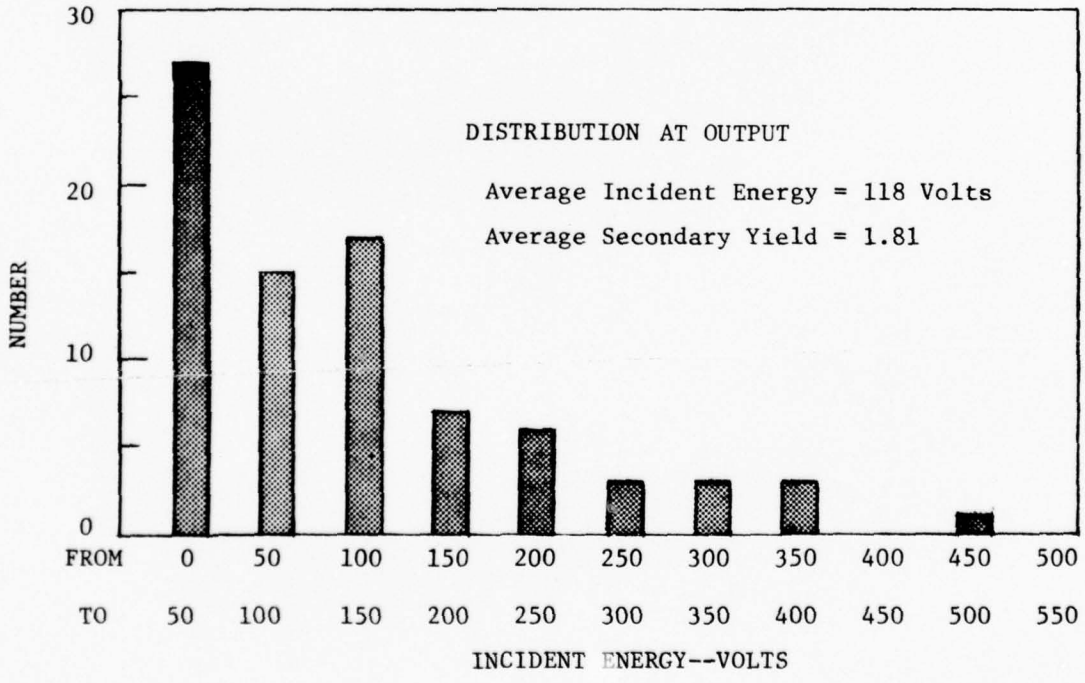

FIGURE 65--TYPICAL ENERGY DISTRIBUTIONS OF RODS INCIDENT ON CATHODE AT INPUT AND OUTPUT

TABLE XIII

INCIDENT ENERGY--SPACE CHARGE-FREE CONDITIONS--START OF CHARGE BUILD UP

RF Power = 0.08Po

Frequency	Incident Energy Equation 4.3-2	Incident Energy Computer Model
fo+0.1	513	341
fo+0.3	333	262
fo+0.5	229	197

Note that these energies are much higher than incident energy at output under space charge-limited conditions.

the RF field across the width of a cycloid at its midpoint and later derived more rigorously by Shaw.[14] For the present case it is found that this equation predicts the bombardment energy at the start of the buildup approximately. Values of measured and computed bombardment energy as obtained from this formula are compared in Table XIII.

The results of cathode bombardment suggest that because hub trajectories in the presence of space charge lie closer to the cathode than the space charge free cycloids, they see a lower RF field strength and thus gain less energy from the RF field than they do in the absence of the RF field. On the other hand, there is a component of bombardment energy which is caused by the energy exchange between rods in the hub. This is the source of cathode bombardment in the absence of RF drive as discussed in Section 4.1. The relative constancy of the bombardment energy from input to output suggests that the energy exchange within the hub which is independent of the circuit wave is the major contributor to cathode bombardment and that the energy gained from the RF wave is a lesser contributor to the bombardment. This result was unexpected, and further review of this point is necessary before it should be accepted as properly representing the situation in the real CFA.

Another newly observed phenomenom which deserves comment is the fluctuation in the charge traveling through the spoke in the high power region of the CFA as shown in Figure 60 Consideration has been given to whether these fluctuations represent

a real effect or simply a numerical instability in the computer model. It has been found that such fluctuations persist when the number of rods emitted per time step is increased from 48 to 64 and then to 96. The number of rods in the simulation increases by a factor of about 2.5 times over this range. It has also been found that the effect persists when the number of rods per step remains at 48 but the time step size is halved. Elimination of space charge smoothing at the cathode does not change it. Smoothing of the charge array by averaging every charge with the four surrounding charges--with up to four smoothing passes through the charge array--was also tried and found to have no effect on the spoke charge fluctuations. Finally, it has been found that the effect is also present when uniform thermionic emission and no secondary emission is assumed. It is our present belief that the spoke charge fluctuations are probably a real effect. These fluctuations have a significant effect on the pass-to-pass variations as will be discussed in Section 4.4.

Physically the spoke charge fluctuations appear to result from an instability at the base of the spokes. As rods pass underneath, the base of a spoke at branch point is reached where the rod either enters the spoke or returns to the hub. How this branch is taken may depend critically on the total x directed field. Thus, for example, consider a trajectory in the moving frame of reference as shown in Figure 66. If the rod velocity at the top of a cycloid is less than the local E_x/B, where E_x is the sum of the d.c., RF and space charge fields, there will be a net upward force on the rod, and it will proceed along the upper branch of

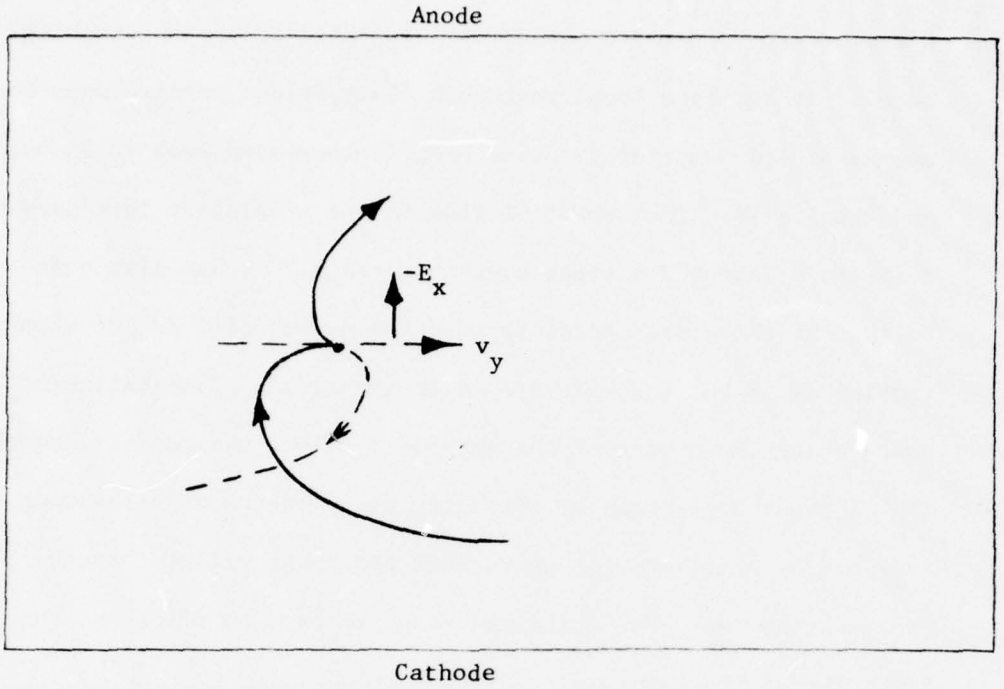

FIGURE 66

POSTULATED MECHANISM FOR INSTABILITY AT THE BASE OF THE SPOKE. Trajectory reaching top of a trajectory loop can either go upward (solid curve) or downward (dotted curve) depending on whether $-E_X$ is greater or less than Bv_y. Small changes in E_x can, therefore, make a large change in current drawn into a spoke.

the trajectory. If the rod velocity is greater than the local E_x/B velocity, the net force will be downward, and the rod will return to the hub along the lower branch in Figure . Thus, small changes in the local E_x can appreciably change the amount of charge entering a spoke.

It is postulated that the fluctuation in charge flowing through the spoke is a result of space charge fields affecting the amount of current entering the base of the spoke. Thus, a group of charges moving through the spoke produces a field at the base of the spoke which lowers the E_x in this region and shuts off entry of further charge into the spoke. Once the group of charges has reached the anode and been collected, E_x at the base of the spoke increases, and a new group of charges starts through the spoke.

The first rarification of charge in the spoke always starts immediately after the spoke has shrunk to a narrow width and the circulation of spoke charge shown in Figure 60 has stopped. Apparently charge is drawn to the anode faster than it can be supplied into the base of the spoke. This rarification is immediately followed by a group of charges entering the spoke, and the fluctuations described above begin.

4.3.2 Effect of Increasing the Cathode Voltage

Increasing the cathode voltage causes an increase in the E_x field at the base of the spoke and draws additional current into the spokes. As a consequence the current increases rapidly as a function of voltage and the typical "flat" V-I curve of a CFA or magnetron is obtained. Figure 67 shows how the power growth varies with distance as the ratio of cathode to Hartree voltage (V_K/V_H ratio) is increased. The lowest V/V_H ratio in Figure 67 represents the case discussed in the last section. As the V/V_H ratio is increased up to 1.3, the spokes remain stable, although in the broad spoke region they move further forward in the interaction box. Figure 68 shows charge profile plots at the input of approximately the greatest forward position of the spoke. The charge distribution has almost moved to the forward quadrature phase location in these plots.

As the voltage and power increase, the energy of collected electrons increases and efficiency decreases. The energy associated with both x and y directed velocities increases. The y (longitudinal) of velocity is increased because of the increase in average E/B velocity resulting from the increase in cathode voltage. The x (transverse) velocity is increased because of the higher RF fields which cause the E_x/B drift velocity toward the anode to increase. Table XI summarizes the rod energies just prior to collection at the output for lowest and highest voltage of Figure 67. Figure 68 provides a V-I curve for these three runs. Efficiencies are shown beside the

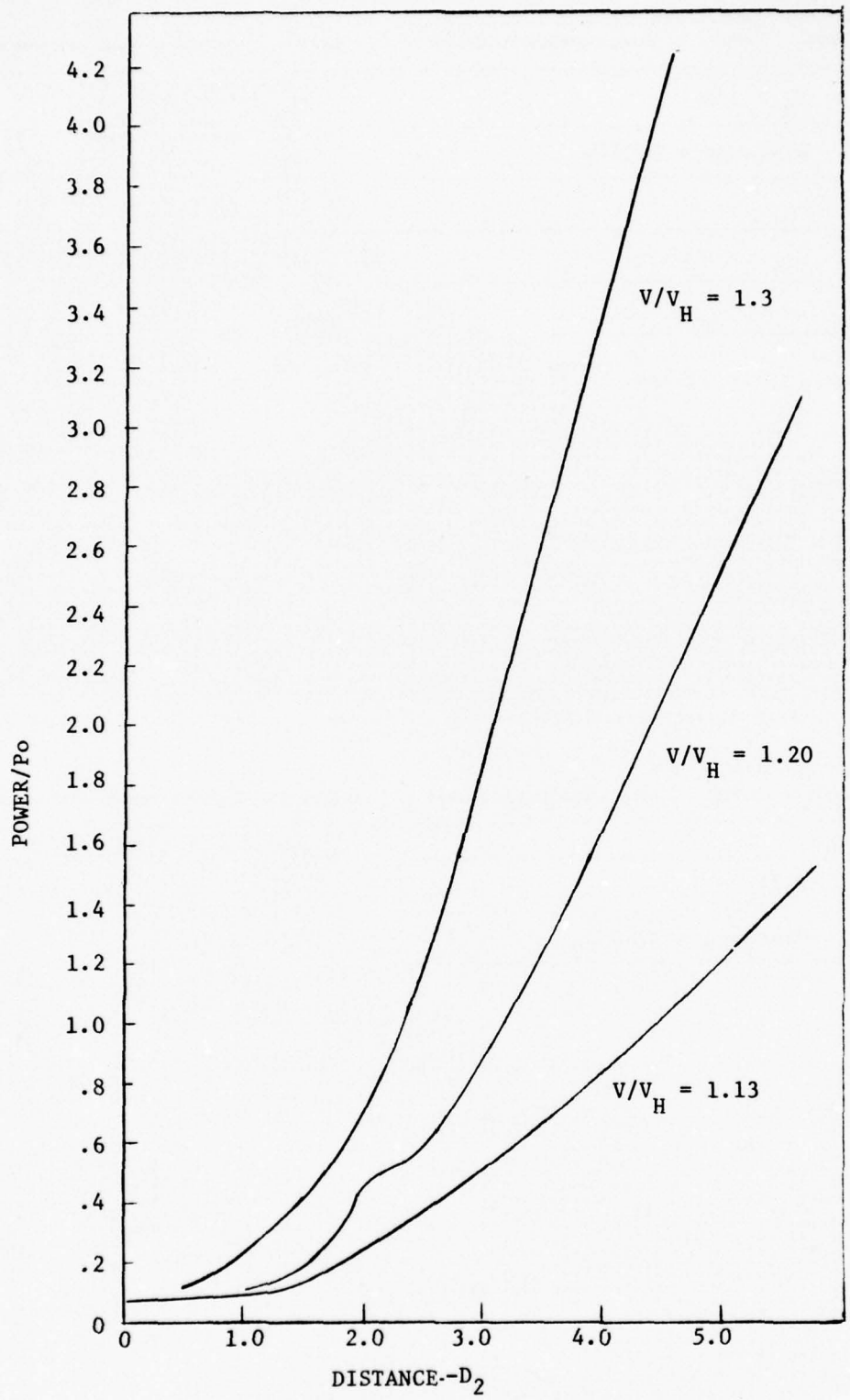

FIGURE 67

PEAK POWER AS A FUNCTION OF DISTANCE FOR CALCULATIONS STARTING FROM AN UNMODULATED HUB--DIFFERENT CATHODE VOLTAGES.

$f = f_o + 0.3$, $P_{in} = 0.08$ Po

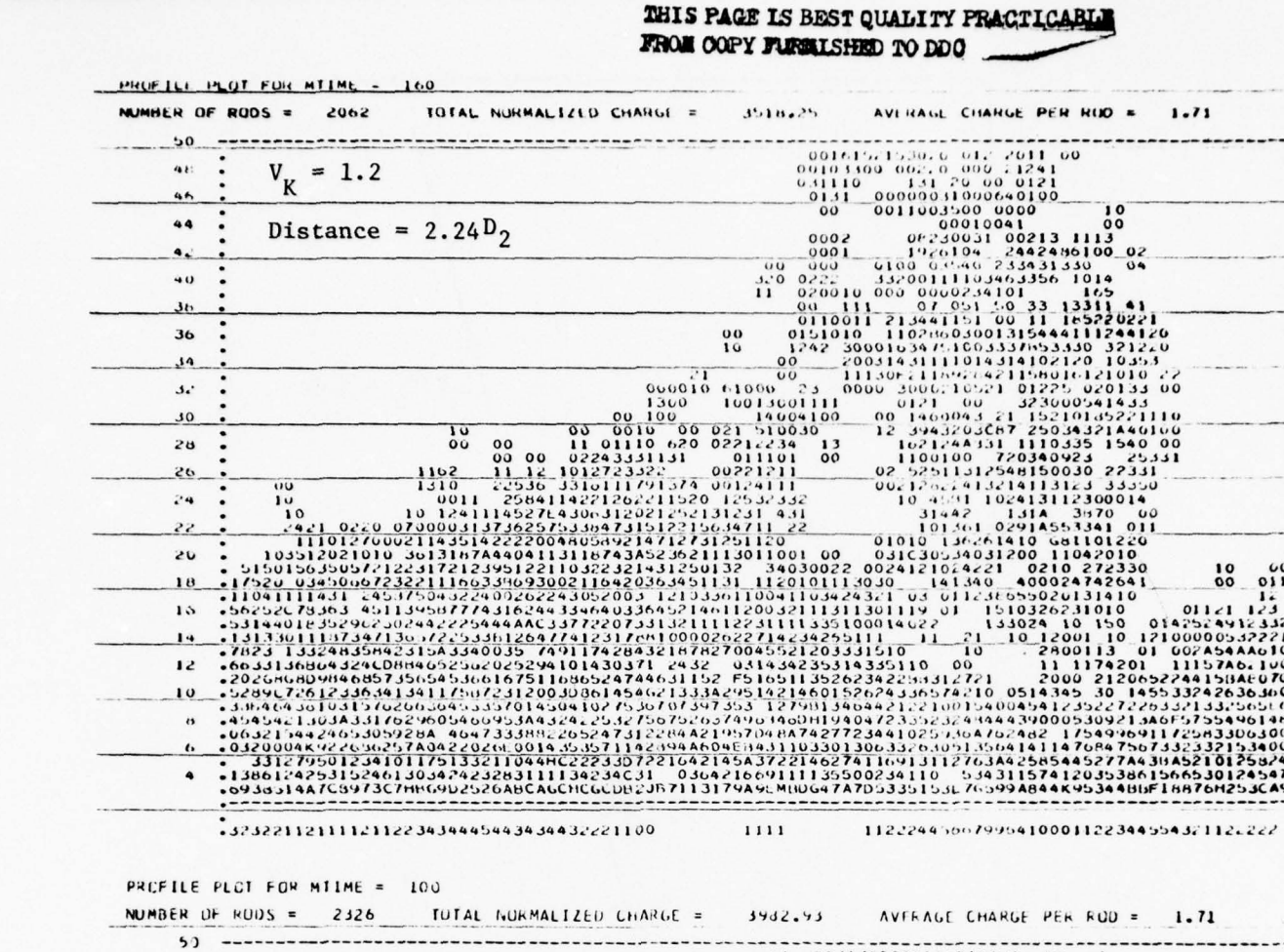

FIGURE 68--CHARGE PROFILES FOR V_K/V_H = 1.2 (top) and 1.3 (bottom) FOR COMPUTATION OF FIGURE 67 AT LOCATIONS WHERE CHARGE BUNCH IS AT APPROXIMATELY ITS FURTHEST POINT FORWARD IN THE INTERACTION BOX.

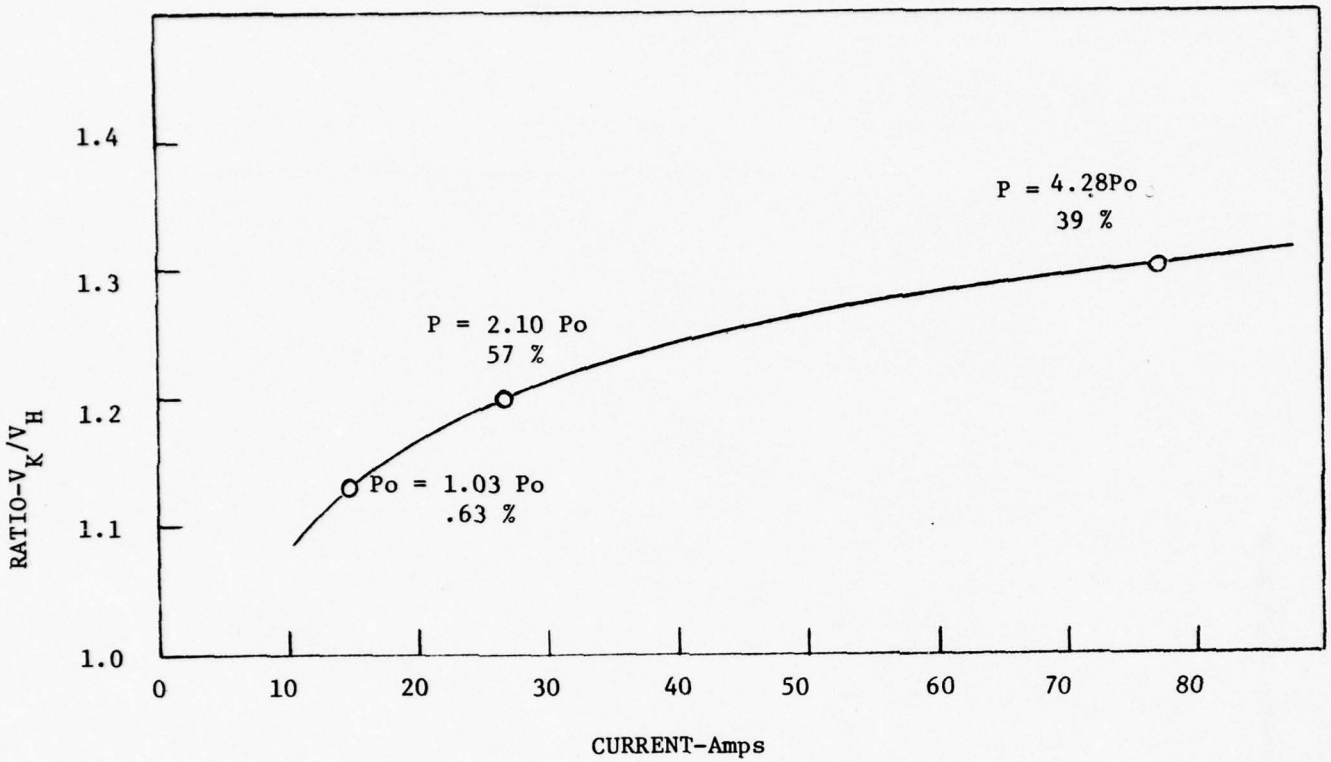

FIGURE 69

COMPUTED V-I CURVE FOR THE COMPUTATION STARTING FROM AN UNMODULATED HUB. Powers and efficiencies are shown adjacent to the experimental points. $D = 4.52D_1$

calculated points. This type of behavior with a very flat V-I curve and decreasing efficiency at high currents is typical of CFA's. The essential nature of this behavoir appears to be properly modeled by the computer program.

4.3.3 Effect of Increasing Frequency

A series of runs similar to those discussed in the last section were made with the frequency increased to the top edge of the operating band. The input conditions were as presented in Table V except that the voltage was increased in steps and a previously generated hub was used as the input rod population. The results of these calculations are shown in Figure 70. The power increased with increasing voltage except at the highest voltage. Here we finally reached a point where the broad spoke near the input cannot be contained by the RF fields and moves forward into the unfavorable phase. Figure 71 shows charge profile plots for this region of the calculation.

A comparison of the power growth curves for the midband and high frequency case is given in Figure 72. These curves are plotted for approximately the same ratio of cathode to Hartree voltage. The power gorwth is considerably more rapid at midband. The ratio of power at midband to power at the high frequency for $D = 5D_1$ is 1.76. A ratio of only 1.26 would be expected from the characteristic current difference ($\simeq V_o^{3/2}$). The higher ratio apparently results from the difference in interaction impedance and the more rapid RF field decay away from the anode in the high frequency case.

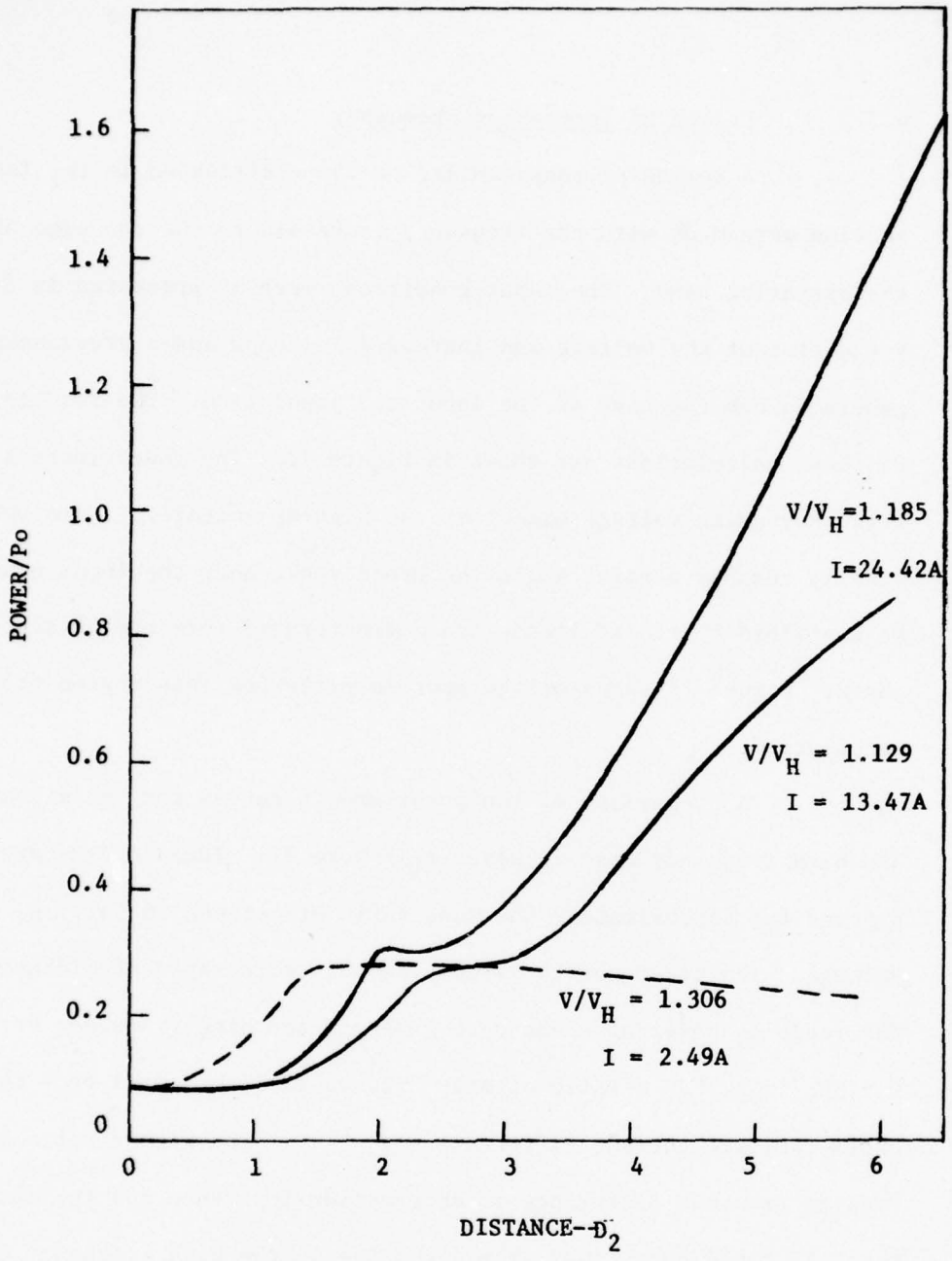

FIGURE 70

PEAK POWER AS A FUNCTION OF DISTANCE FOR CALCULATIONS STARTING FROM AN UNMODULATED HUB--DIFFERENT CATHODE VOLTAGES AT UPPER BAND EDGE. $F = f_o + 0.5$, $P_{in} = 0.08$ Po. Note vertical scale difference relative to Figure 67.

FIGURE 71

CHARGE PROFILE PLOTS FOR CALCULATION STARTING FROM UNMODULATED HUB AT THE UPPER END OF THE VAND WITH V_K/V_H = 1.3. These plots cover the region from 0.78 to 1.81 inches in Figure 70. Plots are presented for every 20 time steps of the calculation. These plots show the center of the charge distribution moving toward a position leading the wave by about 90 degrees. From step 140 on the charge distribution remains approximately the same. As shown in Figure 70, this condition does not result in power growth.

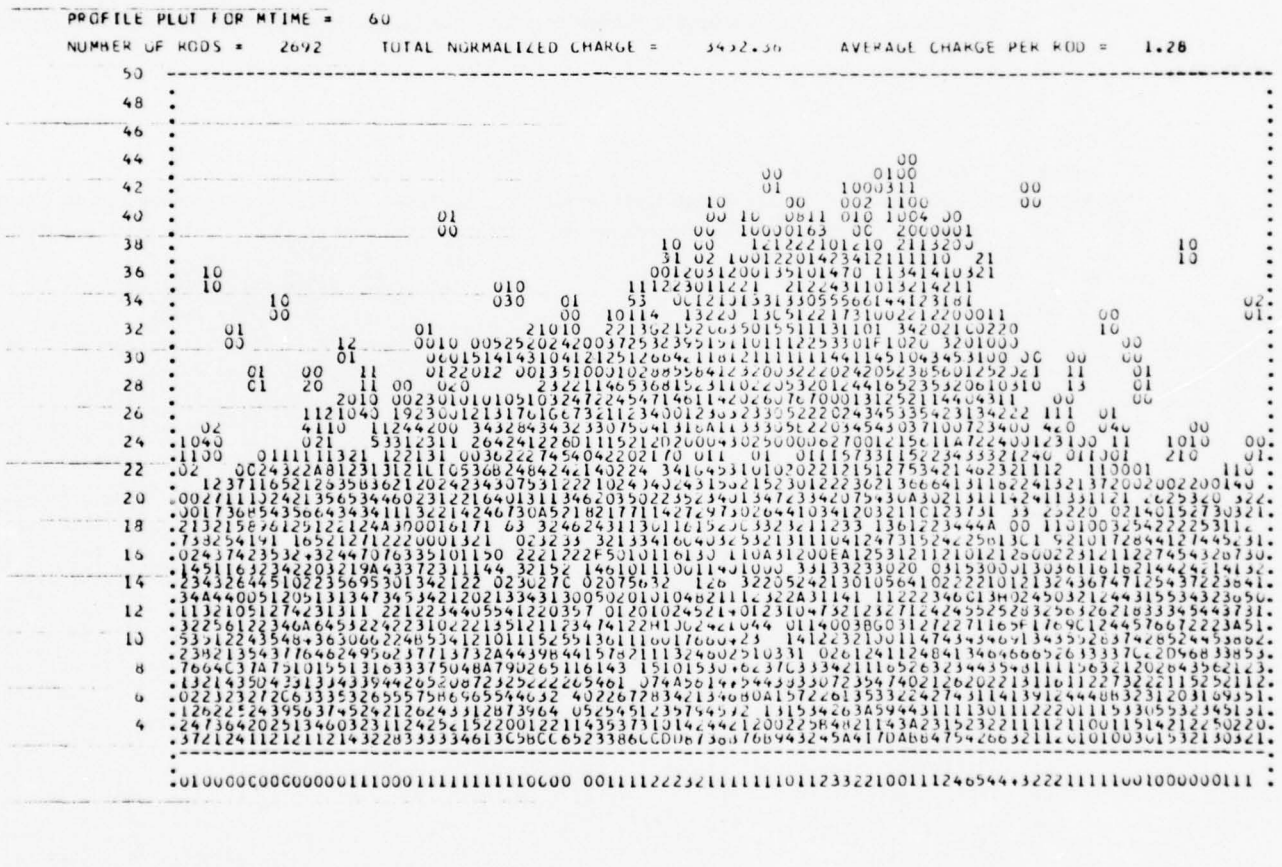

FIGURE 71 (continued)

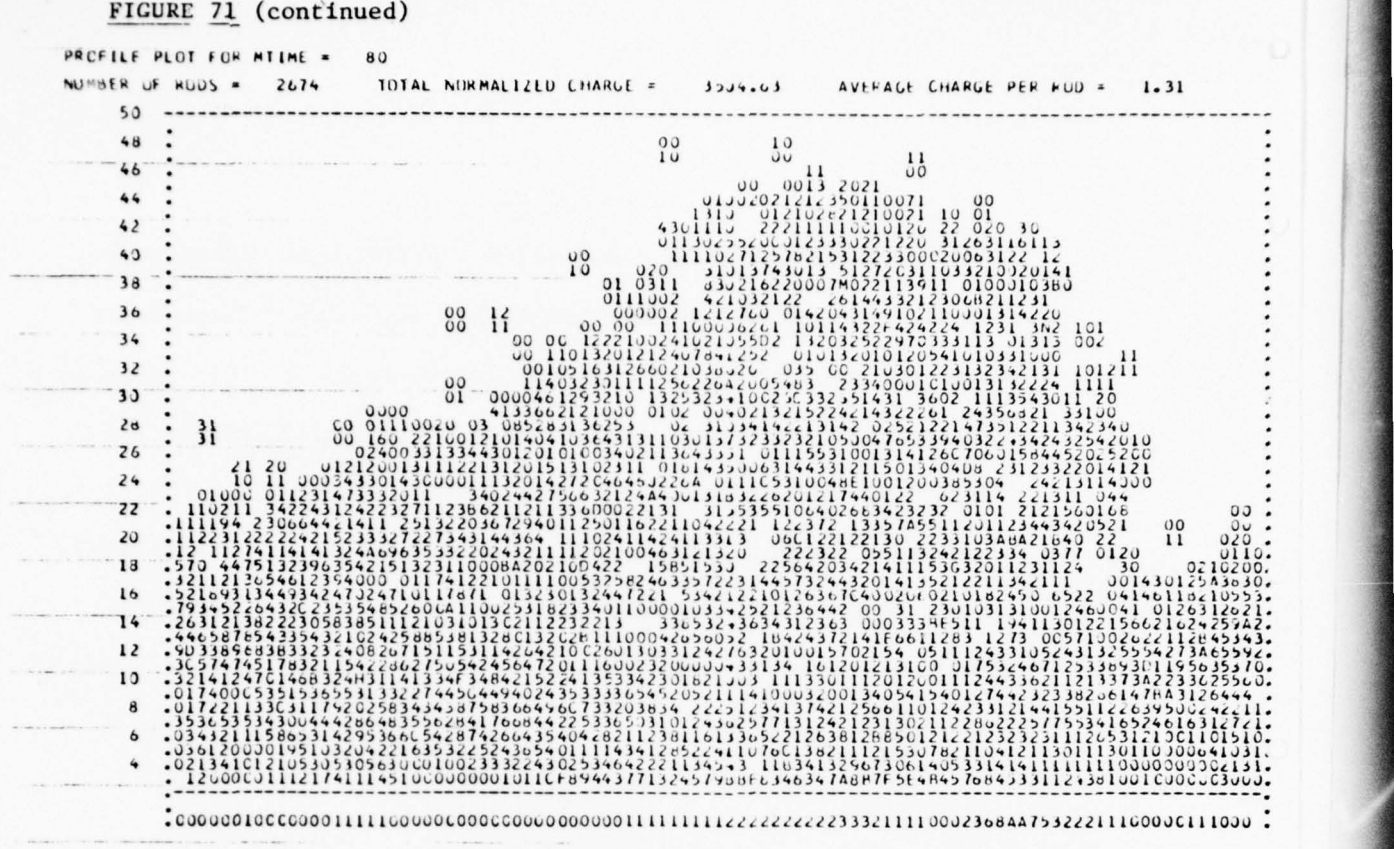

FIGURE 71 (concluded)

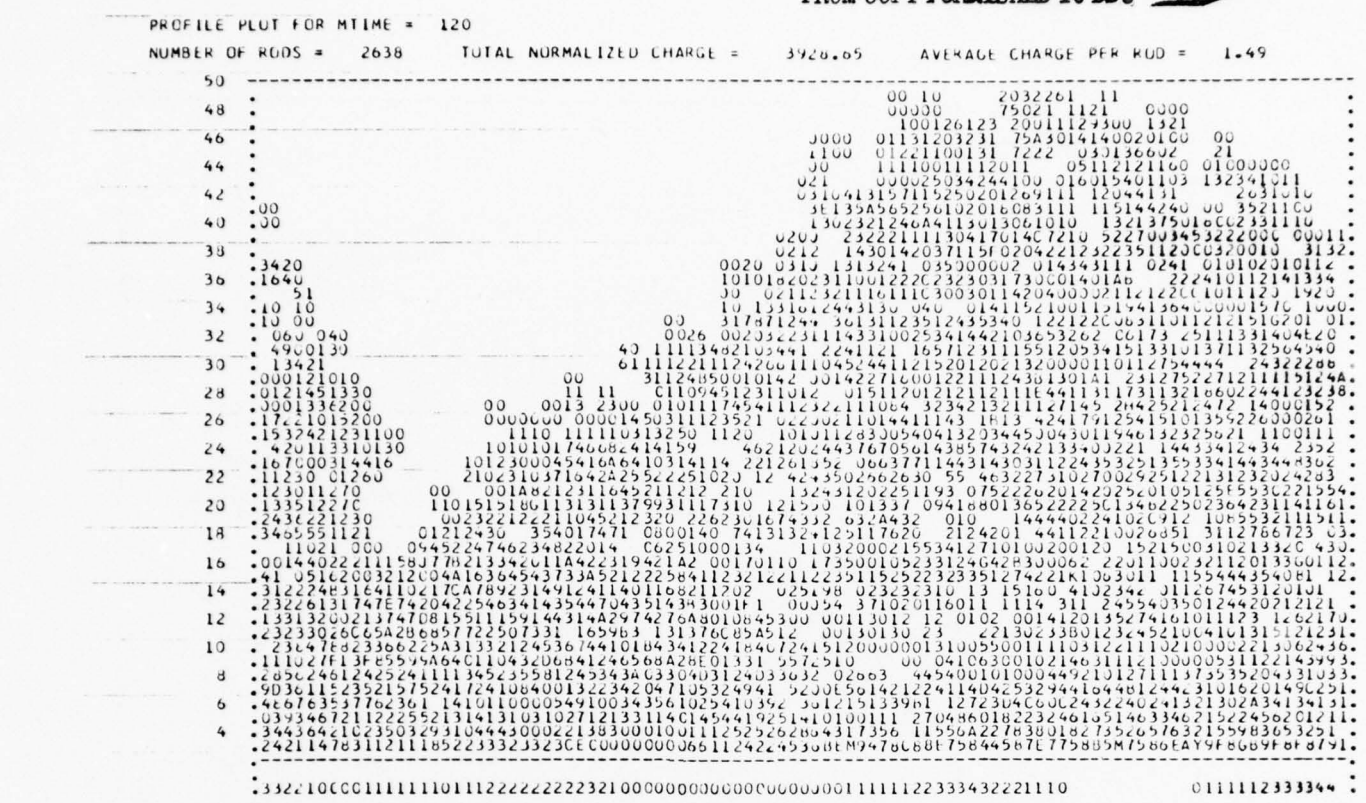

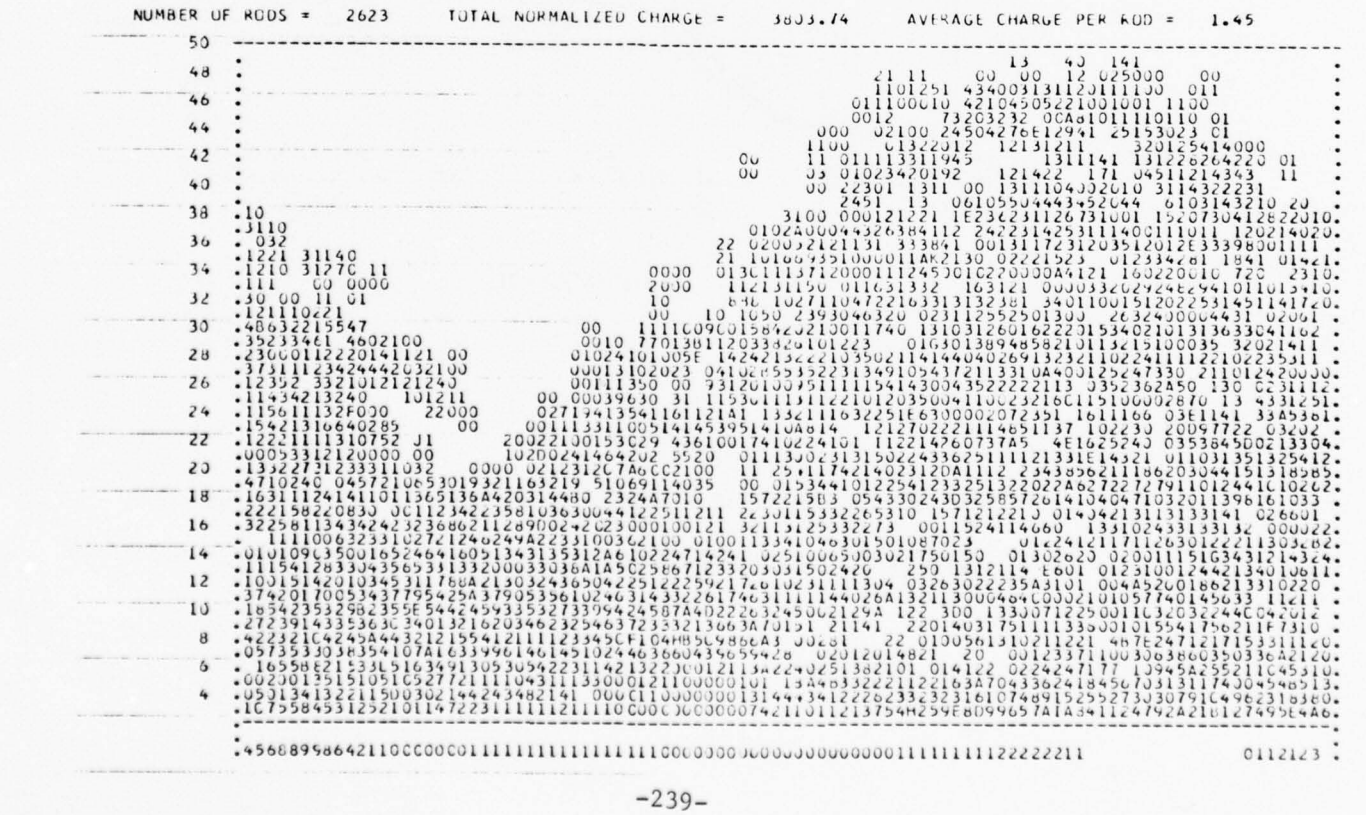

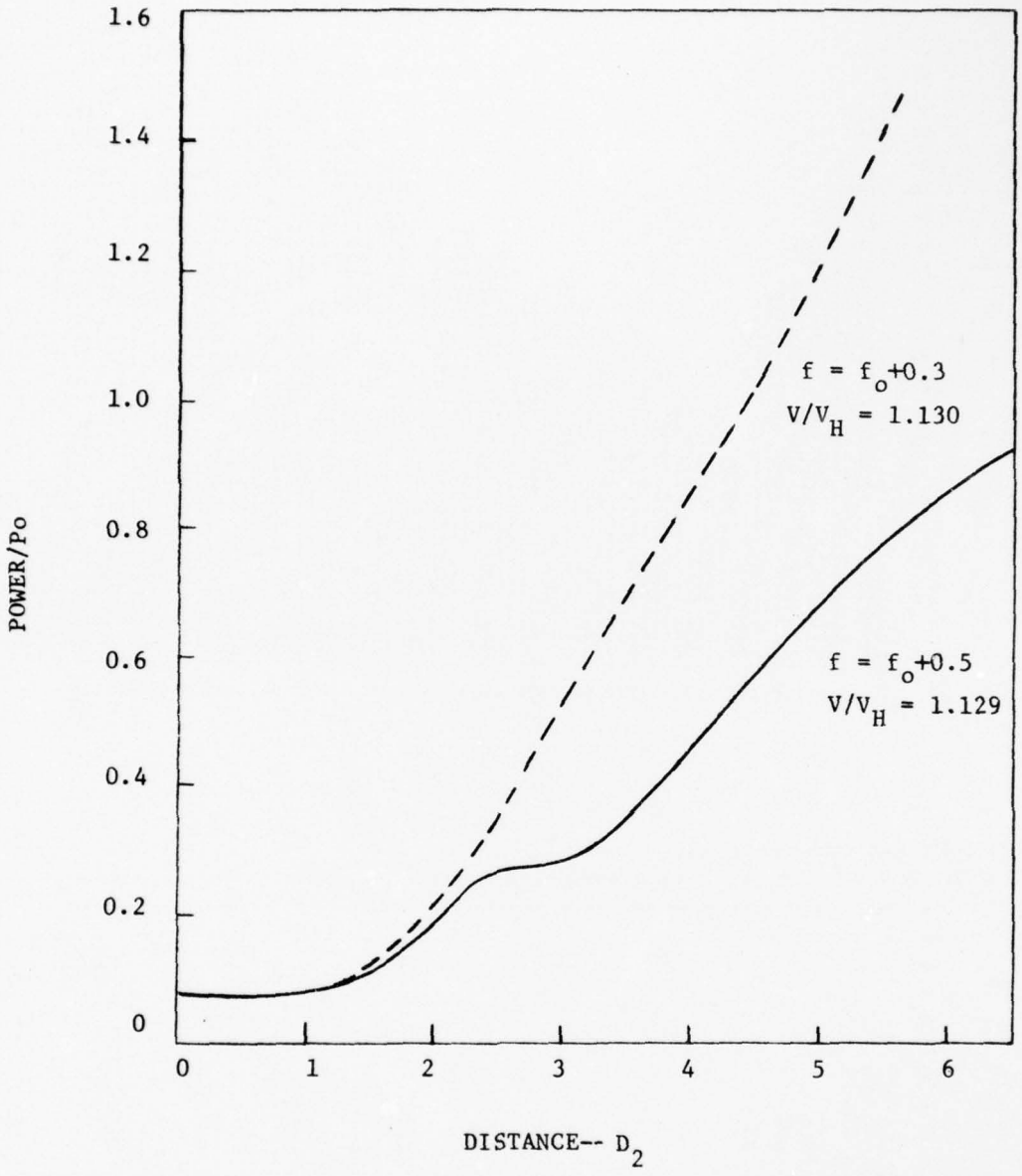

FIGURE 72

COMPARISON OF POWER AS A FUNCTION OF DISTANCE FOR CALCULATIONS STARTING FROM AN UNMODULATED HUB AT MID BAND AND AT UPPER BAND EDGE.

4.3.4 Effect of Varying Anode-Cathode Spacing and Interaction Width

Two brief studies were conducted at the high frequency end of the band on the effect of varying anode-cathode spacing or interaction width. The results are shown in Figure 73 and 74. We have included a curve for the same voltage from the results of the prior section in Figure 73 and a curve from Figure 73 in Figure 74 for comparison.

Figure 73 shows that decreasing the interaction spacing significantly increases the rate of power growth. Figure 74 shows that doubling the interaction width (without changing the impedance) increases the power by more than a factor of two. This occurs because at each point along the interaction space in the double width calculation, the fields are higher than in the comparison calculation because of the higher rate of power growth. The discussion in Section 2.12 showed that the power should increase by a factor of two if the width were doubled and the impedance halved. Thus the present calculation also represents the effect of increasing impedance. The results are reproduced in terms of an impedance comparison in Figure 75. Both Figures 74 and 75 show that the magnitude of the RF fields are significantly affecting the power growth. This conclusion is at variance with the point of view sometimes expressed that circuit impedance variations have little effect on the performance in the high power region of a CFA.

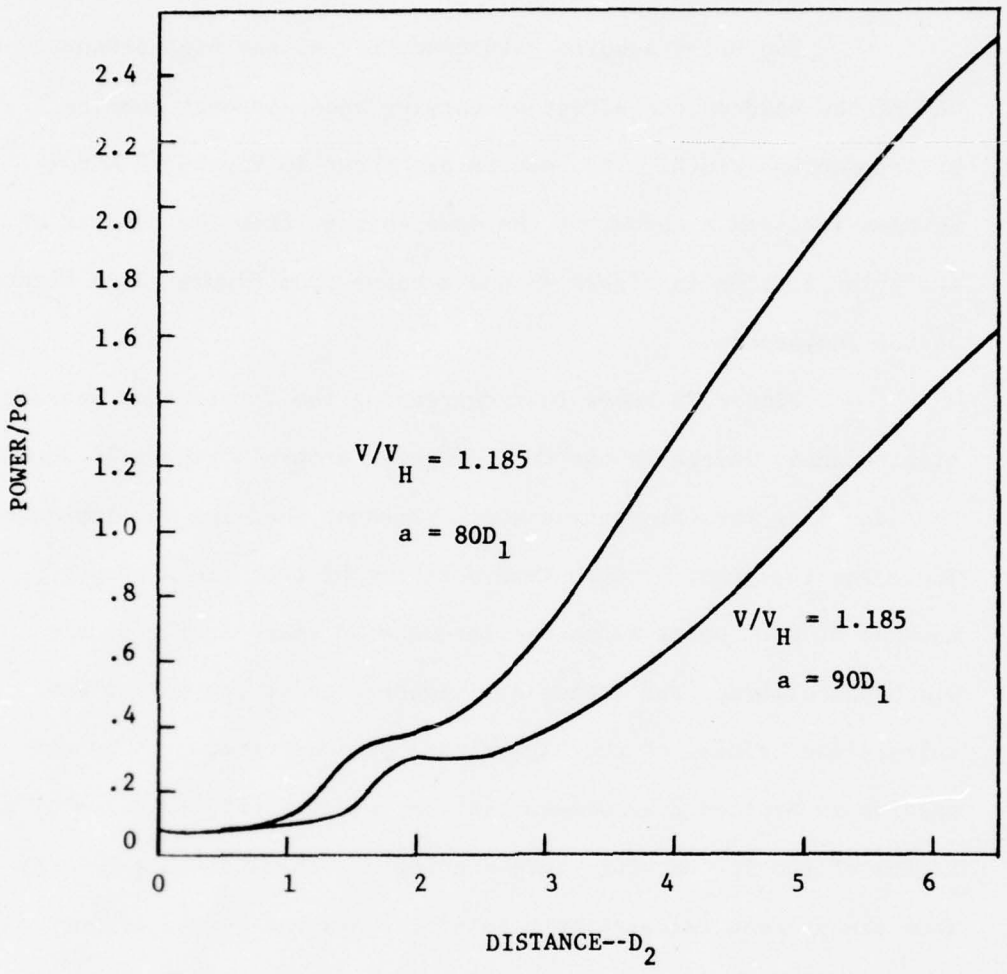

FIGURE 73

PEAK POWER AS A FUNCTION OF DISTANCE FOR CALCULATIONS STARTING FROM AN UNMODULATED HUB--DIFFERENT ANODE-CATHODE SPACINGS AT UPPER BAND EDGE. $f = f_o + 0.5$, $P_{in} = 0.08$ Po. Note vertical scale change relative to Figure 70.

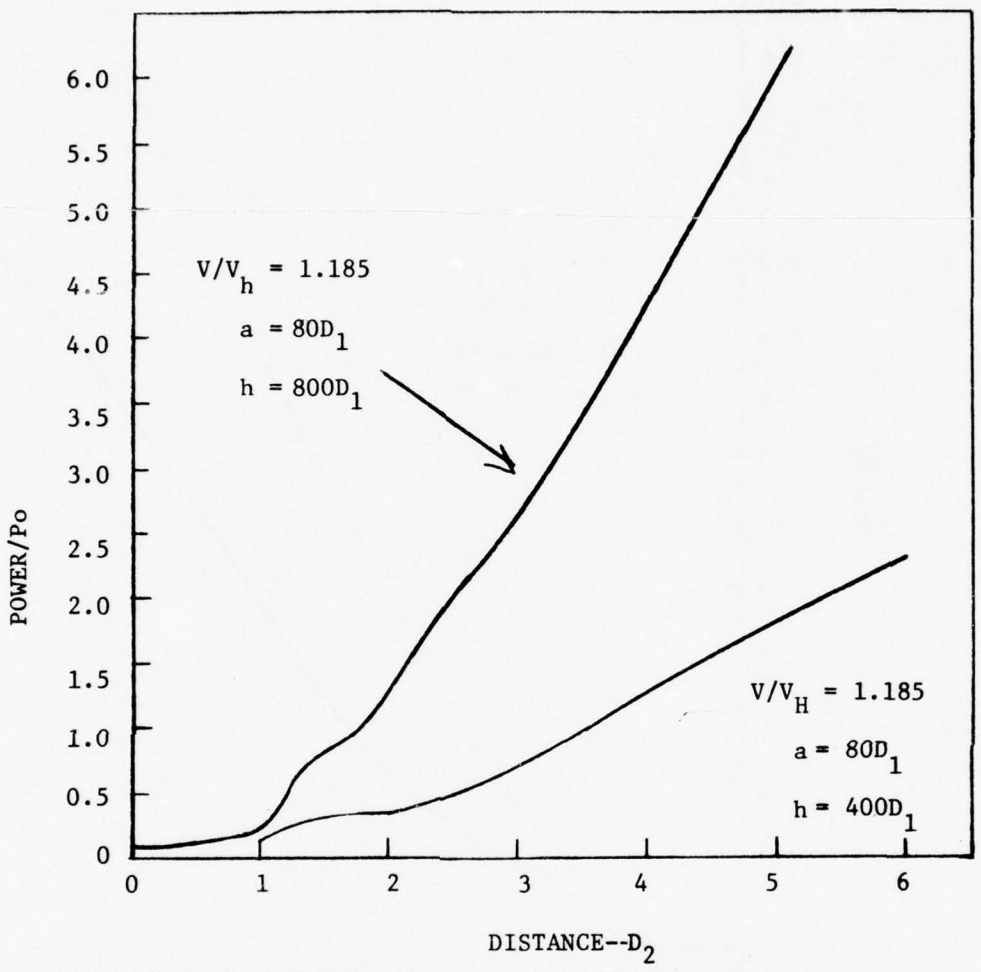

FIGURE 74

PEAK POWER AS A FUNCTION OF DISTANCE FOR CALCULATIONS STARTING FROM AN UNMODULATED HUB--DIFFERENT INTERACTION WIDTHS AT UPPER BAND EDGE. $f = f_o + 0.5$, $P_{in} = 0.08$ Po. Note further vertical scale change.

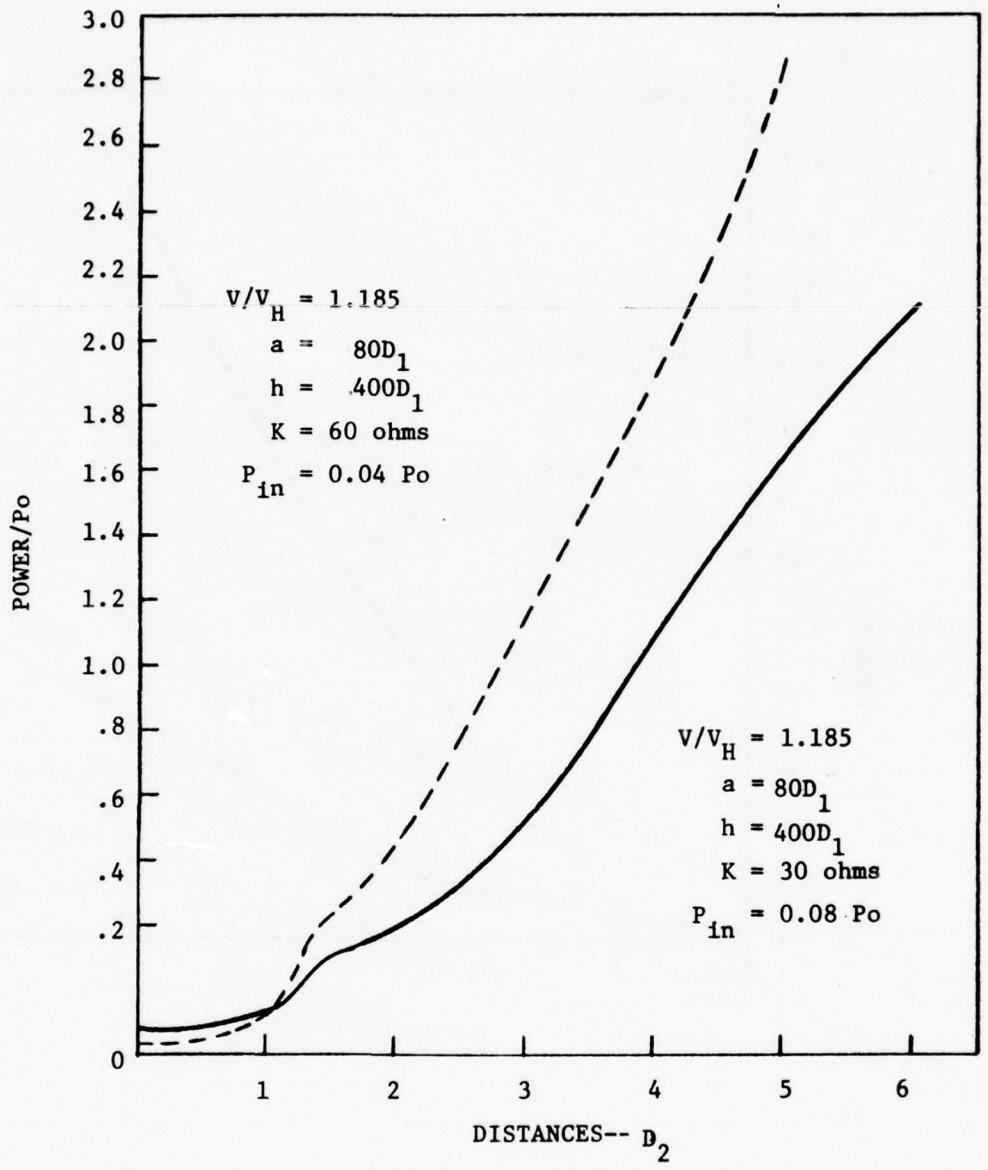

FIGURE 75

PEAK POWER AS A FUNCTION OF DISTANCE FOR CALCULATIONS STARTING FROM AN UNMODULATED HUB--DIFFERENT INTERACTION IMPEDANCES AT UPPER BAND EDGE. $f = f_o + 0.5$.

4.4 Effect of Recirculating Charge

In this section we have so far discussed the interaction in the absence of charge recirculating from output to input above the hub level. In practice there can be significant amounts of such charge. The recirculated charge can have important effects. It can both increase gain and increase noise. How we go about using the recirculated charge can thus make major changes in the performance of a CFA.

4.4.1 Effect of Recirculated Charge Power Growth

Figure 76 shows the "debunching" of charge in the drift space for the mid-band case of Figure 28. When the RF fields which focus the spoke are removed, the spoke rotates forward and downward. The charge is not completely "debunched" by the time it reaches the input, but there is substantial reduction in the bunching and a further decrease in the effect of the charge because it has moved away from the anode. There is essentially no anode dissipation in the drift region. Cathode dissipation continues, however, at about the same rate it occurred in the main interaction space.

Variations in the distribution of recirculated charge at the input are responsible for the pass-to-pass variations in the computed output. Figure 77 shows the variation in charge distribution at the input for successive passes of the mid-band case. The pass number corresponds to the pass number in Figure 36. The peak output power of the pass is recorded on each of the charge distributions of Figure 77.

FIGURE 76

ROD PROFILE PLOTS SHOWING DEBUNCHING OF SPOKE IN DRIFT SPACE. These plots are for a mid band case as shown in Figures 28 and 29. End of circuit occurs at time step 323 and end of drift space (i.e., start of next pass) occurs at time step 370. Plots are shown every 10 time steps. Interaction box moves forward $0.14\,D_2$ in 10 yime steps.

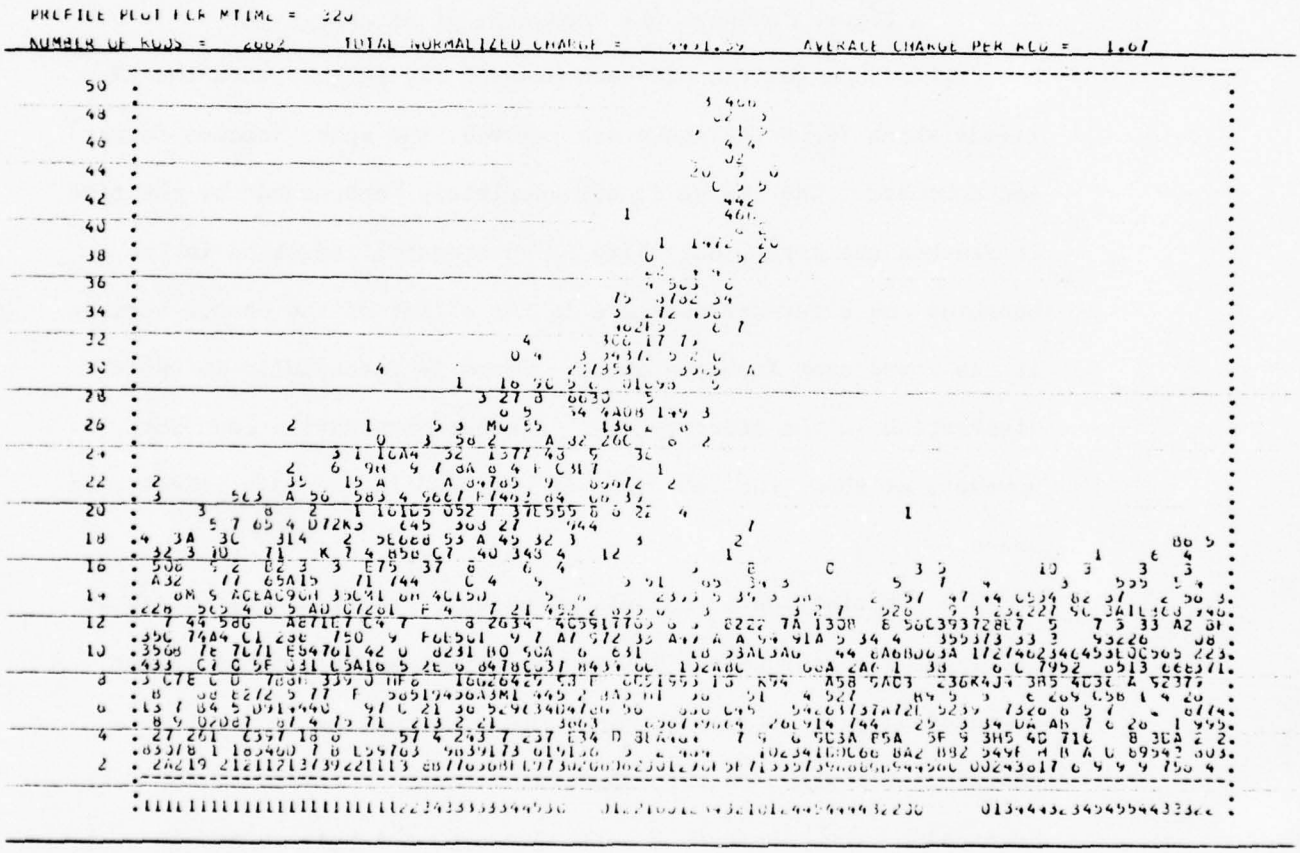

FIGURE 76 (continued)

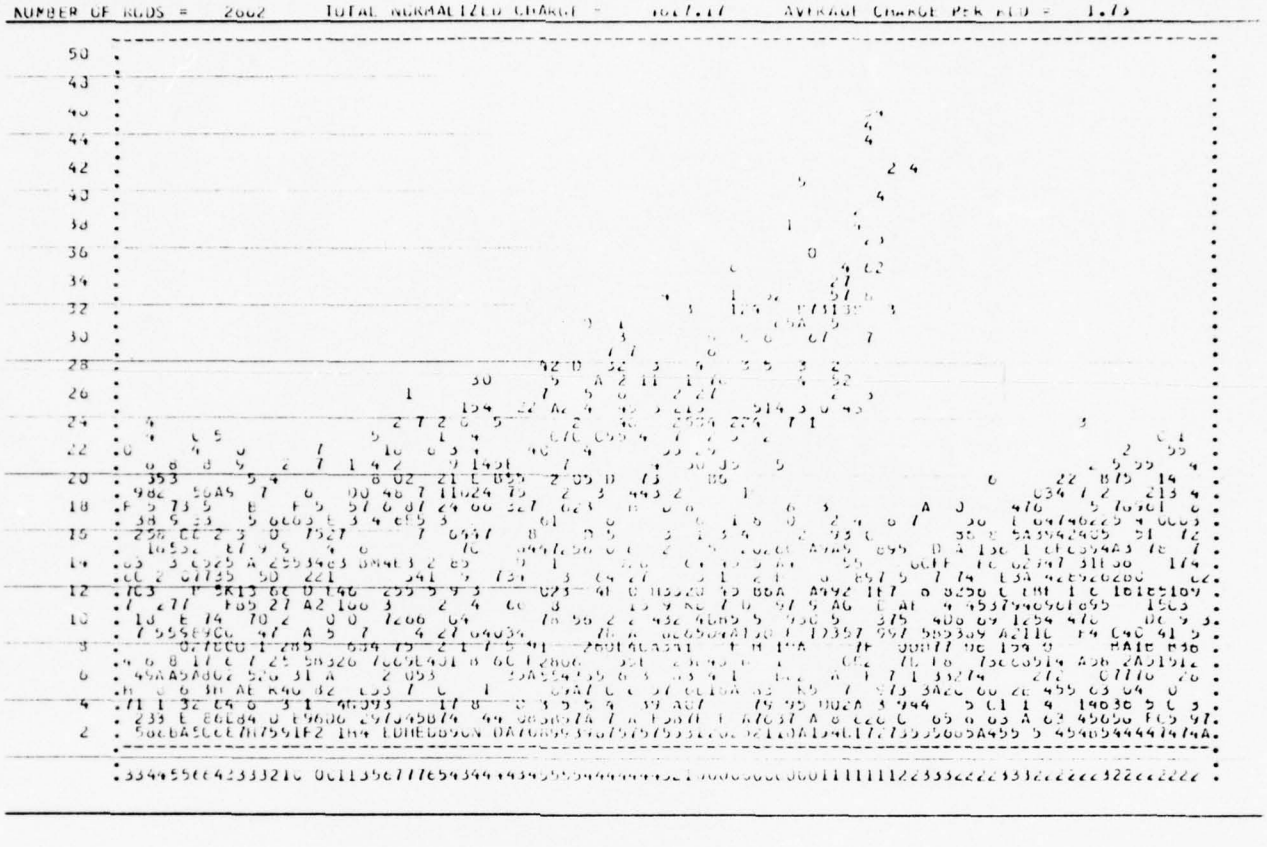

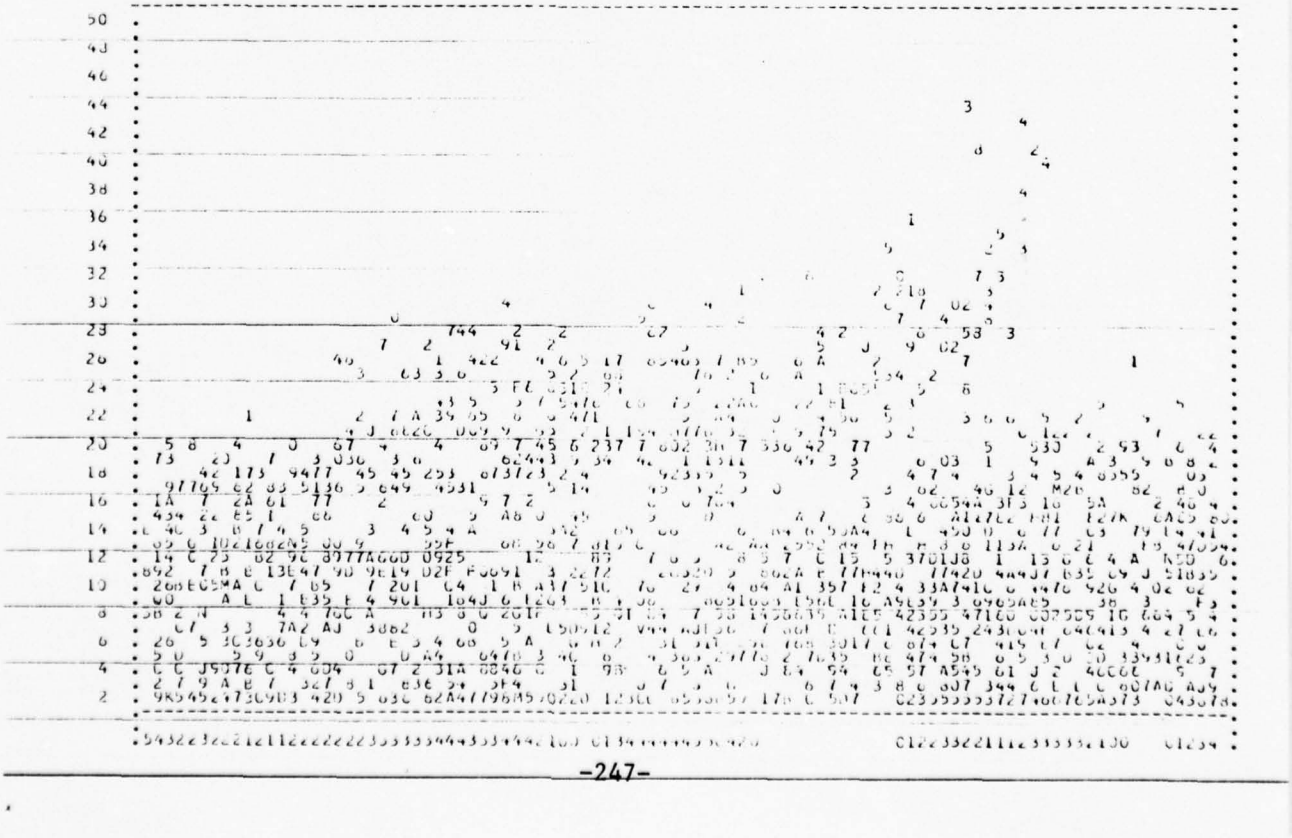

PREFILE PLOT FOR MTIME = 350

NUMBER OF RODS = 2002 TOTAL NORMALIZED CHARGE = AVERAGE CHARGE PER ROD = 1.14

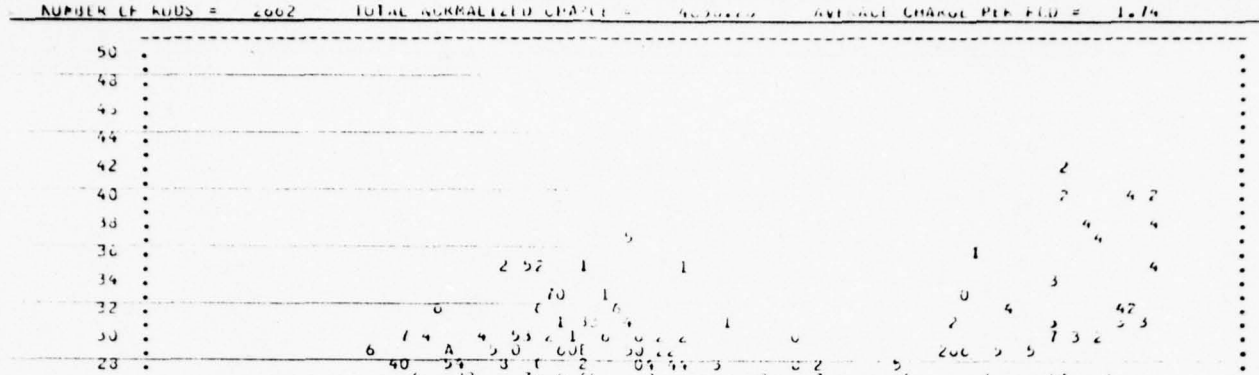

PREFILE PLOT FOR MTIME = 360

NUMBER OF RODS = 2002 TOTAL NORMALIZED CHARGE = AVERAGE CHARGE PER ROD = 1.12

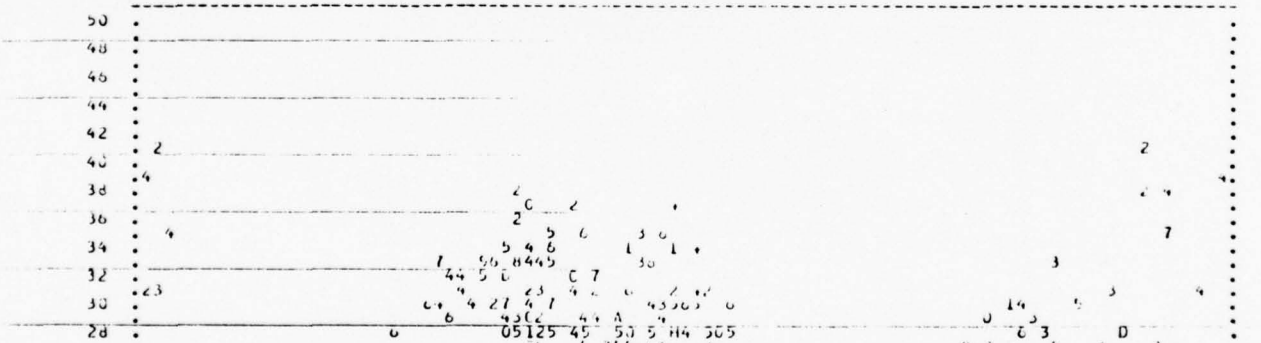

FIGURE 76 (concluded)

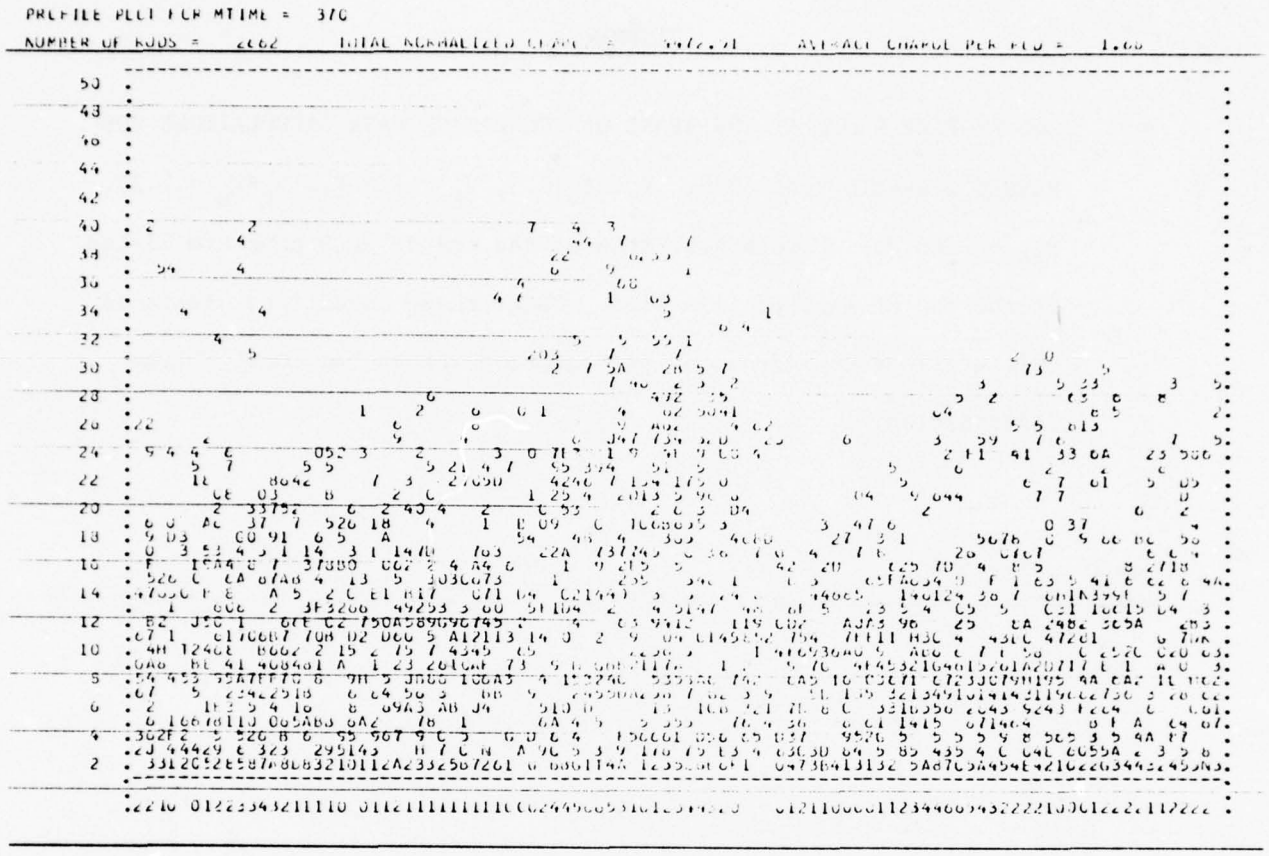

FIGURE 77

ROD PROFILE PLOTS AT THE START OF SUCCESSIVE PASS CALCULATIONS FOR PASSES 2-6--MID BAND CASE. $f = f_o + 0.3$, $V_K = 1.3\ V_1$, $V_K/V_H = 1.13$, $P_{in} = 0.08\ Po$. Powers generated by the end of each pass are listed at the top of each profile plot. Under these conditions, there is only a slight dependence of the output power on the input charge distribution.

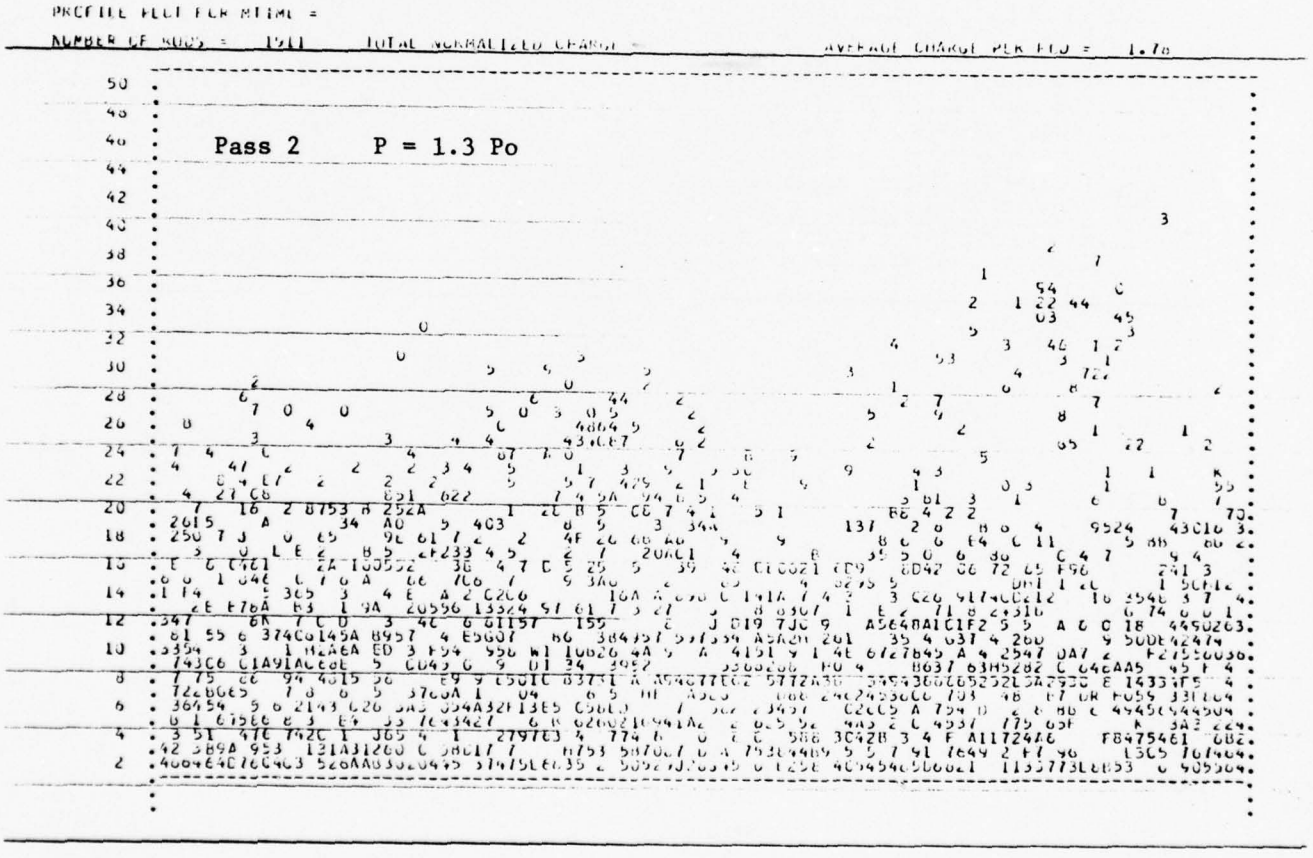

FIGURE 77 (continued)

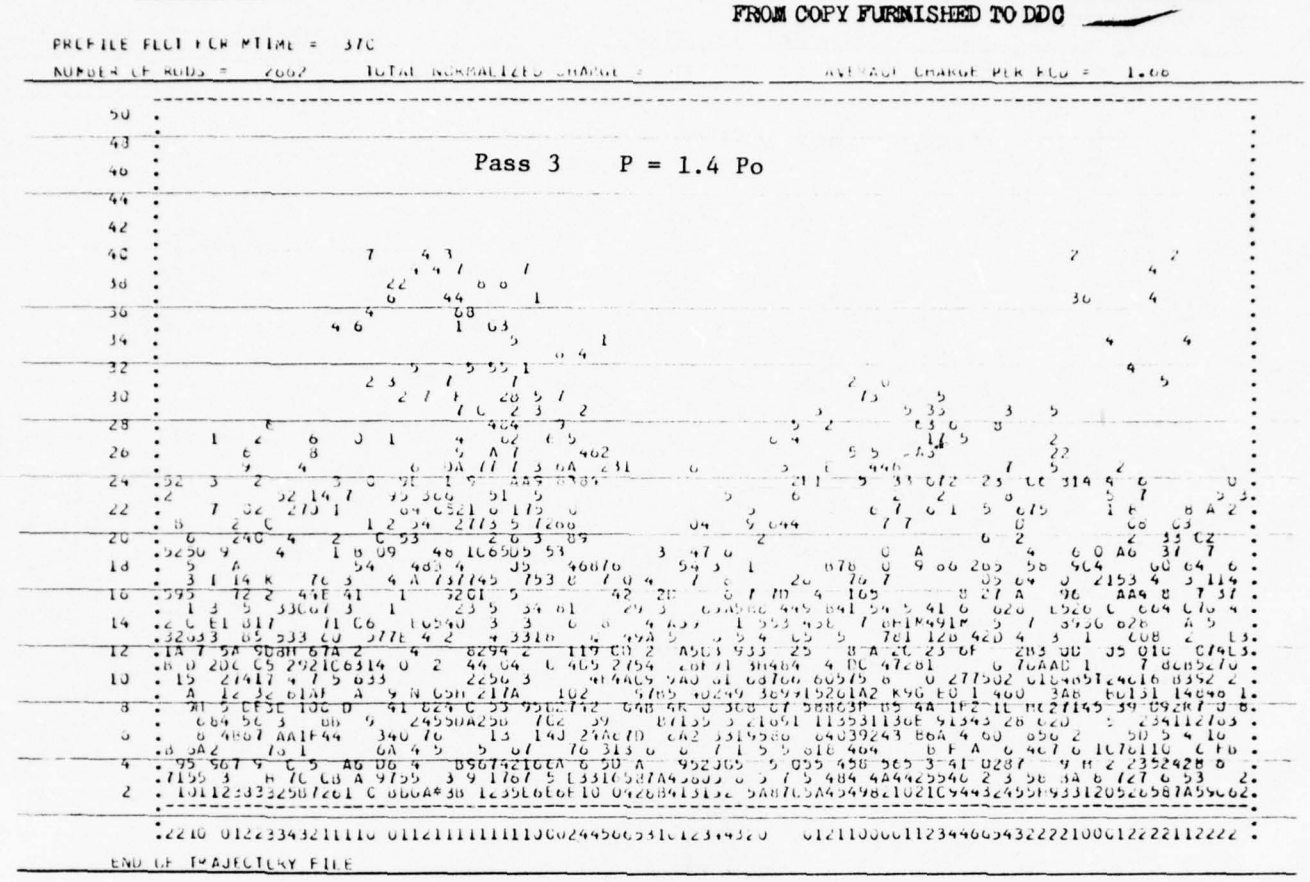

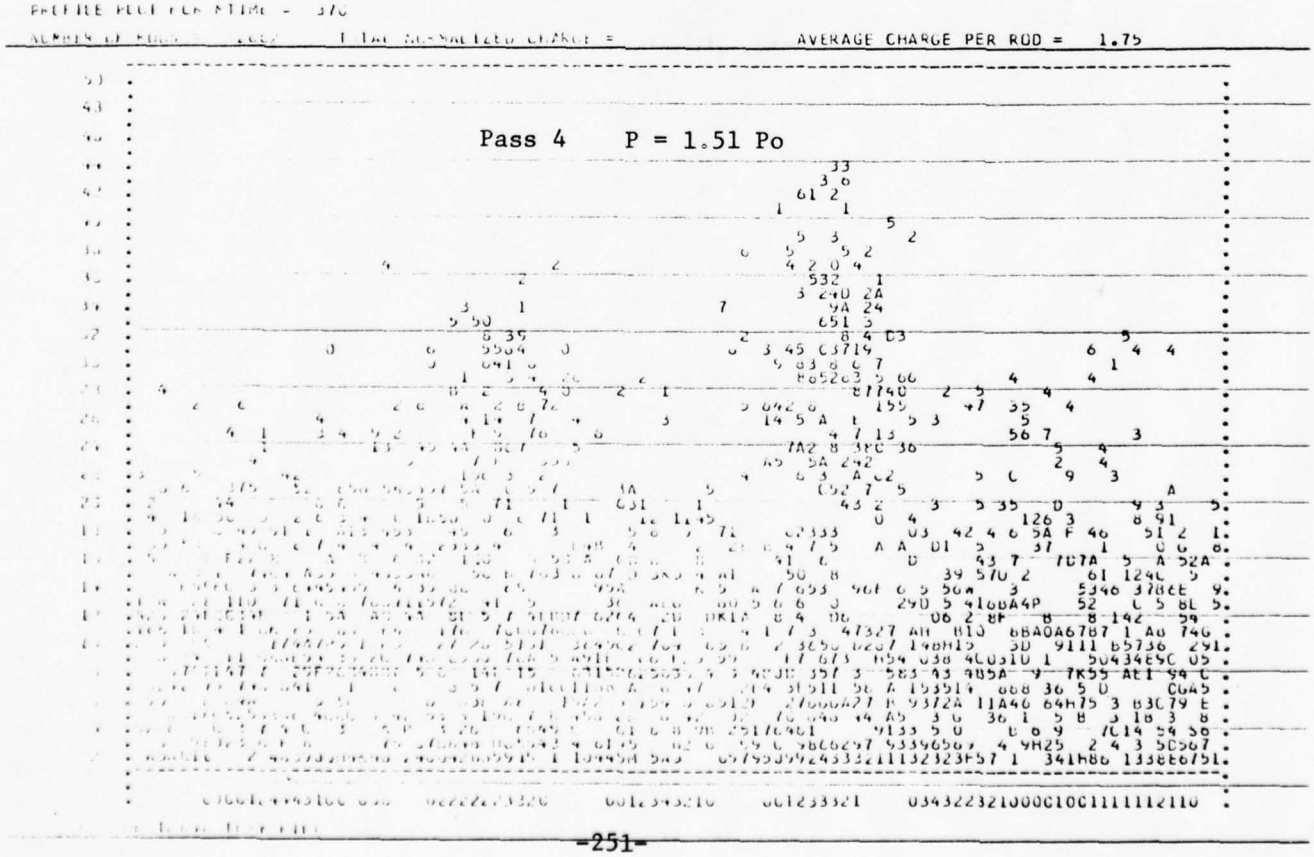

FIGURE 77 (concluded)

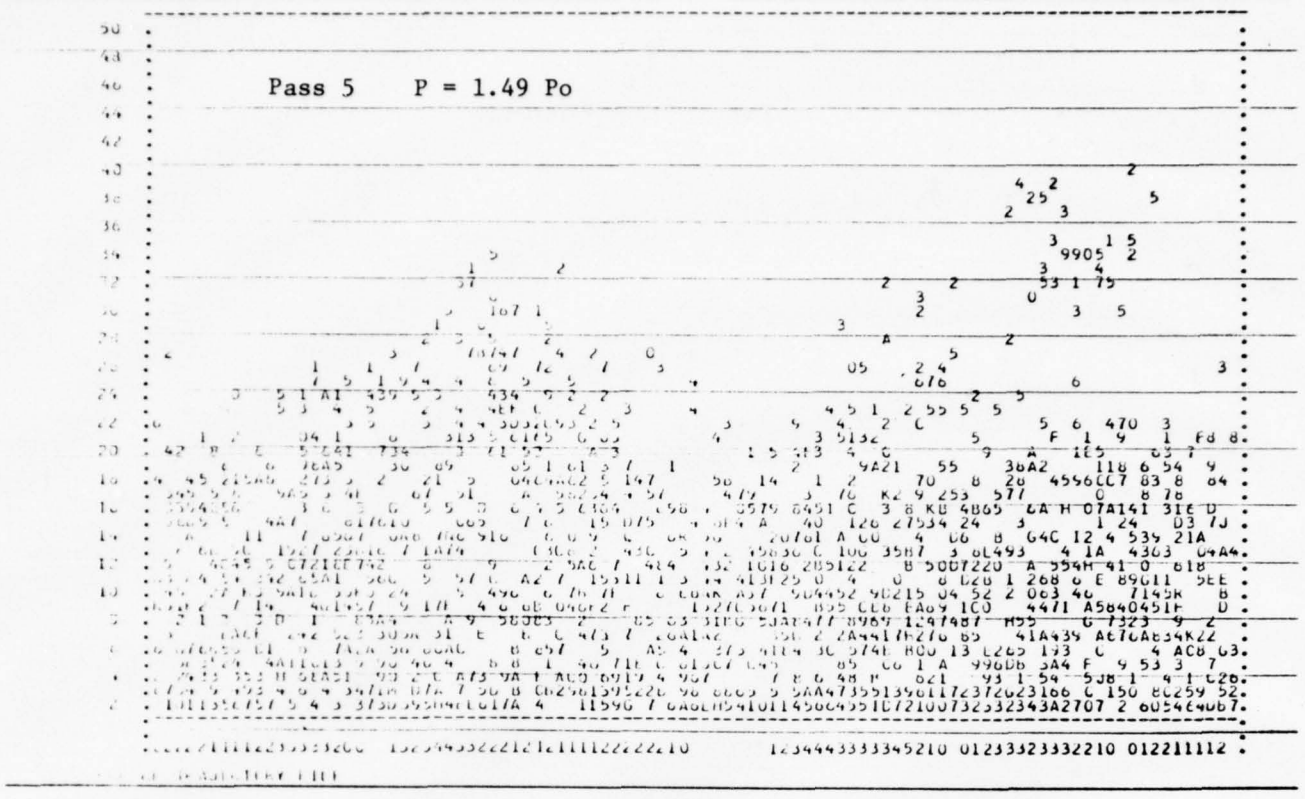

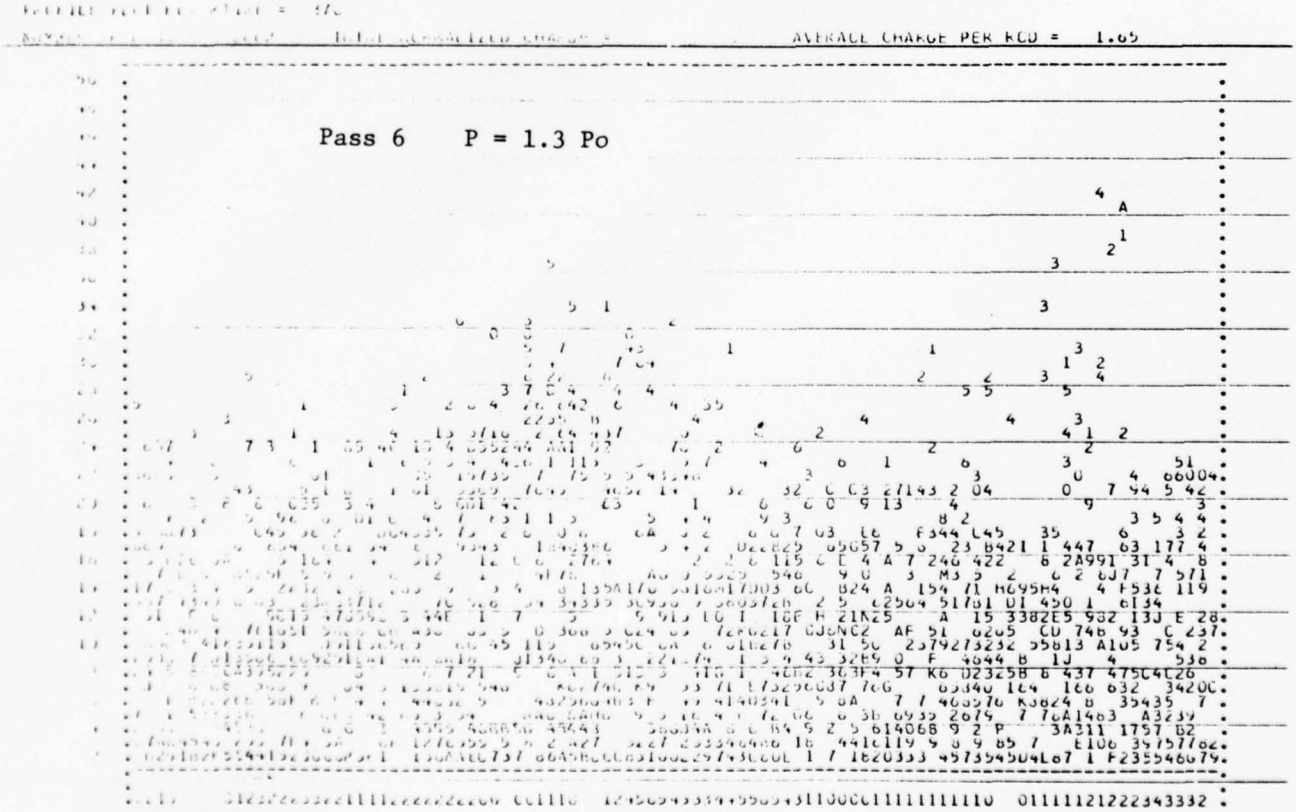

The location of the residual bunching at the input is not simply related to the effect it has on the power growth at the input because the residual bunch drifts in the interaction box early in the calculation. This drifting is shown in Figure 78 which shows the charge distributions at the input over a number of time steps. This drifting occurs because the electric fields above the hub surface are higher than required for E/B synchronism of the recirculating charge with the circuit wave. The location of the level for E/B synchronism is shown in Figure 78, and the actual field at the center of the interaction box is shown in Figure 79. As a result of the drifting of the residual bunch, the worst place for it to return is not in the center of the unfavorable phase but rather just at the point it is going to drift into the unfavorable phase.

Figure 80 compares the power growth for a low power reentrant pass with the power growth without recirculating space charge which was previously presented in Section 4.3. It is seen that even for the worst case of phasing of the recirculated bunch with the RF wave, the rate of power growth is greater than it is in the absence of recirculated charge. Regardless of the phase of the recirculated bunch, the RF input wave appears to eventually capture it in the favorable phase and use it to enhance the gain at the input.

If the input signal amplitude is decreased so that the circuit current wave amplitude is more nearly comparable with the induced current caused by the residual bunching at the input, then

FIGURE 78

ROD PROFILE PLOTS NEAR THE INPUT OF A MID BAND CALCULATION. Plots are presented for every 10 time steps. Interaction box moves forward 0.14 D_2 in 10 time steps. These plots show charge distribution above hub drifting forward in the interaction box. On rod is circled in these plots so that its position may be followed.

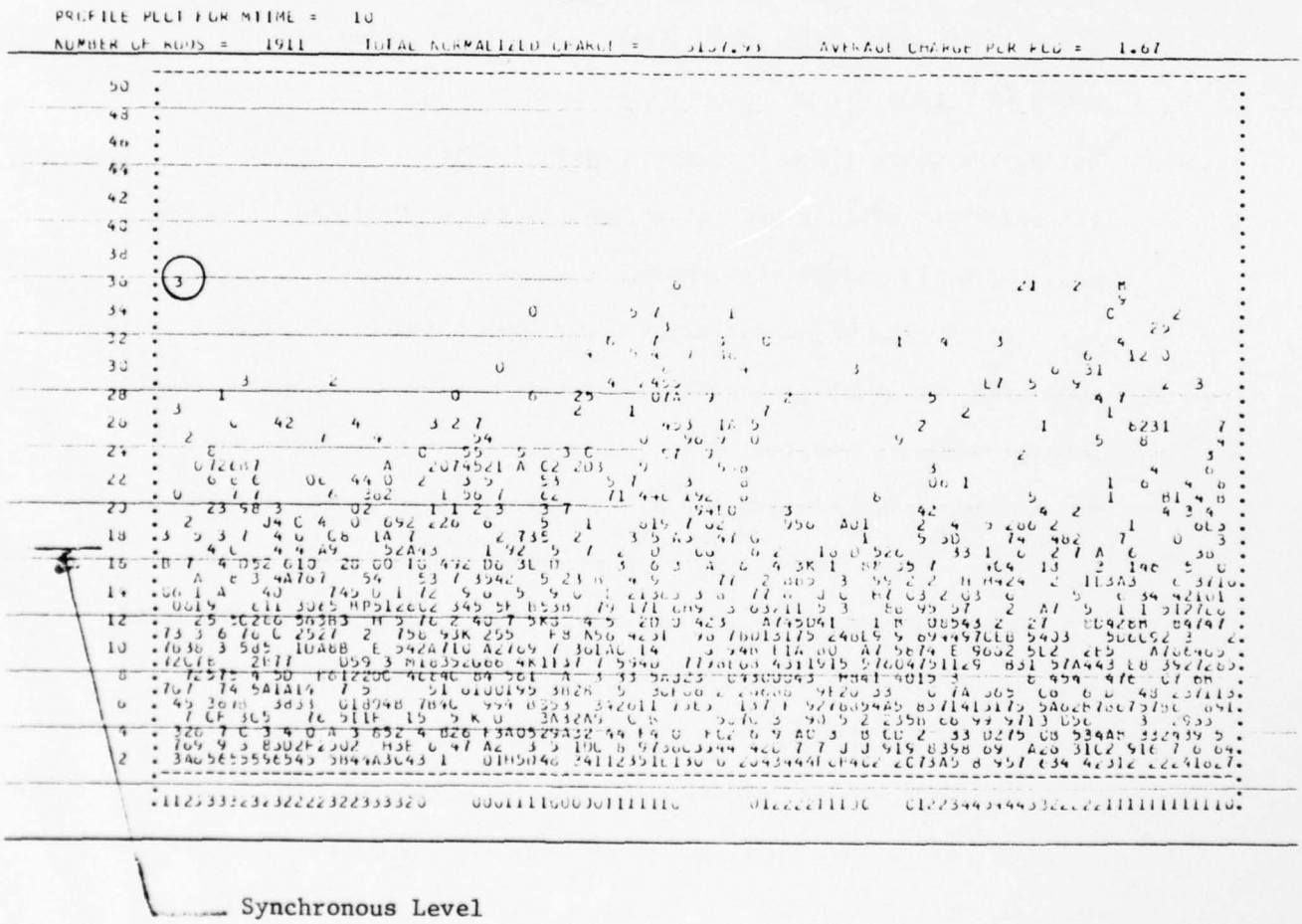

FIGURE 78 (continued)

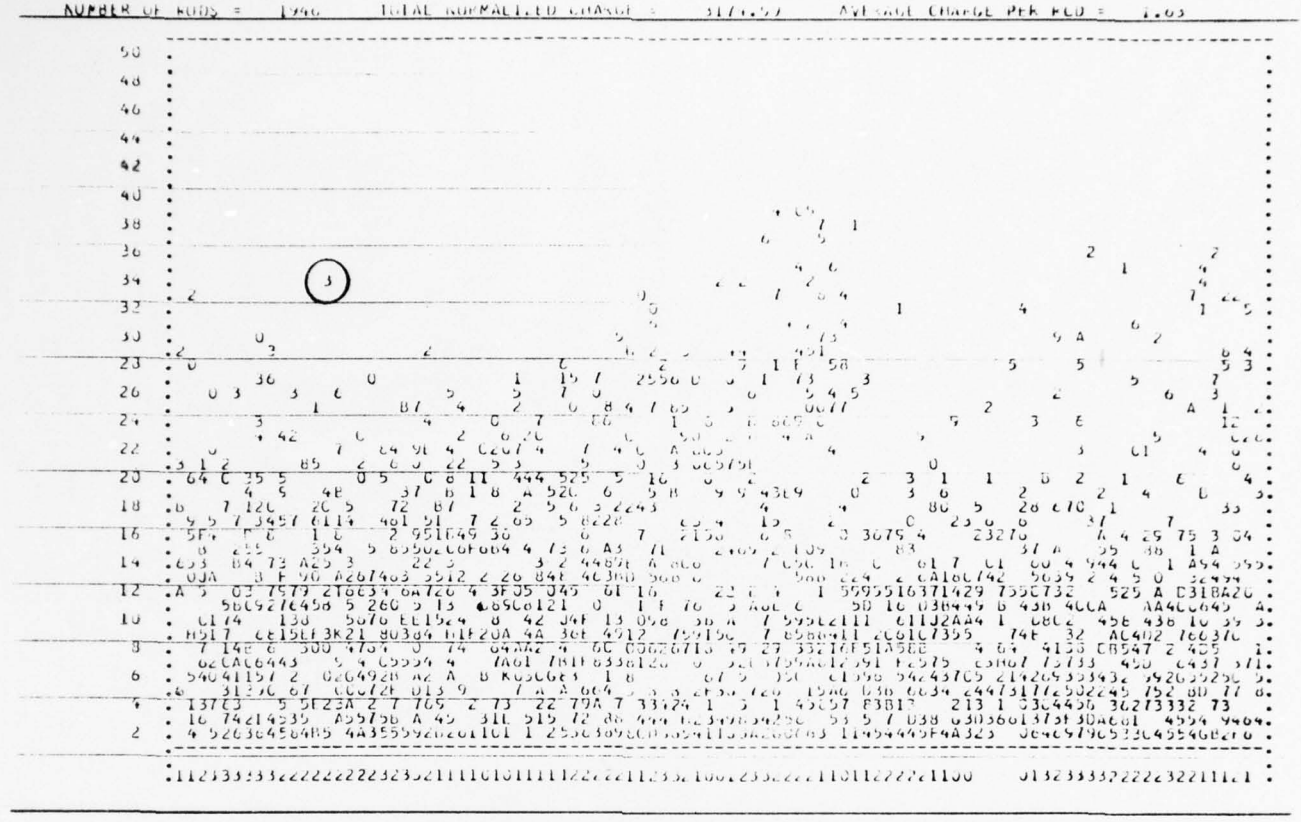

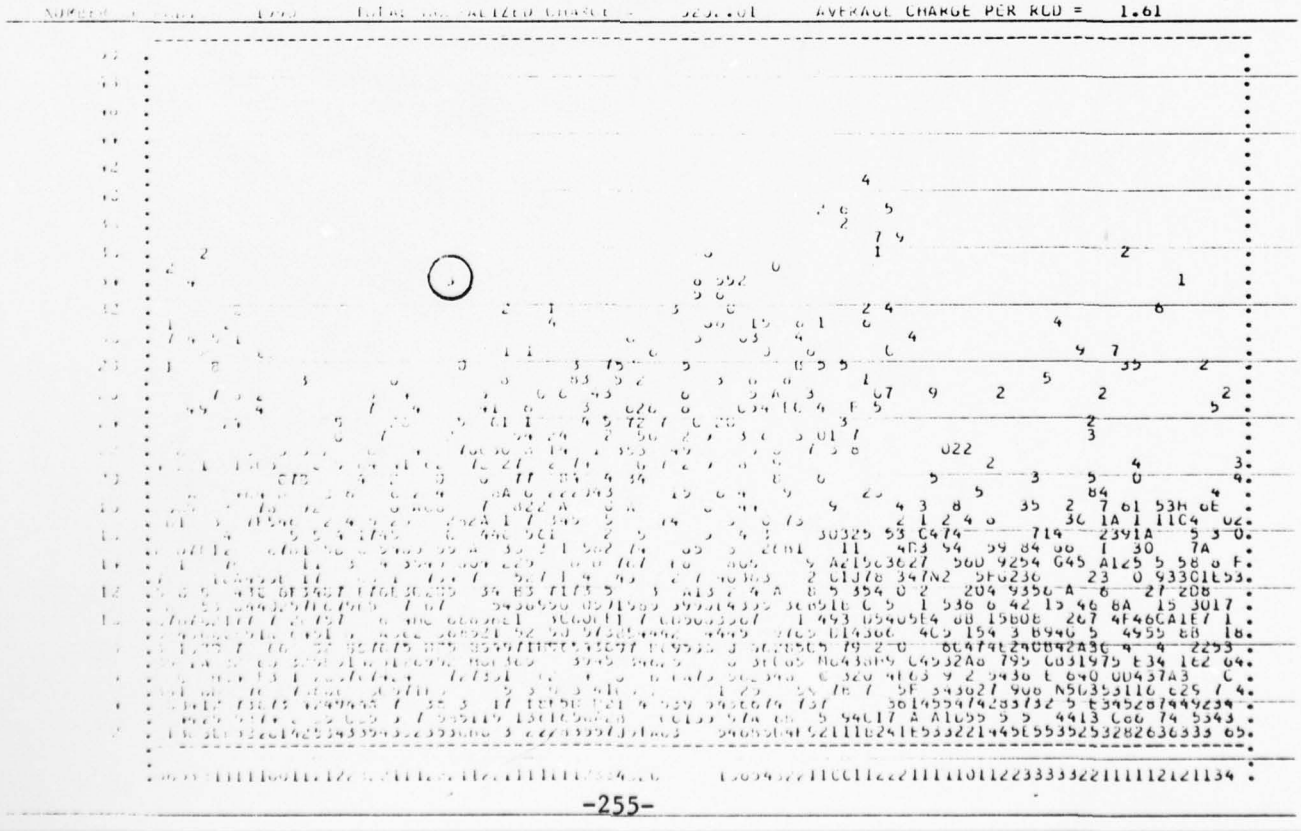

FIGURE 78 (continued)

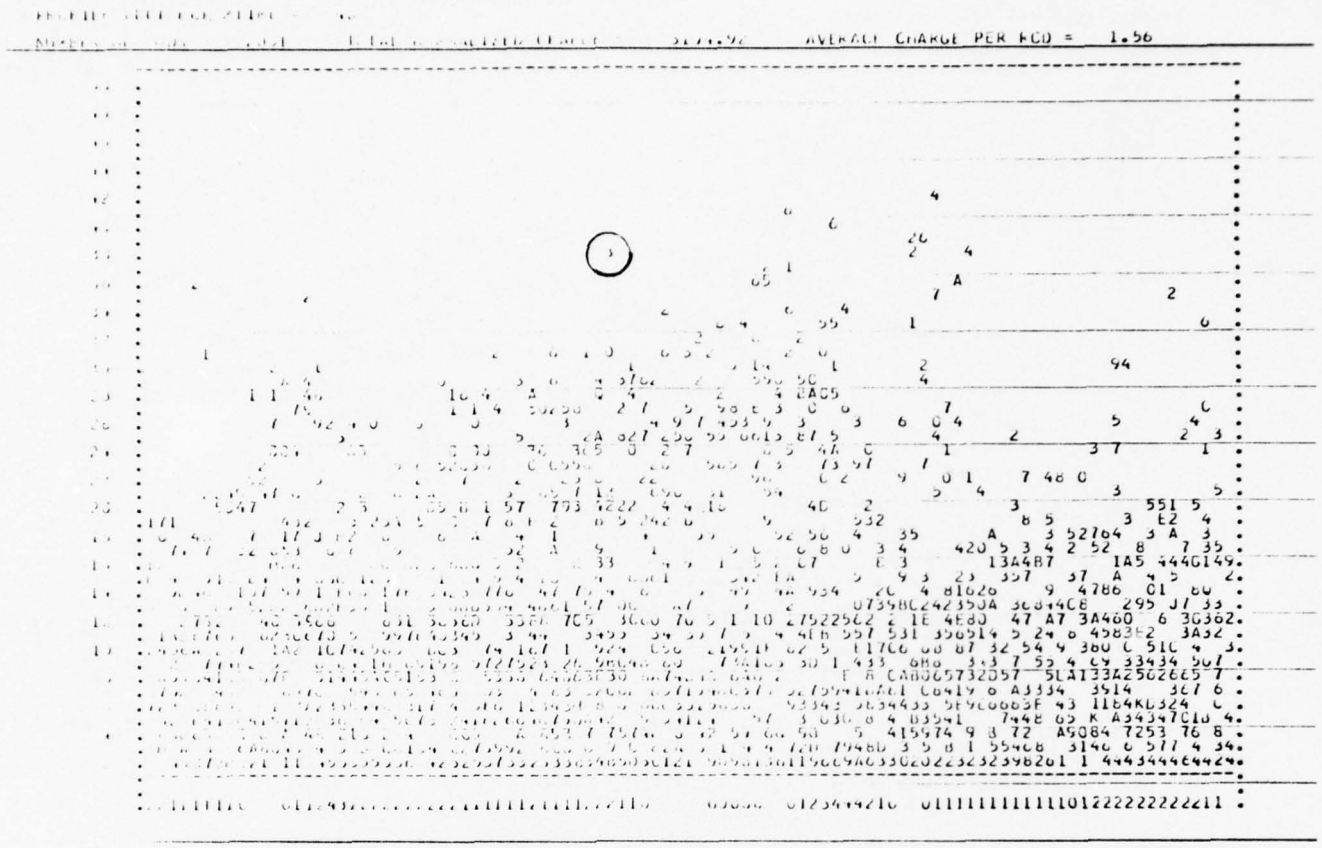

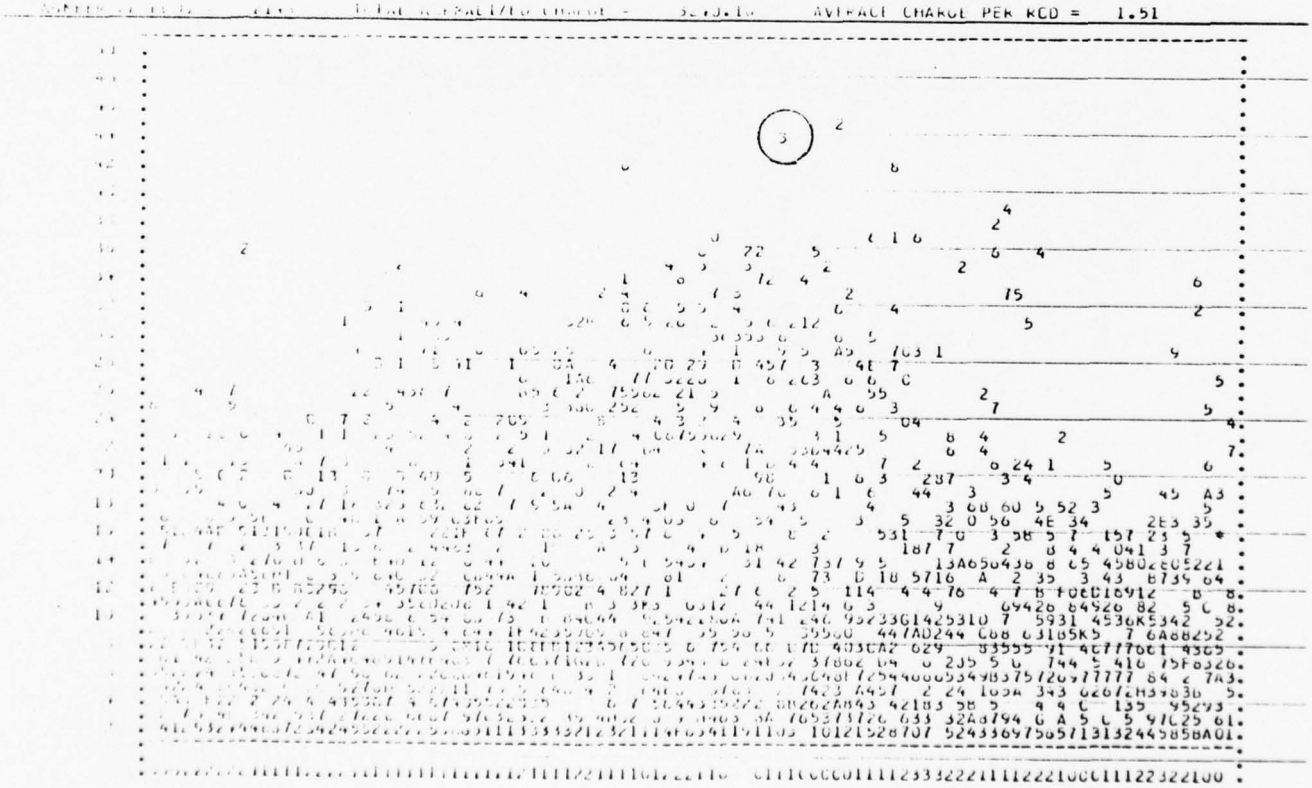

FIGURE 78 (concluded)

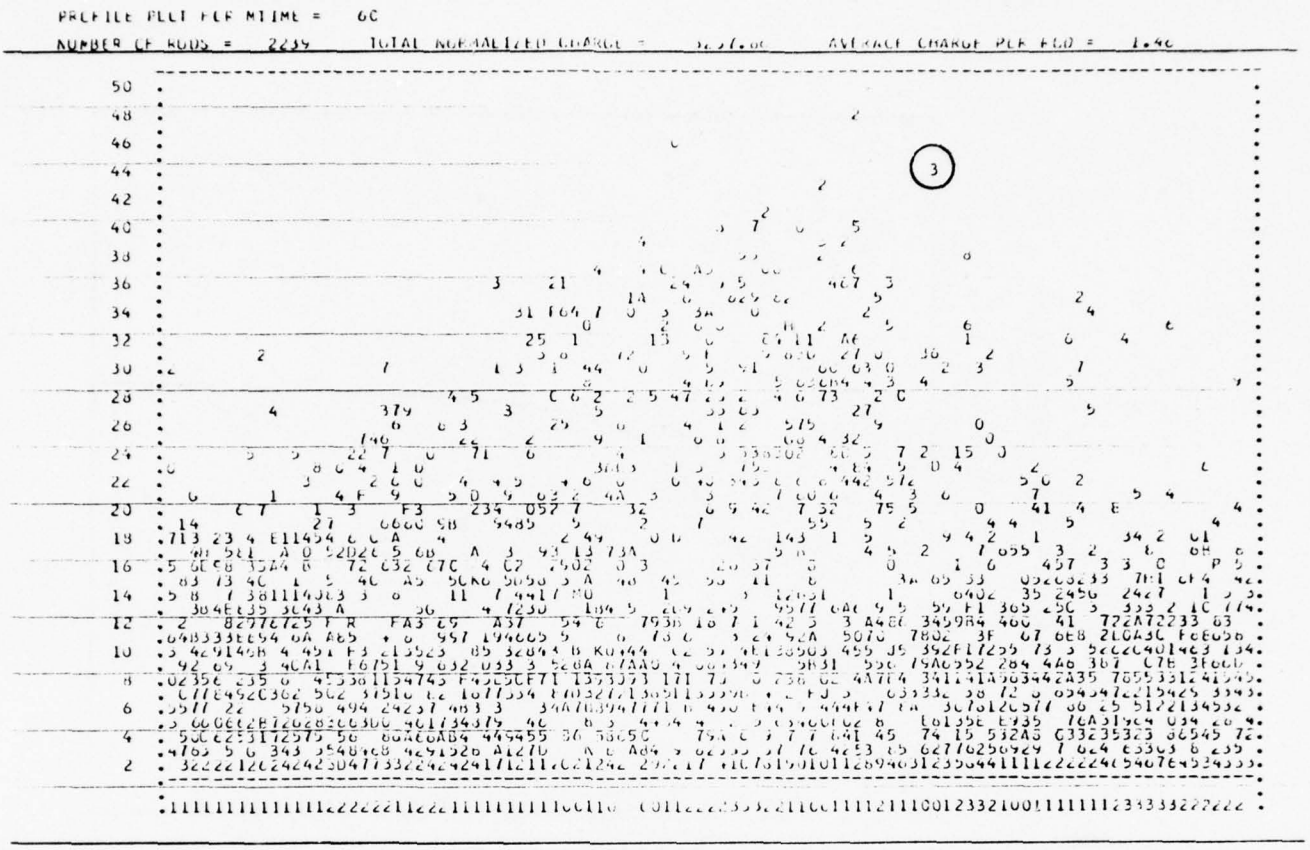

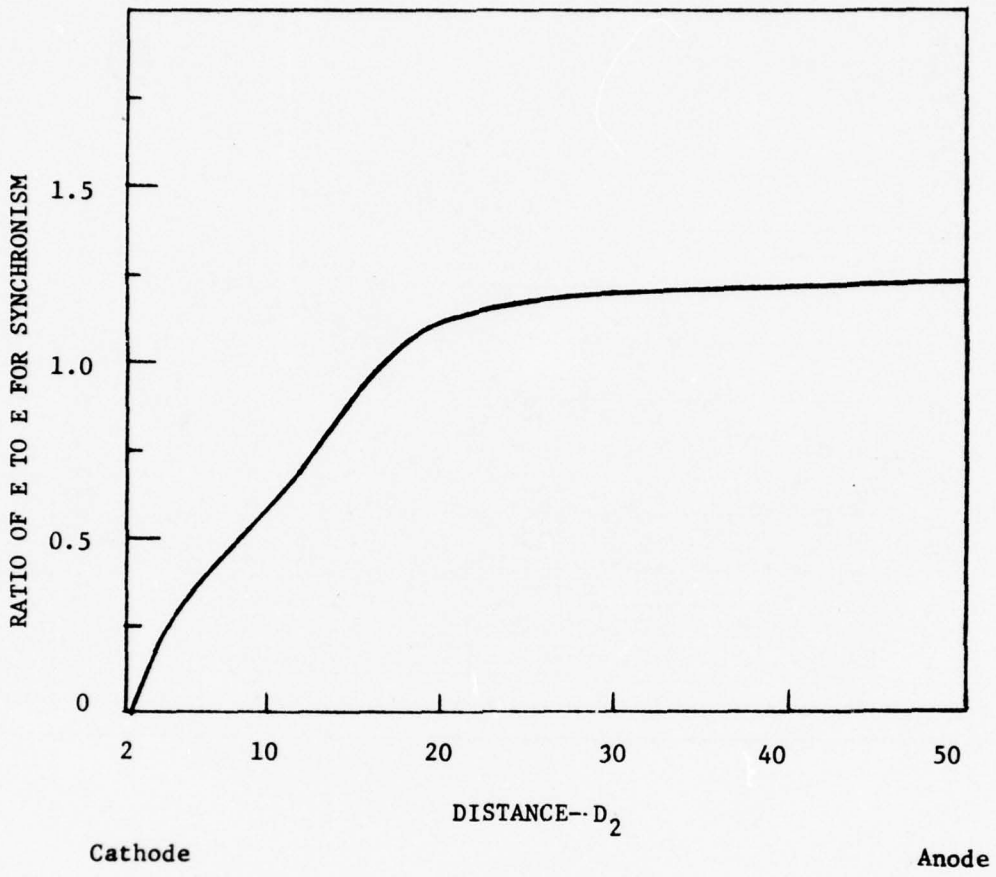

FIGURE 79

TYPICAL D.C. FIELD DISTRIBUTION BETWEEN CATHODE AND ANODE AT INPUT. $f = f_o + 0.3$, $V = 1.3\ V_1$, $V/V_H = 1.13$.

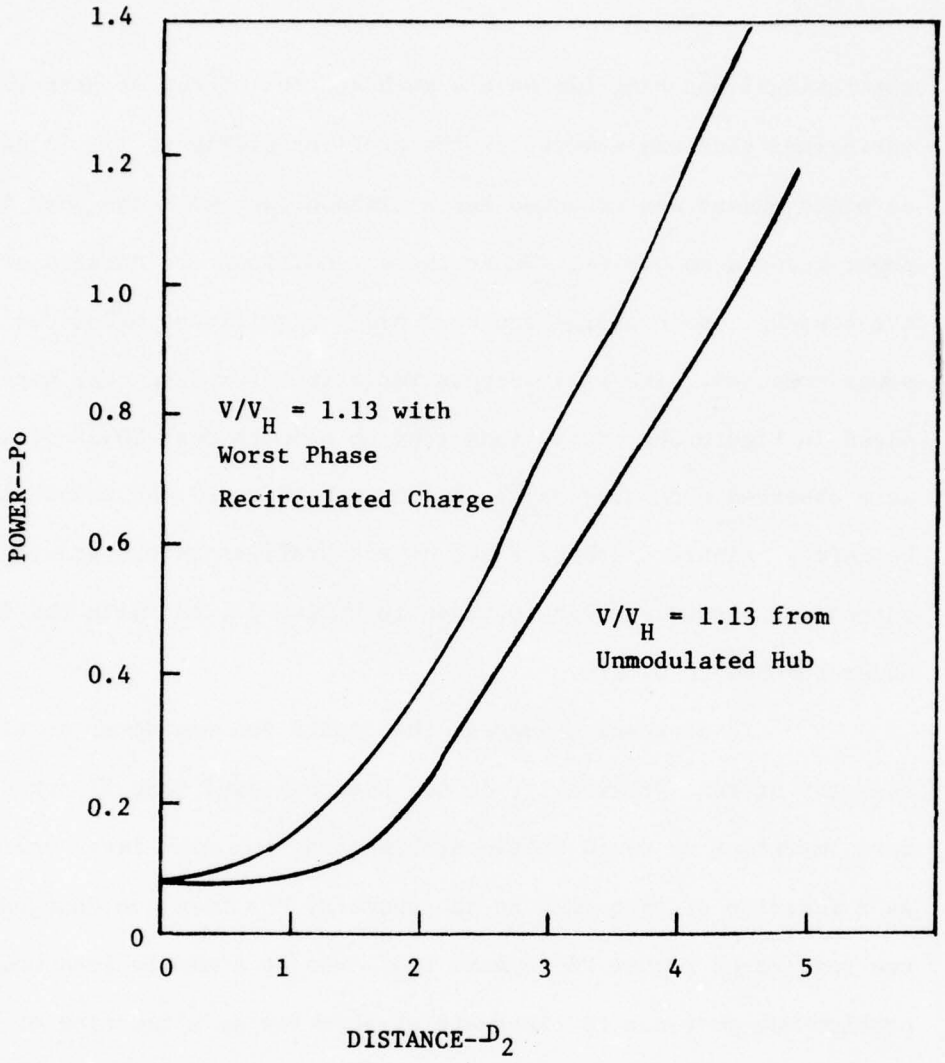

FIGURE 80

POWER AS A FUNCTION OF DISTANCE AT MID BAND FOR CALCULATION STARTING FROM UNMODULATED HUB AND FOR CALCULATION STARTING FROM RECIRCULATED CHARGE DISTRIBUTION GIVING LOWEST OUTPUT POWER. $f = f_o + 0.3$, $V_K = 1.13$ V, $V_K/V_H = 1.13$

the residual bunching can have a much greater effect on pass-to-pass variations than was evident in the profiles of Figure 77. A set of eight passes was computed for a midband case with the peak input power reduced to 0.01Po. Under these conditions the details of the residual space charge bunching had a significant effect on the power computed. The pass-to-pass variations for this case were shown in Figure 36. Variations from no gain to over 20 dB of gain were observed depending on the amount and phase of the residual bunching. Figure 81 shows a set of rod profiles at the start of successive passes similar to those in Figure 77, but with the input power reduced to 0.01Po.

These results suggest that operation may never settle to a steady state. Previously, it had been believed that if debunching were imperfect we would obtain stable gain, but with large variations as a function of frequency as the phase of the feedback changed. Instead the results of Figure 78 suggest that even at a single frequency, the problem may continue to fluctuate erratically as a function of time. As discussed in the next section, such a signal could be represented as a sine wave plus random noise. A problem in a high gain design is how to avoid these deleterious effects of incomplete debunching in the drift space. Two possible approaches to this are discussed in Section 5.

If the output of the CFA occurs in the region of a broad spoke, the debunching takes place somewhat differently. The same tumbling occurs in the drift space, but the debunching seems more

FIGURE 81

ROD PROFILE PLOTS AT THE START OF SUCCESSIVE PASS CALCULATIONS FOR PASSES 2-8--MID BAND CASE WITH REDUCED DRIVE POWER. $f = f_o + 0.3$, $V_K = 1.3\ V_1$, $V_K/V_H = 1.13$, $P_{in} = 0.01$ Po. Powers generated at the end of each pass are listed at the top of each profile plot. In this case, there is great dependence of the output power on the input power charge distribution.

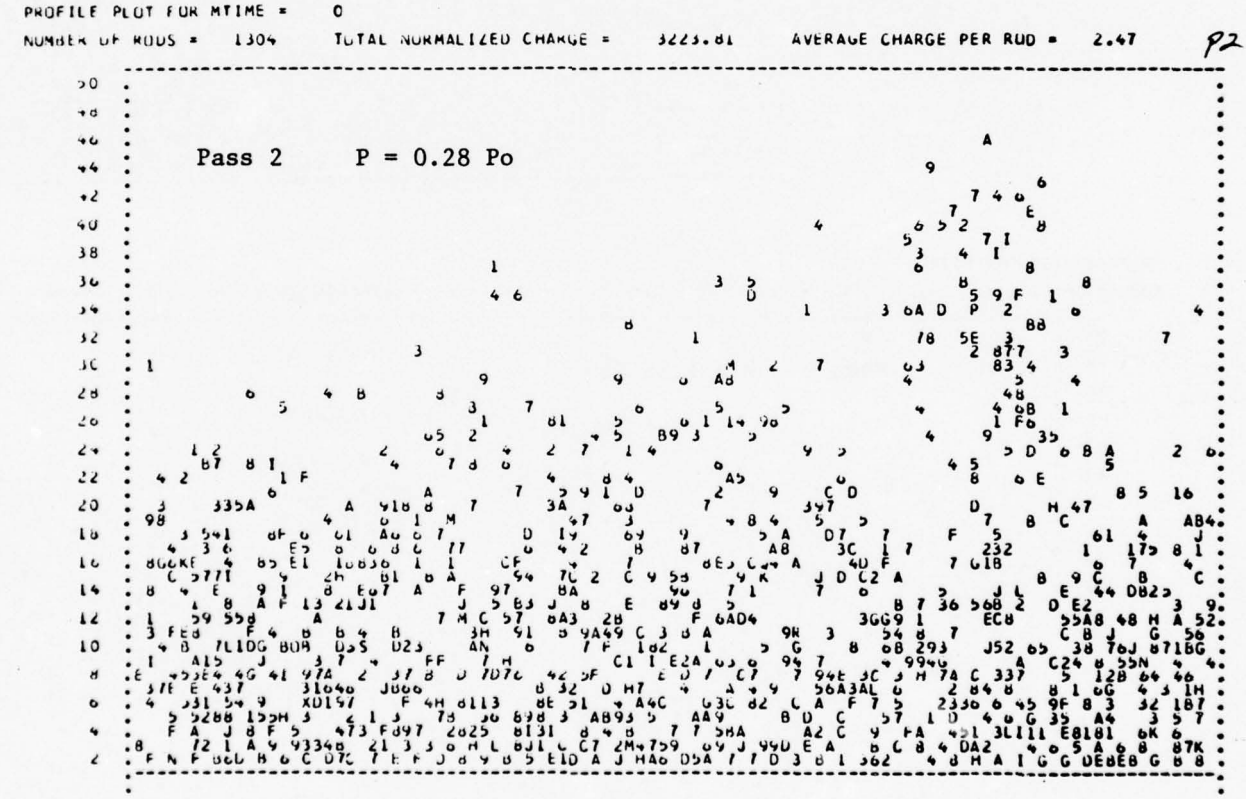

FIGURE 81 (continued)

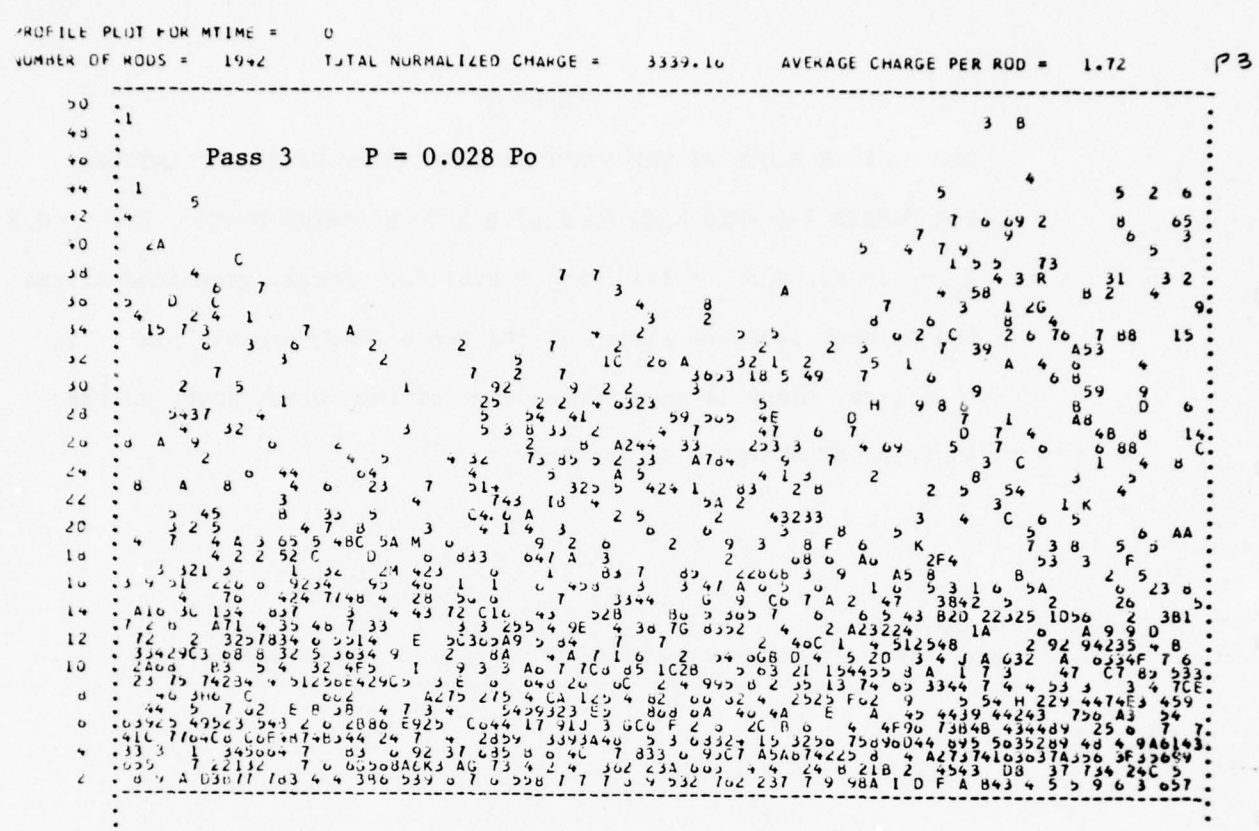

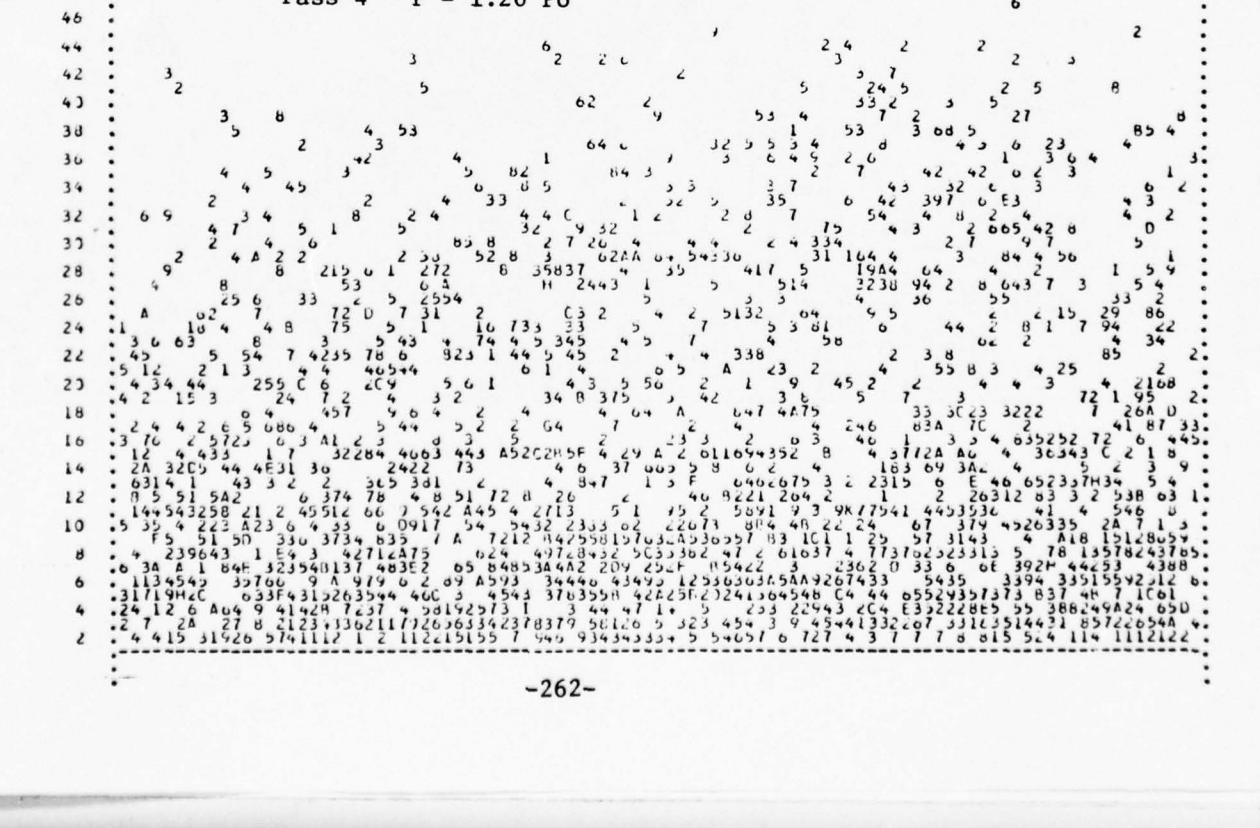

FIGURE 81 (continued)

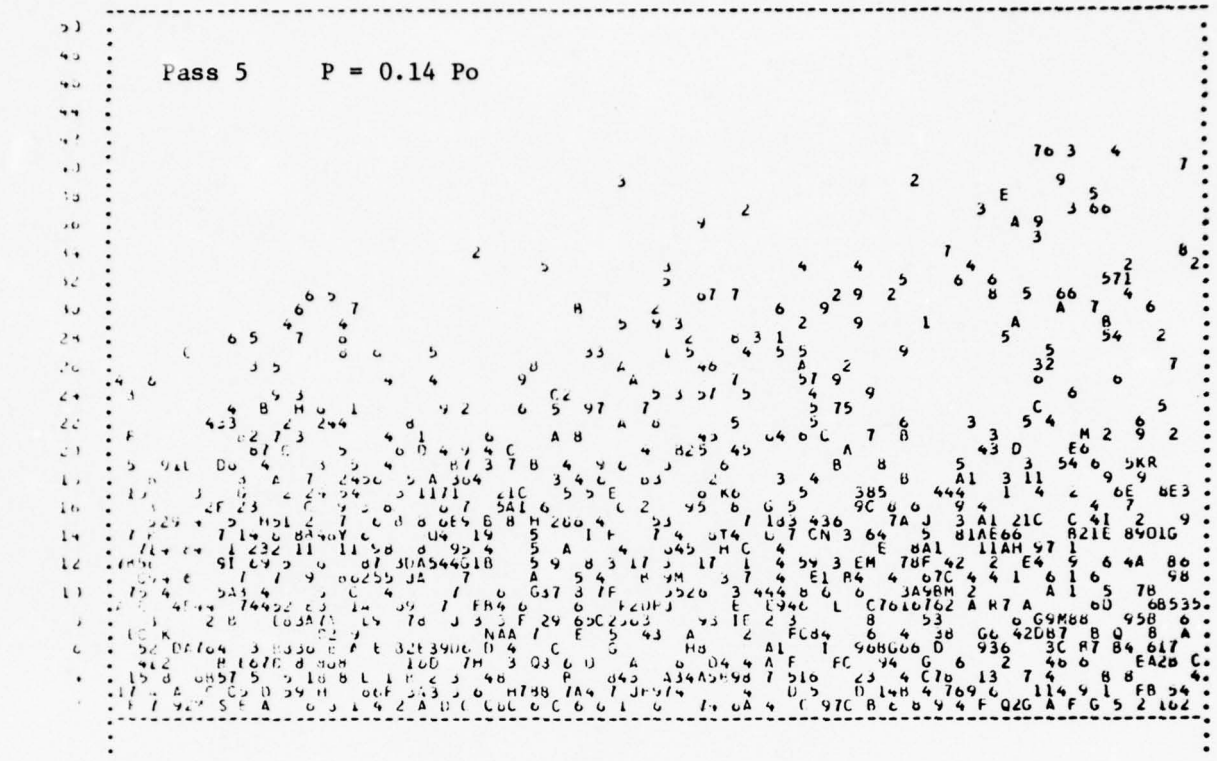

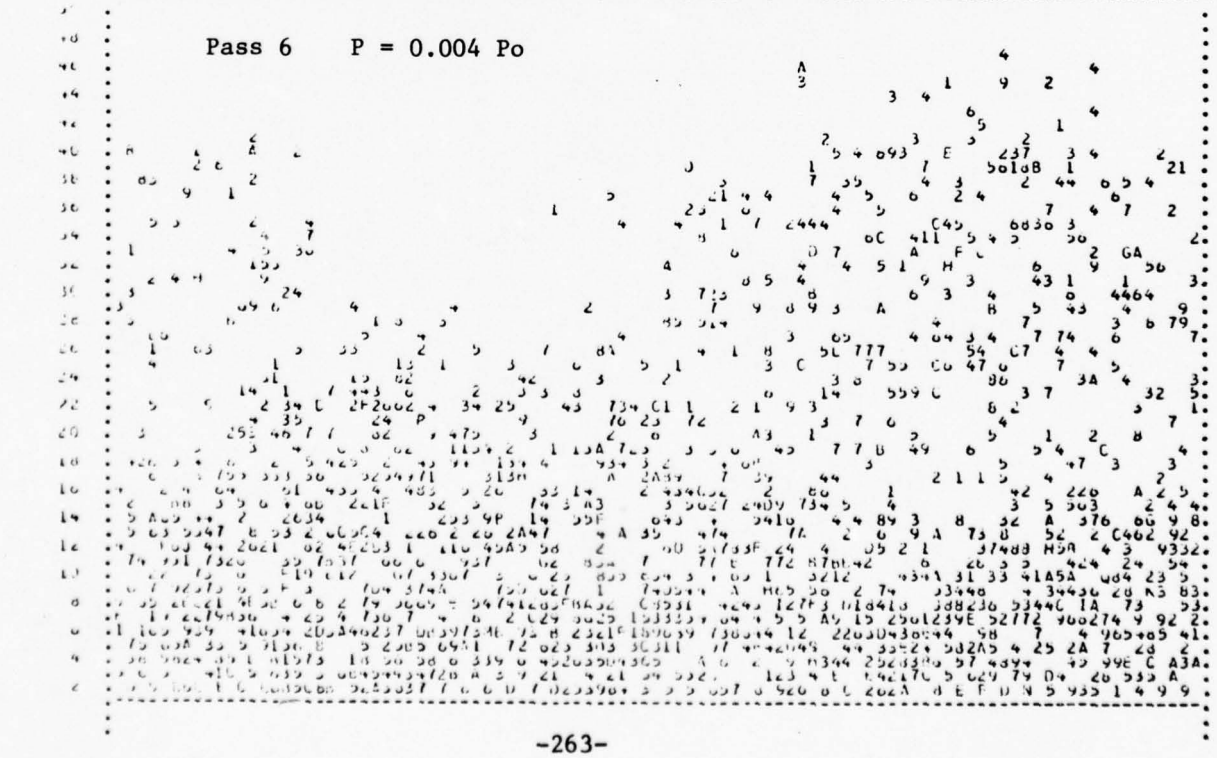

FIGURE 81 (concluded)

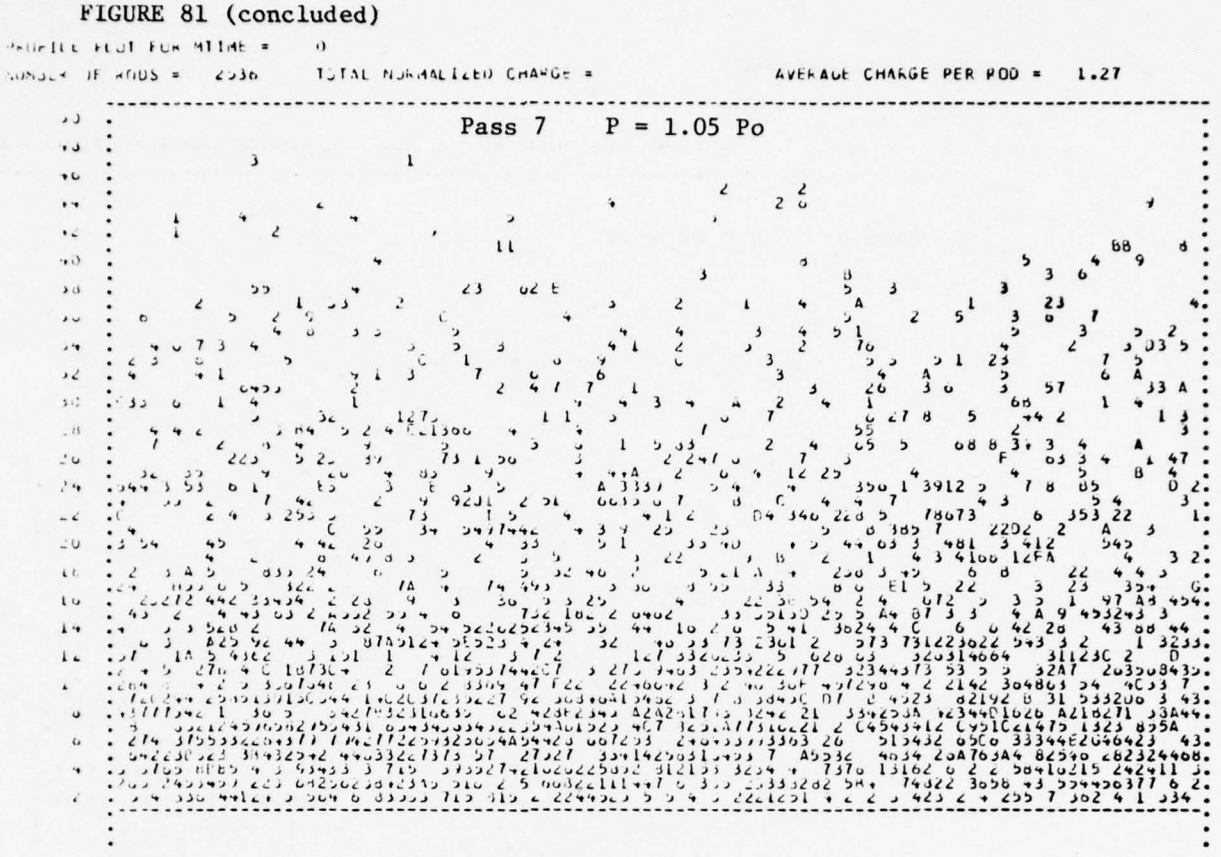

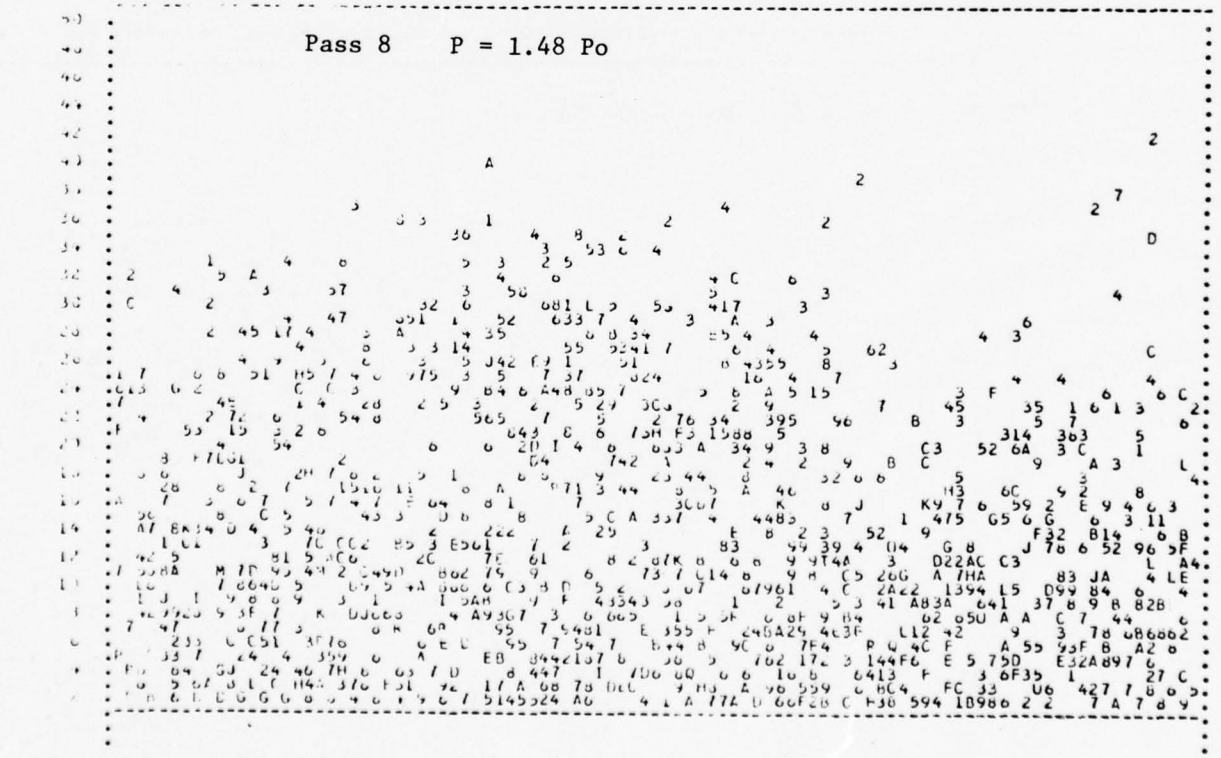

complete, and the entire region from the hub surface to the anode becomes filled with charge. Figure 82 shows the charge at the end of the interaction space for Pass 4 of a calculation at the high end of the band. Figure 83 shows the debunching of this charge in the drift space.

A charge distribution of the kind shown in Figure 83 can lead to either very high or very low gain on the subsequent pass, depending on the location of the level within the charge at which the E_x/B ratio is equal to the circuit wave velocity. If this level is close to the anode, the recirculated charge will interact with the wave, and the gain will be high. If the synchronous layer is far from the anode, there will be a substantial charge above this layer which has a velocity greater than synchronism. This is the problem which developed in the high frequency case for $V/V_H = 1.18$. (See Figure 40.) On the early passes there was substantial gain, but the calculation ended where the spoke was still broad. This gradually led to a broad recirculated charge distribution with a synchronous layer far from the anode and thus essentially no gain.

The attainment of a broad charge distribution at the input is not bad is we adjust the synchronism conditions to properly utilize it. This is apparently what we are accomplishing with the anode-cathode spacing taper in the SFD-261. This tube is made to perform satisfactorily over the band by changing from a uniform to a tapered interaction space geometry. (The taper is that of Table VII.) This taper increases the spacing at the input and hence reduces the velocity of the recirculated charge near the anode so that it interacts properly with the circuit wave. The computer modeling

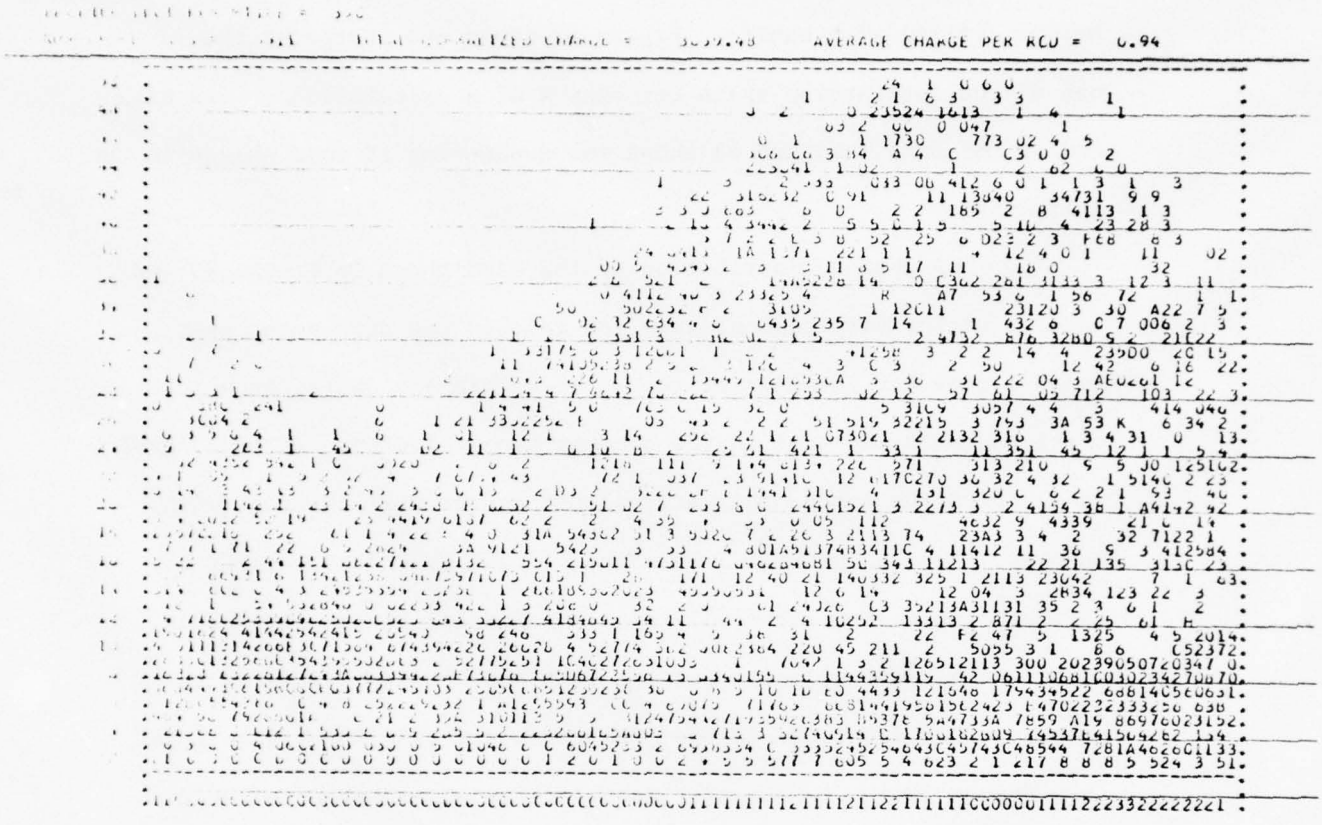

FIGURE 82

ROD PROFILE PLOT OF BROAD CHARGE DISTRIBUTION EXISTING AT THE END OF THE FOURTH PASS OF A CALCULATION AT THE UPPER END OF THE BAND. $f = f_o + 0.5$, $V_K = 1.28\ V_1$, $V_K/V_H = 1.185$.

FIGURE 83

ROD PROFILE PLOTS SHOWING DEBUNCHING OF THE DISTRIBUTION OF FIGURE 81 IN THE DRIFT SPACE. Drift space starts at time step 350 and ends at Step 400. Plots are shown every 10 time steps. Interaction box moves forward $0.13\ D_2$ in 10 time steps.

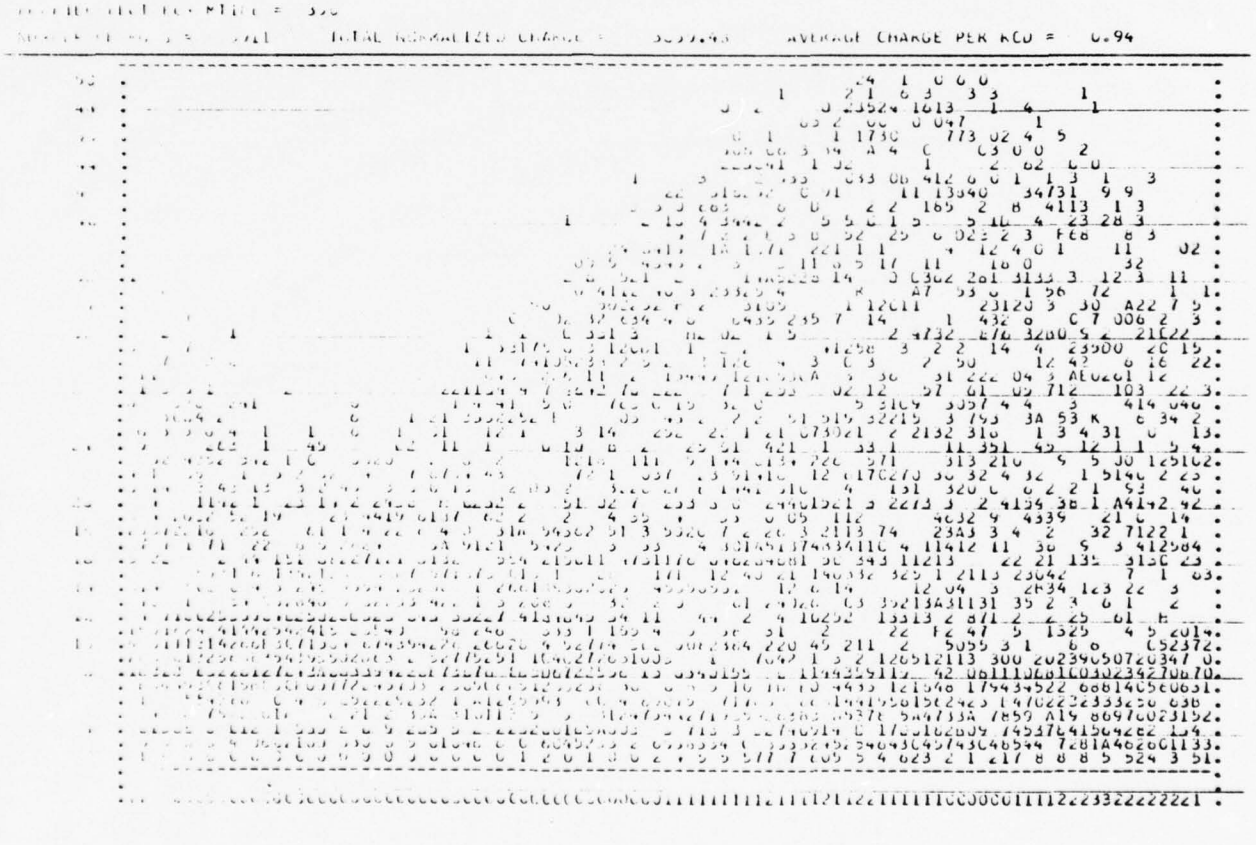

FIGURE 83 (continued)

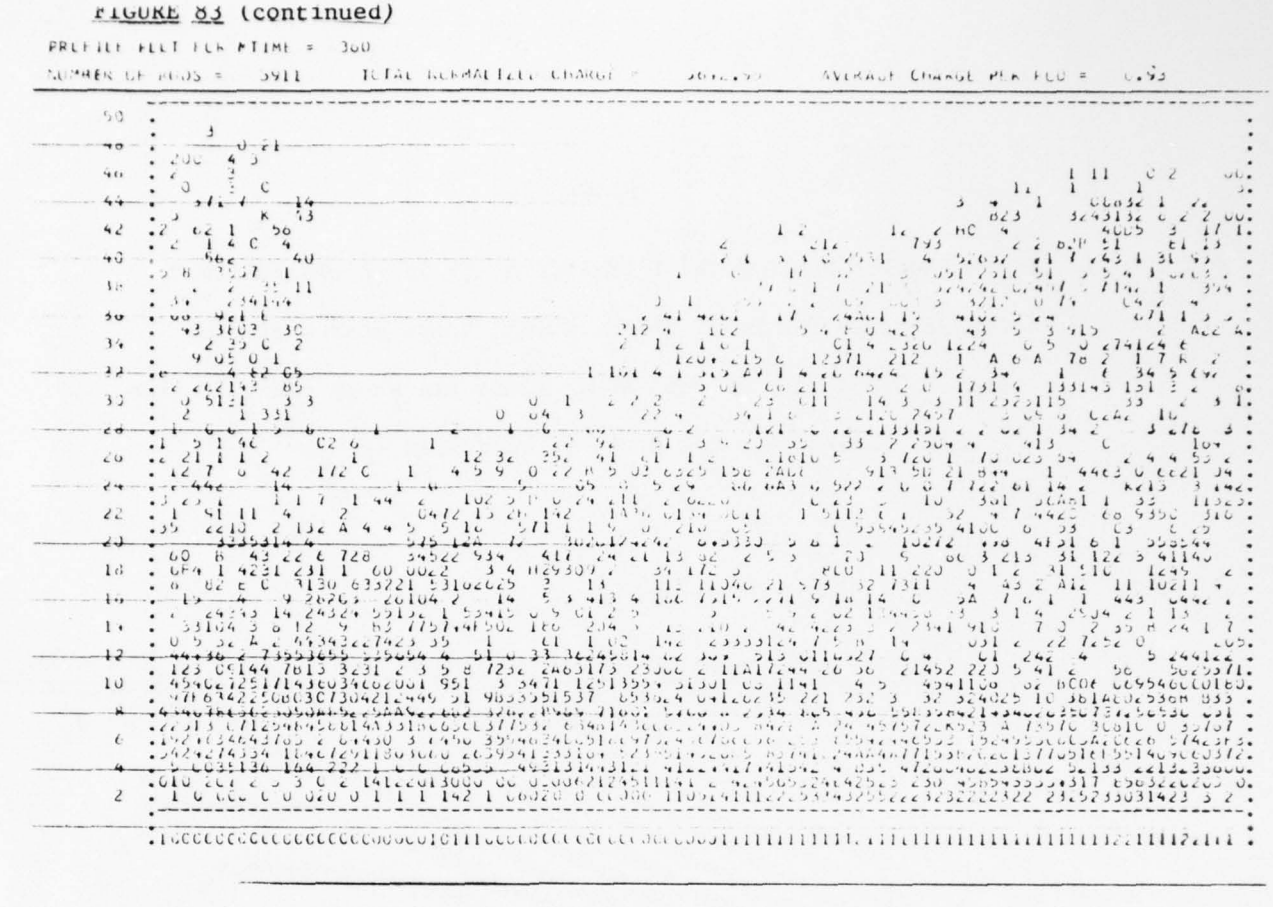

FIGURE 83 (continued)

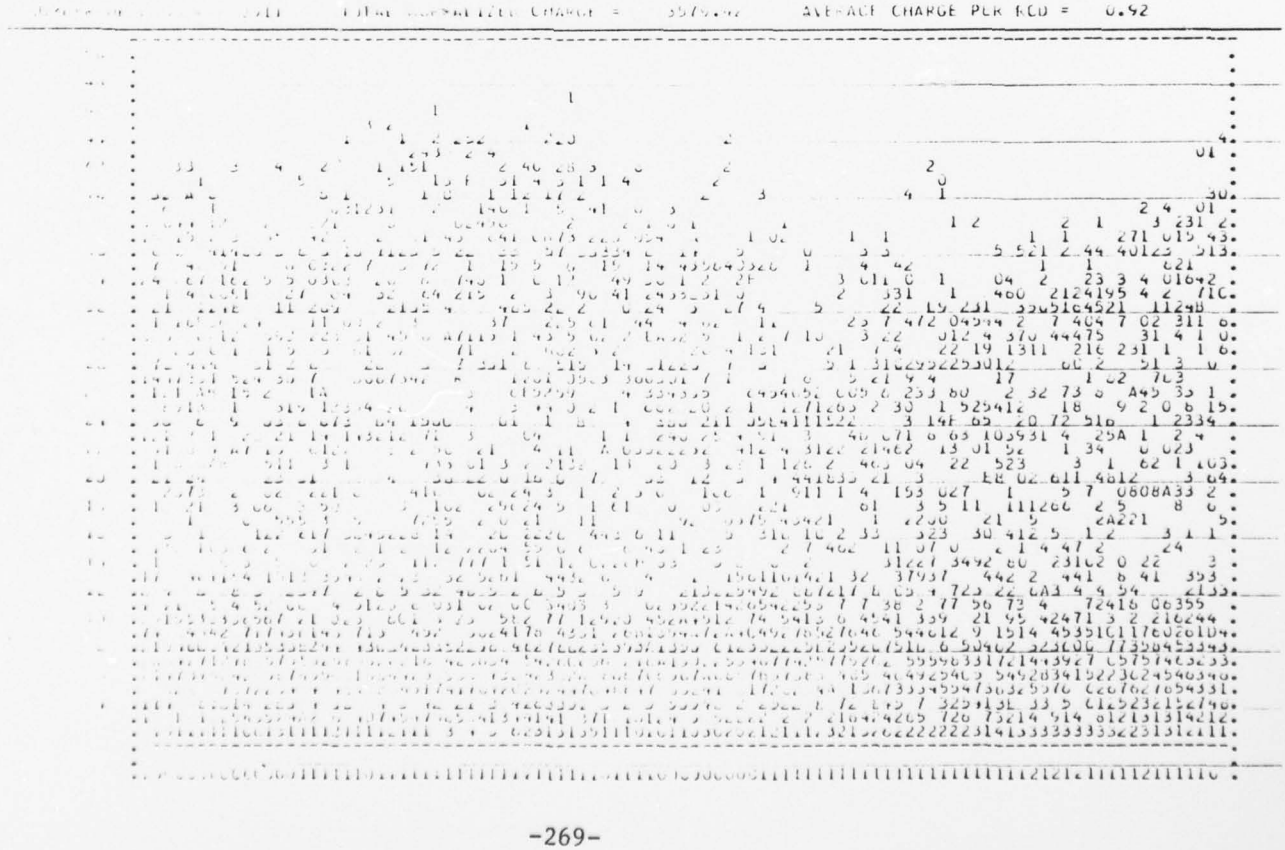

Figure 83 (concluded)

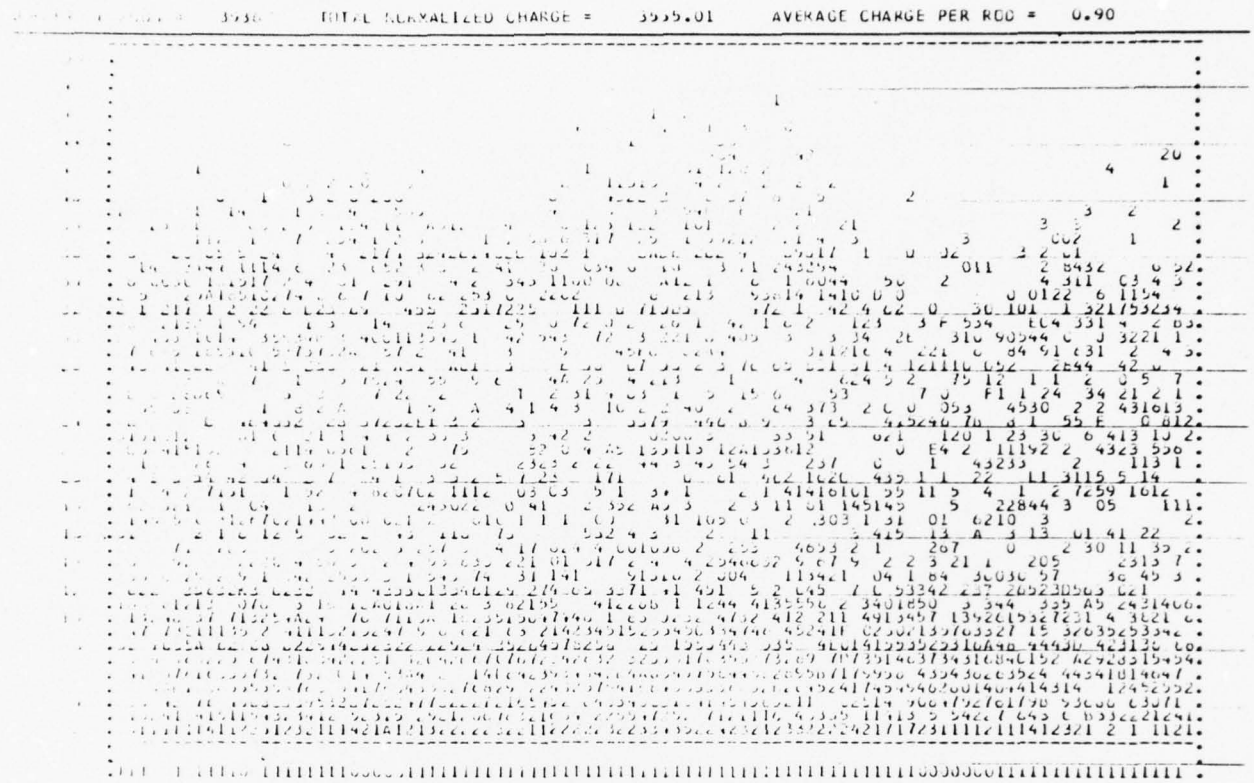

studies thus suggest that the main role of the taper is to optimize the interaction space for interaction with the recirculated charge at the input and the hub at the output.

In Section 5 we will discuss a possible design which utilizes a broad charge distribution at the input which was, in turn, generated by tapering the interaction space just before the output to draw charge above the hub surface.

4.4.2 Effect of Recirculated Charge on Noise

It has been suggested that pass-to-pass variations of the type shown in Figure 36 actually occur in a real CFA. Our discussion up to now has tacitly assumed that the effect is a real one and not just a numerical effect. If such variations do occur, they will make themselves evident in the form of noise. Band limited noise in the presence of a coherent signal shows up in the time domain as amplitude and phase modulation of the signal at a rate whose maximum frequency is limited by the bandwidth. Using the circuit bandwidth (about twice the operating bandwidth of the CFA), we find that the maximum modulation period is about one-fifth of the time it takes for one transit of the RF wave around the CFA.

The computer model implies output variations (the pass-to-pass variations) which occur at a periodicity corresponding to the transit time of the space charge around the CFA (typically 18 wavelengths). Thus if in the computer model we start a calculation and follow one wavelength through the CFA, 18 similar ones follow it before the space charge of the first wavelength has returned to the input. When this charge has returned to the input, the input conditions change and remain fixed for a new 18 wavelengths. The pass-to-pass variations in the computer model thus imply a random step function of output as shown in Figure 84. A random function of this nature with its harmonics could well fill the CFA pass band with the broadband noise that is observed.

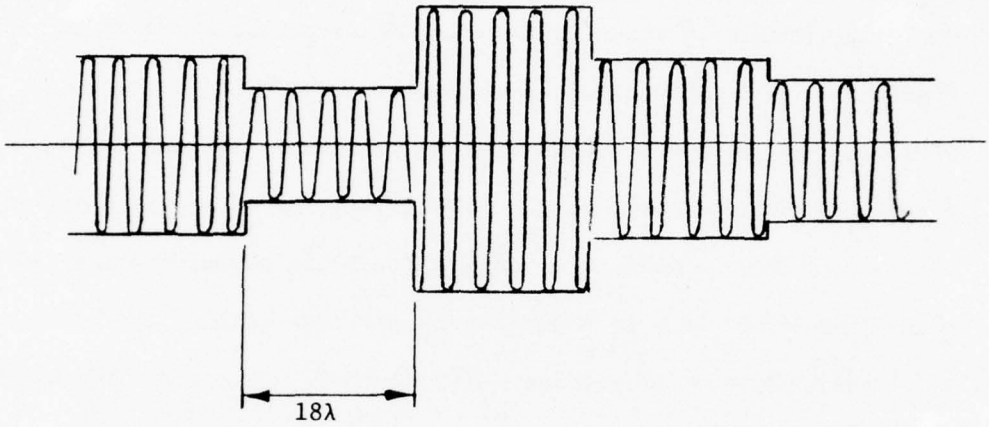

FIGURE 84

SPECTRUM OF THE OUTPUT WAVEFORM IMPLIED BY THE COMPUTER SIMULATION MODEL. Sudden changes occur when there is a change in recirculated charge distribution.

The waveform of Figure 84 could not actually be transmitted by the CFA because of its bandwidth limitation. There would be some smoothing of the sudden transitions. In addition, over a long period of time the detail of the 18 succeeding wavelengths probably changes so that they are not as identical as shown in Figure 84. A waveform such as shown in Figure 84 would suggest periodicities in the spectrum with a periodicity of 1/18 the base frequency. No such periodicity is observed in the measured spectra.

There appears to be at least a rough correlation of the conditions which lead to high pass-to-pass variations in the computer model with those which produce noisy operation of a CFA. Figure 36 shows the pass-to-pass variations for the calculations reported in Section 3. Also shown are the pass-to-pass variations observed when the input power is dropped to 1 KW. Low input powers or high applied voltages are regions of high noise in a CFA, and they are also regions of high pass-to-pass variations in the computer model. The correlation is, however, imperfect, e.g., for the lowest voltage at mid-band the percentage variations are larger than they are for the next highest voltage, whereas the noise output increases continuously with increasing voltage.

We have attempted to estimate the order of magnitude of the envelope variations which might occur in a real CFA in the presence of broadband random noise to see how they compare to pass-to-pass variations generated by the computer model. It appears that the broadband noise in the round cathode instrumented

CFA integrated over the full frequency spectrum could amount to as much as 1% of the total output. (This is a crude estimate from spectrum photographs.) Using a broadband noise output, we have tried to estimate the magnitude of the envelope fluctuations by the method shown in Figure 85. We have started with an interfering coherent signal 20 dB down on the carrier and have found that it results in a modulation envelope with a ratio of a maximum-to-minimum instantaneous power of about 1.5. If we split the interfering signal into two coherent sidebands having the same total power, we find the ratio increases to 1.75. For the higher peak to rms ratios characteristic of random noise, we could expect ratios of maximum-to-minimum power as high as two for only 1% noise power content. Thus a real CFA appears capable of substantial short term variations in power.

The above type of analysis has led us to question whether the pass-to-pass variations as determined from the computer model are perhaps too small. Since there are no random inputs to the model, this is entirely possible. The possibility of adding randomness to the emission procedure should be considered in the future.

Correlation of CFA noise with the space charge recirculation and the consequent pass-to-pass variations would be compatible with the finding that noise may be reduced by a scraper electrode on the anode side of the drift space.

If the pass-to-pass variations are indeed a source of noise, they appear to represent a source of noise other than at

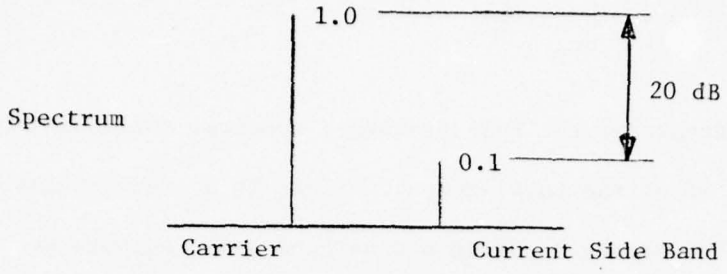

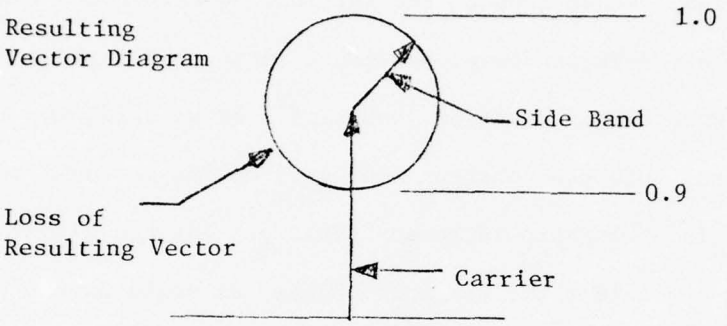

$$\frac{\text{Pi Max}}{\text{Pi Min}} = \frac{(1.1)^2}{(0.9)^2} = 1.49$$

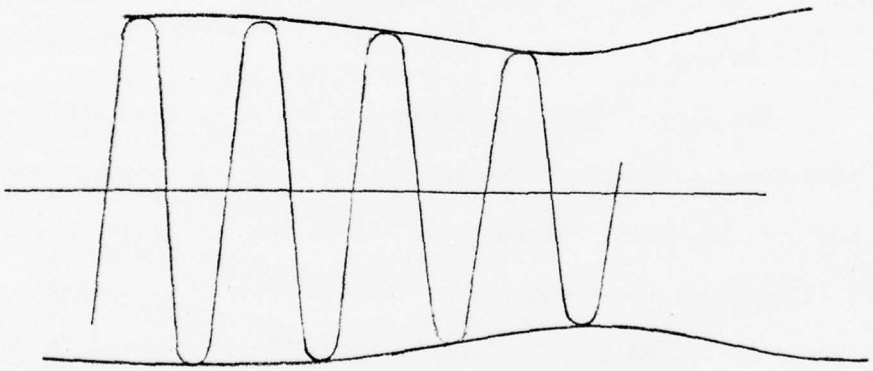

Resulting Modulated Waveform

FIGURE 85

SKETCH OF ILLUSTRATING INTERFERENCE OF A CARRIER AND A SINGLE COHERENT SIDE BAND. Spectrum is shown at top. Vector diagram of addition of carrier and side band in a frame of reference rotating at the carrier frequency is shown in the center. Resulting modulated waveform is shown at bottom.

the cathode. The variations may be enhanced by other variations such as the variation in spoke density at the output which may in turn relate to variations at the cathode. However, there is the possibility that some of the variations lie in the feedback process itself. The variations may actually have a pseudo-random nature similar to that of a random number generator used in computer modeling.

It is our present hypothesis that the pass-to-pass variations represent an imperfect model of an instability which is capable of causing noise in a real CFA. It is possible that a real CFA includes additional effects which are not included in the model because of the lack of random inputs to the model. A correlary to this hypothesis is that changes to a CFA which permit the computer model to run with smaller pass-to-pass variations will in turn reduce the noise output of a CFA. It is to be emphasized that this is a hypothesis--not an established result.

The discussion of noise and pass-to-pass variations helps shed insight on how noise will eventually be represented in a computer model; it will simply appear as random variations of amplitude and phase of the output wave. Processes which are capable of producing such variations are thus potential sources of noise. Processes which do not readily affect the output are not likely sources of noise.

5.0 APPROACHES TO CFA DESIGN BASED ON THE COMPUTER MODELING STUDIES

The computer modeling studies are as yet incomplete, and in the case of the tapered interaction cases, they are certainly flawed. However, the general description of forward wave CFA performance which is arising from these studies will probably not be basically altered by future refinements to the modeling. It is therefore meaningful to see what the modeling studies tell us about how we should go about designing a CFA for 20 dB gain.

The discussion in Section 4.2 showed that we cannot increase gain simply by increasing length. The interaction in an emitting sole CFA is not the usual coupling of circuit and space charge waves which gives rise to small signal gain but is rather a large signal effect which requires "capturing" of the space charge by the RF fields. Below certain values of input power, the RF fields become too weak for the interaction to take place effectively.

We could design a CFA in which the input power is adequate to draw charge from the hub. Unfortunately, the output power which may be efficiently obtained from such a CFA is only about 13 to 15 dB above the input power. Many CFA's, the SFD-261, included work in this mode of operation.

One could consider improving the interaction at the input by increasing the hub velocity until it becomes more nearly synchronous with the RF wave. A design of the type shown in Figure 86 was investigated on a study program for the U. S. Air Force Avionics

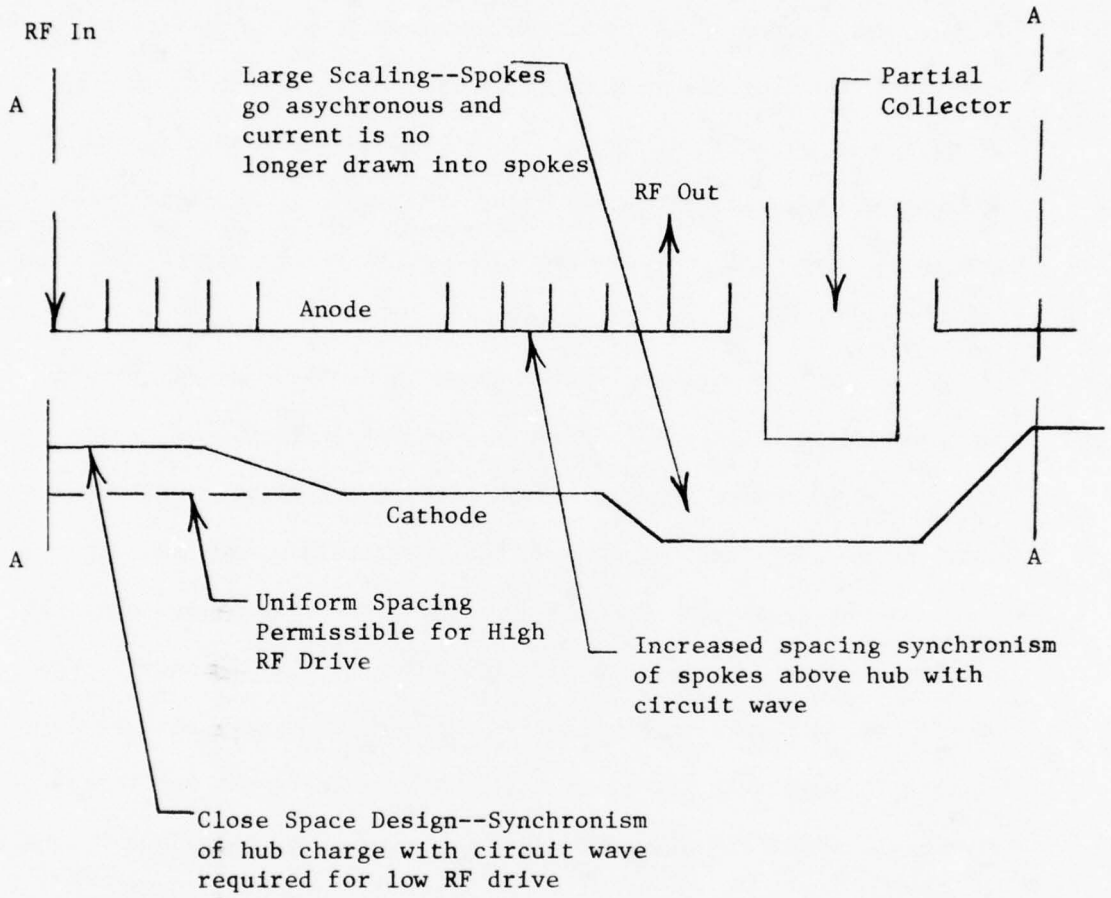

FIGURE 86

SKETCH SHOWING REGIONS OF A PARTIALLY REENTRANT CFA. Sketch is unwrapped into linear form. Actual CFA is in circular format and is joined at Planes A-A. Sketch is not to scale--vertical dimension greatly exaggerated.

Laboratory.[5] The concept here was to skim off recirculating charge above the hub by a skimmer electrode in the drift space to minimize noise. Interaction with a weak RF signal was to be obtained by increasing the cathode to Hartree voltage ratio near the input to about 1.4 by using a relatively close anode-cathode spacing. Once charge was drawn above the hub level, the anode-cathode spacing was to be increased to lower the V_K/V_H ratio to the normal operating range for the formation of spokes.

The computer simulation showed that 20 dB of gain could be obtained in this manner. However, it was difficult to control the amount of charge drawn above the hub at the input. Our simulations resulted in a large amount of charge drawn from the hub over a short distance. Further down the tube, this charge impinged on the anode in a highly concentrated manner. The high dissipation density would have severely limited average power capability. This study is reported in detail in the final report on the Air Force contract. While the approach of Figure 86 was not ruled out by our failure to arrive at a satisfactory design in this initial study, it did appear that the approach is more difficult to successfully implement than some other possible approaches.

The alternative to making a weak input signal interact with the hub is to have it interact with recirculating space charge above the hub level. This is apparently what is being accomplished with the various taper geometries discussed in Volume 1 of this report, which describes the experimental effort. On the above

referenced Air Force contract we made a preliminary design simulation of a CFA having an anode-cathode spacing tapered as shown in Figure 87. The spacing at the input was intended to optimize interaction with the recirculating space charge. Further down the CFA the spacing was changed to a value which would draw fresh charge from the hub and continue the interaction. The change in spacing was introduced at a point where most of the recirculating charge had been drawn up to the anode. By the end of the second region, narrow well formed spokes were formed. If these spokes were allowed to proceed into the drift space, they did not yield enough charge above the hub at the input to provide the required gain. Thus, another spacing change was made over a short distance at the output to draw additional charge from the hub. This provided the charge required above the hub required to obtain the desired gain at the input.

The simulation of this design was of a preliminary nature without the calculation of a number of passes. Simulations were conducted only at the highest frequency in the band where it is hardest to get gain. The process of synthesizing the design and the detailed results are presented in the final report on the Air Force study.[5] The design was for an X-band CFA at the 150 kW peak output power level. This design employed a double helix, slow wave circuit of the type sketched in Figure 88. Characteristics of this assumed circuit were obtained by frequency

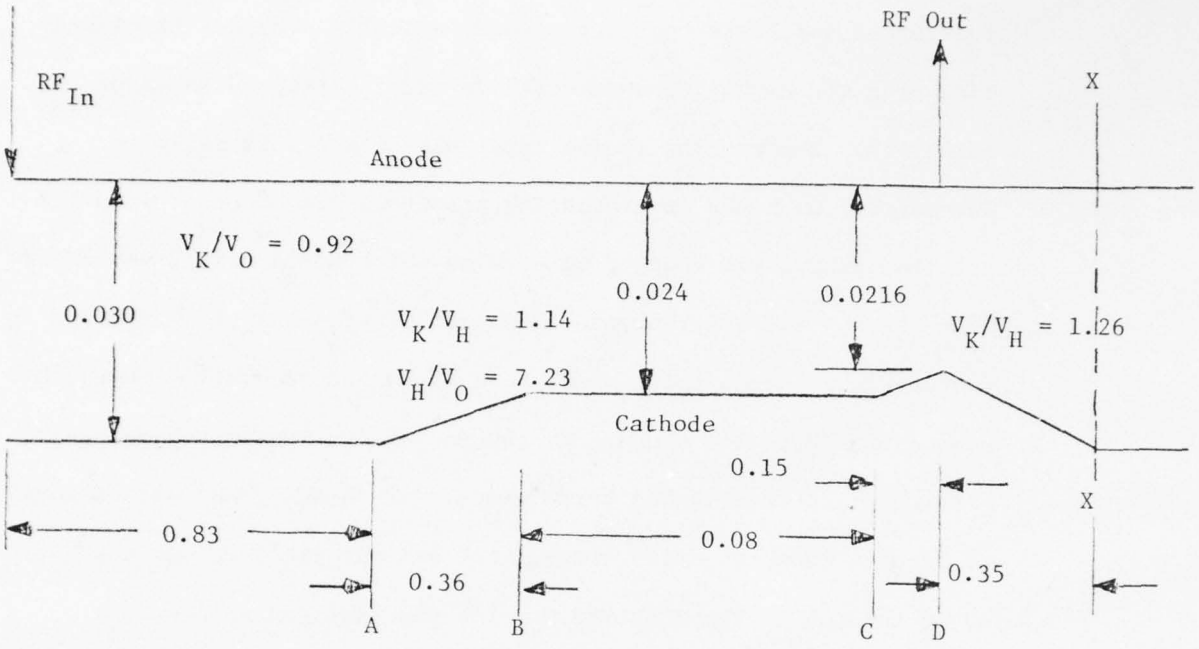

DISTANCE--Inches

FIGURE 87

ANODE-CATHODE SPACING TAPER SYNTHESIZED FOR A REENTRANT X-BAND DESIGN. Interaction space in circular format is closed on itself at plane X-X. Vertical scale is exaggerated by a factor of 20.

AD-A065 736 VARIAN ASSOCIATES BEVERLY MASS F/G 9/1
CFA DESIGN IMPROVEMENT PROGRAM. VOLUME II. COMPUTER MODELING ST--ETC(U)
JUN 78 H L MCDOWELL N00123-75-C-1294
UNCLASSIFIED NL

4 OF 4
AD
AD 65736

END
DATE FILMED
5-79
DDC

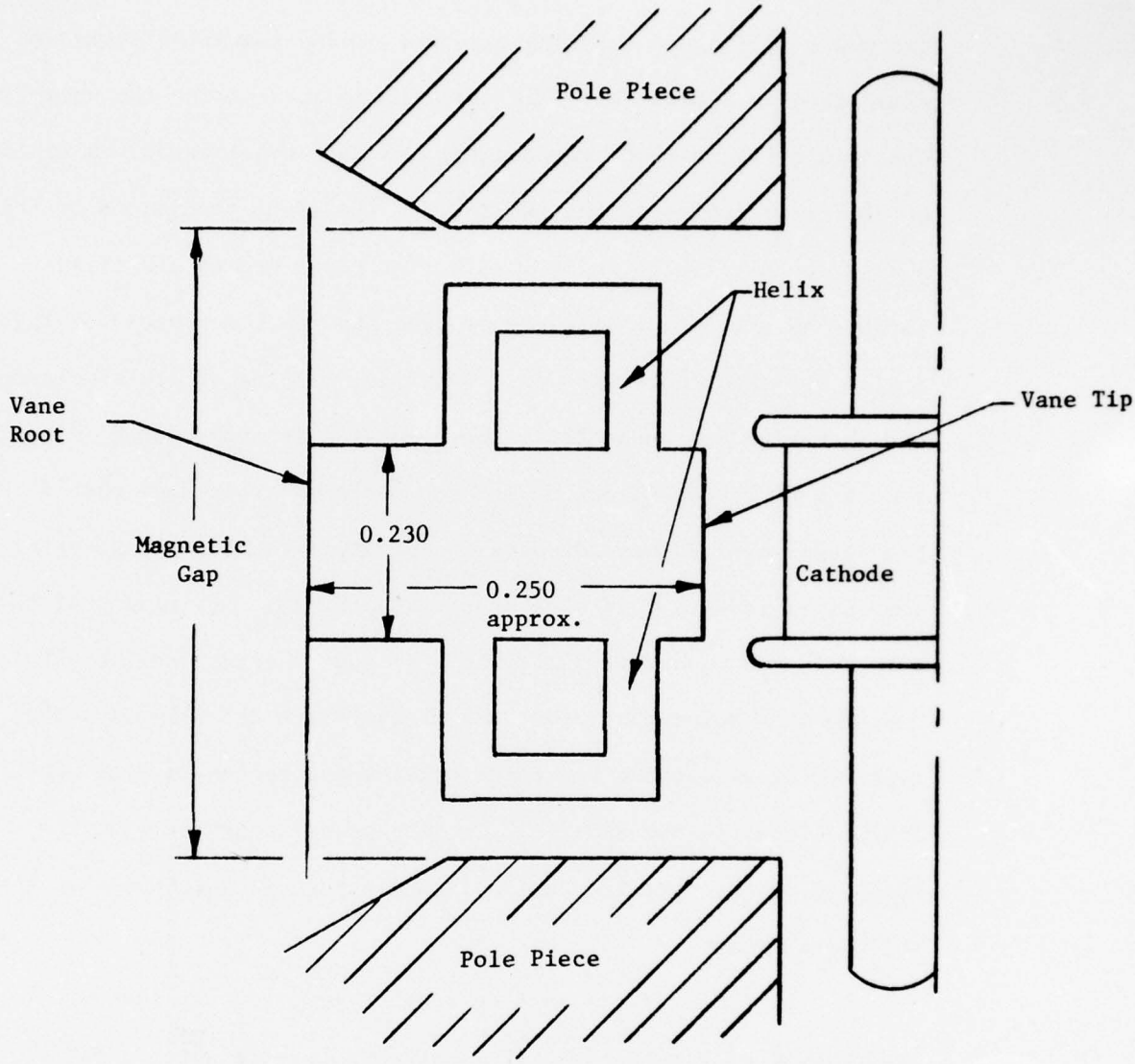

FIGURE 88

DOUBLE HELIX, COUPLED VANE CIRCUIT WITH DIMENSIONS FOR AN X-BAND CFA. Pitch of the circuit at the anode bore is 0.024 inch for the forward wave CFA designs studied.

and power scaling an existing circuit. These characteristics are summarized in Table XIV. This circuit had about twice the normalized width (width/free space wavelength) and half the interaction impedance of the circuit used in the SFD-261. The input conditions of the simulation are listed in Table XV. The power growth and dissipations as a function of distance from the input computed for this design are shown in Figure 89. The final results of the simulation are summarized in Table XVI. These results are reproduced directly from the final report on the Air Force study. They show that a peak power of 1 kW was adequate to develop a peak output power of 150 kW. This is a gain of approximately 22 dB. Efficiency of this X-band design was about 50%. This CFA had an electrical length (length in wavelengths) about 50% greater than the SFD-261. The relative anode-cathode spacing in the output region is also about 10% less than in the SFD-261. These changes, together with the taper design to optimize recirculating charge, are responsible for the higher gain.

If this design were scaled to the frequency and output power level of the SFD-261, it would operate with about 1/8th of the present input power and have an average power capability several times that of the SFD-261. The price paid for these improvements would be a physically larger tube. These results are quoted only to show how the computer model may in the future be employed in CFA design. No suggestion that this specific design should be

TABLE XIV

PROPERTIES OF FORWARD WAVE, SLOW

WAVE CIRCUIT ASSUMED IN THE DESIGN CALCULATIONS

Circuit Pitch (d)	0.024 ins.
Circuit Height (parallel to B) (h)	0.230 ins

Properties as a Function of Frequency

Frequency	9.5	10.0	10.5	GHz
Phase Shift per Section (θ)	90	103	116	degs.
Interaction Impedance (K)	20	16	15	ohms
Attenuation per Inch	1.39	1.39	1.39	dB/in
PHase Velocity/C	0.076	0.070	0.066	
Synchronous Voltage (Vo)	1525	1290	1121	volts

TABLE XV

PRELIMINARY REENTRANT CFA DESIGN

SIMULATION--CONDITIONS OF THE SIMULATION

Circuit--Double helix coupled vane--See Figure 88 and Table XIV.

Anode-Cathode Spacing	0.030-0.022 See Figure 80
Active Circuit Length	90 periods 2.154 inches
Drift Space Length	15 period 0.360 inches
Anode Bore Diameter	0.802 inches
Diameter at Vane Root	1.300 inches (approx.)
Vane Thickness Tip	0.012 inches (half of period)
Vane Thickness Root	0.026 inches (slot width fixed vane tapers)
Vane Thermal Impedance	5.7 °C/watt
Frequency	10.5 GHz
Cathode Voltage	-9262 volts
Magnetic Flux Density	7632 gauss
Peak Input Power	1.0 kW
Ratio V_H/V_O in Power Generating Region-- .024 a-R spacing	7.23
Ratio V_K/V_H--0.024 spacing	1.14

continued

TABLE XV

PRELIMINARY REENTRANT CFA DESIGN

SIMULATION--CONDITIONS OF THE SIMULATION

Anode Cathode Transit Angle--βa
0.024 spacing 1.99 radians

Cathode Secondary Emission Table Employed

Values for Beryllium Cathode

Incident Voltage	Secondary Emission Yield
0.0	0.0
100.0	2.2
200.0	4.2
300.0	5.0
500.0	5.0
2500.0	1.0

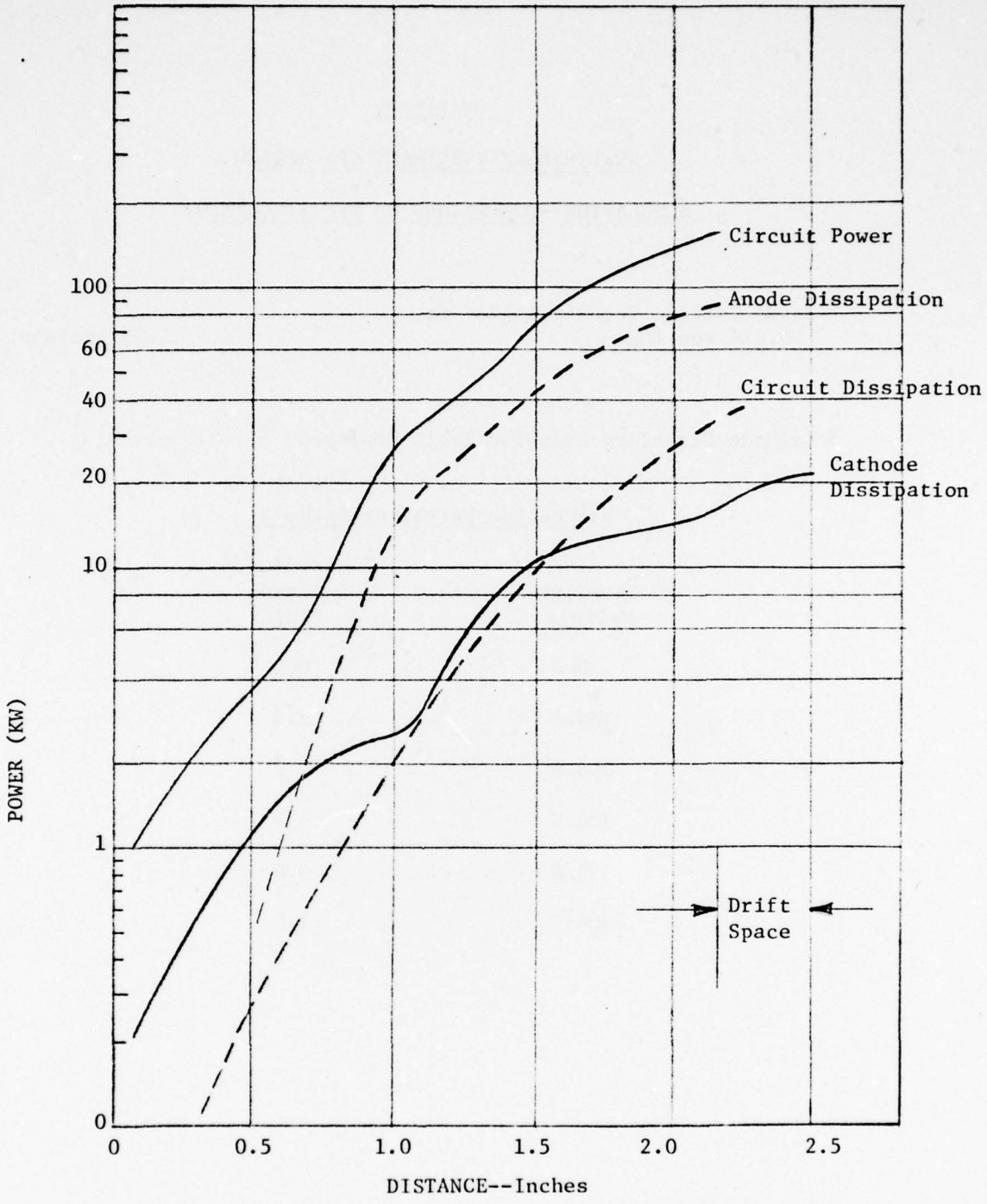

FIGURE 89

CIRCUIT POWER, CUMULATIVE DISSIPATION BY ELECTRON INTERCEPTION ON ANODE AND CATHODE AND CUMULATIVE DISSIPATION IN CIRCUIT ATTENUATION FOR A REENTRANT, X-BAND CFA DESIGN MADE USING THE COMPUTER MODEL.

TABLE XVI

PRELIMINARY REENTRANT DESIGN RESULTS

OF THE COMPUTER SIMULATION

Peak Output Power	158.8 kW
Dissipation by Electron Interception on Anode	91.5 kW
Dissipation by Electron Interception on Cathode	21.0 kW
Dissipation in Anode Circuit Attenuation	34.1 kW
Total Input Power--Sum of Above Powers	305.4 kW
Peak Current (I)	35.5 amps
Cathode Voltage (V_K)	9,262 volts
D.C. Input From $V_K I$	328.5 kW

Should equal sum of powers and dissipations if spoke charge conditions at start and end are identical. Unbalance of 7.5% is acceptable for preliminary calculation.

Gain	22.2 dB
Efficiency--based on average of above d.c. inputs	50 %
Average Output Power at .01 Duty	1,588 watts
Worst Case Average Dissipation per Vane by Electron Interception	20 watts
Worst Case Average Dissipation per Vane in Attenuation	100 watts
Estimated Thermal Impedance of Vane	5.7 °C/watt

continued

TABLE XVI

PRELIMINARY REENTRANT DESIGN RESULTS

OF THE COMPUTER SIMULATION

(continued)

Estimated Temperature Rise Vane Root to Tip	150 °C
(Assumes power dissipated in attenuation flows through half of thermal impedance, power dissipated by interception through whole thermal impedance.)	
Estimate Root Temperature	200 °C
Maximum Average Temperature	350 °C
Estimated Transient Temperature Rise Above Average for 10 Microsecond Pulse Length--(copper vane with maximum dissipation density on vane = 14 x average over vane).	150°C

RF Voltage and Field Ratios

	Input	Output
E_{RF}/E_{DC} at anode	0.045	0.565
E_{RF}/E_{DC} at Brillouin hub surface level	0.004	0.051
V_{RF}/V_{O} at anode	0.154	0.935
V_{RF}/V_{O} at Brillouin hub surface level	0.013	0.163

implemented is intended.

Another type of design simulated gave somewhat unexpected results. This is a non-reentrant design of the kind shown in Figure 90. A thermionic priming source is assumed near the input to initiate the charge build up. Our first pass calculations simulate a design of this type. Studies of this type of CFA have been undertaken on Air Force contracts both for Rome Air Development Center[4] and for the Avionics Laboratory.[5] On the first of these contracts, depressed collector designs for minimizing the efficiency penalty incurred by eliminating reentrancy were studied briefly. Such a collector is shown in the sketch of Figure 90. The simulations of this type of design have shown a surprisingly high gain with efficiency reduction of only 5 to 10 percentage points below a reentrant design. It is conceivable that the elimination of noise associated with reentrancy could make such a design useful for some applications.

Several non-reentrant designs have been studied on the Air Force contracts. Table XVII summarizes conditions for a design using the same slow wave structure as the reentrant design discussed above. Figure 91 shows power and dissipations as a function of length and Table XVIII summarizes the results of the simulation. Figure 91 shows the high dissipation on the cathode near the input which occurs when the hub builds up. Such high cathode dissipation appears to be characteristic of these non-reentrant designs. Cathodes for

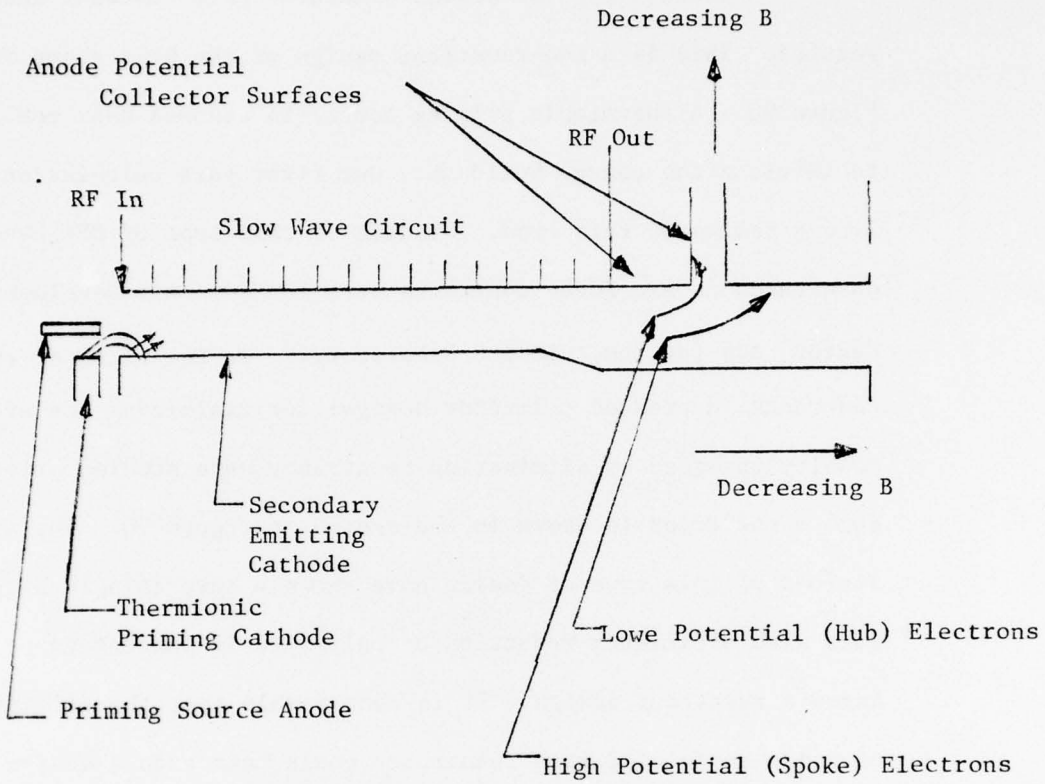

FIGURE 90

SCHEMATIC OF A NON-REENTRANT, EMITTING SOLE CFA. Such a CFA is simulated by the first pass calculations.

TABLE XVII

PRELIMINARY NON-REENTRANT CFA DESIGN--CONDITIONS

OF THE COMPUTER SIMULATION

Circuit--Double helix coupled vane--See Figure 88 and Table XIV.

Anode-Cathode Spacing	0.024 inches
Active Circuit Length	84-104 sections
	2.01-2.507 inches
Tube Format--Linear (Alternate design in circular format maintaining non-reentrant electronics is possible--circular format thermal impedances would be lower because of thickening of vanes at root.)	
Vane Thermal Impedance	9 °C/watt
Frequency	10.5 GHz
Cathode Voltage	-9262 volts
Magnetic Flux Density	7632 gauss
Peak Input Power	1.0 kW
Ratio V_H/V_O	7.32
Ratio V_K/V_H	1.14
Anode-Cathode Transit Angle--βa	1.99 radians
Cathode Secondary Emission Table	

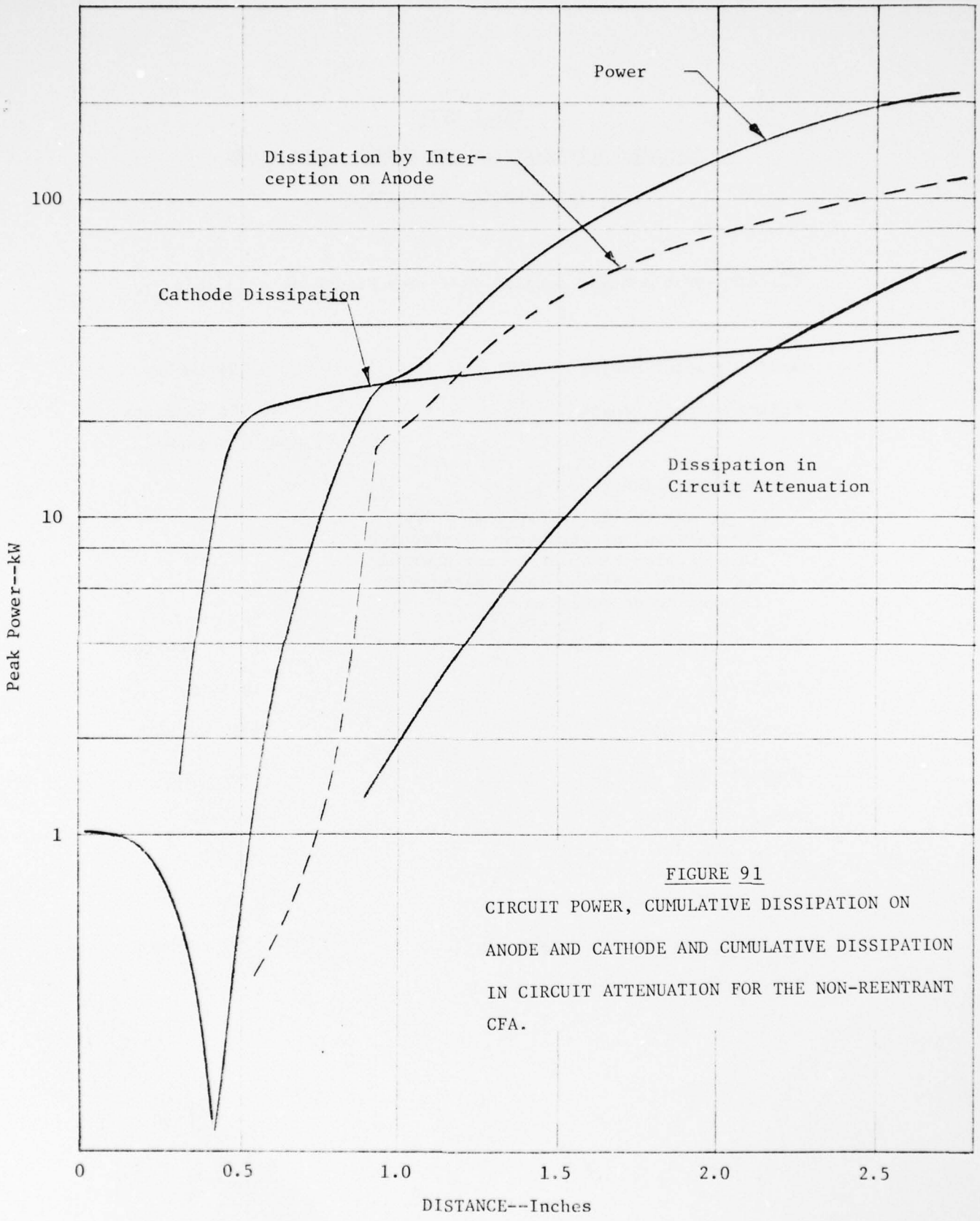

FIGURE 91

CIRCUIT POWER, CUMULATIVE DISSIPATION ON ANODE AND CATHODE AND CUMULATIVE DISSIPATION IN CIRCUIT ATTENUATION FOR THE NON-REENTRANT CFA.

TABLE XVIII

PRELIMINARY NON-REENTRANT CFA
DESIGN--RESULTS OF THE COMPUTER SIMULATION

	84 Sections	104 Sections	
Peak Output Power	133.4	209.9	kW
Gain	21.2	23.2	dB
Dissipation by Electron Interception on Anode	76.9	117.2	kW
Dissipation by Electron Interception on Cathode	32.8	37.7	kW
Estimated Collector Dissipation (See Table XI)	8.8	8.8	kW
Total D.C. Input	279.2	440.8	kW
Efficiency	47.8	47.6	%
Cathode Voltage	-9262		volts
Peak Anode Current	28.1	47.8	amps
Depressed Collector Voltage Relative to Cathode	+850		volts
Depressed Collector Current	5.2	5.2	amps
Assumed Duty	0.01	0.01	
Average Output Power	1334	2099	watts
Worst Cast Average Dissipation Per Vane--Electron Interception on Anode	18.4	14.8	watts
Worst Case Average Dissipation Per Vane--Attenuation	6.4	15.6	watts
Estimated Thermal Impedance of Vane	9.0	9.0	°C/watt
Estimated Average Vane Tip Temperature	395	404	°C

(Assumes power dissipated in attenuation flows through half of thermal impedance--power dissipated by interception through

continued

TABLE XVIII

PRELIMINARY NON-REENTRANT CFA

DESIGN--RESULTS OF THE COMPUTER SIMULATION

(continued)

	84 Sections	104 Sections	
whole thermal impedance. Vane root at 200°C.)			
Estimated Transient Temperature Rise for 10 Microsecond Pulse	150	150	°C

such CFA's would have to be designed with cathode cooling capability near the input comparable with the anode cooling capability. Figure 91 and Table XVIII show a gain on excess of 20 dB and an efficiency only slightly less than a reentrant design. It should, however, be pointed out that the assumed capability of the depressed collector has only been roughly estimated and subjected to neither computer simulation nor experimental verification. (The method of making the estimate is discussed in Reference 4.) Again, Tables XVII, XVIII and Figure 91 are taken directly from an Air Force report.[4]

The non-reentrant CFA obtains its gain at the input in an entirely different manner than the reentrant CFA. The gain mechanism has been considerably clarified by the computer simulation results. It involves initial bunch formation by secondary emission multiplication of the charge near the input in the presence of an RF field. The mechanism is sketched in Figures 92-96 which show sketches of the space charge configuration at various points along the length of the CFA. Each sketch shows one RF wavelength of the CFA. The "favorable phase"--the half wavelength in which electrons give up energy to the RF wave--is shown on the left in each sketch. The "unfavorable phase" is shown on the right.

Figure 92 shows the space charge configuration just downstream from the priming source. The cathode voltage is adjusted for synchronism between the E/B drift velocity of the electrons and the circuit wave. In this region, electrons in the unfavorable phase are absorbing energy from the circuit wave. If the resulting

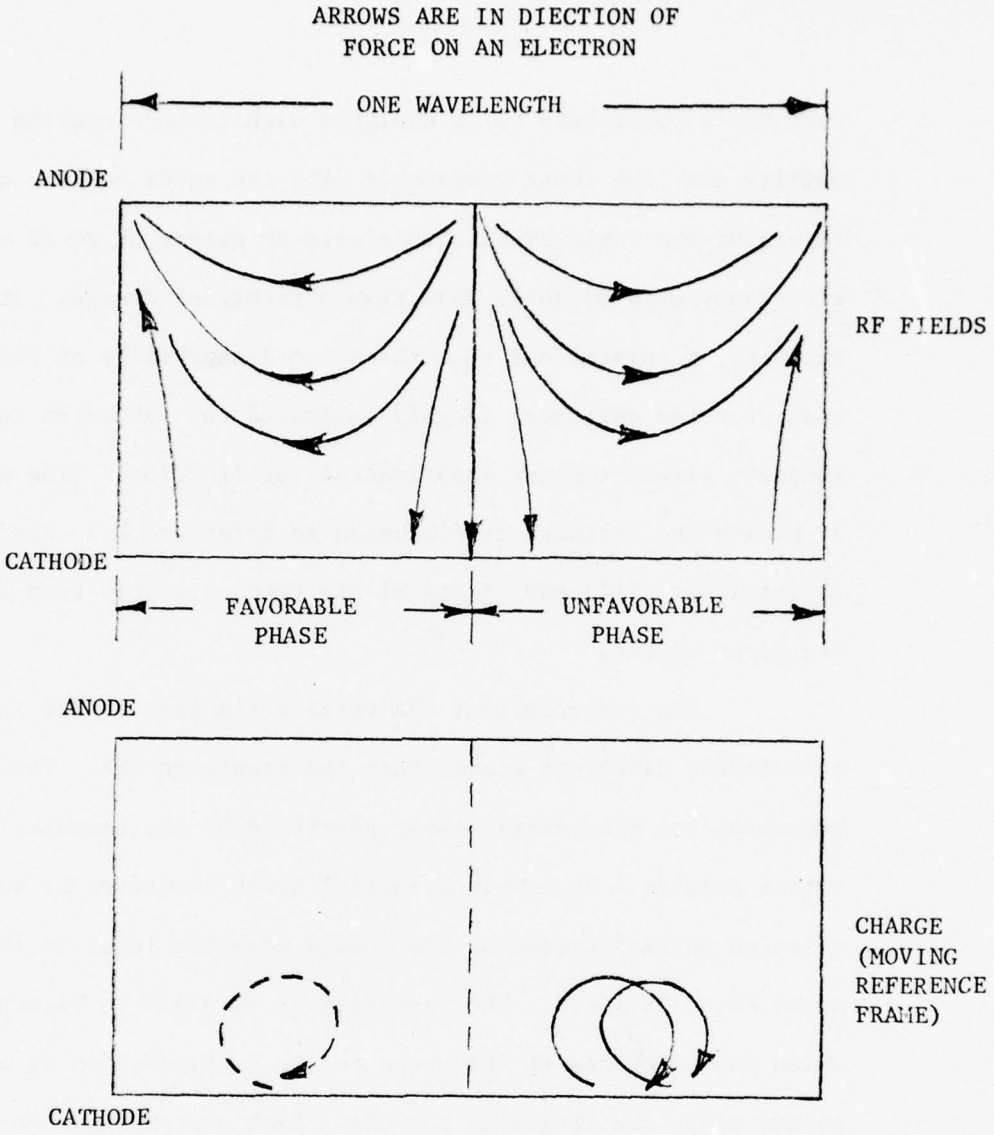

FIGURE 92

EARLY STAGE OF CHARGE BUILD UP--ELECTRONS IN THE UNFAVORABLE PHASE EXECUTE CYCLOIDS AND STRIKE THE CATHODE WITH ENERGY GAINED FROM THE RF WAVE. Sketch shows trajectories in a reference frame moving at the circuit wave velocity. Electrons in the favorable phase do not return to the cathode. Charge multiplication occurs in the unfavorable phase.

cathode bombardment energy per electron is greater than that required for unity secondary emission ratio, the charge in this phase multiplies. The charge in the favorable phase delivers energy to the circuit wave and does not return to the cathode. Since the charge delivered by the priming source is small, the charge in the unfavorable phase where multiplication is occurring rapidly grows until it far exceeds the charge in the favorable phase. During this part of the build up, energy is absorbed from the circuit wave and a bunch is forming in the unfavorable phase.

One of the results of the computer modeling studies is that substantial interchange of energy takes place between electrons within the space charge. Once a significant amount of space charge has built up (e.g., 10% of the ultimate charge), this interchange results in an increase in the average cathode bombardment energy per electron. The energy for the increased bombardment comes from other electrons which lose energy and no longer return to the cathode even though they remain in the unfavorable phase. At the input of the CFA, the cathode bombardment energy per electron is typically less than the value for maximum secondary emission yield. The increase in bombardment energy thus causes an increase in secondary emission yield, and the charge build up proceeds at an increased rate. The charge multiplication in the unfavorable phase now becomes self-sustained by the energy exchange

within the space charge. At the same time, the cathode power dissipation density rises to a high value (5 to 10% of the d.c. input power is dissipated over a short length of cathode). A large bunch of charge thus grows in the unfavorable phase and attenuation of the circuit wave continues. This region of the CFA is sketched in Figure 93.

Once a substantial charge bunch has built up in the unfavorable phase, charge transfer to the favorable phase begins. This region is sketched in Figure 94. This charge transfer occurs by two mechanisms--one is space charge forces in the bunch which tend to make the trailing edge of the space charge cloud rotate upward and backward. The other is a shift in phase of the circuit wave as a result of currents induced in the circuit by the charge bunch in the unfavorable phase. Once such charge transfer has proceeded to an adequate degree, amplification of the circuit wave begins. As the circuit wave grows its fields gradually focus an increasing amount of charge into the favorable phase.

Figure 95 shows a sketch of the space charge after transfer to the favorable phase has occurred. Amplification of the circuit wave is taking place, but the space charge bunch is still rather diffuse. Electrons are circulating within the cloud as indicated in the sketch. Anode dissipation begins when these electrons are first intercepted. In some cases, an initial peak in the dissipation density occurs because of the kinetic energy

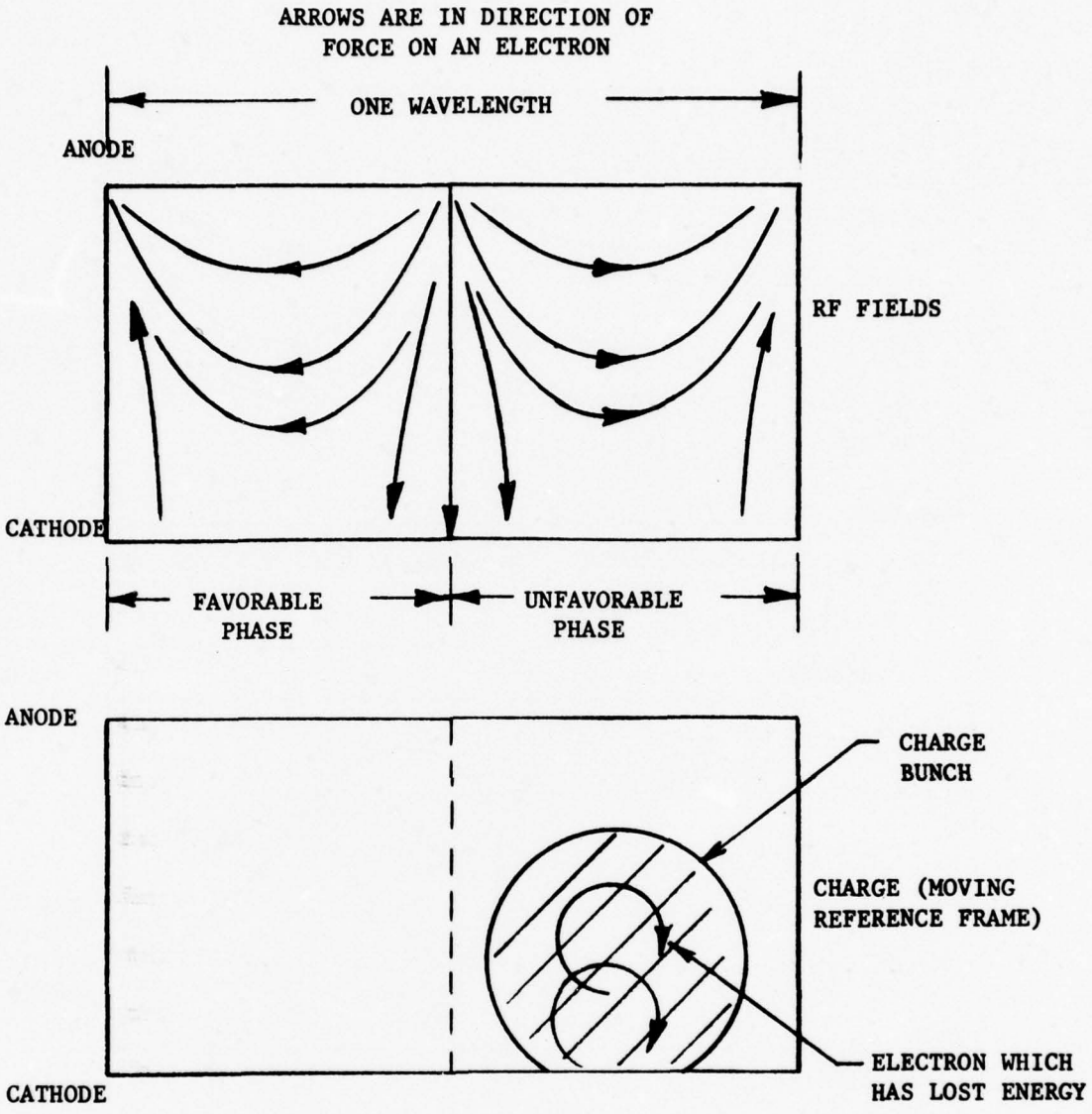

FIGURE 93

SUBSEQUENT STAGE OF CHARGE BUILD UP--ENERGY EXCHANGE OCCURS BETWEEN ELECTRONS IN THE UNFAVORABLE PHASE. This exchange is capable of supplying the cathode bombardment energy required for the build up. At this point, the build up becomes self sustaining.

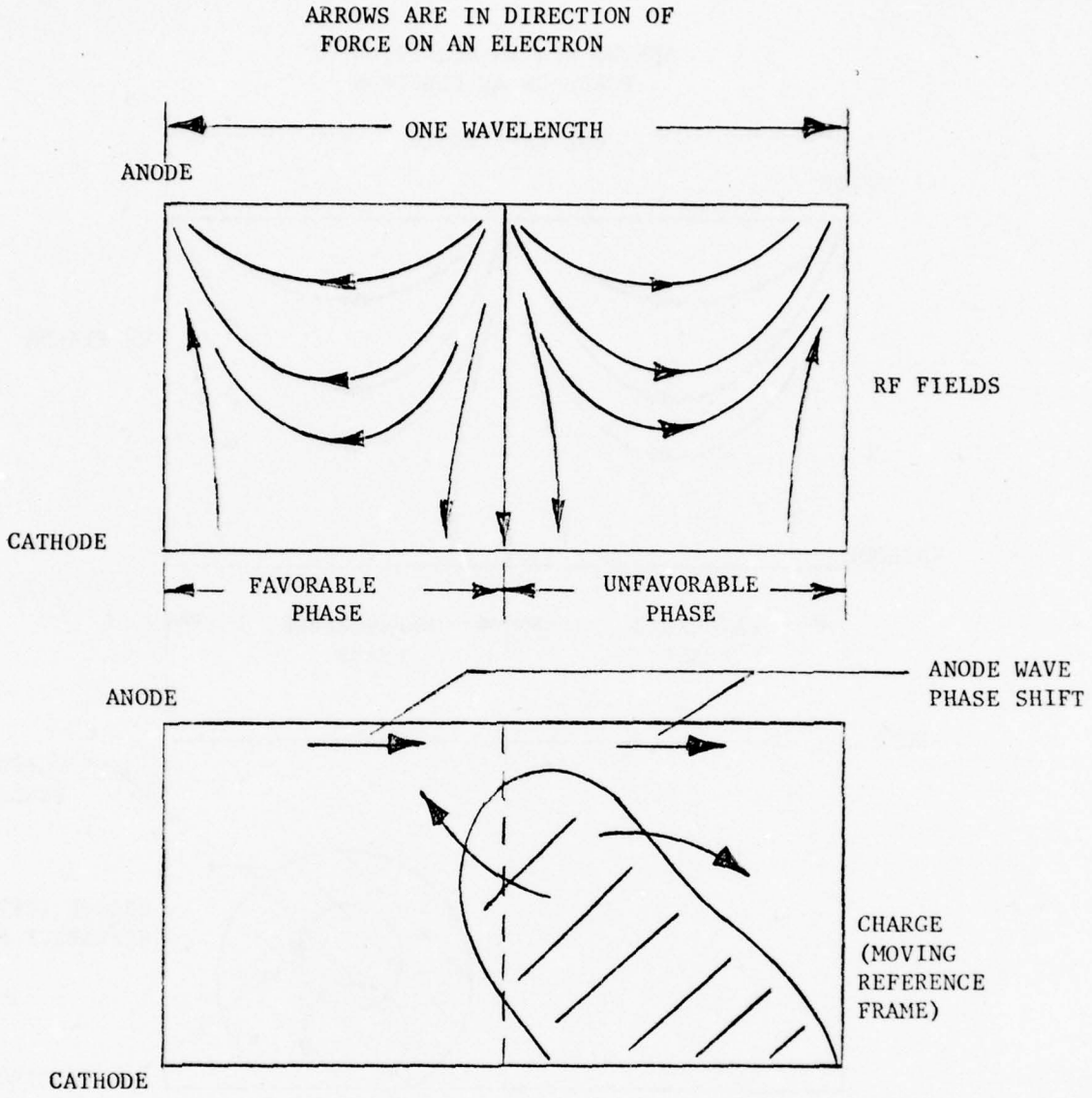

FIGURE 94

BEGINNING OF CHARGE TRANSFER TO THE FAVORABLE PHASE. Space charge forces cause roation of the charge cloud in direction shown by arrows. At the same time, the circuit wave phase shifts forward bringing part of the favorable phase over the charge cloud.

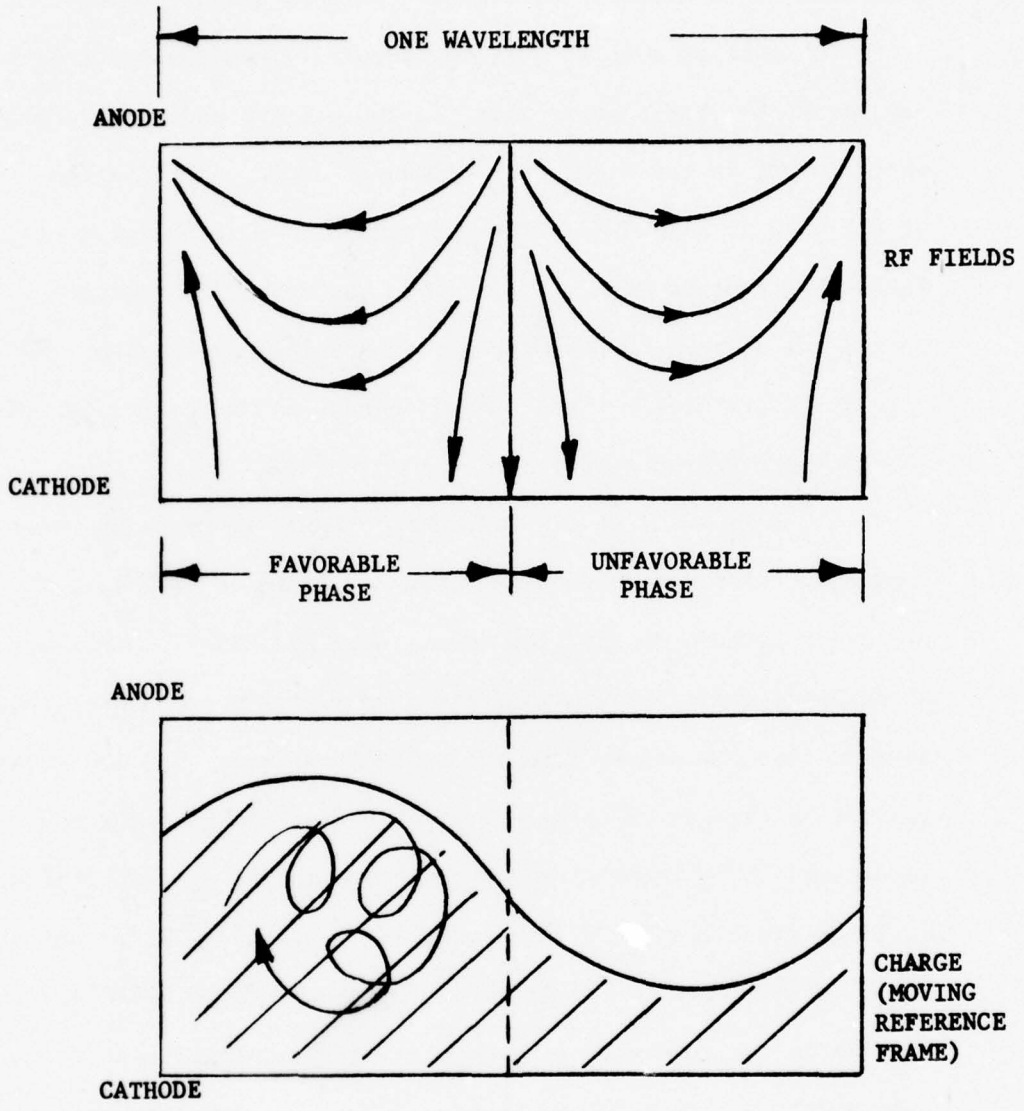

FIGURE 95

CHARGE DISTRIBUTION AFTER TRANSFER OF CHARGE TO THE FAVORABLE PHASE--A DIFFUSE BUNCH FORMS INITIALLY WITH ELECTRON CIRCULATION IN THE BUNCH AS SKETCHED.

associated with electron circulation in this diffuse cloud.

Further down the CFA the growing circuit wave field has organized the space charge into the typical hub and spoke pattern which exists in the high power region of a CFA. This region is sketched in Figure 96. The existence of space charge in this region has changed the d.c. fields so the E/B drift velocity at the hub surface is now slightly (about 10%) higher than the circuit wave velocity. This is the condition we require for high power generation in a CFA.

This model of the interaction leads to computed power growth and dissipation density curves as sketched in Figure 97. A maximum cathode dissipation occurs near the input. A maximum of anode dissipation occurs at the output with a secondary (lower) maximum just downstream from the cathode maximum. The model also leads to a view of the charge multiplication process as a non-linear one. The internal energy exchange in the space charge during build up maintains the process once it is started. An amount of RF power is delivered to the RF wave by the end of the build up which depends on the interaction space parameters, but is relatively independent of the input power--as long as the input power is adequate to initiate the charge build up. Thus, a type of RF saturation occurs early in the CFA.

The bunching which occurs during secondary emission multiplication of the space charge is essential to the gain mechanism in this type of CFA. Our computer simulations have shown that the gain is greatly reduced (e.g., from 20 to 6 dB for the same length)

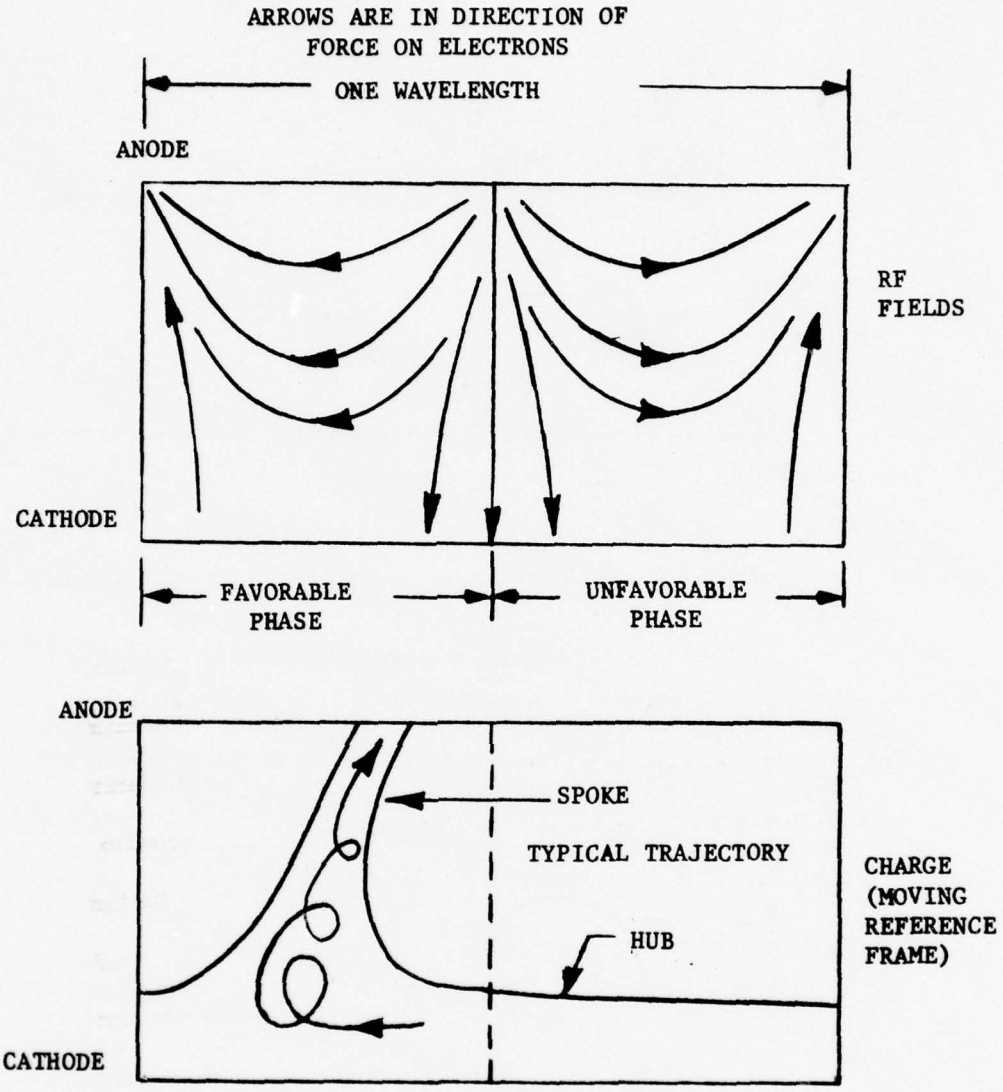

FIGURE 96

CHARGE DISTRIBUTION IN THE HIGH POWER REGION OF THE CFA SHOWING HUB AND SPOKE FORMATION.

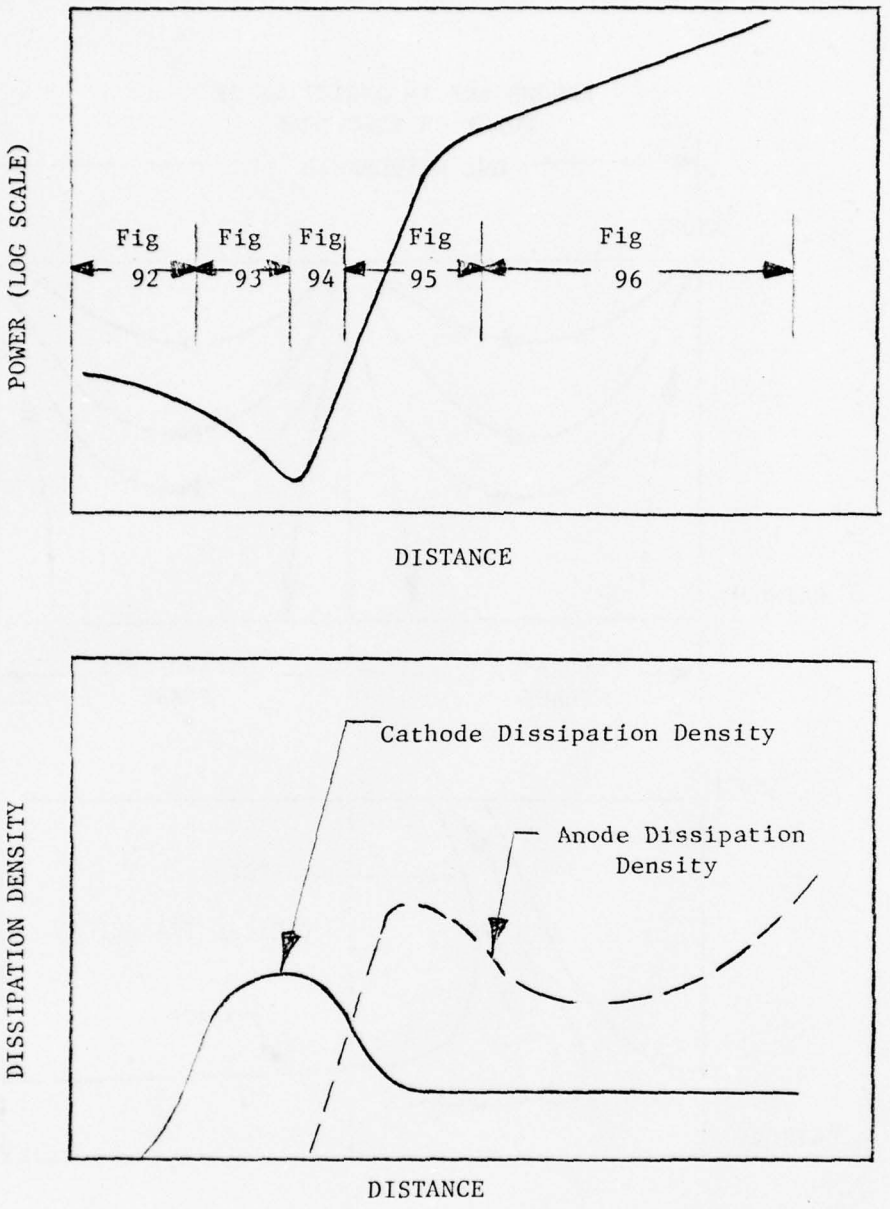

FIGURE 97

SKETCHES OF POWER GROWTH AND DISSIPATION DENSITY AS A FUNCTION OF LENGTH ALONG THE CIRCUIT. FIGURE NUMBERS ON UPPER CURVE SHOW APPROXIMATE REGIONS CORRESPONDING TO FIGURES 92-96.

if the cathode has substantial thermionic emission. If such thermionic emission exists, current is emitted in all phases of the RF wave during the charge build up and the initial bunching does not occur.

6.0 CONCLUSIONS

The computer model has been found to correlate well with an instrumented CFA when the interaction space geometry is uniform around the CFA circumference and operation occurs in the space charge-limited regime. The computer model in its present form is a useful tool for studying such designs.

Further verification of the computer model for emission-limited conditions is required. Proper values of cathode secondary emission ratio are needed for such studies. It is believed that no further modifications to the computer model will be required for studies in the emission-limited region. However, some trial and error adjustment of the input program parameters which control the number of rods emitted may be required to assure that enough rods are always present in the simulation.

The computer model has not properly simulated designs with a tapered interaction space. To obtain a proper simulation it may be necessary to both improve the accuracy of the inputs describing the cathode and to modify the taper procedures in the program.

Use of the computer model has begun to provide an improved understanding of the interaction mechanisms in an emitting sole CFA. Our findings must be taken as tentative at this time and sufject to further verification and possible modification as both further computer simulations and further experiments are conducted. These findings may be described in terms of three summary findings and sixteen more detailed findings as follows.

Three Summary Findings

1. The basic interaction mechanism used to generate high power in an emitting sole CFA does not have a small signal regime. This comes about because electron trajectories in the hub are subsynchronous with respect to the circuit wave. Significant RF field strengths are required to pull electrons from the hub. This means that CFA gain cannot be increased solely by increasing circuit length. Instead some other means must be found to provide some synchronous charge above the hub near the CFA input. Recirculated charge from output to input may be used for this purpose. Modification of the interaction space near the input is necessary to make best use of this recirculated charge. (This is what our taper appears to do in the SFD-261.) Alternately, the interaction space geometry near the input may be modified in a different manner so that charge may be drawn from the hub. Designs with 20 dB gain have been simulated using both of these approaches.

2. The recirculation of charge from output to input may be associated with a noise generation mechanism. The amount of charge in a spoke tends to fluctuate because of an instability at the base of the spoke. The amount of charge in the spoke at the CFA output determines the amount of charge recirculated to the input above the hub surface. In the computer model this charge instability leads to pass-to-pass variations in the computed power. These variations are belived to be symptomatic of noise in an actual CFA. Reduction of noise from this source might be

accomplished either by modifying the interaction space near the output to draw fresh charge into the spokes or alternately eliminating charge recirculation above the hub and changing the interaction space near the input to draw fresh charge from the hub.

3. A different type of gain mechanism exists near the input of a non-reentrant CFA. Selective build up of charge in the phase of the wave for which energy is absorbed by the electrons creates charge bunches. These bunches subsequently transfer to the favorable phase for delivery of RF energy to the circuit wave. This mechanism can give the CFA a gain boost near the input. Designs with 20 dB gain have been simulated on the computer. This type of CFA may incorporate a circuit sever.

Detailed Findings

The detailed findings may be divided into four major areas:

- understanding of charge build up effects in a non-reentrant CFA.
- understanding of hub charge distribution and trajectories in the hub.
- understanding of how spokes form out of the hub.
- understanding of what happens when spokes recirculate through the drift space from output to input.

Findings Concerning Charge Build Up

1. There is substantial energy exchange between electrons and consequently high cathode bombardment energy during the establishment of a space charge hub. In a non-reentrant CFA

the hub must be continuously re-established near the input of the tube. As a consequence, non-reentrant, emitting sole CFA's will have higher cathode bombardment than emitting sole CFA's.

2. If RF fields are present during the charge build up as is the case in a non-reentrant CFA (or a reentrant CFA during starting) and if the cathode is primarily a secondary emitter, the charge build up occurs selectively in the "unfavorable phase" in which electrons gain energy from the RF wave. Subsequent transfer of this charge to the favorable phase can result in a substantial "gain boost" to the CFA.

3. A non-reentrant CFA may incorporate a circuit sever at the point where the charge bunch has built up and is starting to transfer to the favorable phase. (See Reference 4.)

Findings Concerning the Hub

4. The charge distribution and trajectory shapes of electrons in the hub are different from those suggested by simple theoretical models. Because of energy exchange between electrons in the hub, some of the electrons do not return to the cathode.

5. The amount of charge in the hub readjusts rapidly to any change in anode-cathode spacing. Advantage may be taken of this fact in designing the collector of a non-reentrant, emitting sole CFA--i.e., by increasing the spacing prior to the collector to reduce the charge entering the collector region.

Findings Concerning Spoke Formation

6. Weak RF fields cannot draw charge from the hub into the spokes at the normal operating voltages of the CFA.

This finding is in direct contradiction with the view previously held. It had been thought that if the E/B drift velocity at the top of the hub were made equal to the circuit wave velocity (V-cathode equal to V-Hartree), charge could be drawn from the hub by weak RF fields. The reason this does not happen is that the average velocity of the electrons in the hub is much less than the velocity of the circuit wave. Significant RF field strengths are required to overcome the lack of synchronism and draw charge out of the hub. A consequence of this finding is that the required input power may be not indefinitely decreased (gain increased) by increasing circuit length.

7. Charge can be drawn up into the spokes by increasing the space charge velocity relative to the circuit wave. The ratio of these velocities is usually expressed in terms of the ratio of cathode voltage (V_K) to Hartree voltage (V_H) which is approximately equal to the ratio of the E/B drift velocity at the top of an ideal Brillouin hub to the circuit wave velocity. Increasing the average electron velocity decreases the degree of asynchronism between the hub charge and the circuit wave. For the SFD-261 at mid band, an increase of cathode voltage to about 35% above Hartree is required to draw substantial charge from the hub with a 0.01 Po peak input signal. With a 0.08 Po peak input the cathode voltage need be only 10% above Hartree. The reason why the charge drawn into the spokes is critically dependent on the velocities and fields may be seen be reference to Figure 66.

As a trajectory approaches the base of the spoke a branch point is reached where the trajectory will either go up into the spoke or back down into the hub. The relative values of the electron velocity and the local E/B velocity computed using the sum of d.c., RF and space charge ields determines which way the electron goes. If the electron velocity is greater than the local E/B velocity, the downward magnetic forces will predominate and the electron will return to the hub. If the electron velocity is less than the local E/B velocity, the upward electric field forces will predominate and the electron will go upwards into the spoke. Small changes in the fields can make a large change in the number of electrons drawn into the spokes. This is why the V-I curve of the CFA is so steep.

8. Stable spoke formation occurs only below a certain ratio of cathode-to-Hartree voltage. The higher the RF fields, the higher the maximum ratio of cathode-to-Hartree voltage. This phenomenon had been expected based on space charge-free trajectory studies conducted many years ago. The details differ somewhat from our expectations. For the SFD-261 at the upper end of the operating band a peak input power of 0.08 Po will result in stable spoke formation for a V_K/V_H ratio of 1.2, but not for a V_K/V_H of 1.30. Normal operation is at a V_k/V_H ratio less than 1.2. As the peak input power is decrased the permissible V_K/V_H ratio is reduced. As peak power is further reduced we reach a situation where we cannot

draw a useful amount of charge into the spoke at the maximum V_K/V_H ratio for which stable spokes form. At 0.01 Po peak input, a V_K/V_H ratio of about 1.35 is required to draw useful charge into the spoke. Stable spokes will, however, be formed if the V_K/V_H ratio is dropped to 1.15 once charge has been drawn up from the hub. The reason a lower V_K/V_H ratio is required for spoke formation than for drawing up charge at 0.01 Po drive is that the electric fields above the hub are higher than they are in the hub. Thus a lower voltage is required to obtain wave than is required to obtain synchronism of hub electrons. The requirements for drawing charge and forming spokes are incompatible in the SFD-261 at the 0.01 Po peak input level. They are compatible at the rated drive level of 0.08 Po. Ways around this incompatibility will be discussed below.

9. The flow of charge through the spokes in the high power regime of the CFA is not smooth. An instability occurs at the base of the spokes which causes the charge to flow through the spokes in pulsations. This effect contributes to pass-to-pass variations in our computations and possibly to noise in a real CFA.

This phenomenon has been subjected to a number of tests to detrmine whether it is a numerical instability of the computer model rather than a property of the real CFA. Neither changes in program granularity nor introduction of substantial smoothing of of the potential array have any effect on it. The period of the

instability is relatively long (30 time steps) and does not appear to be related to short time numerical fluctuations. At this time, it appears to be a real phenomenon.

The nature of the instability can be seen by referring to Figure 66. An increase in spoke charge depresses the potential and reduces the fields at the base of the spoke. This, in turn, reduces the charge drawn into the spoke and subsequently results in a spoke of sparse charge. The amount of charge drawn into the spoke tends to be self compensating, but with hunting about an average value.

Findings Concerning Charge Recirculation

10. Debunching of charge in the drift space is incomplete. Debunching is improved when there is a large amount of charge recirculating above the hub surface. The incomplete debunching produces less regeneration than might be expected at first because the recirculating charge is not synchronous with the RF wave at the input. (The reason for this is described in Finding 12 below.)

11. Differences in the space charge distribution at the output from pass-to-pass in our computations causes differences in the amount and distribution of charge at the input of the next pass which affect the gain of the next pass. The pulsations of charge flow through the spokes contributes to charge variations at the output. As a result, the computations show pass-to-pass variations. It is believed that these variations may also exist in a real CFA and that they may be correlated with noise output

of a CFA. If so, this means that the recirculation of charge is associated with a mechanism of noise generation in a CFA. Design modifications which reduce pass-to-pass variations may, therefore, reduce CFA noise. This is a highly tentative hypothesis at this time.

12. The E/B velocity above the hub at the output is greater than the circuit wave velocity. The spokes are kept synchronous with the wave by the RF fields. This condition is necessary to keep charge flowing into the spokes. The charge recirculated above the hub rotates forward and downward and debunches in the drift space. In the case of a uniform interaction geometry it returns to the input with a velocity higher than the circuit wave velocity. If the RF fields at the input are weak, they may have difficulty in interacting with this asynchronous charge. The situation may be improved by tapering the interaction space as shown in Figure 87. The electron velocity relative to the circuit wave velocity is reduced at the input to make it more nearly equal to the wave velocity. Once the rercirculating charge has interacted with the wave, the relative electron velocity may be increased to that required in the high power region of the CFA.

13. Since weak RF fields cannot draw power from the hub at the normal voltages, some other source of charge above the hub must be provided to obtain gain at the input in a high gain CFA. One method was discussed in Finding 7 above. Another method is to use the recirculating charge. To insure that there is enough recirculating charge it appears necessary to increase the V_K/V_H ratio

for a short distance at the output to draw additional charge into the spoke. This charge then recirculates to the input where it can be used to provide the gain until the RF level has grown to a point where additional charge may be drawn from the hub. The use of a fairly large amount of recirculating charge will improve debunching in the drift space. Additional debunching can be accomplished by making the drift velocity slightly variable over the height of the drift space parallel to the magnetic field.

Findings Concerning the Cathode Properties

14. The secondary emission yield of the cathode does not appear to affect performance as long as it is high enough--space charge limitation occurs as long as the emission is adequate. The secondary emission yield does affect the maximum current which may be drawn.

15. The energy of electrons incident on the cathode comes largely from energy exchange within the hub and only secondarily from energy exchange with the RF fields of the circuit wave. As a consequence, the variation in energy of electrons collected on the cathode as a function of disance is comparatively small. Under full space charge-limited conditions, the energy of incident electrons at the output may be no more than the incident energy which results from interaction with the RF input wave during starting and before space charge build up.

Finding Concerning Axial Variation

16. The interaction may be made uniform over the axial height of the circuit by properly shaping the end hats.[8] The design technique involves using the potential distribution in the interaction space as computed by the large signal program and then performing a boundary matching procedure at the edge of the space charge similar to that done when designing an O-type Pierce gun.

Sample Designs

The computer model has also been used in preliminary studies of possible CFA designs having 20 dB of gain. These exercises have indicated how such modeling may in the future become an important part of the CFA design process.

References

1. S.P. Yu, G.P. Kooyers, and O. Buneman, "Time Dependent Computer Analysis of Electron Wave Interaction in Crossed-Fields", Journal of Applied Physics, Volume 36, No. 8, Page 2550, August 1965.

2. S.P. Yu, G.P. Kooyers, and P.A. Vartinian, "Applied Research on Time Sequence Analog of Basic Distributed-Emission, Crossed-Field Interaction", Technical Report AFAL-TR-64-310, Air Force Avionics Laboratory, Wright-Patterson Air Force Base, Ohio, April 1965.

3. Richard Thomas of NRL--Private Communications.

4. H.L. McDowell--Multiband Radar Transmitter Study--Crossed-Field Approaches--Final Report on Contract No. F30602-76-C-0265. RADC-TR-77-317, September 1977.

5. H.L. McDowell--A 10 GHz Coherent Power Source Employing an Emitting Sole, Crossed-Field Amplifier in an Injection Locked Loop. Final Report on Contract No. 33165-76-C-1349 for U.S. Air Force, Avionics Laboratory, WRAPF, December 1977.

6. H.L. McDowell--User's Manual for Distributed Emission Crossed-Field Amplifier Modeling Program--Version DECFA7. Prepared for U.S. Navy Ocean Systems Center, San Diego, California. Contract No. N00123-75-C-1294, December 1977.

7. G.K. Farney and H.L. McDowell, CFA Design Improvement Program, Semi-Annual Report No. 1 (July 1, 1975 - December 31, 1975) for U.S. Navy Ocean Systems Center, San Diego, California. Contract No. N00123-75-C-1294.

8. G.K. Farney and H.L. McDowell--See No. 7. Semi-Annual Report No. 2 (January 1, 1976 - June 30, 1976).

9. H.L. McDowell, Research on Super Power Microwave Amplifiers, Quarterly Reports Nos. 1-4, Contract DA36-039-SC-85379 for U.S. Army Electronics Command, 1961.

10. R.M. Jepsen and M.W. Muller, J. Applied Physics, 22, 1196 (1951).

11. R.M. Jepsen, Enhanced Emission in Okress Crossed-Field Microwave Tubes--Volume I, Academic Press, 1961.

12. G. Hok, Statistical Theory of the Magnetron Space Charge in Okress Crossed-Field Microwave Tubes--Volume I, Academic Press, 1961.

13. J. Feinstein, Planar Magnetron Theory and Applications-In Okress-Crossed-Field Microwave Tubes, Volume 1, Academic Press, 1961.

14. E.K. Shaw, Transactions of IEEE--A Professional Group on Electron Devices.